





KU Leuven  
Biomedical Sciences Group  
Faculty of Pharmaceutical Sciences  
Laboratory for Radiopharmaceutical Research



# Development and evaluation of HDAC and Hsp90 PET ligands

Koen VERMEULEN

Jury:

Promotor: Prof. Dr. Guy Bormans  
Co-promotor: Prof. Dr. Dag Erlend Olberg  
Chair: Prof. Dr. Arthur Van Aerschot  
Jury members: Prof. Dr. Michel Koole  
Prof. Dr. Matheus Froeyen  
Dr. Emmanuelle Briard  
Prof. Dr. Philip Elsinga

Dissertation presented in partial  
fulfilment of the requirements  
for the degree of Doctor in  
Pharmaceutical Sciences

Leuven, 01-07-2019

Doctoral thesis in Pharmaceutical Sciences

Monday 1<sup>st</sup> of July 2019, 17:00h

Auditorium van de Tweede Hoofdwet

Thermotechnisch Instituut

Kasteelpark Arenberg 41

3001 Heverlee

Promotor: Prof. Dr. Guy Bormans

Co-promotor: Prof. Dr. Dag Erlend Olberg

Laboratory for Radiopharmaceutical Research

Faculty of Pharmaceutical Sciences

Herestraat 49, O&N II, box 821

B-3000 Leuven

## DANKWOORD - ACKNOWLEDGEMENTS

Vijf jaar geleden begon ik aan een avontuur om nooit te vergeten. Tijdens mijn masterstage in het Labo voor Radiofarmacie, werd ik geprikkeld om zelf in het wetenschappelijk onderzoek te stappen. Ik ben enorm dankbaar om de kansen die ik toen heb gekregen en ik ben dan ook met ontzettend veel motivatie en enthousiasme mijn project gestart om U vandaag met enige trots mijn boekje voor te stellen. Wat zeker niet vergeten mag worden is dat ik dit avontuur niet alleen ben aangegaan. Op mijn route kreeg ik de kans om talrijke inspirerende collega onderzoekers te ontmoeten. Zonder mijn promotoren, juryleden, collega's, vrienden en familie had ik mijn doctoraatsonderzoek nooit op een succesvolle manier kunnen voltooien. Een welgemeende dankuwel is dus zeker op zijn plaats.

Als eerste en voornaamste wil ik mijn bijzondere dank uitdrukken aan mijn promotor. Guy, bedankt voor de kans die je me hebt gegeven om mijn doctoraat op het labo te starten en de raad en daad onderweg. Het is een talent om individuele mensen binnen een groep te leiden, op hun gemak te stellen en te motiveren. Mede dankzij jou heerst er een leuke sfeer op het labo die ons allen motiveert en die ervoor zorgt dat ik elke dag graag naar het werk kom. Verder sta je altijd open voor vragen of discussies, op elk moment van de werkdag, iets wat enorm geapprecieerd werd en ervoor gezorgd heeft dat ik steeds opnieuw werd uitgedaagd. Daarbuiten heb ik ook mogen ervaren dat professoren ook maar mensen zijn, die graag plezier en leute maken. Met jou op congres gaan was dan ook altijd een ervaring op zich.

Dag Erlend, thank you for the support and feedback, especially during the Santacruzamate A project and my doctoral follow up sessions.

Ook een welgemeende dankuwel aan de Pater Familias van de radiofarmacie. Fons, bedankt voor de verrijkende discussies. Ook al ben je nu op een deugdoend pensioen, je aanwezigheid en betrokkenheid met het labo werd zeer gewaardeerd.

Next, I would like to thank my jury members, Prof. Dr. Michel Koole, Prof. Dr. Mathy Froeyen, Prof. Dr. Philip Elsinga, Dr. Emmanuelle Briard and Prof. Dr. Arthur Van Aerschot, for taking their time to review this thesis manuscript, providing me with feedback which helped to improve it.

Special thanks go out to Dr. Muneer Ahamed, Dr. Joan Lecina and Dr. Emilie Billaud, for guiding me with organic synthesis. Besides work related discussions, I really enjoyed the off topic conversations and I was sad to have to say goodbye to you guys. I wish you all the best in future endeavours.

Een belangrijk deel van het praktisch werk dat uitgevoerd wordt op het labo zou niet mogelijk zijn geweest zonder de vakkundigheid van Julie, Pieter, Ivan, Jeroen, Jana en Michiel. Julie, danku om op te treden als muizen/ratten injectiespecialist/massamoordenaar. Je hebt soms moeten afzien met mijn geplande experimenten gezien mijn protocollen veelal onvolledig waren. Desondanks, is het het toch allemaal op zijn pootjes terecht gekomen dankzij jou hulp. Ivan, Pieter, Jeroen, bedankt om te springen telkens ik vroeg om te springen. Jullie hulp en kennis van HPLC, LC/MS en synthesesmodules heeft meermaals bijgedragen tot een goed verloop van mijn doctoraat. Verder voeg ik hier ook graag Dr. Sofie Celen aan

## Acknowledgements

---

toe. Sofie, bedankt voor de raad en daad bij het opzetten van experimenten en de hulp bij de radiosyntheses. Bedankt voor alles wat je voor het labo doet.

Over de jaren heen heb ik het privilege gehad om met vele interessante collega's, en ondertussen vrienden, samen te werken. Maxime and Bala, we started out together, struggled together and also enjoyed our time here together, a big thank you for the really nice experience! Verder is er ook de 'oude' garde van het labo, Maarten bedankt om me gedurende de masterjaren te begeleiden en warm te maken voor het doctoraatsonderzoek, alsook voor de raad en daad in het begin van mijn doctoraat. Dieter, bedankt voor de veelvuldigheid aan kennisoverdracht. Frederik, bedankt voor de hulp en kennisoverdracht en ook de leuke tijd gedurende de verschillende congressen. Het was ook tof om met jou de opleiding tot radiofarmaceut te volgen ☺. Lieven, ik was blij dat je wegging :-D. Uiteraard ook jij heel erg bedankt voor de uitleg, de hulp tijdens de verschillende radiosyntheses en experimenten. Daarbuiten viel je ook best mee ☺. Joost, ollige Hollander, hartstikke bedankt voor de hulp bij mijn eerste radiosyntheses, ook Pieter wil ik hiervoor nogmaals bedanken. Uta, herzlich dankeschön voor het delen van je uitgebreide ervaringen.

Out with the old, in with the new. Kaat, ik ben blij dat je uiteindelijk in ons team zit. Ik ben er zeker van dat je een knaller van een doctoraat gaat afleggen. Je hebt de leegte die Lieven achter liet ook goed opgevuld. T rence, keep up the good work, you will definitely end up with a nice PhD. Mathilde, merci bien pour les conversations Franco-N erlandais, c' tait vraiment chouette (tof). Irwin and Stephen, it is nice having you guys around, good luck with your PhD.

Naast het doctoreren, heb ik ook meerdere dagen mijn broek versleten aan verschillende practicasessies. Hierbij dan ook een dankuwel aan de mensen die deze practica in goede banen hebben geleid. Steffi, Lieven, Monica, Petra, Herman, Suzy, Jasper, Nicolas en Walter bedankt voor de vijf mooie jaren en de gezellige sfeer die jullie hebben gecre erd in zowel de BOT labo's als bij formulering en bereiding. Practica geven doe je niet alleen, daarom ook nog een geweldige dankuwel aan mijn mede-assistenten. Voor BOT I en BOT III, dankuwel aan Lien, Dani lle, Chlo , Glenn, Juan, Kaat, Michiel, Arno, Donaat en Liesl. Voor formulering en bereiding, bedankt Johan, Philippe, Bart, Jens, Jari, Yannick en Ann-Sofie.

Chantal en An, dankuwel voor de hulp bij de administratie, Rita bedankt om ons labo in orde te houden en ook voor de leuke babbels.

Uiteraard mag ik de mensen van nucleaire geneeskunde/radiofarmacie niet vergeten. Kim, Tjibbe, Marva, Bert (x2), Julie, Sofie, Stef, Martin en al de rest van het team, bedankt voor de aangename conversaties en hulp als er weer iets misliep bij de radiosyntheses. Tjibbe, jammer dat je het niet kon verkroppen dat Jeroen en ik het lozingsrecord hadden gebroken en je er per se over moest gaan, maar het is je gegund ;-).

Verschiedende mensen van de MoSAIC wil ik ook bedanken. Ann, Tine en Jens, bedankt voor de hulp bij de dierexperimenten en het vastleggen van de  $\mu$ PET-scans. Bart, Bryan, Sarah, Melissa, Liesbeth, Shweta, Peter bedankt voor de leuke conversaties en de hulp. Special thanks to Prof. Michel Koole and Dr. Chris Cawthorne, for the superb help with reconstructing data and analysis of  $\mu$ PET scans and the fruitful discussions.

Ook wil ik graag Prof. Matheus Froeyen afzonderlijk bedanken voor zijn hulp bij de moleculaire dockingstudies gedurende het Santacruzamate A project. In this regard, I also want to thank Dr. Michaël Schneckenburger and Prof. Marc Dietrich from the LBMCC in Luxembourg for the fruitful discussions and the collaboration on the HDAC project.

Evelyne en de professoren van het switch labo, Prof. Schymkowitz en Prof. Rousseau, hartelijk bedankt voor de samenwerking met het [<sup>11</sup>C]NMS-E973 project. Ik vind dat we er zeker iets moois van hebben gemaakt.

Thank you to the people from Novartis, Emmanuelle, Yves and Joseph. Thank you for the fruitful discussions concerning [<sup>11</sup>C]YC-72-AB85. Emmanuelle, a big thank you for showing interest in the poster I presented at ISRS 2017 concerning [<sup>11</sup>C]NMS-E973, as this opened the door for the [<sup>11</sup>C]YC-72-AB85 project.

Bedankt ook aan alle homeboys and flygirls van Geel/Olen en de matties van farma om de nodige ontspanning buiten het doctoreren te verzorgen.

Een dikke merci aan de schoonfamilie, Gery en Carine, Axelle en Jente, Vincent en Geertrui, bedankt om me op te nemen in het warme Limburgse nest!

Een allegrootste merci gaat uit naar de belangrijkste mensen in mijn leven, Ma en Pa bedankt voor de steun over de afgelopen jaren (eigenlijk over al mijn levensjaren), ik kan altijd op jullie rekenen en dat brengt me groot plezier. Ook Dr. Karen Vermeulen (de 1<sup>ste</sup> Dr. K. Vermeulen van de familie), expert in kiekens en wonend in het kiekensbos wil ik bedanken. Karen mercikes om mijn grote zus te zijn, je bent daar echt mee gezegend. Je bent altijd een groot voorbeeld voor mij geweest. Jonas, bedankt om er mee voor te zorgen dat er binnenkort een uitbreiding van de familie komt, ik kan er al niet op wachten en ge zijt ook nen toffe Pé!

Charlotte, het is moeilijk om met woorden te beschrijven wat je voor mij betekent. Jouw onuitputtelijke toewijding, energie, efficiëntie en goesting in het leven is bewonderingswaardig en uitermate aanstekelijk. Zonder jouw steun en begrip was mijn doctoraatsperiode een pak lastiger geweest. Bedankt voor het aanhoren van mijn klaagzang als er weer eens een experiment of radiosynthese mislukte. Ook bedankt voor de tijd die je hebt besteed aan het nalezen van teksten en presentaties en voor het optreden als testpubliek. Dit hoofdstuk is nog maar pas afgerond of het nieuwe staat al voor de deur. Ik kan nu volop gaan uitkijken naar onze mooiste dag en ik ben er zeker van dat er samen met jou alleen maar meer mooie dagen zullen volgen! Voor alles wat je voor me doet en je onvoorwaardelijke liefde, een ongelooflijke dankjewel.

Mercikes,

Koen





# TABLE OF CONTENTS

<b>DANKWOORD - ACKNOWLEDGEMENTS</b>	i
<b>TABLE OF CONTENTS</b>	v
<b>LIST OF ABBREVIATIONS</b>	vii
<b>CHAPTER I</b>	1
1. EPIGENETICS	3
2. HISTONE DEACETYLASE	4
3. HDAC6	7
4. HEAT SHOCK PROTEINS	10
5. LINK BETWEEN EPIGENETICS, HDAC(6) AND HSP90	16
6. MOLECULAR IMAGING	17
7. MOLECULAR IMAGING OF HDACS	24
8. MOLECULAR IMAGING OF HSP90	28
<b>OBJECTIVES AND OUTLINE OF THE THESIS</b>	32
<b>CHAPTER II</b>	33
1. INTRODUCTION	36
2. MATERIALS AND METHODS	38
3. RESULTS AND DISCUSSION	44
4. CONCLUSION	50
<b>CHAPTER III</b>	51
1. INTRODUCTION	54
2. MATERIALS AND METHODS	58
3. RESULTS	63
4. DISCUSSION	69
5. CONCLUSION	72
<b>CHAPTER IV</b>	73
1. INTRODUCTION	76
2. MATERIALS AND METHODS	79

## **Table of contents**

---

3. RESULTS	85
4. DISCUSSION	96
5. CONCLUSIONS	100
<b>CHAPTER V</b>	101
1. INTRODUCTION	104
2. MATERIALS AND METHODS	108
3. RESULTS	115
4. DISCUSSION	121
5. CONCLUSIONS	124
<b>CHAPTER VI</b>	125
1. PET IMAGING OF HDACS	127
2. PET IMAGING OF HSP90	130
3. FUTURE PERSPECTIVES	135
<b>SUMMARY</b>	137
<b>SAMENVATTING</b>	140
<b>REFERENCES</b>	144
<b>SCIENTIFIC ACKNOWLEDGEMENTS AND CONFLICT OF INTEREST</b>	157
<b>CURRICULUM VITAE</b>	159
<b>LIST OF PUBLICATIONS</b>	160

# LIST OF ABBREVIATIONS

%ID	Percentage of injected dose
[ <sup>18</sup> F]FDG	2-[ <sup>18</sup> F]fluoro-2-deoxy-D-glucose
17-AAG	17-allylamino-17-demethoxy-geldanamycin
AD	Alzheimer's disease
ADME	Absorption, distribution, metabolism and excretion
AHA1	ATPase homologue 1
AKT	Protein kinase B
ALS	Amyotrophic lateral sclerosis
AMPA	α-amino-3-hydroxy-5-methyl-4-isoxazolepropionic acid
ANOVA	Analysis of variance
AR	Androgen receptor
ATCC	American Type Culture Collection
AUC	Area under the curve
BBB	Blood-brain barrier
BHB	Bloed-hersenbarrière
B <sub>max</sub>	Maximum density of receptors
BP	Binding potential
BSA	Bovine serum albumin
BTB	Blood-testis barrier
BUZ	Ubiquitin binding domain of HDAC6
CD	C-terminal domain
CDK1/5	Cyclin-dependent kinase 1 or 5
CHIP	Carboxy terminus of Hsp70-interacting protein
CNS	Central nervous system
CpG	Cytosine-phosphoryl-guanine
Cpm	Counts per minute
CTCL	Cutaneous T-cell lymphoma
D <sub>2</sub> R	Dopamine 2 receptor
DAPI	4, 6-diamidino-2-phenylindole
DBU	1,8-diazabicyclo[5.4.0]undec-7-ene
DC <sub>50</sub>	Half-maximal depolymerisation concentration
DCM	Dichloromethane
DLU	Digital light units
DIPEA	N,N-Diisopropylethylamine

## List of abbreviations

---

DMAP	4-dimethylaminopyridine
DMEM	Dulbecco's Modified Eagle's Medium
DMF	N,N-dimethylformamide
DMSO	Dimethylsulfoxide
ECM	Extracellular matrix
EDC-HCl	N-(3-Dimethylaminopropyl)-N'-ethylcarbodiimide hydrochloride
EGFR	Epidermal growth factor receptor
eHsp90	Extracellular Hsp90
EOS	End of synthesis
ER	Endoplasmic reticulum
ESI	Electrospray ionisation
EtOAc	Ethylacetate
EtOH	Ethanol
FACS	Fluorescence-activated cell sorting
FDA	Food and Drug Administration
FEt	Fluoroethyl
FITC	Fluorescein isothiocyanate
FKBP52	FK506-binding protein 52
GABA	$\gamma$ -aminobutyric acid
GAPDH	Glyceraldehyde 3-phosphate dehydrogenase
GC	Gas chromatography
GR	Glucocorticoid receptor
Grp94	94 kDa glucose regulated protein
GSK3 $\beta$	Glycogen synthase kinase-3 beta
H <sup>-</sup>	Hydride
H <sup>+</sup>	Proton
H <sub>2</sub>	Hydrogen gas
H2A	Histone 2A
H3K14	Lysine 14 of histone 3
HAT	Histone acetyl transferase
HBD	Hydrogen bond donors
HD	Huntington's disease
HDAC	Histone deacetylase
HER2	Human epidermal growth factor receptor 2
HIF-1 $\alpha$	Hypoxia-inducible factor-1 $\alpha$
HPLC	High-performance liquid chromatography
HSF1	Heat shock factor 1

---

Hsp	Heat shock protein
Hsp90 $\alpha$	Hsp90AA1
Hsp90 $\beta$	Hsp90AB1
HSR	Heat shock response
IC <sub>50</sub>	Half-maximal inhibitory concentration
i.p.	Intraperitoneal
i.v.	Intravenous
K <sub>D</sub>	Equilibrium dissociation constant
KDAC	Lysine deacetylase
K <sub>i</sub>	Inhibitory constant
MA	Molar activity
MDCK	Madin-Darby Canine-Kidney
MD	Middle domain
MM	Multiple myeloma
MMP2	Matrix metalloproteinase 2
MPO	Multiple parameter optimization
MRI	Magnetic resonance imaging
MT	Microtubule
MTOC	Microtubule organizing centre
Mw	Molecular weight
MDR1	Multi-drug resistance protein 1
NAD <sup>+</sup>	Nicotinamide adenine dinucleotide
ND	N-terminal ATP binding domain
NES	N-terminal nuclear export signal
NHP	Non-human primate
NLS	Nuclear localisation signal
NMP	N-methyl 2-pyrrolidone
NMRI	Naval Medical Research Institute
NSB	Non-specific binding
NSCLC	Non-small cell lung cancer
p.i.	Post injection
PBMC	Peripheral blood mononuclear cells
PBS	Phosphate buffered saline
PD	Parkinson's disease
PD-L1	Programmed death ligand 1
PET	Positron emission tomography
PFP	Protein free plasma

## List of abbreviations

---

P-gp	P-glycoprotein
Ppm	Parts per million
PSA	Prostate specific antigen
PTCL	Peripheral T-cell lymphoma
PTM	Post-translational modification
PUMA	p53 upregulated modulator of apoptosis
Ras	Retrovirus-associated DNA sequences
RCP	Radiochemical purity
RCY	Radiochemical yield
RMS	Root mean square
ROI	Region of interest
RPD3	Reduced potassium dependency 3
RP-HPLC	Reversed phase-HPLC
RCSB-PDB	Research Collaboratory for Structural Bioinformatics–Protein Data Bank
SAHA	Suberoylanilide hydroxamic acid
Sirt	Sirtuins
SMA	Spinal muscular atrophy
SPECT	Single photon emission computed tomography
SUV	Standardized uptake value
T <sub>1/2</sub>	Half-life
TAC	Time activity curve
Tau	Tubulin associated unit
TBS	Tris buffered saline
TEA	Triethylamine
TFA	Trifluoroacetic acid
TGF- $\alpha$	Tumour growth factor $\alpha$
THF	Tetrahydrofuran
TLC	Thin layer chromatography
TMS	Trimethylsilane
TOF-HRMS	Time-of-flight high-resolution mass spectrometer
tPSA	Topological polar surface area
TRAP1	Tumour necrosis factor receptor associated protein 1
Tris	Tris(hydroxymethyl)aminomethane
UPS	Ubiquitin-proteasome system
VCP/p97	Valosin-containing protein/protein 97
$\beta^+$	Positron
$\nu$	Neutrino
x	

# CHAPTER I

---

## GENERAL INTRODUCTION

---





## 1. EPIGENETICS

Epigenetics describes the study of the regulation of gene expression by post-translational modifications (PTMs), without altering the underlying DNA sequence itself [1]. In mammalian cells, DNA is found in a highly condensed state in the nucleus. DNA compaction is mediated by interactions of the core DNA strand, consisting of interlinked nucleotides (purine or pyrimidine bases and phosphorylated deoxyribose backbone), with multiple folding proteins forming chromatin, which is further condensed as chromatid. Ultimately, chromosomes are formed by connection of 2 sister chromatids *via* a centromere. Chromatin consists of 147 base pairs coiled around a histone octamer, constituting two copies of histone 2A (H2A), H2B, H3 and H4, forming the nucleosome. The coiled DNA is further 'capped' by H1, which acts as a linker histone mediating compaction of the chromatin fibre (**Figure 1**) [2,3]. It has to be noted that other proteins also contribute to DNA condensation, but histones are by far the most abundant. The highly condensed chromatin state, heterochromatin, disables effective transcription, whereas the more open euchromatin state enables transcription of the underlying DNA. It is thus clear that chromatin is not a rigid structure only used for DNA packaging, but a dynamic complex, influenced by multiple environmental factors. The regulation of DNA expression *via* chromatin modulation can generally be altered by 1) nucleosome remodelling, mediated by covalent modifications on histones, which promotes or inhibits DNA transcription. 2) Methylation of cytosine on DNA, which leads to inhibition of transcription [4].

PTMs of histones predominantly occur on evolutionary conserved N-termini of histone tails, rich in basic amino acids (lysine and arginine), protruding from the nucleosome cores. However PTMs of histone tails, including methylation, acetylation, phosphorylation, ubiquitination,... can occur on several amino acids (serine, tyrosine, arginine, lysine,...). Other modifications exist but are not as intensely studied. Together, these PTMs contribute to epigenetic regulation of the chromatin/nucleosome complex, and are thus determinant factors in the control of downstream gene expression and gene expression variability [5]. Different epigenetic modifications influence each other and can occur on the same histone tails, ultimately forming a 'histone code'. This code is written by epigenetic writers, read by epigenetic readers and removed by epigenetic erasers [6,7]. One of the most studied epigenetic modifications besides methylation of cytosine on bare DNA or lysine and arginine residues on histones, is the alternate acetylation state of lysine or arginine amino acids on histone tails, mediated by histone acetyl transferase (HAT) and histone deacetylase (HDAC).

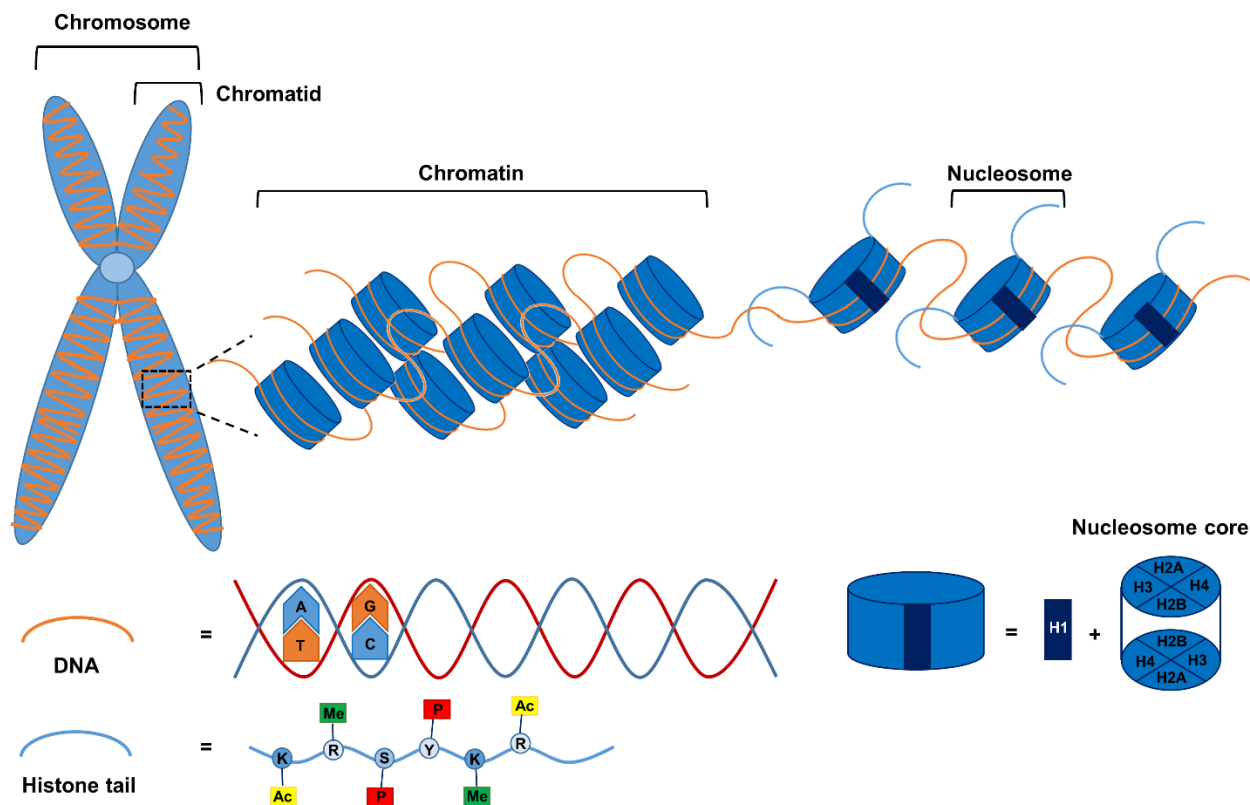


**Figure 1:** Chromosome, chromatids, chromatin and nucleosome structure. Nucleobases: A = Adenine, G = Guanine, T = Thymine, C = Cytosine. Amino acids on histone tails: K = Lysine, R = Arginine, S = Serine, Y = Tyrosine. PTMs on histone tails: Ac = Acetyl, Me = Methyl, P = Phosphoryl. H = Histone.

## 2. HISTONE DEACETYLASE

The addition and removal of acetyl groups is mediated by concerted reactions of HATs and HDACs which catalyse forward and backward acetylation reaction kinetics on amino acid residues. An acetylated state mostly leads to an uncondensed, active chromatin state, whereas the deacetylated state yields a higher degree of interaction between the negatively charged DNA and positively charged histone amino acid sequences (lysine, arginine) forming a condensed, inactive state. This forward and backward catalysis contributes to the acetylated histone homeostasis which in turn influences cellular homeostasis [7]. Clearly, the HAT-HDAC system is very important in regulating the expression of several genes. In addition to transcriptional regulation, the HAT-HDAC system is also a key factor in other chromatin-associated processes like DNA replication, site-specific recombination and DNA repair thereby playing a major role in modulating overall cellular fate [8]. The acetylation homeostasis is closely regulated, as such, aberrant expression levels of one of both regulators can have hazardous consequences [9]. HAT-HDAC activity is not limited to epigenetic modifications of histones, as cytosolic proteins (heat shock proteins (Hsp), cortactin,  $\alpha$ -tubulin) have acetyl binding residues and can be targeted. Further, numerous transcription factors and proteins important in

cellular preservation such as tumour suppressor p53 are known to be controlled by acetylation [10]. When non-histone proteins are targeted, HDACs are often denoted as lysine deacetylases (KDACs) [7].

Currently 18 HDAC isoforms are known, divided into 4 classes based on their sequence homology to yeast HDACs. The various classes differ in protein structure, substrate specificity, subcellular localisation and tissue expression patterns [11]. Class I HDACs (HDAC1, 2, 3, 8) are most closely related to reduced potassium dependency 3 (RPD3), a transcriptional regulator found in yeast (*Saccharomyces cerevisiae*). They are predominantly localised in the cell nucleus, where HDAC3 is able to shuttle between cytoplasm and nucleus *via* a C-terminus which harbours both nuclear import and export signals. Class I HDACs, typically included into multiunit protein complexes [12], can act as transcriptional repressors by deacetylation of histones and other DNA binding proteins, mediating gene expression of genes involved in cell differentiation, cell growth and angiogenesis [13]. Class II HDACs, further divided in Class IIa (HDAC4, 5, 7, 9) and Class IIb (HDAC6, 10) show similarity to HDA1, another deacetylase found in yeast (*Saccharomyces cerevisiae*). These isoforms reside primarily in the cytoplasm, but translocation to the nucleus is possible. Class IIa HDACs are inherently inefficient deacetylases and are often viewed as epigenetic readers, which can recruit other HDACs (such as HDAC3) in multiunit protein complexes to perform the deacetylation reaction [14]. Class IIb HDACs generally act on cytosolic proteins. Important examples are  $\alpha$ -tubulin, Hsp90 and cortactin, with crucial roles in cell motility, differentiation and cell division [15]. All classes except class III use  $Zn^{2+}$  as a catalysing agent to facilitate the deacetylation reaction. Class III HDACs are homologous to the yeast Sir2 and dependent on nicotinamide adenine dinucleotide ( $NAD^+$ ) to perform the hydrolysis of the acetyl-moiety and are denoted as Sirtuins (Sirt). Currently, 7 class III HDAC isoforms are identified (Sirt1-7) [16]. The sole member of class IV, HDAC11, discovered in 2002, is a regulator of the immune response, metabolic pathways and obesity, and is also implied in tumour biology [17,18].

## 2.1. HDACs in cancer

The individual cell fate is generally regulated by expression of different genes. The HAT-HDAC modification pathway of histones is essential in gene transcription. As such, cancer development can arise from imbalances in epigenetic pathways leading to induction of cell proliferation, aberrancies in cell-cycle regulation or reduction of transcription of genes involved in apoptosis and tumour suppression [19]. Furthermore, research has pointed out that several HDACs are overexpressed in different cancers and this is often associated with bad prognosis [20]. HDACs also act on non-histone proteins. One such example is the regulation of the tumour suppressor p53 by HDAC2, as acetylation of p53 is essential for its proper function [10]. Furthermore, it was reported that cancerous cells are more sensitive towards apoptosis induced by HDAC inhibitors which reintroduce transcription of tumour suppressor genes, induce cell cycle arrest and reduce cell motility and invasion by counteracting angiogenesis and metastasis [21]. The involvement of HDAC in cancer initiation and progression is depicted in **Figure 2**.

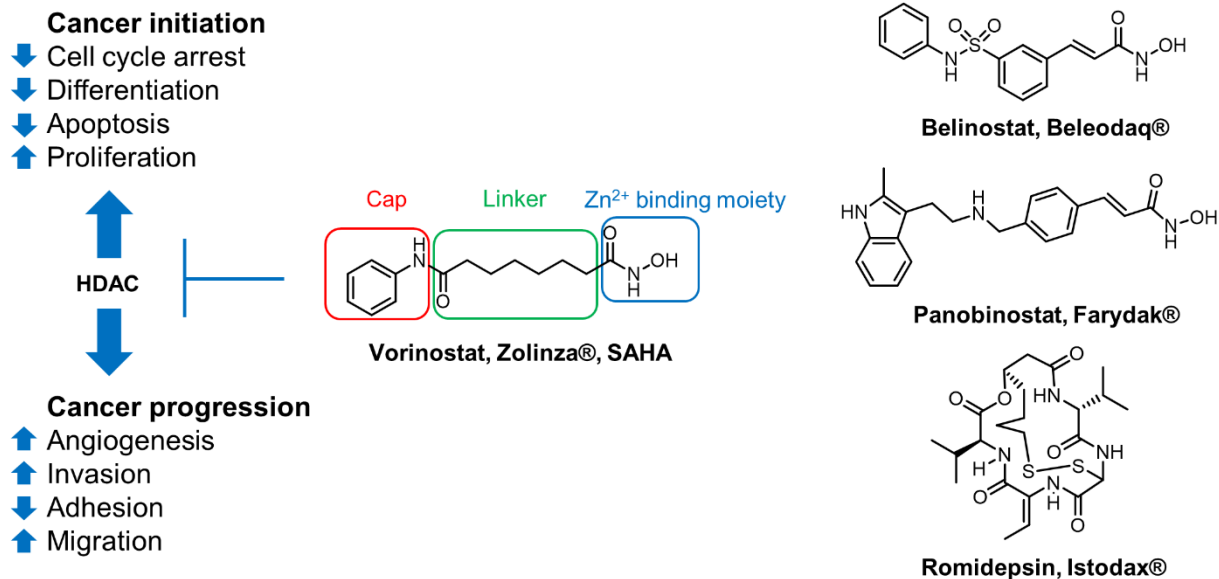


**Figure 2:** Role of HDAC in cancer initiation and progression and FDA approved inhibitors. The typical HDAC inhibitor structure is depicted for SAHA. Arrows depict increase or decrease of molecular events or cellular pathways mediated by HDAC in cancer.

## 2.2. HDACs in CNS disorders

Pathological consequences derived from aberrant HDAC expression have been described in many central nervous system (CNS) disorders such as Alzheimer's disease (AD), Parkinson's disease (PD), Huntington's diseases (HD), Amyotrophic lateral sclerosis (ALS), spinal muscular atrophy (SMA), mood disorders, depression and schizophrenia [22]. All HDAC isoforms are expressed in the CNS [23], each having different functions in general brain development and memory formation [24]. Increased acetylation of lysine residues on histone tails of H3 and H4 was observed in multiple brain regions in studies concerning long term potentiation and synaptic plasticity. This indicates the occurrence of epigenetic alterations of histones in situations where learning, fear consolidation and spatial memory formation occur [22]. Neurodegeneration is part of the normal aging process, in part mediated by changes in gene expression and transcriptional plasticity. This process could be diminished by treatment with HDAC inhibitors, as observed in a study conducted on aged rats [25]. Similarly in neurodegenerative diseases such as AD, synaptic plasticity related genes were found to be less acetylated compared to normal conditions and increased expression of HDAC2 was observed in early stages of human AD [26]. It was also implied that loss of HDAC2 in mice accelerated extinction learning and improved the working memory [27]. Increased acetylation of lysine 14 on histone 3 (H3K14), induced by HDAC inhibition, had antidepressant effects in a chronic social defeat mouse model [28]. Furthermore, antidepressant effects were also observed in mice, attributed to treatment with HDAC6 selective inhibitors [29].

### 2.3. HDAC inhibitors

Inhibition of HDACs is a proven strategy to combat several diseases resulting from dysregulation of the HDAC homeostasis, including oncological, neurodegenerative, and immune disorders [7]. Inhibitors of Zn<sup>2+</sup>-dependent HDACs typically, contain (1) a 'cap' group, which interacts with the surface of the catalytic pocket of the HDACs, (2) a linker, which can contain different aromatic or alkyl chains, connected to (3) a Zn<sup>2+</sup> binding moiety (**Figure 2**). Chelation of the Zn<sup>2+</sup>-ion can be executed with multiple functional groups, not limited to, carboxylic acids, benzamides, thiol groups or hydroxamic acids [30].

Currently several clinical trials are evaluating different potential HDAC inhibitors for treatment of a plethora of diseases [31], although initial clinical trials revolved around cancer therapy [32]. FDA approved drugs include pan-HDAC inhibitors Vorinostat, Zolinza<sup>®</sup> (Suberoylanilide hydroxamic acid (SAHA)) and Romidepsin, Istodax<sup>®</sup> both used for the treatment of cutaneous T-cell lymphoma (CTCL). Belinostat, Beleodaq<sup>®</sup>, is applied for the treatment of peripheral T-cell lymphoma (PTCL) and Panobinostat, Farydak<sup>®</sup>, is used to treat multiple myeloma (MM). FDA approved drugs are depicted in **Figure 2**. HDAC inhibitors are used in monotherapy or in combination with DNA repair pathway inhibitors, topoisomerase inhibitors, proteasome inhibitors, tyrosine kinase inhibitors, hormone therapy or radiotherapy [33]. Currently several preclinical trials are evaluating HDAC inhibitors in the CNS and the carboxylic acid HDAC inhibitors (valproate, phenyl butyrate, sodium butyrate) advanced to clinical trials for the treatment of AD, HD, ALS and SMA [34].

Most current inhibitors in clinical trials target class I HDACs or are general pan-HDAC inhibitors [35]. Simultaneous inhibition of multiple HDAC isoforms can lead to serious adverse effects as was observed in clinical studies. Most common side effects include bone marrow depression, diarrhoea, weight loss, taste disturbances, electrolyte changes, disordered clotting, fatigue and cardiac arrhythmias. The toxicity profile is different for different inhibitors, attributed to their relative selectivity for different HDAC isoforms. To make matters even more complicated, the efficient anti-tumour effect of HDAC inhibitors is often a consequence of the simultaneous inhibition of the different HDAC isoforms resulting in modifications of divergent cellular functions [32,36]. In this respect, research has taken an interest in developing isoform-selective or dual inhibitors. Selective inhibitors for HDAC3, 6 and 8 were reported [37–39] and selectivity is generally configured by modifying the surface binding group, the linker region and/or the Zn<sup>2+</sup>-binding group. (e.g. HDAC6 selectivity can be conferred by bulkier capping groups and a shorter linker region containing an aromatic moiety) [40].

### 3. HDAC6

In 1999 Verdel *et al.* [41] first described HDAC6 and reported that this protein consists of two homologous deacetylase domains. Contrary to class I HDACs, HDAC6 is predominantly localised in the cytoplasm. Evidently, the

main targets of the deacetylation function of HDAC6 occur in the cytosol ( $\alpha$ -tubulin, cortactin and Hsp90). The human HDAC6 sequence includes 8 consecutive serine-glutamic acid-containing tetradecapeptide repeats between the second deacetylase domain and the C-terminal domain, as well as an N-terminal nuclear export signal (NES) that both anchor HDAC6 in the cytoplasm. However, when cell proliferation is arrested, HDAC6 can translocate to the nucleus mediated by a nuclear localisation signal (NLS), also found on the N-terminus [42,43]. Otherwise, HDAC6 is known to deacetylate histone-tails *in vitro*, but not *in vivo* [44] and is itself regulated by PTMs [45]. Over the years it became clear that HDAC6 is a key regulator of multiple cellular signalling and downstream transduction pathways. The regulation of different cellular processes, including cell migration and the degradation of misfolded proteins, are not solely attributed to the deacetylation mechanism as HDAC6 also contains a C-terminal, zinc finger containing, ubiquitin binding domain (BUZ) that is equally important in the control of these processes [46]. The BUZ-domain is able to bind free ubiquitin or ubiquitinated proteins destined for proteasomal degradation [47]. Misfolded or damaged proteins will be marked with a poly-ubiquitin tag directing the proteins to different degradation pathways. The most prominent route is the transport of misfolded proteins to the proteasome. However, if the proteasome becomes oversaturated or inhibited, other processes are required to abrogate the cytotoxic, misfolded or damaged proteins. One process, known as the aggresome-autophagy pathway, is regulated by high affinity binding of HDAC6 to poly-ubiquitinated proteins [48,49]. After HDAC6 binds the (poly-)ubiquitinated tag, the misfolded protein will be transported to the microtubule (MT) associated motor protein, dynein. HDAC6 acts as a bridge between the misfolded “cargo” and the dynein motor. After the cargo is bound to the motor, it is transported *via* the microtubule to a perinuclear location known as the microtubule organizing centre (MTOC) where a new organelle, the aggresome is formed. [50]. Aggresomes can recruit chaperones and proteasome machinery, and activate the autophagy clearance pathway which results in the degradation of the misfolded proteins. Autophagy sequesters damaged organelles and ubiquitinated aggregates in double membrane vesicles called autophagosomes that fuse with lysosomes. More so, HDAC6 enables this by deacetylation of cortactin [45,51]. Inability to remove these misfolded proteins can lead to cell death and is currently investigated in neurodegeneration [48].

### 3.1. HDAC6 in cancer

HDAC6 is a regulator of multiple cellular mechanisms, with a double function as a deacetylation entity and a misfolded protein-clearing agent. Subsequently, aberrant levels of HDAC6 can influence multiple pathways, promoting uncontrolled cell motility/growth, and increased angiogenesis all of which are prerequisites for malignant tumour growth [52]. Many substrates of HDAC6 are also linked to oncogenesis. Hsp90 is critical for the maturation and activity of many (proto)oncological proteins [53]. HDAC6 is required for retrovirus-associated DNA sequences (Ras)-induced, anchorage independent proliferation which is necessary for efficient tumorigenesis. If the cell fails to properly adhere to the surrounding extracellular matrix (ECM) or basement membrane, it will not be able to escape *anoikis*, a type of cell death caused by insufficient cell adhesion [54].

Tumour cells generate an increased amount of misfolded proteins of which a predominant part needs to be actively degraded by the ubiquitin-proteasome system (UPS) or the HDAC6 regulated aggresome-autophagy pathway [50]. Increased migration and invasiveness of hepatocellular carcinoma, overexpressing HDAC6, was observed in a study where the MTs and cortactin acetylation states were altered. HDAC6 abrogation in these cell lines significantly decreased cell motility. More so, overexpression of HDAC6 was seen in 20% of the investigated hepatocellular cell lines. These results suggest a possible role for HDAC6 as a predictor of intrahepatic metastasis [55].

In ovarian cancer, abnormally high levels of proteasomes and HDAC6 expression were seen in low- and high-grade ovarian carcinomas compared with benign lesions [56]. A combined inhibition of the UPS and HDAC6 caused detrimental cytotoxicity in the ovarian cancer cell lines. This combination therapy had no effect on the viability of healthy cell lines or bone marrow-derived progenitor cells [57].

Treatment of several lymphoma cell types with the HDAC6-specific inhibitor ACY-1215 (Ricolinostat) disabled the aggresome pathway leading to an upregulation of misfolded proteins and activation of the already constitutively activated UPS, inducing apoptosis. Dual targeting of both misfolded protein clearance systems with Bortezomib and Ricolinostat *in vitro* and *in vivo* (OCI-Ly10 inoculated mouse model), led to an increase in malignant cell death [58]. Similar results were obtained in MM cells where both Bortezomib and Tubacin (HDAC6 inhibitor) were used [59]. In a cell line of Burkitt's lymphoma, an aggressive B-cell tumour with high metastasis risk, inhibition of HDAC6 led to significant decrease of cell motility, suggesting a role for combination therapy of HDAC6-specific inhibitors and genotoxic agents in advanced stages of Burkitt's lymphoma [60].

Inhibition of HDAC6 in melanoma, stimulated release of tumour antigens which enhanced anti-tumour immunity which resulted in a delay of tumour progression, proliferation decrease and activation of G1 arrest of the melanoma cells [61]. In the murine B16.F10 melanoma cell line, deletion or downregulation of HDAC6 decreased levels of programmed death ligand 1 (PD-L1), an important activator of inhibitory pathways of T-cells [62]. Importantly, it has been observed that HDAC6 inhibition sensitises cancerous cells to chemotherapeutics, but not normal untransformed cells [63].

### **3.2. HDAC6 in CNS disorders**

It has already been reported that pan-HDAC inhibitors could improve long term memory and learning in mice after induction of neuronal loss [64]. HDAC6 is expressed ubiquitously in the brain [65] with high expression in raphe nuclei and more specifically in the serotonergic neurons of mice brain. This data was confirmed in *post-mortem* human brain where in additional regions (substantia nigra and locus coeruleus) high levels of HDAC6 were found [66].

HDAC6 has been implicated in neurodegenerative diseases, such as AD, PD, HD and ALS. Degeneration of neurons and brain structures is often mediated by accumulation of misfolded proteins, which tend to cluster and aggregate with formation of sediments or plaques [67]. Further, discrepancies in the autophagy pathway and disposition of inclusion bodies are observed, which are regulated and processed by HDAC6 and substrates thereof such as the Hsps [68]. The

exact role of HDAC6 in neurodegeneration has to be elucidated further, as reported results are sometimes contradictory with both neuroprotective and neurodegenerative roles attributed to HDAC6 [69]. Possibly, accredited to the bi-functionality of HDAC6 as a deacetylation agent and its involvement in the aggresome pathway *via* its BUZ-domain. It is postulated that initially the formation of aggresomes is beneficial for cell survival however over an extended time period this accumulation can become detrimental.

Because of the localisation in the serotonergic neurons of the raphe nuclei, HDAC6 is implied to mediate the progression of depression and several mood disorders. Furthermore it was stated that the depletion of HDAC6 in serotonergic neurons opposed the hypertrophic induced effect of social defeat in the raphe nuclei [70]. Two HDAC6-selective inhibitors (ACY-738 and ACY-775) were shown to have antidepressant-like properties upon acute and chronic administration to mice as assessed in a tail suspension test and a social defeat study [29].

### 3.3. HDAC6 inhibitors

Currently, some HDAC6 selective inhibitors are evaluated in clinical trials as monotherapy or in combination with other small molecules or monoclonal antibodies [71]. Ricolinostat is being evaluated in monotherapy for treatment of MM and lymphoma, or together with Lenalidomide, Bortezomib or Dexamethasone for the treatment of MM and lymphoma, and together with Nab-paclitaxel in metastatic breast cancer. ACY-241 (Citarinostat) is evaluated in combination with Nivolumab for the treatment of non-small cell lung cancer (NSCLC). Inhibitor KA2507 is evaluated in PD-L1 overexpressed solid tumours in relapsed patients [71]. Clinical studies with HDAC6 inhibitors in CNS have yet to be performed.

## 4. HEAT SHOCK PROTEINS

The Hsp family is part of a big cluster of molecular chaperones important for folding, maturation and clearance of aberrantly expressed proteins. Molecular chaperone proteins maintain cell proteostasis by assisting “client” proteins in their co-translational folding, stabilisation and multiprotein assembly thus avoiding their aggregation and subsequent ubiquitination and degradation. Chaperone proteins are organised in interactive networks termed the “chaperome” with both serial and parallel-organized functions. Chaperones also stabilize or refold client proteins induced in stress conditions such as a sudden rise in temperature, hence the name “heat shock” proteins. Of note, not all molecular chaperones are Hsps as only 20% of the chaperome is heat inducible. [72,73]. Hsps are classified according to their approximate molecular weight, with major classes Hsp100, Hsp90, Hsp70, Hsp60 and the smaller family members Hsp33 and Hsp27 [74].



## 4.1. Hsp90

The 90 kDa members of the eukaryotic Hsp-family, Hsp90 can predominantly be found in the cytosol, whereas 2-3% of the Hsp90 pool has a nuclear localisation [75,76]. Hsp90 occurs as two major isoforms: the inducible Hsp90AA1 (Hsp90 $\alpha$ ) and the constitutively expressed Hsp90AB1 (Hsp90 $\beta$ ), expressed in a 2:1 ( $\alpha$  vs  $\beta$ ) ratio which are 85% identical in human cells [77]. Other Hsp90 paralogues exist which are restricted to the endoplasmic reticulum (ER) and mitochondria, respectively 94 kDa glucose regulated protein (Grp94) and tumour necrosis factor receptor associated protein 1 (TRAP1). In contrast to other Hsps, Hsp90 is more selective towards client engagement as it predominantly processes near-native state folded client proteins, already possessing a tertiary structure [78]. In a stress-free environment the Hsp90 family makes up 2% of all the soluble cellular proteins, whereas their fraction increases to 6-7% in cancer cells and up to 10% during cellular stress [79–81]. The Hsp90 family are ATP-dependent proteins existing as homodimers, part of an ATPase/kinase superfamily. Other members include DNA gyrase, histidine kinase and the DNA mismatch repair protein MutL, which have a unique ATP binding pocket [82]. Hsp90-mediated processes function with the help of a complex of co-chaperones (chaperone machinery) consisting of different cofactors with binding preferences for specific Hsp90 conformations. Several cofactors regulate the ATPase activity of Hsp90, others modulate/maturate the substrate processing. Hsp90 co-chaperones are also implied in recognition of client proteins, as an inherent client protein recognition domain has yet to be discovered [76]. Moreover, the Hsp90 complex is regulated by PTMs such as acetylation, nitrosylation and phosphorylation [72]. The client proteins processed by the Hsp90 machinery are abundant, over 400 have been reported encompassing kinases, transcription factors, E3-ubiquitin ligases, steroid hormone receptors and other essential signalling proteins [83,84]. As many of the client proteins of Hsp90 are involved in multiple oncogenic pathways and contribute to the different hallmarks of cancer [85], Hsp90 can be a valuable target for the treatment of several malignancies. The role of Hsp90 in cancer is well documented in literature, however recent publications also inquire a role of Hsp90 in neurodegenerative diseases such as AD, PD, HD and neuroinflammation [86,87].

Hsp90 alternates between an ADP and ATP bound state, mediating ATP binding *via* the N-terminal ATP binding domain (ND). In the ATP bound state, a 'lid' consisting of several conserved amino acid residues, closes off the ATP-binding region. However, this conformational change does not occur in the ADP bound state [88]. The ND is linked *via* a charged linker sequence to a substrate interacting middle domain (MD), which is involved in the ATP hydrolysis and controls the adherence of client proteins and co-chaperones. Co-chaperone, ATPase homologue 1 (AHA1) promotes the association of the ND and MD, increasing the ATP hydrolysis rate [81]. Another well studied co-chaperone of Hsp90, p23, stabilizes the interaction of Hsp90 with several client proteins [89]. The C-terminus domain (CD) of Hsp90 contains a dimerization region which is pivotal for the chaperoning function as it regulates the dimerization of two Hsp90 protomers. Dimerization is initiated by ATP binding which will subsequently induce a conformational change, The ND shifts from an open V-shape to a closed, compact, twisted conformation. In the

closed state the N-termini dimerize and associate with the MD, ATP is hydrolyzed and the NDs dissociate, returning Hsp90 back to its original state with the release of ADP [90]. The Hsp90 cycle is depicted in **Figure 3**.

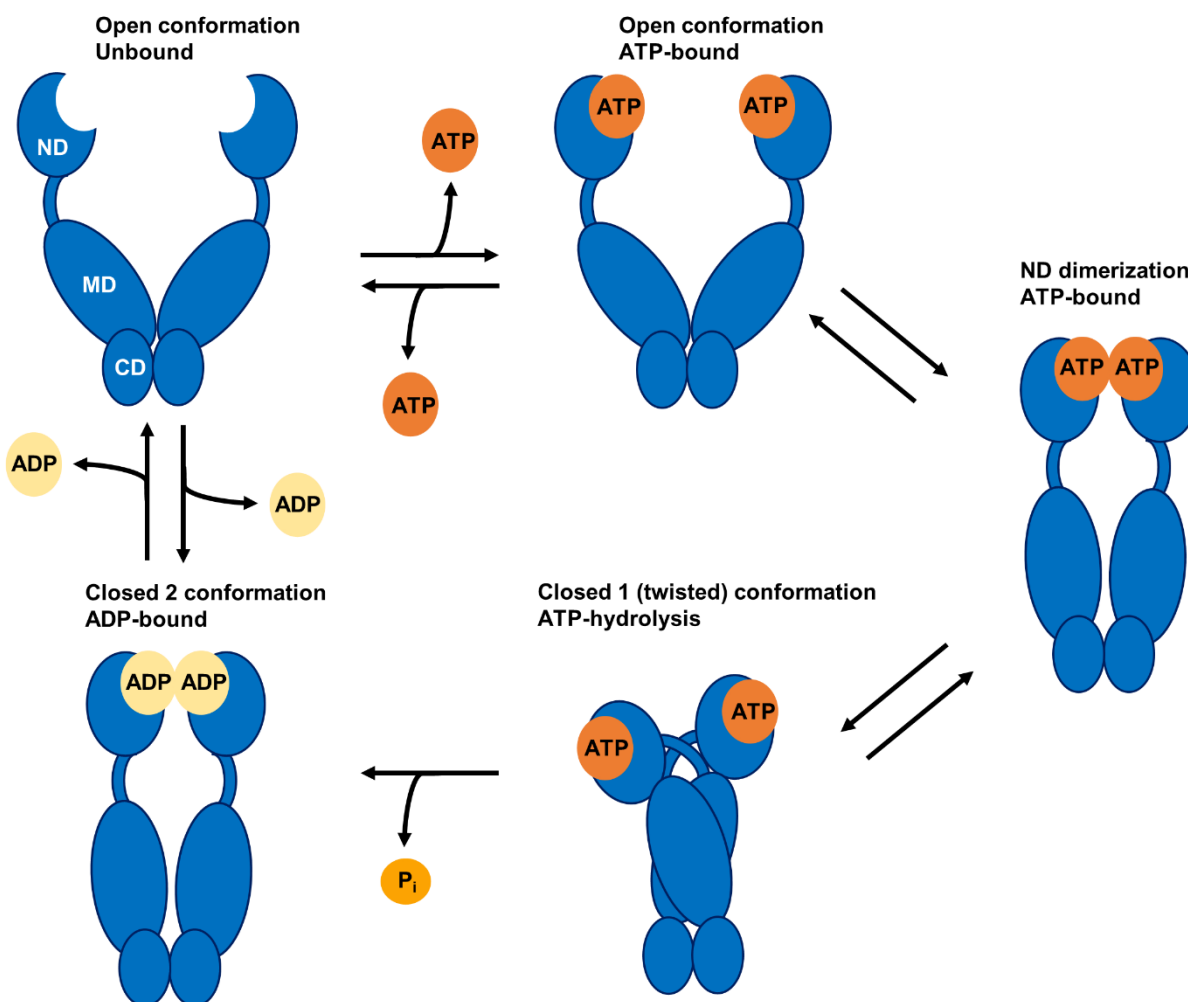


**Figure 3:** Simplified example of the Hsp90 chaperone cycle. Adapted from [88]. ND = N-terminal domain, MD = Middle domain, CD = C-terminal domain.

## 4.2. Hsp90 in cancer

At first sight, Hsp90 targeted therapy is counterintuitive and can have disastrous cellular consequences as Hsp90 is abundantly expressed throughout the cells of eukaryotes (2% of total protein count). However, Hsp90 inhibition is generally well tolerated, besides adverse effects such as reversible night blindness and gastro-intestinal problems [91]. In 2003, Kamal et al. found an intrinsic difference between binding affinity of Hsp90 inhibitors to oncogenic and constitutively expressed Hsp90. Hsp90 was found to adopt a tumour-specific conformation in multi-chaperone complexes resulting in a 100-fold increase of affinity for the ATP-site binding inhibitor 17-allylamino-17-demethoxy-

geldanamycin (17-AAG, **Figure 4**) [92]. Later this multi-chaperome complex was further analysed and identified as the epichaperome, a highly connected network of chaperones (Hsp70, Hsp90 Hsp110), co-chaperones, and other folding enzymes, designated to conserve cell survival and present in many types of cancer [93,94]. Increased connectivity between the different partners of the complex, induced various rates of dependability of the different parts of the epichaperome on each other. Tumour cells in which virtually all subsets are connected, were highly sensitive to inhibition of only one member of the epichaperome. In accordance to the principle of lethality and centrality in which disruption of highly connective networks is detrimental for cell survival, whereas low connectivity networks are more resistant by activation of compensatory molecular events or pathways. As was proven in studies with PU-H71, which was more strongly bound to Hsp90 complexed in the epichaperome [93,94]. However, in untransformed cells, the different components of the chaperome/epichaperome are found in loose dynamic complexes or as free entities [95]. Tumour cells responsive to PU-H71 were classified as type 1 tumours and less responsive ones as type 2. It was suggested that type 1 tumours express a biochemically altered network of chaperones, the epichaperome. Type 2 tumours do express a certain degree of connectivity of chaperome substructures but to a lesser extent compared to type 1. For type 2 tumours, inhibition of Hsp90 can be compensated by induction of Hsp70 and related co-chaperones *via* a heat shock response (HSR) [93]. It is hence important to note that in many cancers the overexpression of Hsp90 plays a secondary role as primarily the connectivity between the different subsets of the chaperome is essential in tumour cell survival [96]. Further, PU-H71 was defined as an epichaperome inhibitor, rather than a plain Hsp90 inhibitor [97]. In a sense, tumour cells are “addicted” to the chaperome and epichaperome to protect themselves against the strain of abundantly produced (misfolded) proteins, [80,84] and the epichaperome can potentially be used as a cancer biomarker [94]. As a member of the epichaperome, Hsp90 shows higher inhibitor affinity and/or is upregulated in many types of cancers making it a valuable target in drug development.

In normal cells, Hsp90 is confined to the intracellular space but in different tumour cells (fibrosarcoma [98], melanoma [99], breast cancer [100]) vast expression of Hsp90 was observed on the cell surface (eHsp90). Exogenous Hsp90 does not occur in untransformed cells, except for tissue damage and consequent wound healing. Both Hsp90 $\alpha$  and Hsp90 $\beta$  are actively secreted from tumour cells or cells under stress (heat, hypoxia, gamma irradiation) triggered by hypoxia-inducible factor-1 $\alpha$  (HIF-1 $\alpha$ ) or cytokines including tumour growth factor- $\alpha$  (TGF- $\alpha$ ), *via* an exosome secretion pathway [101,102]. Knock-out experiments showed that Hsp90 $\beta$  is essential for tumour cell survival whereas Hsp90 $\alpha$  is required for tumour cell motility and invasion [103]. It was observed that eHsp90 $\alpha$  but not Hsp90 $\beta$  interacts and activates the matrix metalloproteinase 2 (MMP2) promoting cancer cell migration [104]. Exogenous Hsp90 was also observed to interact with the human epidermal growth factor receptor 2 (HER2) tyrosine kinase in metastatic breast cancer. However, it was not specified which isoform of Hsp90 was responsible for the interaction [100]. Tsutsumi et al. observed absence of internalisation of their cell-impermeable Hsp90 inhibitor DMAG-N-oxide after binding to eHsp90 in melanoma cells [103]. Crowe *et al.* in turn demonstrated eHsp90-specific active internalisation of their fluorescent (HS-27 and HS-131) and radiolabelled ( $^{125}\text{I}$ HS-111) probes, in mammary tumour

cells [105]. Internalisation was blocked with an antibody against the C terminal of Hsp90. Wang *et al.* found in patients with oesophageal squamous cell carcinoma that eHsp90 $\alpha$  promotes metastasis and can be used as prognostic marker and as a therapeutic target [106].

### 4.3. Hsp90 in CNS disorders

The localisation of Hsp90 was assessed in rat brain, where it was found expressed in the cytoplasm of almost all neurons but to a lower degree in glial cells. Further, Hsp90 brain expression levels were higher compared to liver and kidneys [107]. Using the 4C5 antibody, cell surface Hsp90 was found to be associated with cell migration in the developing rat brain [108]. Other experiments with the 4C5 antibody show upregulation of Hsp90 in Schwann cells after sciatic nerve injury, important for Schwann cell migration after injury [109].

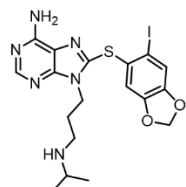
Many neurodegenerative diseases originate from accumulation of aggregated proteins resulting from clustering of misfolded proteins. A major part of the clearance of these misfolded proteins is mediated by Hsp70 and Hsp90. Several co-chaperones and client proteins of Hsp70/Hsp90 are implicated in formation of aggregates in neurodegenerative diseases. The Hsp90 co-chaperone p23 for example binds  $\gamma$ -secretases, important in the A $\beta$  production pathway and formation of plaques. Furthermore, silencing of p23 gene expression reduced pathological hyperphosphorylated tubulin associated unit (tau) load [110]. Depletion of independent members of the chaperome, loss of function or loss of interaction between different subsets of the chaperome are implied as hallmarks in aging and neurodegenerative diseases [111]. It has been postulated that similarly to cancer pathology, Hsp90 stabilizes defective proteins, preventing degradation of these proteins by the proteasome, enabling aggregate formation. Further, in PD it was observed that chaperome interactions in normal conditions are rewired leading to an increased connectivity of the chaperome networks, similar to epichaperome formation observed in cancer [95]. Acute cellular stress will induce a shift of Hsp90 to a stress state, leading to an increased interaction with co-chaperones and other cofactors of the chaperome. This state will be attained in chronic stress conditions, creating a continuous degradation of neuronal networks [94,95]. In preclinical studies investigating the contribution of Hsp90 to CNS pathologies, inhibition of Hsp90, induces nuclear activation of HSF-1, with consequent expression of other Hsps (Hsp40, Hsp70) ameliorating synaptic plasticity [112]. Intense Hsp90 immunoreactivity was observed in Lewy bodies and Lewy neurites in brain sections of patients with synucleinopathies and brain sections of  $\alpha$ -synuclein (M83) mice [113]. Hsp90 expression levels were higher in temporal cortices of AD patients vs age matched controls and Hsp90 was observed to co-localise with senile plaques and reactive microglia in AD brain sections [114].

### 4.4. Hsp90 inhibitors

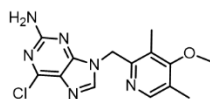
Currently, several Hsp90 inhibitors are being developed and over 15 advanced to oncological clinical trials (**Figure 4**) [115]. Molecules are typically based on purine, resorcinol, quinone, indazole or benzamide scaffolds. However, this list is not limitative and new chemical entities with affinity for Hsp90 are continued to be discovered [115]. The mechanism of action of most Hsp90 inhibitors is based on disrupting the interaction between ATP and the N-terminal

ATP binding domain of Hsp90. Inhibition of the ATP pocket will restrain Hsp90 in the ADP-bound state, client proteins will be ubiquitinated and probed for subsequent degradation by the proteasome [90]. However, CD inhibitors are also currently under investigation. These inhibitors destabilize the chaperone complex, leading to the release of co-chaperones and substrates and subsequent degradation of client proteins [115].

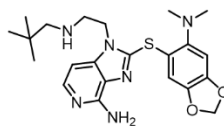
### Purine



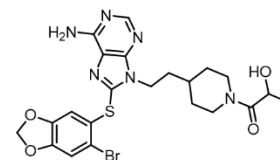
**PU-H71**  
Phase I  
 $IC_{50} = 43$  nM



**BIIB021**  
Phase I/II  
 $K_i = 1.7$  nM

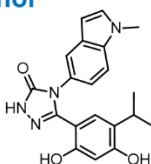


**DEBIO-0932**  
Phase I  
 $IC_{50} = 100$  nM

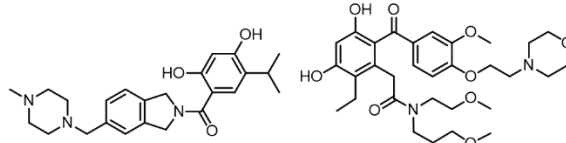


**MPC-3100**  
Phase I/II  
 $IC_{50} = 60$  nM

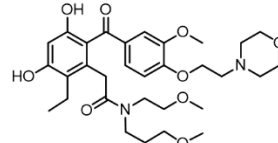
### Resorcinol



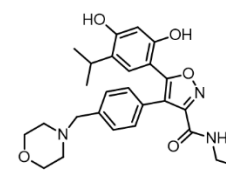
**Ganetespiib**  
Phase I/II/III  
 $IC_{50} = 4$  nM



**Onalespiib**  
Phase I/II  
 $IC_{50} = 18$  nM

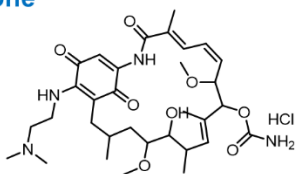


**KW-2478**  
Phase I  
 $IC_{50} = 4$  nM

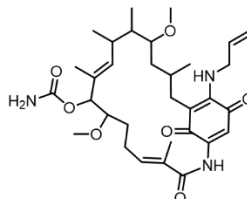


**Luminespiib**  
Phase I/II  
 $IC_{50} = 13$  nM

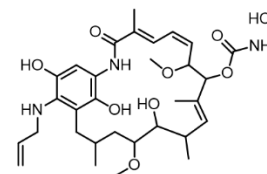
### Quinone



**Alvespimycin**  
Phase I/II  
 $IC_{50} = 62$  nM

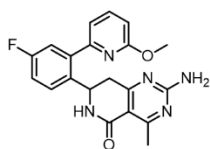


**Tanespimycin (17-AAG)**  
Phase I/II/III  
 $IC_{50} = 6$  nM

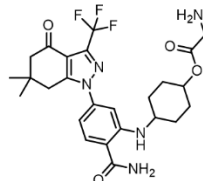


**Retaspimycin (IPI-504)**  
Phase I/II/III  
 $EC_{50} = 63$  nM

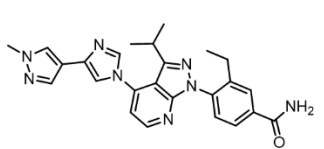
### Others (Indazole-4-one, Benzamide)



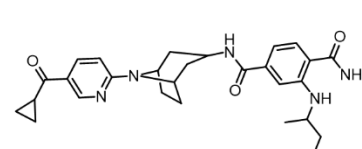
**HSP990**  
Phase I  
 $IC_{50} = 0.6$  nM



**SNX-5422**  
Phase I  
 $IC_{50} = 41$  nM



**TAS-116**  
Phase I  
 $K_i = 35$  nM



**XL888**  
Phase I  
 $IC_{50} = 24$  nM

**Figure 4:** Hsp90 inhibitors investigated in clinical trials divided in structural classes. Clinical trial phases are indicated as well as affinity values for Hsp90 $\alpha/\beta$  [116–129].

Although over 15 Hsp90 inhibitors have been evaluated in clinical trials and initial preclinical results looked promising, many of the compounds have not lived up to expectations. Acute inhibition of Hsp90 is generally well tolerated. However, repetitions of high-level inhibition of Hsp90 induced by intermittent bolus injections, commonly used to assess anti-cancer drugs in a clinical setting, affects Hsp90 in healthy cells. This narrows the therapeutic window of anti-Hsp90 drugs [130]. This results in frequent adverse effects (gastrointestinal problems, reversible night blindness) which limits the further use or evaluation of these compounds. In cancer cell lines, the binding kinetics of Hsp90 inhibitors depend on the degree of connectivity between individual chaperone members, with fast dissociation of inhibitors from Hsp90 in untransformed cells and long retention to Hsp90 of highly structured, multichaperone complexes (epichaperone) [94]. Moreover, Hsp90 inhibition *via* the N-terminal ATP binding domain induces a HSR *via* release of heat shock factor 1 (HSF1), which upregulates transcription of the pro-survival Hsps, Hsp27, Hsp40 and Hsp70 [131]. The use of combinatorial approaches simultaneously targeting Hsp90 and Hsp70 or Hsp90 and HSF1 can bypass this compensatory effect, increasing the effectiveness of drug treatment. The development of CD inhibitors, where induction of the HSR is less pronounced, can also be an alternative [132].

### 5. LINK BETWEEN EPIGENETICS, HDAC(6) AND HSP90

Under 5% of the total Hsp90 pool resides in the nucleus where it functions as a housekeeping protein for several nuclear transcription factors. Other client proteins of Hsp90 include histone methyltransferases, which are overexpressed in several cancers. Hypermethylation of cytosine-phosphoryl-guanine (CpG)-islands in the promoter regions of tumour-suppressor genes has been implied to inactivate transcription of these genes, promoting cancer initiation, proliferation and progression. HDAC1, residing in the cell nucleus, deacetylates and activates nuclear Hsp90. Inhibition of HDAC1 induces hyperacetylation of Hsp90, which further leads to a decreased methylation of CpG islands [78,133]. Hsp90 is considered as an important element at the intersection between genetics and epigenetics and at the level of proteostasis, acting as a capacitor of phenotypical variation. Loss of Hsp90 was observed to induce suppressed phenotypes in experiments on fruit flies, implying a role of Hsp90 as an intracellular regulator of adaptation [134].

In normal conditions, Hsp90 is embedded in a complex with Hsp70, HSF1, co-chaperones p23 and immunophilin, FK506-binding protein 52 (FKBP52) and HDAC6, residing in the cytoplasm. Cellular stress will induce the release of HSF1, which will translocate to the nucleus, leading to the transcription of stress proteins including Hsp90 thus creating a feedback loop in which Hsp90 regulates its own transcriptional expression [135]. HSF1 is a transcription factor important in activating the HSR in abundance of accumulating misfolded proteins in times of cellular stress and proteasome inhibition. Under cellular stress, HDAC6 will bind ubiquitinated proteins and recruit valosin-containing protein/protein 97 (VCP/p97) to the complex where the interaction between HSF1 and Hsp90 will be broken by the segregase activity of VCP/p97 [51]. This interaction is of great importance as it was shown that HSF1

activation does not occur in the absence of HDAC6 or VCP/p97 [136]. However, in cases of proteasome inhibition, heat shock leads to HSF1 activation even in the absence of HDAC6 [137]. HSF1 activation is thus dependent on the type of cellular stressor [76]. Abrogation of HDAC6 induces hyperacetylation of Hsp90, subsequent dissociation of p23 which will result in loss of chaperone activity, as was observed for the glucocorticoid and androgen receptors (GR, AR) as the maturation of these receptors is dependent on the acetylation state of Hsp90 [138]. The HDAC6-Hsp90 interplay is also required for AR hypersensitivity and AR nuclear localisation in castrate resistance prostate cancer cells [139]. Moreover, deacetylation of Hsp90 by HDAC6 disables the degradation of various oncoproteins and both HDAC6 and HSF1 are required to maintain transformed phenotypes of established cancer cell lines [53].

Another co-chaperone and client protein of Hsp70/Hsp90 is the ubiquitin ligase carboxy terminus of Hsp70-interacting protein (CHIP), known as a quality control regulator of the Hsp70-Hsp90 chaperoning pathway, which ubiquitinates client proteins and probes them for degradation [140]. CHIP is implied as a mediator in the removal of hyperphosphorylated tau (also a client protein of Hsp90) after inhibition of Hsp90 [141]. Further, CHIP probes HDAC6 for degradation, and regulates its expression [80]. HDAC6 levels correlate with tau burden, where lower HDAC6 expression induces tau clearance. As inhibition of HDAC6 and Hsp90 promotes the clearance of misfolded proteins such as tau [142], efforts are being made to develop Hsp90-HDAC6 dual inhibitors [143].

## 6. MOLECULAR IMAGING

Different *in vivo* imaging modalities such as optical imaging, nuclear imaging and magnetic resonance imaging (MRI) allow the examination of biological processes on a cellular or molecular basis, enabling quantification, characterization and visual representation of the target (enzyme, receptor, transporter, protein aggregates,..) in 3D. In contrast to imaging techniques such as computed tomography (CT) which gives anatomical information [144]. In the case of nuclear imaging modalities (positron emission tomography (PET) and single photon emission tomography (SPECT)), radiolabelled molecular probes are used. These compounds are labelled with a radioisotope, with generally a fairly short half-life ( $T_{1/2}$ , min to days). PET and SPECT are sensitive imaging modalities, allowing visualisation and quantification of targets such as neuroreceptors expressed in nano-to-femtomoles per milligram tissue levels [145].

### 6.1. Positron emission tomography

PET is a highly sensitive, non-invasive molecular imaging technique used to study and visualise physiology and distribution of drugs by the detection of positron-emitting radionuclides, coupled to a pharmaceutical vector molecule or drug. PET uses unstable isotopes of low atomic mass elements (C, N, O, F) abundantly found in biomolecules. Incorporation of radioactive analogues of these atoms enables direct labelling of drug molecules without interfering with their biological activity. The high sensitivity of PET enables identification of the onset of the disease at considerably earlier stages, before morphological changes occur [145]. PET-probes are administered at

'tracer' concentrations, evading any sort of pharmacological effect. Implementation of molecular imaging in the general drug development stream can accelerate the development of potential drugs against a specific target. Pharmacodynamics can be examined, drug target interaction can be established and dose-occupancy studies can be conducted [146].

The PET principle is based on the simultaneous detection of 2  $\gamma$ -rays originating from the annihilation of a positron ( $\beta^+$ ) and an electron. A PET-radionuclide will decay by emission of a  $\beta^+$ -particle and a neutrino ( $\nu$ ), the latter to fulfil the quantum mechanical rule of conservation of energy and angular momentum. The  $\beta^+$ -particle will travel a short distance depending on its kinetic energy, denoted as the positron range (up to 0.5 cm for fluor-18, 1-2 cm for carbon-11). The positron will collide with an electron in the surrounding tissue, forming an intermittent positronium, which rapidly disappears by an annihilation event (conversion of mass to energy). Two  $\gamma$ -ray photons of 511 keV are emitted back to back over an angle of approximately  $180^\circ$  (**Figure 5A**). These two  $\gamma$ -rays travel through the body and can be detected simultaneously (within a time interval of 10 ns), allowing to localise the imaginary "line of response" along which the annihilation event took place. Combination of an extended set of lines of response thus allows to reconstruct an image reflecting the concentration of the radionuclide in the body. The spatial resolution of PET imaging systems is limited by the positron range. In this respect, PET isotopes with shortest positron range yield the highest resolution. Further,  $\gamma$ -rays are emitted over an angle of approximately  $180^\circ$ , this can differ up to  $0.25^\circ$ . This phenomenon of non-collinearity also contributes to resolution restrictions especially in large bore PET cameras. Since this is an angular effect, the resolution decreases as the distance between two opposite detectors increases [147]. Generally, a resolution of 4 mm can be obtained by state of the art PET scanners [148]. Small animal PET scanners ( $\mu$ PET, **Figure 5B**) are limited to a resolution of  $< 2$  mm [149]. Hybrid imaging techniques such as PET/MRI (**Figure 5C**) and PET/CT allow combination of morphological and functional imaging. Where molecular and anatomical changes can be detected simultaneously with high accuracy. State of the art PET-technology research is investigating total body PET with increased sensitivity (up to 40-fold) compared to normal PET scanners [150].

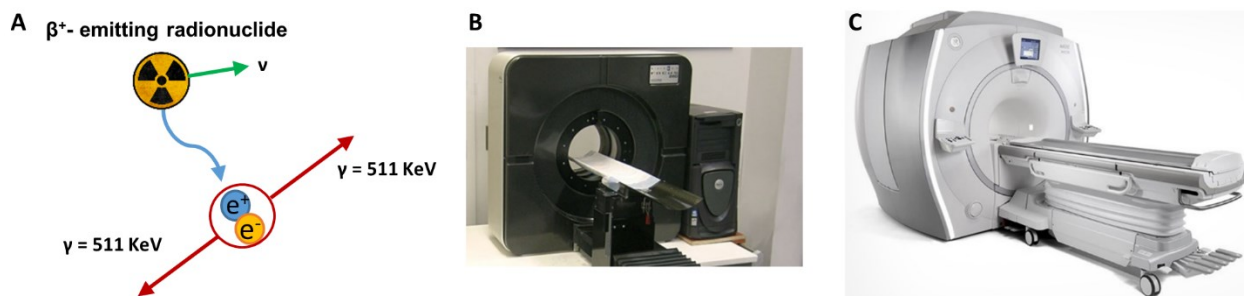


**Figure 5:** A) Depiction of the annihilation event which produces the two characteristic (511 KeV)  $\gamma$ -rays used in PET imaging ( $e^+$  = positron,  $e^-$  = electron,  $\nu$  = neutrino). B) Siemens FOCUS™ 220  $\mu$ PET scanner. C) GE Signa PET-MRI scanner used in the UZ Leuven.



In recent years there has been a steady increase of PET radiopharmaceuticals compared to development of new SPECT tracers. In PET imaging, mechanical collimation is omitted, increasing detector efficiency 100-fold compared to SPECT. The spatial resolution of PET is also higher with less influence of scattered photons. Attenuation correction is more efficient and the imaging contrast is also better compared to SPECT [151]. A disadvantage of PET is the cost and the availability of PET radioisotopes which commonly need to be generated by a cyclotron. Because of the short  $T_{1/2}$  of routinely use PET isotopes (carbon-11, fluorine-18, nitrogen-13, oxygen-15) an in-house cyclotron is generally required [152].

**Table 1:** Commonly used PET radionuclides [148,153].

Radionuclide	$T_{1/2}$	Nuclear reaction	Mode of decay*	Decay product	Energy (MeV)	Average range of $\beta^+$ in H <sub>2</sub> O(mm)
<sup>11</sup> C	20.4 min	<sup>14</sup> N(p, $\alpha$ ) <sup>11</sup> C	$\beta^+$ (100%)	<sup>11</sup> B	0.960 ( $\beta^+$ E <sub>max</sub> )	1.2
<sup>13</sup> N	10.0 min	<sup>16</sup> O(p, $\alpha$ ) <sup>13</sup> N	$\beta^+$ (100%)	<sup>13</sup> C	1.199 ( $\beta^+$ E <sub>max</sub> )	1.8
<sup>15</sup> O	2.0 min	<sup>14</sup> N(d,n) <sup>15</sup> O	$\beta^+$ (100%)	<sup>15</sup> N	1.732 ( $\beta^+$ E <sub>max</sub> )	3.0
<sup>18</sup> F	109.7 min	<sup>18</sup> O(p,n) <sup>18</sup> F	$\beta^+$ (97%)	<sup>18</sup> O	0.634 ( $\beta^+$ E <sub>max</sub> )	0.6
		<sup>20</sup> Ne(d, $\alpha$ ) <sup>18</sup> F	EC (3%)			
<sup>64</sup> Cu	12.7 h	<sup>64</sup> Ni(p,n) <sup>64</sup> Cu	$\beta^+$ + EC (61%)	<sup>64</sup> Ni	0.653 ( $\beta^+$ E <sub>max</sub> )	0.7
			$\beta^-$ (39%)	<sup>64</sup> Zn	0.3293-1.675 0.5794	
<sup>68</sup> Ga	67.6 min	<sup>68</sup> Ge/ <sup>68</sup> Ga-generator	$\beta^+$ (89%)	<sup>68</sup> Zn	1.899 ( $\beta^+$ E <sub>max</sub> )	3.5
			EC (11%)		0.227-2.821	
<sup>76</sup> Br	16.0 h	<sup>76</sup> Se(p,n) <sup>76</sup> Br	$\beta^+$ (55%)	<sup>76</sup> Se	3.382 ( $\beta^+$ E <sub>max</sub> )	
			EC (45%)		0.599	
<sup>82</sup> Rb	1.3 min	<sup>82</sup> Sr/ <sup>82</sup> Rb-generator	$\beta^+$ (100%)	<sup>82</sup> Kr	3.378 ( $\beta^+$ E <sub>max</sub> )	7.1
			$\beta^+$ (32%)		1.221, 1.545, 1.988	
<sup>86</sup> Y	14.7 h	<sup>86</sup> Sr(p,n) <sup>86</sup> Y	IT (68%)	<sup>86</sup> Sr	( $\beta^+_{1,2,3}$ E <sub>max</sub> )	1.9, 2.8, 3.7
			$\beta^+$ (23%)		0.433-1.920	
<sup>89</sup> Zr	3.3 days	<sup>89</sup> Y(p,n) <sup>89</sup> Zr	EC (77%)	<sup>89m</sup> Y	0.902 ( $\beta^+$ E <sub>max</sub> )	1.3
			$\beta^+$ (26%)		0.909	
<sup>124</sup> I	4.2 days	<sup>124</sup> Te(p,n) <sup>124</sup> I	$\beta^+$ (26%)	<sup>124</sup> Te	2.138, 1.535 ( $\beta^+_{1,2}$ E <sub>max</sub> )	4.4, 2.8
			EC (74%)		602	
<sup>152</sup> Tb	17.5 h	<sup>143</sup> Nd( <sup>12</sup> C,5n) <sup>152</sup> Tb		<sup>152</sup> Gd	2.040-2.970 ( $\beta^+$ E <sub>max</sub> )	
		<sup>144</sup> Nd( <sup>12</sup> C,4n) <sup>152</sup> Tb	$\beta^+$ (17%)			
		<sup>145</sup> Nd( <sup>12</sup> C,3n) <sup>152</sup> Tb	EC (83%)			
		Spallation on Ta <sup>§</sup>				

\* abundance in %, EC = electron capture, IT = isomeric transition. § = proton-induced spallation on Tantalum.

Typical radionuclides, used for PET imaging are listed in **Table 1**. These radionuclides can be divided in pure PET radionuclides ( $^{11}\text{C}$ ,  $^{13}\text{N}$ ,  $^{15}\text{O}$ ,  $^{18}\text{F}$ ,  $^{68}\text{Ga}$ ,  $^{82}\text{Rb}$ ) with high branching factors for  $\beta^+$ -decay and non-pure radionuclides ( $^{64}\text{Cu}$ ,  $^{76}\text{Br}$ ,  $^{86}\text{Y}$ ,  $^{89}\text{Zr}$ ,  $^{124}\text{I}$ ,  $^{152}\text{Tb}$ ) where  $\beta^+$ -decay is generally not the main decay route or where decay is not directly to a ground state [148]. Furthermore several of these isotopes ( $^{64}\text{Cu}$ ,  $^{68}\text{Ga}$ ,  $^{82}\text{Rb}$ ,  $^{86}\text{Y}$ ,  $^{89}\text{Zr}$ ,  $^{152}\text{Tb}$ ) are radio-metals, which require complexation *via* coordination chemistry, which limits the use of these isotopes in small molecules [154]. The labelled probe has to be synthesized, purified, analysed and formulated preferably in minutes. Roughly, recommended time spent on production and formulation of the radiotracer cannot exceed 3 isotope half-lives, to ensure sufficient labelled material to administer to a subject [154].

PET can be applied as a diagnostic, routinely used imaging modality in clinics. Where a relatively large amount of short scans are conducted in a high capacity, low complexity fashion. PET can also be used as a research tool in a low capacity, high complexity manner. Here scan times are usually longer compared to routine diagnostic scans and more complex or specific PET tracers are used. Furthermore, PET scans in the research environment typically require additional studies such as arterial blood sampling and kinetic modelling.

The predominant PET tracer used is the fluorine-18 labelled glucose derivative, 2- $^{18}\text{F}$ fluoro-2-deoxy-D-glucose ( $^{18}\text{F}$ FDG) (**Figure 6A**).  $^{18}\text{F}$ FDG is used to image glucose metabolism and is hence taken up in organs or tissues with high glucose consumption such as brain and heart. Because of the high uptake in glucose consuming tissue which correlates with tissue glucose metabolism,  $^{18}\text{F}$ FDG is applied in diagnostic imaging of cancer, inflammation, cardiology and neurology [155]. The  $T_{1/2}$  of fluorine-18 (109.8 min) enables transport of fluorine-18 labelled molecules to facilities which have PET scanners but lack a cyclotron. As such  $^{18}\text{F}$ FDG produced in the nuclear medicine department of UZ Leuven can be used in hospitals all over Belgium and is widely available in western countries.

Patients suffering from common neurodegenerative disease such as AD are usually diagnosed at later stages of disease development, when symptoms occur. A definite diagnosis can only be determined *post-mortem* and current drug treatments only offer symptomatic relief. PET allows early detection of aberrancies in cell homeostasis and can quantify the amount of protein aggregates such as tau and beta-amyloid. In this regard, PET can play an important role in development of new drugs against neurodegenerative diseases as it can provide an objective quantification of a biomarker so that the drug treatment effect can be evaluated faster and more accurately than evaluation based on monitoring of e.g. cognitive decline. In addition, PET potentially allows determination of pharmacodynamic parameters such as drug-occupancy in early phase evaluation of new CNS drugs [156].

Initial PET-radiopharmaceutical research revolved around labelling of small molecules, but recently there is a growing interest in labelling larger biomolecules such as peptides or antibodies. This PET-branch is called immuno-PET, where high affinity and selective biomolecules are labelled with longer lived isotopes (zirconium-89 ( $T_{1/2}$  3.3 days or iodine-124 ( $T_{1/2}$  4.2 days)). These longer  $T_{1/2}$  are required to complement the slow blood clearance of larger biomolecules. In this regard, imaging takes place several days after injection, increasing the radiation burden to the patient.

However efforts are being made to couple shorter lived isotopes such as fluorine-18 or gallium-68 to smaller biomolecules (< 60 kDa) or fragments of antibodies such as nanobodies which exhibit more rapid blood clearance [157]. The field of theranostics combines therapeutic and diagnostic radio-isotopes. Ideally the radionuclide used exists as different isotopes, with different decay modes. As such pharmacokinetics will not differ and accurate estimations of dosimetry can be conducted. An example of such a radionuclide is terbium (Tb). Four Tb isotopes have been identified, Terbium-149 ( $\alpha$ -decay, targeted  $\alpha$ -therapy), Terbium-152 ( $\beta^+$ -decay, PET), Terbium-155 ( $\gamma$ -decay, SPECT), Terbium-161 ( $\beta^-$  decay and Auger electron decay,  $\beta^-$ /Auger electron therapy). These isotopes can be incorporated in the same vector molecule and as such be used for imaging and therapy, where the effect of therapy can be followed up. However the production and purification of Tb isotopes is both time and resource expensive [158].

## 6.2. Cyclotron and production of PET-tracers

Radionuclides that decay by positron emission can be produced by bombardment of stable nuclei with high energetic particles (protons, deuterons). Both incident particle and nucleus are positively charged and the resulting coulomb repulsion will require the incident particle to possess a high kinetic energy. This can be mediated by acceleration of the charged particle in a cyclotron. The cyclotron (**Figures 6B**) comprises a large metal container wherein a high vacuum is applied. Hydride ions ( $H^-$ ) and protons ( $H^+$ ) are generated by flowing hydrogen gas ( $H_2$ ) over a plasma in the ion source located at the centre of the cyclotron after which the negatively charged hydrogen atoms are extracted by the high voltage on the D's.  $H^-$ 's are accelerated by a high frequency alternating voltage applied on electrodes, denoted as 'Dee' in accordance with the historical D-shape. A magnetic field is generated by two magnetic coils which reside on the top and bottom of the cyclotron. The magnetic field (Lorentz force) engages the  $H^-$ 's to follow a circular path, during which the high voltage on the D's is reversed in polarity, creating an attraction/repulsion force, which accelerates the charged particles as they move across the gap between the D's and the adjacent magnetic hills at ground potential. During one turn hydride ions are accelerated four times resulting in an increase of the radius of their circular path. When the cloud of  $H^-$ 's has acquired enough velocity and thus kinetic energy (18-30 MeV for isotope production) it will pass through a stripper foil (carbon) where it loses its electrons and consequently the hydride ion is converted to a proton. The positively charged  $H^+$ 's will be forced outwards from the original trajectory by the magnetic field force, leave the cyclotron and hit the target where the nuclear reaction occurs (**Table 1**).

Only miniscule mass amounts of radioisotopes are produced by the cyclotron (picomoles to nanomoles scale). Dealing with these tiny amounts has led to increasingly specialized and miniaturized apparatuses for reacting and manipulating radiolabelling reactions. The newly synthesized radionuclides are transferred to designated automated or remote controlled synthesis modules housed in lead shielded "hot cells" (**Figure 6C-D**). The radionuclide can be directly incorporated in a precursor molecule, or *via* the use of an intermediate prosthetic group, which reacts with the precursor compound. Common reactions in carbon-11 chemistry transform the cyclotron generated  $[^{11}C]CH_4$  or  $[^{11}C]CO_2$  into  $[^{11}C]CH_3I$  or the more reactive  $[^{11}C]CH_3OTf$  (methyltriflate). Since PET labelling reactions are performed

with low mass amounts of radioisotopes, a vast stoichiometric excess of precursor will yield pseudo-first order reaction kinetics. Because of this, reactions which normally take days to complete, can be finished in a matter of seconds or minutes. It's also worth noticing that even small amounts of impurities in solvents or reagents can have significant effects (side reactions, lower reaction yield) when performing such small-scale reactions with distorted stoichiometry. Even though highly specialised equipment is used, only one in thousand molecules produced after radiosynthesis is marked with a radioactive label. The incident particles (deuteron or protons) mostly lose their energy *via* heat. As such nuclear reactions are rather ineffective. Contamination of the radionuclide with stable isotopes occurs *via* contact with materials from the environment during irradiation or transfer (target holder or transfer tubes), which 'dilutes' the radionuclide [154].

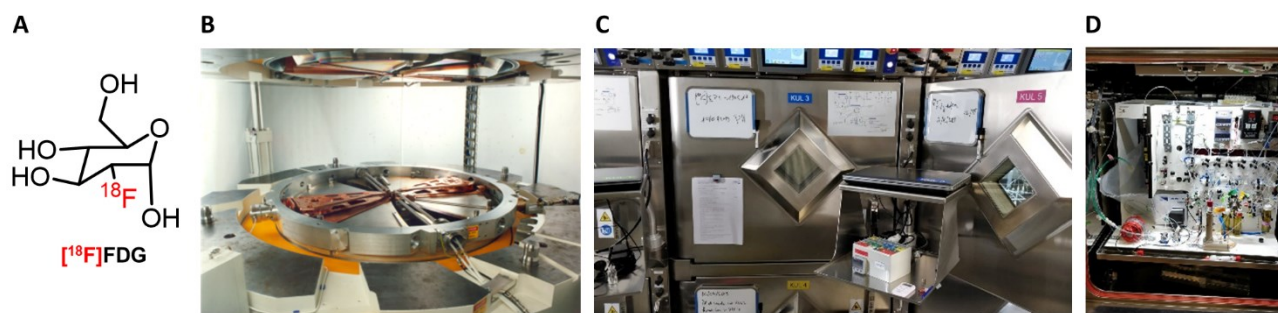


**Figure 6:** A) Chemical structure of [<sup>18</sup>F]FDG. B) Cyclotron internal view. C) Lead shielded hot cells. D) Radiolabelling synthesis module.

Before a PET tracer can be administered it has to be of pharmaceutical quality. Characterisation, formulation, purification and sterilisation needs to be done rapidly with respect to the short half-life of commonly used PET-radionuclides. PET tracers are often characterised by high-performance liquid chromatography (HPLC) in conjunction with suitable radioactivity detectors. Important parameters for radiopharmaceuticals are radiochemical yield (RCY), radiochemical purity (RCP), molar activity (MA) and radionuclidical purity. RCY is the ratio of the amount of activity of the final product relative to the starting activity and is typically noted as decay or non-decay corrected. The RCP is the proportion of radioactivity in the targeted chemical form (the tracer) relative to the total radioactivity of the radionuclide and is typically required to be  $\geq 90$ -95%, as an example <sup>18</sup>F-fluoride is a potential radiochemical impurity of [<sup>18</sup>F]FDG. RCP and chemical purity can be assessed by HPLC, thin layer chromatography (TLC) and gas chromatography (GC). Radionuclidical impurities comprise other radionuclides present in the sample (e.g. <sup>68</sup>Ge in a <sup>68</sup>Ga labelled radiopharmaceutical). The MA is a measure of the radioactivity per total amount (in mole) of compound (GBq/ $\mu$ mol or Ci/ $\mu$ mol) and is of importance in studies targeting saturable targets (e.g. receptors, transporters, enzymes). Low MA can result in underestimation of the target concentration or pharmacological activity at the target, resulting in side effects (e.g. Carfentanil can give rise to pharmacological effects at low doses (1.5  $\mu$ g)) [159].

When a tracer is administered, the general pharmacokinetics (absorption, distribution, metabolism and excretion (ADME)) apply [160]. Typically PET-tracers are administered intravenously (i.v.) and thus absorption can be neglected. Ideally, a good PET tracer expresses affinity (nM-range) and selectivity (> 100 selective over other isoforms or other receptors) for its target. Moreover tracer binding should preferentially be reversible with a low fraction of non-specific binding (NSB). NSB is caused by non-saturable binding of the tracer to tissue (e.g. hydrophile-lipophile balance based binding to lipophilic components of white brain matter) and will reduce the signal-to-noise ratio [161]. When intracellular targets are imaged, radiotracers need to cross the cell membrane. In this case, tracer lipophilicity needs to be sufficiently high to cross this barrier, but not too high to avoid non-specific interaction with the phospholipid double membrane layer. The blood-brain barrier (BBB) and the blood-testis barrier (BTB), consist of closely aligned endothelial cells interconnected with tight junctions and require even more rigid properties to allow free diffusion [162,163]. The BBB is one of the biggest hurdles to overcome in CNS PET imaging as besides a structural barrier, it also incorporates drug efflux transporters such as P-glycoprotein (P-gp) and multi-drug resistance protein 1 (MDR1) [164]. A rule of thumb implies that PET radiotracers should be uncharged at physiologic pH, have a logD value ranging from 2 to 3, a topological polar surface area (tPSA) value under 90 Å<sup>2</sup> and a molecular weight (Mw) under 500 Da to be able to efficiently pass BBB or BTB [161].

Metabolism arising from interaction of the tracer molecule with metabolic enzymes [165] can influence interpretation of acquired data and increase background signals as the PET camera detects the radionuclide and not the pharmaceutical carrier molecule. More so, undesired labelled metabolites can interact with the molecular target under investigation distorting the signal at the biological target under investigation. However, tracer metabolism benefits blood clearance, which in turn decreases background signals arising from radioactivity in blood. [166].

PET is a truly quantitative imaging technique. Important information about physiological and biochemical events can be obtained by monitoring the distribution and concentration of the labelled probe in the body over time. Dose occupancy studies can be performed, where the binding potential (BP), the ratio of the maximum density of receptors ( $B_{max}$ ) and the dissociation constant ( $K_D$ ), of the ligand to these receptors is measured. The affinity of a PET tracer ideally lies in the pico-to-nanomolar range and should be at least four times higher than the  $B_{max}$  ( $B_{max}/K_D > 4$ ) [167]. The low amount of injected PET-tracer (picomoles to nanomoles, combination of radioactive and stable molecules) meets the requirements for microdose studies. Induction of pharmacological effects is thus avoided and highly pharmacologically active drugs, can be administered at tracer doses [168]. Microdosage is part of the exploratory investigational new drug approach, which is used to accelerate drug development as only a limited number of toxicity studies are required before conducting the microdose approach [169]. Further, this approach will also facilitate transition of preclinical studies to the clinic as determined in European legislation by two directives (2001/20/EC and 2001/83/EC) [164].

## 7. MOLECULAR IMAGING OF HDACS

Several PET probes targeting HDACs have been developed (**Figure 7-13**) [170]. Initial research revolved around structural modifications of the pan-HDAC inhibitor SAHA resulting in [ $^{18}\text{F}$ ]FAHA, [ $^{18}\text{F}$ ]DFAHA, [ $^{18}\text{F}$ ]TFAHA (**Figure 7**) [171,172]. These compounds exhibited selectivity as substrates for class IIa HDACs over class I HDACs, due to the substitution of the hydroxamate functional group by a fluoro-acetyl moiety. The performance of these tracers for HDAC imaging in brain was evaluated in rats or non-human primates (NHP) and it was observed that an increasing number of fluorine atoms correlated with higher brain uptake and substrate efficiency. With accumulation of tracers in regions with high expression of HDAC4-5 (nucleus accumbens, hippocampus, amygdala and cerebellum). [ $^{18}\text{F}$ ]TFAHA binding in brain could be blocked by pre-administration of high doses of SAHA. Owing to the substrate feature of these compounds, the deacetylation function of class IIa HDACs could be visualised with formation of [ $^{18}\text{F}$ ]mono, di or tri-fluoroacetate, which conferred selectivity for class IIa HDACs. The authors suggested that [ $^{18}\text{F}$ ]TFAHA can be readily translated to the clinic where it can be further used to visualise class IIa HDACs in brain diseases. [ $^{18}\text{F}$ ]SAHA [173] and [ $^{18}\text{F}$ ]FESAHA [174] (**Figure 7**) were evaluated for visualisation of tumour HDAC expression. [ $^{18}\text{F}$ ]FESAHA was evaluated in a mouse model of LNCaP prostate carcinoma. However, tumour retention was low and the tracer suffered from defluorination leading to high bone uptake. Hence this compound was determined to be unsuitable for further investigations. [ $^{18}\text{F}$ ]SAHA (**Figure 7**) was evaluated in an ovarian cancer mouse model, where accumulation of the tracer in tumour was observed. The uptake could be blocked as assessed by SAHA pre-treatment. [ $^{18}\text{F}$ ]SAHA can further be used in clinical studies were SAHA or other HDAC inhibitors are evaluated. [ $^{18}\text{F}$ ]FETSAHA (**Figure 7**), a fluoroethyltriazole analogue of SAHA was synthesised *via* click labelling and evaluated in RR1022 sarcoma bearing rats where specific radioactivity accumulation in the tumour was observed, combined with rapid blood clearance [175]. Although sometimes promising results were obtained, none of these tracers advanced to clinical trials.

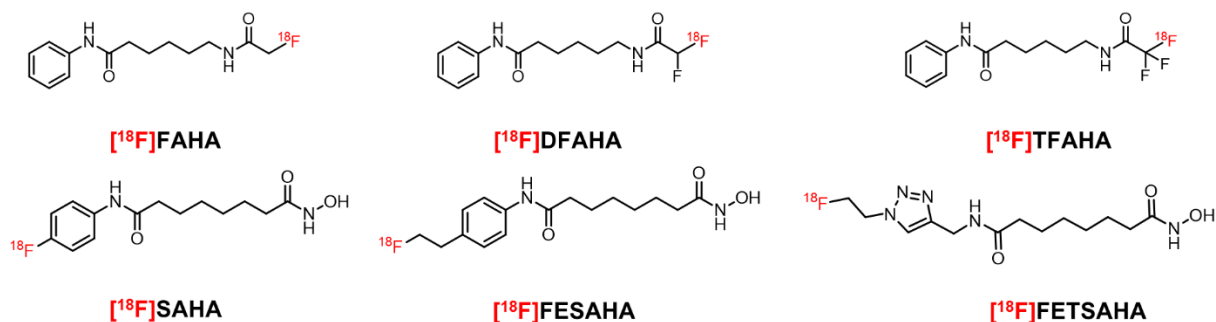


**Figure 7:** SAHA based HDAC PET tracers.

Three hydroxamate containing HDAC inhibitors were radiolabelled with carbon-11 (**Figure 8**). Pan-HDAC inhibitors Belinostat and Panobinostat (**Figure 2**) were modified to incorporate a carbon-11 methyl group, respectively yielding [ $^{11}\text{C}$ ]CN89 and [ $^{11}\text{C}$ ]CN107. The HDAC8 selective inhibitor PCI34051 was radiolabelled by substituting a methoxy moiety with [ $^{11}\text{C}$ ]CH $_3$ O. All three tracers were evaluated in rats and NHP but none of the three compounds efficiently passed the BBB [176]. Further, a fluorine-18 analogue of Panobinostat (**Figure 8**) was radiolabelled *via* isotopic exchange after introduction of a BF $_3$ -moiety to the core Panobinostat structure. RCYs were acceptable, but because of this labelling method, MA was rather low (407 kBq/mmol). Interestingly, the tracer was administered *via* convection enhanced delivery (application of a pressure gradient at the tip of an infusion catheter) directly to the brain of glioma bearing mice, allowing for image-guided delivery of HDAC inhibitors, which normally do not cross the BBB. This method was used to study drug delivery to hardly accessible, life threatening diffuse intrinsic pontine glioma [177]. [ $^{18}\text{F}$ ]Panobinostat was retained for at least 1 h. However, it is not clear if the tracer was specifically bound to HDACs as blocking studies were not conducted.

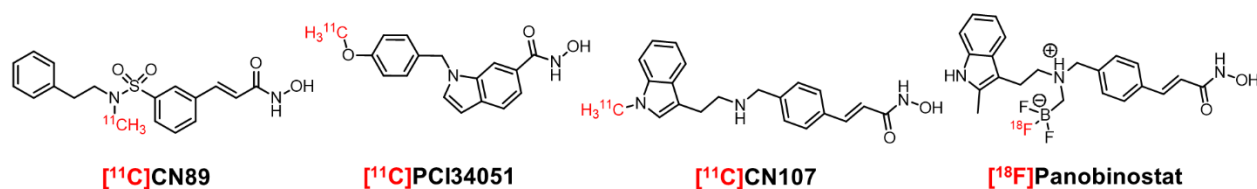


**Figure 8:** Hydroxamic acid based HDAC PET tracers.

The tritiated, benzamide class I HDAC inhibitor, [ $^3\text{H}$ ]CI-994 (Tacedinaline) was used to evaluate the distribution of HDAC1, 2 and 3 in mouse brain sections and BP was determined in an *in vitro* autoradiography experiment. The observed distribution was in line with western blot analysis where the highest density of class I HDACs was found in cerebellum, hippocampus and cortex. Binding of [ $^3\text{H}$ ]CI-994 on brain sections could be efficiently blocked with SAHA [178]. However, the corresponding carbon-11 labelled CI-994 (**Figure 9**) was later found not to pass the BBB, attributed to its high *t*PSA value (119.16) [179]. Absence of brain uptake in both rodents and NHP was also observed for the benzamide class I HDAC inhibitor [ $^{11}\text{C}$ ]MS-275 (**Figure 9**). Pre-treatment with MS-275 (Entinostat) or the P-gp inhibitor Verapamil did not alter the low brain uptake of [ $^{11}\text{C}$ ]MS-275 [180]. Further, in an elaborate study, 17 benzamide HDAC inhibitors, based on CI-994 and MS-275 scaffolds were radiolabelled *via* N-methylation with [ $^{11}\text{C}$ ]CH $_3$ I or [ $^{11}\text{C}$ ]CH $_3$ OTf or N-acetylation using [ $^{11}\text{C}$ ]AcCl. The carbon-11 tracers were evaluated in NHP  $\mu$ PET studies with arterial blood sampling, as potential brain tracers. One tracer, [ $^{11}\text{C}$ ]26 (**Figure 9**) was identified as a useful HDAC brain PET tracer, with potential use as a benchmark in the development of other PET tracers for imaging of HDAC in the CNS [179].

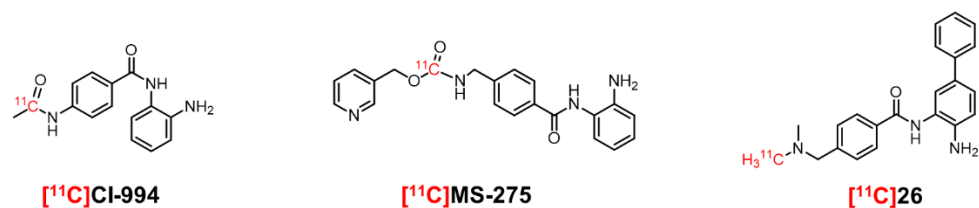


**Figure 9:** Benzamide based HDAC PET tracers.

The carboxylic acid-based weak HDAC inhibitors valproic acid, butyric acid and phenylbutyric acid (**Figure 10**), were radiolabelled with carbon-11 *via* interaction of [<sup>11</sup>C]CO<sub>2</sub> with the appropriate Grignard precursors. Only limited brain uptake of the compounds was observed in NHP [181]. Evaluation of [<sup>64</sup>Cu]CUDC-101 (**Figure 11**) in an MDA-MB-231 breast cancer xenograft model, showed high tumour-to-background contrast, suggesting that also radio-metal-based ligands can be used for cancer HDAC-PET imaging. The specificity of this tracer was assessed by blocking with CUDC-101 [182]. These compounds however, were only tested in preclinical studies.

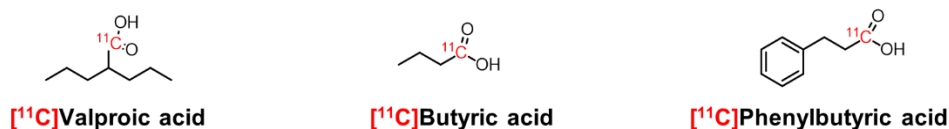


**Figure 10:** Carboxylic based HDAC PET tracers.

Molecular imaging of Sirt1 expression in rat brain was accomplished using 2-[<sup>18</sup>F]-BzAHA (**Figure 11**), an aminohexanoicanilide compound. Uptake of the tracer was observed in the hypothalamus, hippocampus, nucleus accumbens, and locus coeruleus. Moreover, binding of this tracer could be blocked using EX-257, a non-structurally related Sirt1 inhibitor. This tracer shows promise as a tool to visualise Sirt1 *in vivo* in brain with potential translation to the clinic [183]. A Sirt2 PET tracer, 12-[<sup>18</sup>F]DDAHA (**Figure 11**), was developed and evaluated *in vitro* where it was observed to be taken up rapidly in Sirt2 expressing tumour cells. However, *in vivo* PET studies on 9L-glioma bearing rats showed rapid defluorination and consequent bone (skull) uptake, which severely hampered interpretation of PET signals in brain/glioma [184].



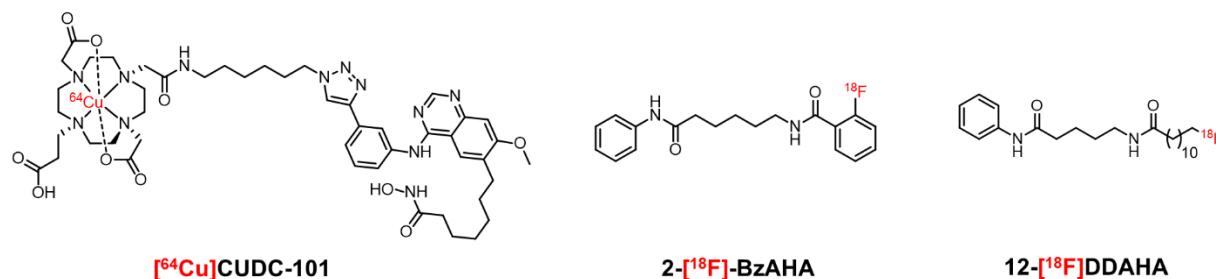


**Figure 11:** Radiometal containing HDAC PET tracer ( $[^{64}\text{Cu}]$ CUDC-101) and Sirtuin PET tracers (2- $[^{18}\text{F}]$ BzAHA and 12- $[^{18}\text{F}]$ DDAHA).

$[^{11}\text{C}]$ Martinostat (**Figure 12**), an adamantyl based hydroxamic acid compound, first reported by Wang *et al.* [185] showed good brain uptake, high affinity for HDAC1, 2, 3 and 6 (low nM-range) and HDAC-specific brain retention in rats and NHP. Specificity of binding was also assessed by pre-treatment with SAHA in NHPs where tracer binding was efficiently blocked in heart, kidney, pancreas and spleen. This compound was the first HDAC tracer which advanced to clinical trials where it was evaluated in healthy volunteers and in patients with schizophrenia or schizoaffective disorder. Here, it was observed that relative HDAC expression in disease conditions was lower in the dorsolateral prefrontal cortex compared to healthy individuals. It was concluded that changes in brain HDAC expression correlated with memory and cognition [186–188]. Further, several fluorine-18 analogues of Martinostat were developed (**Figure 12**).  $[^{18}\text{F}]$ CN146, a fluoroethyl (FET) analogue was not further evaluated as its HDAC binding affinity was markedly reduced.  $[^{18}\text{F}]$ MGS3, a fluoro-benzene analogue, showed a similar distribution pattern as  $[^{11}\text{C}]$ Martinostat in baboon brain but implementation of this tracer in clinical trials was hampered due to low RCYs [189]. Recently, the same research group introduced  $[^{18}\text{F}]$ Bavarostat (**Figure 13**), where fluorine-18 was introduced *via* a newly reported deoxyfluorination method involving a ruthenium catalyst. This compound, also equipped with an adamantyl moiety, was found to be a selective HDAC6 PET probe (Half-maximal inhibitory concentration ( $\text{IC}_{50}$ ) = 60 nM, > 80-fold selectivity over other HDACs) capable of passing the blood-brain barrier (BBB).  $[^{18}\text{F}]$ Bavarostat was evaluated in rats and NHPs where blocking studies with Bavarostat indicated saturable binding. Blocking with a non-structural related HDAC6 inhibitor was not performed due to the lack of well characterised brain penetrant HDAC6-selective inhibitors. However, in *in vitro* autoradiography studies, Tubastatin A was able to reduce tracer binding with 40% in cerebellum similar to blocking with Bavarostat. This tracer can be used to visualise HDAC6 in human brain [190].



**Figure 12:** Martinostat based HDAC PET tracers.

In 2012 Butler *et al.* developed Tubastatin A, a tryptoline based hydroxamic acid compound with high selectivity for HDAC6 and an  $IC_{50}$  of 15 nM, which had potential beneficial neuroprotective properties. Treatment of cells increased tubulin acetylation levels, without affecting histone acetylation. In the same paper, KB631 was introduced with even higher affinity ( $IC_{50} = 1.4$  nM) and selectivity for HDAC6 ( $> 3500$  vs HDAC1) [191]. The radiosynthesis of [ $^{11}C$ ]Tubastatin A (**Figure 13**) was first reported by Lu *et al.* in which carbon-11 was inserted as [ $^{11}C$ ]CO in the hydroxamic acid moiety *via* a Pd-mediated pathway, however this method was not generic as it could not be implemented in the synthesis of three other hydroxamate bearing molecules [192]. [ $^{11}C$ ]KB631, reported by Lu *et al.* [193] (**Figure 13**), was synthesized by conventional radioalkylation with [ $^{11}C$ ]CH<sub>3</sub>I in alkaline conditions on the tryptoline moiety. This compound was further evaluated as a potential imaging tool for HDAC6 in the brain. However,  $\mu$ PET studies performed on rats and NHP showed only limited brain uptake of the compound and a detailed report of this tracer was never published. In **Chapter III**, [ $^{11}C$ ]KB631 is used to visualise HDAC6 in B16.F10 melanoma bearing mice.

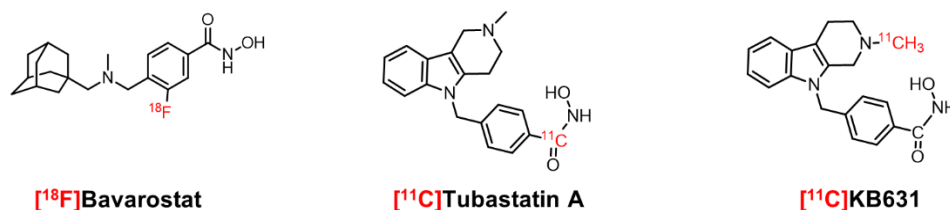


**Figure 13:** HDAC6 selective PET tracers.

## 8. MOLECULAR IMAGING OF HSP90

Hsp90 inhibition is generally well tolerated, however ground-breaking successes in clinical trials are yet to occur [194]. Disruption of the Hsp90-dimer or inhibition of the Hsp90 function will induce a compensatory shift of client protein processing to Hsp70 or other members of the chaperome [131]. Recent studies suggested embedment of Hsp90 in a highly structured network with other members of the chaperome, called the “epichaperome”, in stress conditions, where a collapse of the network is reported after inhibition of one of the subsets. The availability of an Hsp90 PET probe can accelerate drug development and elucidate the role of Hsp90 in disease initiation and progression. Only a limited number of Hsp90 PET tracers have been reported, and these specifically target tumour Hsp90. Other studies used PET to visualise changes in metabolic pathways or client proteins of Hsp90 after administration of Hsp90 drugs [91].

PU-H71 (**Figure 4, Purine**), an iodine containing purine based Hsp90 inhibitor, was determined to be an effective inhibitor of the epichaperome [93,97]. PU-H71 is a pan-selective Hsp90 inhibitor with a two-fold higher affinity towards the ER residing Hsp90 paralogue, Grp94 (Grp94  $IC_{50} = 26$  nM vs Hsp90 $\alpha$   $IC_{50} = 43$  nM) [120]. [ $^{124}I$ ]PU-H71 (**Figure 14**) was synthesized by iododestannylation in good yields [195]. The biodistribution was explored in MDA-

MB-468/ASPC1 mouse xenografts, representatives of respectively type 1 (high chaperome connectivity) and type 2 (low chaperome connectivity) tumours [93]. The tracer showed relatively slow kinetics but tracer uptake in the MDA-MB-468 (type 1) tumour persisted over 48 h, whereas tracer uptake in the ASPC1 (type 2) tumour gradually decreased over 48 h. [<sup>124</sup>I]PU-H71 was further used in a clinical trial in patients harbouring different types of cancers (breast cancer, lymphoma, gynaecologic malignancies). PU-PET was conducted 24 h after injection of [<sup>124</sup>I]PU-H71 to identify Hsp90 responsive tumours as part of a clinical study (NCT01393509) [93]. The same research group has recently developed [<sup>124</sup>I]PU-AD, which will be evaluated in a clinical trial (NCT03371420) to visualise Hsp90 in patients with AD and different cancers. However, results have not yet been published.

Recently, a radiolabelled analogue of the well-characterised Hsp90 inhibitor Ganetespib (**Figure 4, Resorcinol**) was reported. [<sup>18</sup>F]PTP-Ganetespib (**Figure 14**) was radiolabelled by click chemistry in good RCY. This compound was further evaluated in mice bearing MDA-MB-231 or MC7 breast cancer. *In vitro*, Ganetespib efficiently blocked the accumulation of the tracer. But in *in vivo*  $\mu$ PET studies, an initial weak tumour uptake was observed compared to other organs. The uptake of the tracer in the tumour was maintained and wash out was slower compared to other organs, but the accumulation was not sufficient to further progress with this compound. *In vivo* determination of binding specificity was also not performed [196].

A copper-64-labelled dimeric Sansalvamide A decapeptide (<sup>64</sup>Cu]Di-San A1, **Figure 14**) was used to evaluate Hsp90 expression in in a mouse model of pancreatic PL45 cancer. Copper-64 was chelated with NOTA and conjugated to the core Sansalvamide structure in good RCYs. The tracer remained stable in phosphate buffered saline (PBS) and mice serum and was evaluated *in vitro* in PL45 pancreatic tumour cells where it showed specific binding to the cells as assessed by blocking with 17-AAG (**Figure 4, Quinone**). *In vivo* uptake in PL45 tumours was demonstrated in biodistribution and  $\mu$ PET studies. Specific binding *in vivo* was also observed after pre-treatment of 17-AAG. Tumour-to-muscle ratios showed adequate tumour uptake as well as clearance *via* the hepatobiliary circuit [197]. An iodine-131 radiolabelled monoclonal antibody targeting Hsp90 $\alpha$  (<sup>131</sup>I]HSP90 $\alpha$ -mAB) was evaluated in DU145 prostate cancer bearing mice with SPECT. Radiolabelling was performed using chloramine-T and the compound was observed to specifically bind to DU145 cells *in vitro*. *In vivo*, tumour uptake was specific and the location of the tumour was clearly identified as compared with [<sup>18</sup>F]FDG (**Figure 6A**) [198].

Radiolabelled [<sup>125</sup>I]HS-111, which uses a scaffold based on Hsp90 inhibitor SNX-2112 to bind the ATP-binding domain of Hsp90, was evaluated together with fluorescent tethered analogues (HS-27 (fluorescein isothiocyanate (FITC) and HS-69 (near-infrared fluorophore)) in breast cancer cells and breast cancer mice models. Importantly, these inhibitors were designed to target eHsp90, as they lack properties to permeate the cell membrane. However, it was observed that the probes were actively internalised in cells, which highly expressed eHsp90. Binding of the probes *in vivo* was determined to be Hsp90-specific, assessed by blocking studies with PU-H71 and 17-AAG [199]. Later on, HS-131 was introduced, tethered to a Cy5 dye, which allowed for more cost-effective and reproducible imaging of eHsp90. HS-131 was demonstrated to selectively target oncogenic eHsp90, with higher binding to active mammary tumour cells

corresponding to higher expression of eHsp90. Again this probe was actively internalised *via* eHsp90, however the exact internalisation mechanism remains unknown. Furthermore, internalisation of the HS probes was blocked using an antibody against the C-terminal of Hsp90 [105]. The authors concluded that eHsp90 can be a valuable target for visualisation of cancer cell metastasis and invasiveness and can play a defined role as a biomarker of malignant cell behaviour.

[<sup>64</sup>Cu]DOTA-anti-hAXL, targets the AXL tyrosine kinase (client protein of Hsp90), which was used to assess the effect of Hsp90 inhibition with 17-AAG (**Figure 4, Quinone**) on AXL expression in a triple negative breast cancer mouse model. PET/CT imaging showed a remarked decrease of AXL upon 17-AAG treatment, further it was observed that the epithelial-to-mesenchymal transition, closely related to metastasis, was significantly inhibited [200]. In a squamous cell carcinoma mice model, the endothelial growth factor receptor (EGFR), (also a client protein of HSP90) was used as biomarker for response monitoring after administration of Onalespib (**Figure 4, Resorcinol**). Radiolabelled anti-EGFR antibody [<sup>124</sup>I]Cetuximab uptake was compared with [<sup>18</sup>F]FDG in mice inoculated with high EGFR A431 tumour and low EGFR UM-SCC74B tumours, treated with Onalespib. Reduced uptake of [<sup>124</sup>I]Cetuximab was observed in the A431 tumour after treatment with Onalespib, indicating a decrease of EGFR. [<sup>18</sup>F]FDG uptake was similar for both tumours, indicating no unchanged glucose metabolism of the tumours [201]. HER2-PET with [<sup>68</sup>Ga]Dota-F(ab')<sub>2</sub>-herceptin, was compared with [<sup>18</sup>F]FDG in mice bearing BT474 breast tumours in mice that were treated with 17-AAG. One day after treatment, decreased HER2 levels were observed with HER2-PET whereas [<sup>18</sup>F]FDG uptake was unaltered. This indicates that Hsp90 client degradation occurs without altering tumour glycolysis [202]. Glycolysis can be affected at later time points in the treatment, as reduction of tumour volume has effects on metabolism.

In the clinic, [<sup>18</sup>F]FDG was used to study the effects of Hsp90 inhibition on metabolic pathways in different cancers. In two separate studies, [<sup>18</sup>F]FDG was used in combination with Hsp90 inhibitors Retaspimycin HCl (IPI-504, **Figure 4, Quinone**) or BIIB021 (**Figure 4, Purine**) in patients with metastatic gastrointestinal stromal tumours and soft-tissue sarcoma. Reduced uptake of [<sup>18</sup>F]FDG after BIIB021 treatment was already observed after 2 doses. Almost 40% of the patients treated with IPI-504 showed a partial metabolic response in the tumour resulting from Hsp90 inhibitor treatment [203,204]. [<sup>89</sup>Zr]Trastuzumab and [<sup>89</sup>Zr]Bevacizumab have been used to evaluate the effect of HSP90 inhibitor Luminespib (**Figure 4, Resorcinol**) in respectively, HER2-positive and estrogen receptor-positive metastatic breast cancer patients [205]. Here, therapy with Luminespib fulfilled expectations, as degradation of HER2 could be picked up with the [<sup>89</sup>Zr]Trastuzumab-PET.

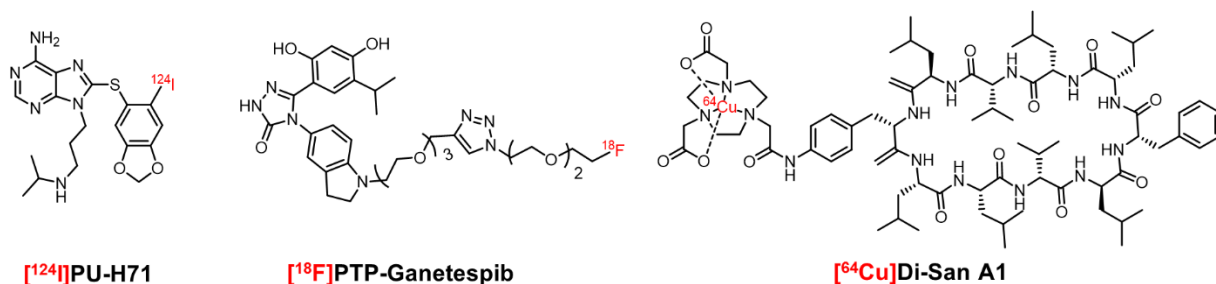


**Figure 14:** Hsp90 PET tracers.

At the start of this PhD-project only a limited number of HDAC PET tracers were selected for development. These tracers were based on Santacruzamate A which was reported to possess high affinity (pM range) for HDAC2. This HDAC isoform was reported to be implied in neurodegenerative diseases and several cancers [206]. To our knowledge, these were the first compounds with subnanomolar affinity for HDAC2. The anti-HDAC6 compound, KB631, was reported with an  $IC_{50}$  value of 1.4 nM for HDAC6 and 3700-fold selectivity over HDAC1 [191]. HDAC6 was also found overexpressed in neurodegenerative diseases and several cancers [48,51]. Although KB631 was unable to pass the BBB [193], it still could be of value in HDAC6 PET imaging in cancer, as this line of research was unexplored.

The aberrant role of Hsp90 has predominantly been reported in oncology. A limited number of reports are however also mentioning a role and overexpression of Hsp90 in neurodegenerative diseases [110]. A first Hsp90 PET tracer [<sup>124</sup>I]PU-H71 showed tumour uptake, but kinetics were rather slow and a high-signal-to-noise ratio was only obtained 24-48 h after tracer injection [93]. Also, iodine-124 has a long  $T_{1/2}$  (4.2 days) and a low branching factor for  $\beta^+$ -decay (26%) with concomitant high energy  $\gamma$ -decay which increases radiation burden. Although [<sup>124</sup>I]PU-H71 is a very useful tool for epichaperome PET imaging, we believe that the Hsp90 PET field could also benefit from a tracer labelled with a PET radionuclide with a shorter half-life. As such, we started the search for compounds that could be radiolabelled with carbon-11 or fluorine-18.

The potent Hsp90 inhibitor NMS-E973 ( $K_D = 0.35$  nM) was evaluated against numerous tumour cell lines and showed efficiency against intracranial implanted melanoma [207,208]. Hence this compound showed great promise for further evaluation as a PET imaging tool for Hsp90 in both CNS and oncological disorders.

Later on in this PhD-project YC-72-AB85 ( $IC_{50} = 19$  nM), a derivative of HSP990 (an Hsp90 inhibitor evaluated in clinical trials) [209] was explored in cooperation with researchers from Novartis. This compound was previously shown to pass the BBB and allowed carbon-11 radiolabelling.

## OBJECTIVES AND OUTLINE OF THE THESIS

The main goal of this research was the development and evaluation of PET tracers targeting HDAC isoforms, HDAC2 and 6, and Hsp90. As such, this thesis is divided in four research chapters, two concerning the development and evaluation of HDAC tracers and the other two based on research conducted with two Hsp90 tracers. A general introduction about the two subjects can be found in **CHAPTER I**.

In **CHAPTER II**, we aimed to develop selective HDAC2 PET tracers, based on literature reported compounds Santacruzamate A and Santacruzamate A-SAHA hybrid. These compounds were evaluated for HDAC2 affinity *in vitro* against recombinant proteins and in *in silico* molecular docking studies. Furthermore, bioisosteres of these compounds were developed and attempts at radiolabelling were made.

**CHAPTER III** describes the evaluation of [<sup>11</sup>C]KB631, a selective HDAC6 PET tracer in a B16.F10 melanoma tumour model. *In vitro* autoradiography was performed on B16.F10 melanoma and PC3 prostate carcinoma and brain sections of rats and mice. Further, tracer binding specificity was assessed *in vivo* in healthy and diseased mice. Lastly, a  $\mu$ PET study on B16.F10 melanoma inoculated mice was performed.

**CHAPTER IV**, details the evaluation of [<sup>11</sup>C]NMS-E973, a potent Hsp90 PET tracer, in a B16.F10 melanoma tumour model. NMS-E973 was tested against a panel of tumour cells in comparison with Ganetespib, a small molecular Hsp90 inhibitor currently evaluated in clinical studies. *In vitro* autoradiography experiments were performed on different tumours and this tracer was thoroughly assessed *in vivo* in biodistribution studies and  $\mu$ PET experiments.

A very promising Hsp90 PET tracer, [<sup>11</sup>C]YC-72-AB85, was developed and evaluated. Data is presented in **CHAPTER V**. This compound is able to efficiently pass the BBB and as such is evaluated as a brain Hsp90 PET tracer. *In vitro* autoradiography studies were performed on different tumour slices and rodent brain.  $\mu$ PET studies were performed in rats, a biodistribution study was performed on B16.F10 melanoma inoculated mice and tracer uptake was compared in different organs against healthy counterparts.

A general discussion of the work performed in this dissertation is held in **CHAPTER VI**.

---

# SYNTHESIS, ENZYME ASSAYS AND MOLECULAR DOCKING STUDIES OF FLUORINATED BIOISOSTERES OF SANTACRUZAMATE A AS POTENTIAL HDAC TRACERS

---

Muneer Ahamed<sup>1\*</sup>, **Koen Vermeulen**<sup>2\*</sup>, Michaël Schnekenburger<sup>3</sup>, Lise Román Moltzau<sup>4,9</sup>, Finn Olav Levy<sup>4,9</sup>, János Marton<sup>8</sup>, Mathy Froeyen<sup>5</sup>, Dag Erlend Olberg<sup>6</sup>, Marc Diederich<sup>3,7</sup> and Guy Bormans<sup>2</sup>

<sup>1</sup> Centre for Advanced Imaging, University of Queensland, Brisbane, Australia

<sup>2</sup> Laboratory for Radiopharmaceutical Research, Department of Pharmaceutical and Pharmacological Sciences, KU Leuven, Leuven, Belgium

<sup>3</sup> Laboratoire de Biologie Moléculaire et Cellulaire du Cancer, Hôpital Kirchberg, 9, rue Edward Steichen, L-2540 Luxembourg, Luxembourg

<sup>4</sup> Department of Pharmacology, Institute of Clinical Medicine, University of Oslo and Oslo University Hospital, Oslo, Norway

<sup>5</sup> Laboratory for Medicinal Chemistry, Rega Institute of Medical Research, KU Leuven, Leuven, Belgium

<sup>6</sup> School of Pharmacy, University of Oslo and Norwegian Medical Cyclotron Centre, Oslo, Norway

<sup>7</sup> Department of Pharmacy, Research Institute of Pharmaceutical Sciences, College of Pharmacy, Seoul National University, Seoul, Republic of Korea and Tumor Microenvironment Global Core Research Center, College of Pharmacy, Seoul National University, Seoul 151-742, South Korea

<sup>8</sup> ABX advanced biochemical compounds, Biomedizinische Forschungsreagenzien GmbH, Radeberg, Germany

<sup>9</sup> Center for Heart Failure Research, Faculty of Medicine, University of Oslo, Oslo, Norway

\*These authors contributed equally to this work.

Manuscript published in Letters in Drug Design & Discovery 2017; 14(7):1-11

Supplementary information: <http://www.eurekaselect.com/146931/article>





## Abstract

Histone deacetylases emerged as important epigenetic regulators of gene expression. In order to identify potential PET tracers for visualisation of HDACs, *in vitro* and *in cellulo* activities of compounds reported as potent HDAC2-selective inhibitors were evaluated. Marked differences were observed between reported activity values and the values obtained in our assays for some of the compounds. To determine the structural basis of activity of these inhibitors, we also performed molecular docking studies to better understand their interaction patterns and binding modes with HDAC2. The low affinity compounds **5**, **6** and **7** did not show equal number of key  $\pi$ - $\pi$  interactions and hydrogen bonding compared to high affinity compounds **1**, **2** and **3**. These findings possibly explain the poor inhibition observed in *in vitro* assays. These preliminary experimental and computational results indicate that HDAC affinity values of compounds **5**, **6** and **7**, reported in literature, should be reconsidered and interpreted with caution.

## 1. INTRODUCTION

Histone deacetylases (HDACs) are essential post-translational regulators responsible for deacetylation of acetylated lysine residues on histone and non-histone substrates [210,211]. HDACs are divided into four major classes: class I (HDAC1, 2, 3 and 8), class II (HDAC 4, 5, 6, 7, 9 and 10), class III also called sirtuins (Sirt1 to 7) and class IV (HDAC11). All of them are Zn<sup>2+</sup>-dependent metalloproteins except class III HDACs which use nicotinamide adenine dinucleotide (NAD<sup>+</sup>) as a cofactor in the deacetylation process [212,213]. The development of new drugs acting as inhibitors of the HDAC enzymatic activities (HDAC inhibitor) is a proven strategy for many diseases including central nervous system disorders (CNS), cardiac diseases and different forms of cancer [214–217].

Prototypical Zn<sup>2+</sup>-dependent HDAC inhibitors consist of (1) a capping group, also called surface recognition domain, usually a hydrophobic and aromatic group which mediates the interaction with the rim of the binding pocket and occludes the entrance of the active site pocket. (2) A linker region with a linear or cyclic structure, which enables  $\pi$ - $\pi$  stacking with aromatic amino acids in the HDAC pocket and is important for increased affinity. (3) A Zn<sup>2+</sup>-chelating group and optionally (4) an internal cavity binding moiety. Numerous natural and synthetic HDAC inhibitors have been identified in recent decades [218]. These inhibitors are classified according to their structure into five categories: short-chain fatty acids, hydroxamic acids, cyclic peptides, benzamides and macrocycles. Other compounds, such as polyketides, ortho-anilides, chalcones, tropolones and sulfur containing compounds also display HDAC inhibitory activity [20,37].

So far there are four US Food and Drug Administration (FDA)-approved HDAC inhibitors in clinics for cancer therapy. In 2006, suberoylanilide hydroxamic acid (SAHA, Vorinostat, Zolinza®; **1, Figure 1**) was approved as a first in class hydroxamic acid-based inhibitor for the treatment of cutaneous T-cell lymphoma (CTCL). In 2009, the class I-specific inhibitor Romidepsin (FK228, Istodax®) (**Figure 2 in Chapter I**), a thiol-based depsipeptide, also gained approval for the treatment of CTCL. In 2011, Romidepsin was also approved for treatment of patients with peripheral T-cell lymphoma (PTCL) who have received at least one prior therapy. Two additional hydroxamic acid-based pan-HDAC inhibitors, PXD101 (Belinostat, Beleodaq®) and LBH-589 (Panobinostat, Farydak) (**Figure 2 in Chapter I**) were approved in 2014 and 2015, respectively. PXD101 received approval for treatment of refractory or relapsed PTCL and LBH-589 was approved for patients with multiple myeloma (MM) who received at least two prior regimens including an immunomodulatory agent and the proteasome inhibitor Bortezomib [219].

Noteworthy, many of these inhibitors target multiple HDAC isoforms and thus can cause toxic side effects [215]. Increasing evidence suggest that these side effects could be limited by only targeting a number or ideally only one HDAC isoform, involved in a specific disease or disease subtype, ultimately providing therapeutic tools for personalised treatment [35,220–222].

In this context, the search for selective HDAC inhibitors is an ongoing hot topic. A major HDAC isoform that is involved in various diseases is HDAC2, which functions as an important factor in cell development, cytokine signalling involved

in immune responses and is often significantly overexpressed in cancers such as acute myeloid leukaemia [215], gastric, [223] and colon cancer [224–226]. In addition, HDAC2 is part of various co-repressor complexes with HDAC1 and 3, often aberrantly recruited by oncogenic fusion proteins [7]. It also controls pro-apoptotic factor p53 [10], regulates memory formation and synaptic plasticity [227], and is involved in the maintenance of cardiac hypertrophic responses [228]. Consequently, HDAC2 can be a valuable target in the search for cures for these pathologies.

### 1.1. HDAC enzyme activity inhibition values from the literature

Compound **2** (**Figure 1**) was first reported by Rajagopal *et al.* [229], who showed that it expressed a pan-HDAC half-maximal inhibitory concentration ( $IC_{50}$ )-value of 1.1 nM. Subsequently, Wang *et al.* modified compound **2** by adding an additional N-methyl group to form **3** (Martinostat, **Figure 1**). Which could be labelled with carbon-11 and used as a positron emission tomography (PET) tracer for HDAC imaging [230]. Compound **3** was found to inhibit HDAC2 ( $IC_{50}$  = 2.0 nM) but lacked isoform-selectivity. Notwithstanding its use as a lead for the development of HDAC2-selective inhibitors. A fluorethyl (FEt) analogue of Martinostat (CN146, **4**, **Figure 1**), where a fluorethyl moiety was inserted in the position of the methyl, was later reported by the same research group. This compound showed a similar binding preference for the same HDAC isoforms as Martinostat. Although the targets were not altered, the affinity was roughly 100-fold reduced [189].

Pavlik *et al.* recently reported the selective and potent HDAC2 inhibitor Santacruzamate A, (**5**, **Figure 1**), with an exceptional  $IC_{50}$  value of 119 pM for HDAC2 [206]. Moreover, in the same article a Santacruzamate A-SAHA hybrid (**6**, **Figure 1**) was described to have good inhibitory activity towards HDAC2 ( $IC_{50}$  of 3.5 nM).

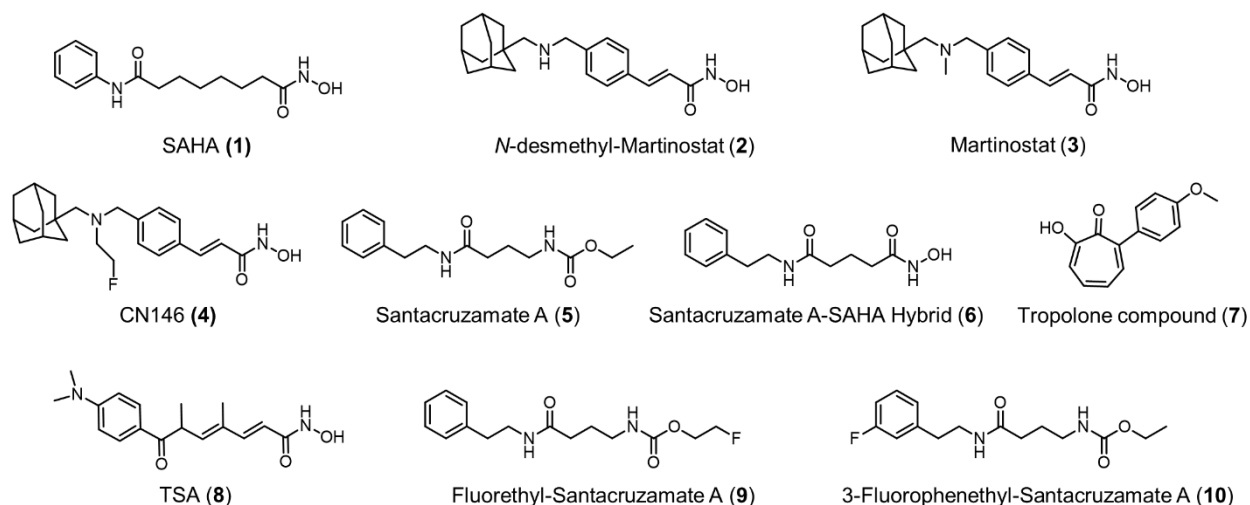


**Figure 1:** Structures of potent HDAC inhibitors investigated in this study.

The synthetic products (Santacruzamate A, **5** and Santacruzamate A-SAHA hybrid, **6**) as well as the natural product (isolated from a cyanobacterium) Santacruzamate A (**5**) were evaluated for isozyme-selective inhibition of HDAC2 and HDAC4, which are class I and class IIa HDACs, respectively. It was reported that all three compounds selectively inhibited HDAC2 with relatively little inhibition of HDAC4. In contrast, SAHA completely inhibited both class I and II HDACs at a concentration of 1  $\mu$ M. On this basis, IC<sub>50</sub> values were determined for HDAC2, HDAC4 and HDAC6. SAHA showed an IC<sub>50</sub> value of 86 nM for HDAC2, whereas it was reported that the Santacruzamate A compound expressed picomolar IC<sub>50</sub> values for HDAC2 (**Table 1**). All three compounds showed IC<sub>50</sub> values > 1  $\mu$ M against HDAC4. IC<sub>50</sub> values for HDAC6 obtained with the natural and synthetic Santacruzamate A and compound **6** were found to be 434, 433 and 386 nM respectively, while SAHA showed limited selectivity with an IC<sub>50</sub> of 39 nM [206].

Ononye and co-workers reported  $\alpha$ -aryl substituted tropolone scaffolds as potent HDAC2-selective inhibitors. In particular compound **7** was reported to have an inhibitory constant (K<sub>i</sub>) of 0.81 nM [231,232]. These tropolone derivatives are believed to form a strong bond with the catalytic Zn<sup>2+</sup>-ion mediated *via* an  $\alpha$ -hydroxy ketone group. Besides high affinities for HDAC2 they were also reported to exhibit cytotoxicity in cancer cells.

During the course of our investigation, Liu Wen *et al.* reported a biological study performed with Santacruzamate A (**5**) as well as analogues thereof, where they observed no inhibition of HDAC2 even at a concentration of 2  $\mu$ M [233]. We recently started an investigation in search of isozyme-selective HDAC2 inhibitors for potential use as cancer drugs and also as potential PET tracers for *in vivo* imaging of HDAC2. In this context, we report preliminary results of compounds **1-10** (**Figure 1**), determining their pan-HDAC and HDAC2 inhibition potency. Further, these *in vitro* results are compared with *in silico* docking studies.

## 2. MATERIALS AND METHODS

### 2.1. Cell culture, total protein extraction and *in vitro* HDAC activity assays (Luxembourg)

Chronic myeloid leukemia K-562 cells (American Type Culture Collection (ATCC), Manassas, USA) were cultured in RPMI 1640 (BioWhittaker®, Lonza, Verviers, Belgium) supplemented with 10% heat-inactivated fetal calf serum (BioWhittaker®) and 1% antibiotic-antimycotic (BioWhittaker®) at 37 °C in humid atmosphere and 5% CO<sub>2</sub>. Cells were harvested, washed in cold phosphate buffered saline (PBS) (1x), and lysed in MPER® (Thermo-scientific, Erembodegem-Aalst, Belgium) supplemented by 1x protease inhibitor cocktail (Complete EDTA-free, Roche, Prophac, Luxembourg, Luxembourg) according to manufacturer's instructions. HDAC activity assays were carried out as previously described [234]. For total HDAC activity assay, 10  $\mu$ g of K-562 total protein extracts was used. The quantity of enzymes per well, concentration of substrates and cofactor, and incubation times were used as previously reported [235]. IC<sub>50</sub> values were determined using GraphPad Prism 6.0.

## 2.2. Fluorogenic HDAC2 assay (Oslo)

HDAC2 activity in the presence of the different inhibitors was measured by using HDAC fluorogenic assay kits from BPS Bioscience, (CA, USA) or Active Motif (CA, USA). The HDAC2 enzyme was obtained from BPS Bioscience (concentration as recommended by producer (BPS Bioscience) or 56 ng/reaction (using assay from Active Motif)).

## 2.3. Experimental section

### (E)-3-(4((((3R,5R,7R)-Adamantan-1-ylmethyl)amino)methyl)-phenyl)-N-hydroxy acrylamide [2, N-Desmethyl-Martinostat]

*Colourless Powder*,  $^1\text{H}$  NMR ( $\text{CD}_3\text{OD}$ ):  $\delta$  1.58-1.77 (m, 13H), 1.98-2.02 (m, 3H), 2.67 (s, 2H,  $\text{CH}_2$ ), 4.25 (s, 2H,  $\text{CH}_2$ ), 6.54 (d,  $J$  15.7 Hz, 1H,  $\text{CH}$ ), 7.54-7.65 (m, 5H, *Ar*).  $^{13}\text{C}$  NMR ( $\text{CD}_3\text{OD}$ ):  $\delta$  29.5 (3C), 33.4, 37.5 (3C), 40.7 (3C), 52.9, 59.9, 120.1, 129.5, 132.0, 133.6, 137.7, 140.5, 166.0. HRMS (ESI) calculated for  $\text{C}_{21}\text{H}_{29}\text{N}_2\text{O}_2$   $[\text{M}+\text{H}]^+$ : 341.2224. Found: 341.2244.

### (E)-3-(4((((3R,5R,7R)-Adamantan-1-ylmethyl)(methyl)amino)methyl)-phenyl)-N-hydroxy acrylamide [3, Martinostat]

*Colourless Powder*,  $^1\text{H}$  NMR ( $\text{CD}_3\text{OD}$ ):  $\delta$  1.46 (brs, 6H,  $\text{CH}_2$ ), 1.56-1.68 (m, 6H,  $\text{CH}_2$ ), 1.85 (brs, 3H), 2.03 (brs, 2H), 2.13 (s, 3H,  $\text{CH}_3$ ), 3.46 (s, 2H,  $\text{CH}_2$ ), 6.38 (d,  $J$  = 15.8 Hz, 1H,  $\text{CH}$ ), 7.24-7.48 (m, 5H, *Ar*).  $^{13}\text{C}$  NMR ( $\text{CD}_3\text{OD}$ ):  $\delta$  30.1 (3C), 36.3, 38.4 (3C), 42.4 (3C), 46.4, 66.0, 72.1, 118.3, 128.7 (2C), 130.6 (2C), 135.1, 141.1, 143.61, 166.5. HRMS (ESI) calculated for  $\text{C}_{22}\text{H}_{31}\text{N}_2\text{O}_2$   $[\text{M}+\text{H}]^+$ : 355.2380. Found: 355.2390.

### (E)-3-(4((((3R,5R,7R)-Adamantan-1-ylmethyl)(2-fluoroethyl)amino)methyl)-phenyl)-N-hydroxyacrylamide [4, CN146]

*Colourless Powder*,  $^1\text{H}$  NMR ( $\text{CD}_3\text{OD}$ ):  $\delta$  1.55-1.68 (m, 12H,  $\text{CH}\&\text{CH}_2$ ), 1.80-1.88 (m, 3H,  $\text{CH}\&\text{CH}_2$ ), 2.87-2.95 (m, 2H,  $\text{CH}_2$ ), 4.14-4.32 (m, 2H,  $\text{CH}_2$ ), 4.52-4.60 (m, 4H, 2- $\text{CH}_2$ ), 6.37 (d, 1H,  $J$  15.2,  $\text{CH}$ ), 7.22-7.29 (m, 2H, *Ar*), 7.42-7.49 (m, 3H, *Ar*).  $^{13}\text{C}$  NMR ( $\text{CD}_3\text{OD}$ ):  $\delta$  30.0, 37.0, 38.1, 42.3, 54.2, 60.0, 60.9, 66.3, 82.1, 83.8, 118.7, 128.8, 129.0, 129.1, 135.5, 141.6, 166.6. HRMS (ESI) calculated for  $\text{C}_{23}\text{H}_{32}\text{FN}_2\text{O}_2$   $[\text{M}+\text{H}]^+$ : 387.2442. Found: 387.2406.

### [3-[2-(phenyl)-ethylcarbamoyl]-propyl]-carbamic acid ethyl ester [5, Santacruzamate A]

*Colourless Powder*, mp: 114-115 °C, Lit. [206] mp. 112-113 °C.  $R_f$  [A] = 0.64,  $R_f$  [B] = 0.76.  $^1\text{H}$  NMR ( $\text{CDCl}_3$ )  $\delta$  1.22 (t,  $J$  = 7.1 Hz, 3H,  $\text{CH}_3\text{CH}_2\text{O}$ ), 1.79 (pent,  $J$  = 6.8 Hz, 2H, 3- $\text{CH}_2$ ), 2.16 (t,  $J$  = 7.0 Hz, 2H, 2- $\text{CH}_2$ ), 2.82 (t,  $J$  = 7.1 Hz, 2H,  $\text{PhCH}_2\text{CH}_2$ ), 3.16 (dd,  $J$  = 6.1, 12.3 Hz, 2H, 4- $\text{CH}_2$ ), 3.51 (dd,  $J$  = 7.0, 13.0 Hz, 2H,  $\text{PhCH}_2\text{CH}_2$ ), 4.08 (q,  $J$  = 7.1 Hz, 2H,  $\text{CH}_3\text{CH}_2\text{O}$ ), 4.93 (br s, 1H, *NH*), 5.93 (br s, 1H, *NH*), 7.18-7.31 (m, 5H,  $\text{PhCH}_2\text{CH}_2$ ).  $^{13}\text{C}$  NMR ( $\text{CDCl}_3$ )  $\delta$  14.6 ( $\text{CH}_3\text{CH}_2\text{O}$ ), 26.1 (C-3), 33.6 (C-2), 35.6 ( $\text{PhCH}_2\text{CH}_2$ ), 40.1 (C-4), 40.6 ( $\text{PhCH}_2\text{CH}_2$ ), 60.8 ( $\text{CH}_3\text{CH}_2\text{O}$ ), 126.4 (Ph-C4), 128.6 (Ph-C2,6), 128.7 (Ph-C3,5), 138.8 (Ph-C1), 157.1 ( $\text{NHCOOEt}$ ), 172.5 ( $\text{CH}_2\text{CONH}$ ). HRMS (ESI) calculated for  $\text{C}_{15}\text{H}_{23}\text{N}_2\text{O}_3$   $[\text{M}+\text{H}]^+$ : 279.1703. Found: 279.1709.

**N<sup>1</sup>-Hydroxy-N<sup>5</sup>-(2-phenethyl)-pentanediamide [6, Santacruzamate-SAHA Hybrid]**

*Yellow Powder*, <sup>1</sup>H NMR (CDCl<sub>3</sub> and a drop of CD<sub>3</sub>OD): δ 1.82-1.86 (m, 2H, CH<sub>2</sub>), 2.03-2.06 (m, 2H, CH<sub>2</sub>), 2.13-2.18 (m, 2H, CH<sub>2</sub>), 2.79-2.84 (m, 2H, CH<sub>2</sub>), 3.37-3.48 (m, 2H, CH<sub>2</sub>), 7.19-7.32 (m, 5H, Ar). <sup>13</sup>C NMR (CDCl<sub>3</sub> and a drop of CD<sub>3</sub>OD): δ 22.0, 32.1, 35.1, 35.5, 40.8, 126.4, 128.6, 128.7, 139.0, 169.2, 173.9. HRMS (ESI) calculated for C<sub>13</sub>H<sub>19</sub>N<sub>2</sub>O<sub>3</sub> [M+H]<sup>+</sup>: 251.1390. Found: 251.1385.

**α-(4-Methoxyphenyl) [7, Tropolone compound]**

*Yellow Powder*, <sup>1</sup>H NMR (CDCl<sub>3</sub>): δ 3.86 (s, 3H, OCH<sub>3</sub>), 6.95-7.00 (m, 2H, Ar), 7.03-7.09 (m, 1H, Ar), 7.31-7.43 (m, 2H, Ar), 7.46-7.51 (m, 2H, Ar), 7.56-7.61 (m, 1H, Ar). <sup>13</sup>C NMR (CDCl<sub>3</sub>): δ 55.5, 113.9 (2C), 122.1, 127.5, 130.9 (2C), 132.3, 136.5, 138.8, 140.6, 159.9, 170.5, 171.4. HRMS (ESI) calculated for C<sub>14</sub>H<sub>13</sub>O<sub>3</sub> [M+H]<sup>+</sup>: 229.0859. Found: 229.0848.

**(3-Phenethylcarbamoyl-propyl)-carbamic acid 2-fluoro-ethyl ester [9, FEt-Santacruzamate A]**

**Method A:** All operations were carried out in a dry reaction vessel under argon atmosphere. 1,8-Diazabicyclo[5.4.0]undec-7-ene (DBU)-CO<sub>2</sub> complex (470 mg, 2.4 mmol) was suspended in anhydrous CH<sub>3</sub>CN (10 mL) and cooled to 0 °C in an ice-water bath. A solution of 4-amino-N-phenethyl-butylamide (**13**, free base, 412 mg, 2 mmol) in anhydrous CH<sub>3</sub>CN (15 mL) was added dropwise (60-70 min) with stirring. 2-FEt-bromide (380 mg, 240 μL, 3 mmol) was added and the reaction mixture was stirred for 24 h at room temperature. The clear solution was poured into a separation funnel containing water (30 mL) and the resulting suspension was extracted with chloroform (4 x 50 mL). The combined organic phase was washed with brine, dried (Na<sub>2</sub>SO<sub>4</sub>) and concentrated under reduced pressure. The crude product was purified by column chromatography on silica gel (80 g Kieselgel, eluent: ethylacetate-chloroform 7:3 (v/v), 50 mL fractions). Yield: 172 mg (30 %).

**Method B:** To a solution of 4-amino-N-phenethyl-butylamide (**13**, free base, 412 mg, 2 mmol, 1 eq.) in anhydrous N,N-dimethylformamide (DMF) (40 mL) was added Cs<sub>2</sub>CO<sub>3</sub> (1.95 g, 6 mmol, 3 eq.) and tetrabutylammonium trifluoromethanesulfonate (2.35 g, 6 mmol, 3 eq.). CO<sub>2</sub>-gas (20 mL/min) was bubbled through the suspension for 60 min at room temperature. Thereafter, 2-FEt-bromide (760 mg, 480 μL, 6 mmol) was added and the reaction mixture was stirred for further 24 h at room temperature. The solvent was removed under reduced pressure. Water (30 mL) was added to the residue and the suspension was extracted with chloroform (4 x 50 mL). The combined organic layer was washed with brine (20 mL) and dried (Na<sub>2</sub>SO<sub>4</sub>). The solvent was removed in vacuum and the residue was purified by column chromatography on silica gel as described above.

Yield: 390 mg (65%). mp. 98-99 °C. *R<sub>f</sub>* [C] = 0.27, *R<sub>f</sub>* [D] = 0.47, *R<sub>f</sub>* [E] = 0.24. <sup>1</sup>H NMR (CDCl<sub>3</sub>) δ 1.80 (pent, *J* = 6.9 Hz, 2H, 3-CH<sub>2</sub>), 2.17 (t, *J* = 7.0 Hz, 2-CH<sub>2</sub>), 2.81 (t, *J* = 7.0 Hz, 2H, PhCH<sub>2</sub>CH<sub>2</sub>), 3.18 (q, *J* = 6.4 Hz, 2H, 4-CH<sub>2</sub>), 3.51 (dd, *J* = 7.0 Hz, 13.0 Hz, 2H, PhCH<sub>2</sub>CH<sub>2</sub>), 4.21-4.31 (m, 2H, CH<sub>2</sub>CH<sub>2</sub>F), 4.50-4.61 (m, 2H, CH<sub>2</sub>CH<sub>2</sub>F), 5.21 (br s, 1H, FCH<sub>2</sub>CH<sub>2</sub>CONHCH<sub>2</sub>), 5.89 (br s, 1H, CONHCH<sub>2</sub>), 7.17-7.31 (m, 5H, PhCH<sub>2</sub>CH<sub>2</sub>). <sup>13</sup>C NMR (CDCl<sub>3</sub>) δ 25.8 (C-3), 33.6 (C-2), 35.6 (PhCH<sub>2</sub>CH<sub>2</sub>), 40.3 (C-4), 40.5 (PhCH<sub>2</sub>CH<sub>2</sub>), 63.7 (d, <sup>2</sup>*J*<sub>C,F</sub> = 20.1 Hz, CH<sub>2</sub>CH<sub>2</sub>F), 81.8 (d, <sup>1</sup>*J*<sub>C,F</sub> = 169.5 Hz, CH<sub>2</sub>CH<sub>2</sub>F),

126.4 (Ph-C4), 128.6 and 128.7 (Ph-C2,6 or Ph-C3,5), 138.8 (Ph-C1), 156.4 (COONHCH<sub>2</sub>), 172.4 (NHCOCH<sub>2</sub>). <sup>19</sup>F-NMR (CDCl<sub>3</sub>): δ 224.6 (tt, *J* = 29.4 and 47.8 Hz). ESI-MS *m/z*: 297 [M+H]<sup>+</sup>. C<sub>15</sub>H<sub>21</sub>N<sub>2</sub>O<sub>3</sub> (296.34).

### 3-[2-(3-Fluorophenyl)-ethylcarbamoyl]-propyl]-carbamic acid ethyl ester [**10**, 3-Fluorophenethyl-Santacruzamate A]

4-[(Ethoxycarbonyl)amino]butanoic acid (**12a**, 700 mg, 4 mmol) was dissolved in anhydrous dichloromethane (DCM) (14 mL) under argon atmosphere. The solution was cooled to 0 °C. Triethylamine (TEA) (1.2 mL, 870 mg, 8.6 mmol) and 3-fluorophenethylamine (0.6 mL, 4.6 mmol) were added consecutively. Afterwards N-(3-Dimethylaminopropyl)-N'-ethylcarbodiimide hydrochloride (EDC-HCl) (900 mg, 4.7 mmol) was added in one portion. A catalytic amount of 4-Dimethylaminopyridine (DMAP) (30 mg) was added, the resulting mixture was stirred for 1 h at 0 °C and then for 16 h at room temperature. The reaction mixture was diluted with DCM (30 mL) and consecutively washed with 1 M HCl, saturated NaHCO<sub>3</sub> solution and water (20 mL of each). The combined extracts were dried (Na<sub>2</sub>SO<sub>4</sub>) and evaporated to give an oily residue. The crude product was crystallized from hexane.

Yield: 723 mg (61%). mp. 107-109 °C. *R<sub>f</sub>* [A] = 0.58, *R<sub>f</sub>* [B] = 0.75. <sup>1</sup>H NMR (CDCl<sub>3</sub>) δ 1.22 (t, *J* = 7.1 Hz, 3H, CH<sub>3</sub>CH<sub>2</sub>O), 1.79 (pent, *J* = 6.8 Hz, 2H, 3-CH<sub>2</sub>), 2.17 (t, *J* = 6.9 Hz, 2H, 2-CH<sub>2</sub>), 2.82 (t, *J* = 7.1 Hz, 2H, PhCH<sub>2</sub>CH<sub>2</sub>), 3.17 (dd, *J* = 5.8, 11.8 Hz, 2H, 4-CH<sub>2</sub>), 3.51 (dd, *J* = 7.0, 13.0 Hz, 2H, PhCH<sub>2</sub>CH<sub>2</sub>), 4.09 (q, *J* = 7.1 Hz, 2H, CH<sub>3</sub>CH<sub>2</sub>O), 4.92 (br s, 1H, NH), 6.08 (br s, 1H, NH), 6.89-7.27 (m, 5H, PhCH<sub>2</sub>CH<sub>2</sub>). <sup>13</sup>C NMR (CDCl<sub>3</sub>) δ = 14.6 (CH<sub>3</sub>CH<sub>2</sub>O), 26.2 (C-3), 33.5 (C-2), 35.3 (PhCH<sub>2</sub>CH<sub>2</sub>), 40.0 (C-4), 40.4 (PhCH<sub>2</sub>CH<sub>2</sub>), 60.8 (CH<sub>3</sub>CH<sub>2</sub>O), 113.3 (d, <sup>2</sup>*J*<sub>C,F</sub> = 21 Hz, Ph-C4), 115.5 (d, <sup>2</sup>*J*<sub>C,F</sub> = 20.9 Hz, Ph-C2), 124.3 (d, <sup>4</sup>*J*<sub>C,F</sub> = 2.7 Hz, Ph-C6), 129.9 (d, <sup>3</sup>*J*<sub>C,F</sub> = 8.3 Hz, Ph-C5), 141.4 (d, <sup>3</sup>*J*<sub>C,F</sub> = 7.2 Hz, Ph-C1), 157.2 (NHCOOEt), 162.9 (d, <sup>1</sup>*J*<sub>C,F</sub> = 245.7 Hz, Ph-C3), 172.6 (CH<sub>2</sub>CONH). <sup>19</sup>F NMR (CDCl<sub>3</sub>): δ = -113.3 - C<sub>15</sub>H<sub>21</sub>FN<sub>2</sub>O<sub>3</sub> (296.34).

### [3-[2-(3-Bromophenyl)-ethylcarbamoyl]-propyl]-carbamic acid ethyl ester [**14**, 3-bromophenethyl-Santacruzamate A]

**14** was prepared from **12a** (1.9 g, 10.8 mmol) and 3-bromophenethylamine according to the procedure described for compound **10**.

Yield: 2.89 g (75 %). mp. 107-109 °C. *R<sub>f</sub>* [A] = 0.58, *R<sub>f</sub>* [B] = 0.07, *R<sub>f</sub>* [C] = 0.75. <sup>1</sup>H NMR (CDCl<sub>3</sub>) δ = 1.23 (t, *J* = 7.1 Hz, 3H, CH<sub>3</sub>CH<sub>2</sub>O), 1.79 (pent, *J* = 7.0 Hz, 2H, 3-CH<sub>2</sub>), 2.18 (t, *J* = 6.9 Hz, 2H, 2-CH<sub>2</sub>), 2.80 (t, *J* = 7.1 Hz, 2H, PhCH<sub>2</sub>CH<sub>2</sub>), 3.17 (br m, 2H, 4-CH<sub>2</sub>), 3.50 (dd, *J* = 7.0, 13.0 Hz, 2H, PhCH<sub>2</sub>CH<sub>2</sub>), 4.09 (q, *J* = 7.1 Hz, 2H, CH<sub>3</sub>CH<sub>2</sub>O), 4.90 (br s, 1H, NH), 6.12 (br s, 1H, NH), 7.12-7.36 (m, 5H, PhCH<sub>2</sub>CH<sub>2</sub>). <sup>13</sup>C NMR (CDCl<sub>3</sub>) δ = 14.6 (CH<sub>3</sub>CH<sub>2</sub>O), 26.3 (C-3), 33.5 (C-2), 35.2 (PhCH<sub>2</sub>CH<sub>2</sub>), 40.0 (C-4), 40.4 (PhCH<sub>2</sub>CH<sub>2</sub>), 60.8 (CH<sub>3</sub>CH<sub>2</sub>O), 122.5 (Ph-C-3), 127.4 (Ph-C-6), 129.6 (Ph-C-4), 130.1 (Ph-C-5), 131.8 (Ph-C-2), 141.3 (Ph-C1), 157.2 (NHCOOEt), 172.6 (CH<sub>2</sub>CONH). C<sub>15</sub>H<sub>21</sub>BrN<sub>2</sub>O<sub>3</sub> (357.24).

### 2-(2-Pyridinyl)-2-nitrobenzenesulfonamide [236]

The free base of 2-(2-pyridinyl)aniline (CAS RN: [29528-30-1]) was liberated from its dihydrochloride salt (1.5 g, 6.17 mmol, CAS RN: 18471-73-3). Yield: 1.05. 2-(2-pyridinyl)aniline (1.05 g, 6.17 mmol) was dissolved in anhydrous DCM

(10 mL) under argon. The solution was cooled down to 0 °C and pyridine (2 mL) was added. 2-Nitrobenzenesulfonylchloride (2.7 g, 12.1 mmol) was added and the mixture was stirred for 2 h at room temperature. The reaction mixture was poured into a separation funnel containing water (40 mL) and the resulting suspension was extracted with DCM (3 x 50 mL). The combined organic layers were washed with brine (50 mL) and dried (Na<sub>2</sub>SO<sub>4</sub>). The solvent was removed under reduced pressure to yield a yellowish oily residue (3.39 g). The crude product was purified by column chromatography on silica gel (Kieselgel: 100 g, eluent: hexane-ethyl acetate 7:3 (v/v), fractions: 50 mL). The purified product (1.89 g) was crystallised from diethyl ether (25 mL).

Yield: 1.35 g (61 %).  $R_f$  [B] = 0.47,  $R_f$  [D] = 0.23. <sup>1</sup>H NMR (CDCl<sub>3</sub>)  $\delta$  = 7.18 (dt,  $J$  = 7.7 Hz, 1.1 Hz, 1H), 7.24 (ddd,  $J$  = 7.5 Hz, 7.5 Hz, 1.0 Hz, 1H), 7.37 (dt,  $J$  = 7.7 Hz, 1.4 Hz, 1H), 7.51-7.62 (m, 5H), 7.73 (dt,  $J$  = 7.8 Hz, 1.8 Hz, 1H), 7.81 (dd,  $J$  = 8.3 Hz, 0.9 Hz, 1H), 7.92 (dd,  $J$  = 7.6 Hz, 1.5 Hz, 1H), 8.72 (dd,  $J$  = 4.9 Hz, 0.9 Hz, 1H), 13.0 (br s, 1H). <sup>13</sup>C NMR (CDCl<sub>3</sub>)  $\delta$  = 121.6, 121.7, 122.1, 124.5, 124.7, 126.8, 128.8, 130.1, 130.7, 131.9, 133.2, 133.3, 136.1, 137.6, 147.7, 156.6. C<sub>17</sub>H<sub>13</sub>N<sub>3</sub>O<sub>4</sub>S (355.37).

#### **[2-(2-Pyridinyl)phenyl-2-nitrobenzenesulfonamide]silver(I) [17, CAS RN: [1403599-78-9]] [236]**

Silver (I) oxide (410 mg, 1.75 mmol) was suspended in dry CH<sub>3</sub>CN (7 mL) under argon atmosphere. A solution of 2-(2-pyridinyl)phenyl-2-nitrobenzenesulfonamide (1.25 g, 3.5 mmol) in dry CH<sub>3</sub>CN (10 mL) was added dropwise at room temperature. The reaction mixture was stirred at 65 °C for 16 h. The mixture was filtered and the filtrate was evaporated to dryness. Dry hexane (60 mL) was added to the residue and the precipitated product was filtered off. The product was dried *in vacuo*.

Yield: 1.45 g (89 %). <sup>1</sup>H NMR (CDCl<sub>3</sub>)  $\delta$  = 6.73 (d,  $J$  = 7.0 Hz, 1H), 6.86 (d,  $J$  = 6.8 Hz, 1H), 7.08 (d,  $J$  = 7.0 Hz, 1H), 7.2 (t,  $J$  = 7.3 Hz, 1H), 7.25-7.31 (m, 3H), 7.35-7.38 (m, 1H), 7.43-7.48 (m, 3H), 8.61 (br s, 1H). C<sub>17</sub>H<sub>12</sub>AgN<sub>3</sub>O<sub>4</sub>S (462.23).

#### **Nickel [{3-[2-(3-substituted-phenyl)-ethylcarbamoyl]-propyl}-carbamic acid ethyl ester] bromide complex (15)**

[3-[2-(3-Bromophenyl)-ethylcarbamoyl]-propyl]-carbamic acid ethyl ester (**14**, 512 mg, 1.43 mmol) was dissolved in dry toluene (16 mL) under argon. Tetramethylethylenediamine (0.22 mL, 1.43 mmol) and Ni(COD)<sub>2</sub> were added consecutively and the reaction mixture was stirred at room temperature for 16 h. Pentane (64 mL) was added and the mixture was stirred for 15 min at RT. The precipitated solid was filtered and dried *in vacuo*. Yield: 619 mg (81 %) as a beige solid. <sup>1</sup>H NMR and <sup>13</sup>C NMR spectra were not obtained due to the low solubility of the product.

#### **Nickel [{3-[2-(3-substituted-phenyl)-ethylcarbamoyl]-propyl}-carbamic acid ethyl ester] complex [16, 3-(Phenethyl-Santacruzamate A)-nickel aryl complex]**

To a mixture of [2-(2-Pyridinyl)phenyl-2-nitrobenzenesulfonamide]silver (I) (**17**, 227 mg, 0.49 mmol, 1 eq.) and the nickel aryl bromide complex **15** (260 mg, 0.49 mmol, 1 eq.) was added a solution of dry pyridine (79  $\mu$ L, 0.98 mmol, 2 eq.) in dry toluene (4 mL) under argon atmosphere. Dry CH<sub>3</sub>CN (1 mL) was added and the mixture stirred at ambient temperature for 3 min. Thereafter, the solution was filtered and the precipitate was washed with dry DCM (3 x 5 mL).



The solvent was evaporated *in vacuo* and the residue was re-dissolved in dry DCM (8 mL). The solution was filtered through Celite (2 g) and the filtrate was concentrated *in vacuo*. The residue was dissolved in dry DCM (3 mL) under argon and n-pentane (17 mL) was added. The mixture was stirred at room temperature and the precipitate was filtered off (under argon atmosphere). The product was washed with pentane (3 x 5 mL) and dried *in vacuo*.

Yield: 328 mg (87 %), *Yellow Powder*.  $^1\text{H}$  NMR ( $\text{CDCl}_3$ )  $\delta$  = 1.23 (t,  $J$  = 7.0 Hz, 3H,  $\text{CH}_3\text{CH}_2\text{O}$ ), 1.79 (pent,  $J$  = 7.0 Hz, 2H, 3- $\text{CH}_2$ ), 2.17 (t,  $J$  = 7.0 Hz, 2H, 2- $\text{CH}_2$ ), 2.80 (t,  $J$  = 7.0 Hz, 2H,  $\text{PhCH}_2\text{CH}_2$ ), 3.18 (dd,  $J$  = 12.6 Hz, 6.2 Hz, 2H, 4- $\text{CH}_2$ ), 3.50 (dd,  $J$  = 13.0 Hz, 7.0 Hz, 2H,  $\text{PhCH}_2\text{CH}_2$ ), 4.09 (q,  $J$  = 7.0 Hz, 2H,  $\text{CH}_3\text{CH}_2\text{O}$ ), 4.90 (br s, 1H, NH), 6.08 (br s, 1H, NH), 6.77 (d,  $J$  = 7.3 Hz, 1H), 6.97 (d,  $J$  = 7.5 Hz, 1H), 7.09 (d,  $J$  = 7.3 Hz, 1H), 7.12-7.18 (m, 3H,  $\text{PhCH}_2\text{CH}_2$ ), 7.24-7.32 (m, 5H), 7.34-7.36 (m, 2H,  $\text{PhCH}_2\text{CH}_2$ ), 7.37-7.39 (m, 1H), 7.42-7.50 (m, 4H), 7.69 (br t, 1H), 8.57-8.60 (m, 2H).  $^{13}\text{C}$  NMR ( $\text{CDCl}_3$ )  $\delta$  = 14.6 ( $\text{CH}_3\text{CH}_2\text{O}$ ), 26.3 (C-3), 33.6 (C-2), 35.3 ( $\text{PhCH}_2\text{CH}_2$ ), 40.0 (C-4), 40.4 ( $\text{PhCH}_2\text{CH}_2$ ), 60.8 ( $\text{CH}_3\text{CH}_2\text{O}$ ), 122.4, 122.5 (Ph-C-3), 123.1, 123.8, 124.6, 126.0, 127.4 (Ph-C-6), 129.6 (Ph-C4), 129.7, 130.1 (Ph-C-5), 130.3, 130.4, 130.5, 130.6, 130.7, 131.8 (Ph-C-2), 136.1, 137.0, 137.6, 138.1, 141.3 (Ph-C1), 143.1, 147.6, 150.0, 150.4, 157.2 ( $\text{NHCOOEt}$ ), 161.1, 172.5 ( $\text{CH}_2\text{CONH}$ ).  $\text{C}_{37}\text{H}_{38}\text{N}_6\text{NiO}_7\text{S}$  (769.49).

**Synthesis of the hypervalent iodine oxidant [236,237], 1,1'-(Phenyl- $\lambda^3$ -iodanediyl)-bis(4-methoxypyridinium)-bis(trifluoromethanesulfonate) (**18**)**

**18** was synthesized according to the procedure of Weiß and Seubert [237]. All operations were carried out in a dry reaction vessel in anhydrous solvents under argon atmosphere. (Diacetoxyiodo)benzene (3.0 g, 9.3 mmol) was dissolved in DCM (100 mL) under argon atmosphere. Trimethylsilyl trifluoromethanesulfonate (3.4 mL, 18.6 mmol) was added dropwise to this solution at ambient temperature. A solution of 4-methoxypyridine (1.9 mL, 2.03 g, 18.6 mmol) in DCM (15 mL) was added dropwise and the reaction mixture was stirred for 15 min at room temperature. The solvent was removed under reduced pressure and anhydrous diethyl ether (100 mL) was added to the residue. The mixture was stirred for 1 h under argon, the precipitated solid was filtered off and washed with dry diethyl ether (40 mL). The product was dried *in vacuo*.

Yield: 6.06 g (90 %) off white solid.  $^1\text{H}$  NMR ( $\text{CD}_3\text{CN}$ )  $\delta$  = 4.04 (s, 6H, 2- $\text{OCH}_3$ ), 7.30 (d,  $J$  = 6.5 Hz, 4H, H-3,5 pyridine), 7.36 (t,  $J$  = Hz, 7.5 H, H-2,6 Ph), 7.56 (t,  $J$  = 7.5 Hz, 1H, H-4 Ph), 7.85 (d,  $J$  = Hz, 2H, H-3,5 Ph), 8.43 (d,  $J$  = 7.5 Hz, 4H, H-2,6 pyridine).  $^{13}\text{C}$  NMR ( $\text{CDCl}_3$ )  $\delta$  = 58.9 ( $\text{OCH}_3$ ), 94.8 (C-1 Ph), 114.0 (C-3,5 pyridine), 122.1 (q,  $J_{\text{C,F}}$  = 320.7 Hz,  $\text{CF}_3\text{SO}_3$ ), 128.8 (C-4 Ph), 131.6 (C-3,5 Ph), 138.5 (C-2,6 Ph), 144.0 (C-2,6 pyridine), 173.8 (C-4 pyridine).  $^{19}\text{F}$ -NMR ( $\text{CDCl}_3$ ):  $\delta$  = 79.3.  $\text{C}_{20}\text{H}_{19}\text{F}_6\text{I}_2\text{N}_2\text{O}_8\text{S}_2$  (720.40).

### 3. RESULTS AND DISCUSSION

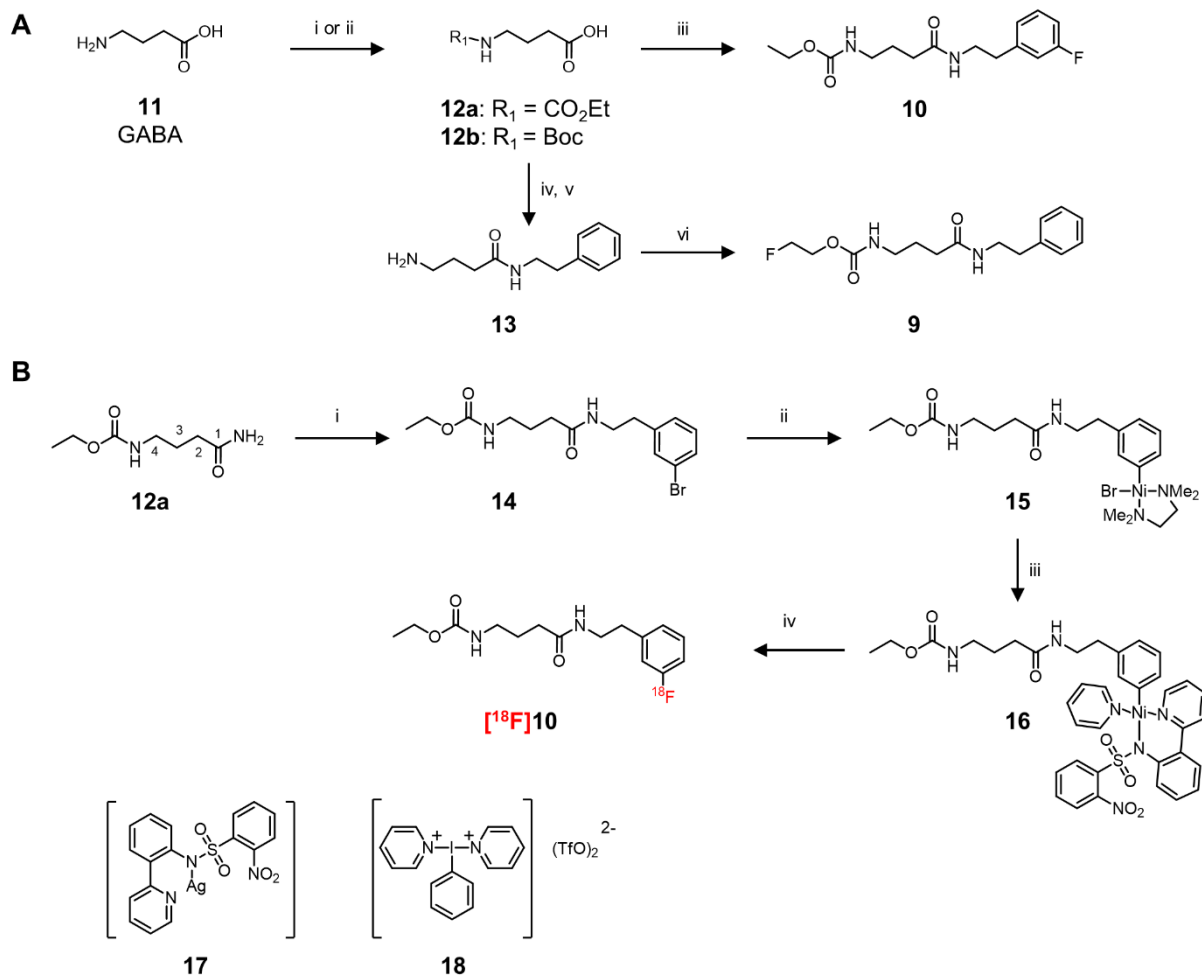
#### 3.1. Chemistry

Several compounds, reported in literature, were selected for evaluation (**Figure 1**). Compounds **2**, **3**, **4**, **5**, **6** and **7** were synthesized according to reported literature procedures [206,229–232,238], whereas compounds **1** and **8** were obtained commercially. Two new fluorinated bioisosteres of Santacruzamate A, (compounds **9** and **10**) were synthesized.

For preparation of Santacruzamate A analogue **10**,  $\gamma$ -aminobutyric acid (**11**, GABA) was first selectively converted to the N-ethoxycarbonyl derivative **12a** with ethyl chloroformate in an aqueous potassium carbonate solution (**Scheme 1**) [206]. Then carbamate **12a** was reacted with 3-fluoro-phenethylamine using EDC-HCl/TEA in the presence of a catalytic amount of DMAP in DCM.

Similarly, FEt-Santacruzamate A, **9** was synthesized from GABA (**11**) in a four-step synthesis (**Scheme 1**). Boc protection of the 4-amino group was performed by reaction of di-tert-butyl dicarbonate in 1 M NaOH-THF mixture to form **12b**, which was further reacted with phenethylamine using EDC-HCl in the presence of a catalytic amount of DMAP in DCM and followed by boc-deprotection with trifluoroacetic acid (TFA) yielding 4-amino-N-phenethylbutyramide **13**. FEt-Santacruzamate A, **9** was prepared from **13** by transcarboxylation, using DBU-CO<sub>2</sub> zwitterionic complex [239], and subsequent O-alkylation with 2-bromofluoroethane. The synthesized compounds were characterised by <sup>1</sup>H-, <sup>13</sup>C- and <sup>19</sup>F-NMR spectra and by ESI-MS. The incorporation of the carboxylate group and the exact position of the 2-FEt-group were demonstrated using 2D-NMR (<sup>1</sup>H-<sup>1</sup>H- COSY and <sup>1</sup>H-<sup>13</sup>C HMBC) experiments. <sup>1</sup>H-<sup>1</sup>H-COSY and <sup>1</sup>H-<sup>13</sup>C HBMC correlations for FEt-Santacruzamate A **9** are listed in **Table S1-A** and **Table S1-B**.

Further in an attempt to radiosynthesize a fluorine-18 labelled analogue of Santacruzamate A ([<sup>18</sup>F]**10**), new nickel complexes **15** and **16** were prepared from 3-bromophenethyl-Santacruzamate A (**14**) by adaptation of a recently described method by Lee *et al.* [236]. The oxidative <sup>18</sup>F-fluorination was performed using 40  $\mu$ L of fluorine-18 in water (170 MBq), and was added to 4 ml CH<sub>3</sub>CN containing 20 mg 18-crown-6, the reagents were mixed well to form a fluorine-18 stock solution. Three experiments were attempted using 1, 2 and 3 mg precursor (**16**) and 1 equivalent of **18**. To each reaction vial, containing precursor (**16**), 400  $\mu$ L of the fluorine-18 stock solution was added *via* a rubber septum. Reactions were run for 1 min at RT and a colour change was observed (yellow and reddish brown for higher amounts of precursors). However, this initial radiosynthetic attempt at oxidative fluorination was unsuccessful as no product was observed either with HPLC or with TLC. However, successful radiosynthesis of [<sup>11</sup>C]**3** starting from precursor **2**, following the previously reported procedure by Wang and co-workers, was performed [230]. And a detailed study on [<sup>11</sup>C]**3** will be published in due course.



**Scheme 1:** Synthesis of fluorinated analogues of Santacruzamate A. **A)** Reagents and conditions: (i) ethyl chloroformate,  $K_2CO_3$ ,  $H_2O$ ,  $0\text{ }^\circ\text{C}$  for 2 h then 16 h, RT; (ii)  $Boc_2O$ , 1 M NaOH, THF, 24 h, RT; (iii) 3-fluorophenethylamine,  $Et_3N$ ,  $CH_2Cl_2$ , DMAP, EDC HCl,  $0\text{ }^\circ\text{C}$  for 1 h then overnight RT; (iv) TFA; (v) phenethylamine,  $Et_3N$ ,  $CH_2Cl_2$ , DMAP, EDC-HCl,  $0\text{ }^\circ\text{C}$  for 1 h then 16 h, RT; (vi): (1) DBU- $CO_2$  complex,  $CH_3CN$ , 1.5 h,  $0-5\text{ }^\circ\text{C}$ , (2)  $BrCH_2CH_2F$ , overnight RT. **B)** Synthesis of the nickel aryl complex precursor for the radiosynthesis of  $^{18}F$ -labelled analogue of Santacruzamate-A. Reagents and conditions: (i) 3-bromophenethylamine,  $Et_3N$ ,  $CH_2Cl_2$ , DMAP, EDC-HCl,  $0\text{ }^\circ\text{C}$  for 1 h then overnight RT; (ii) tetramethylenediamine,  $Ni(COD)_2$ , toluene, RT, 6h; (iii): [2-(2-pyridinyl)phenyl-2-nitrobenzenesulfonamid]silver(I) (**17**), pyridine, toluene,  $CH_3CN$ , RT, 1 min; (iv):  $^{18}F$ , hypervalent iodine oxidant **18**,  $CH_3CN$ .

### 3.2. Pan-HDAC and HDAC2 inhibition assays

Assays were carried out in two different labs in Luxembourg and Oslo, Norway in order to strengthen the confidence of the results. Different assays conditions were used to verify the results. HDAC enzymes were isolated from K562 cell extracts to measure total HDAC activity as previously described [234,235]. HDAC fluorogenic assay kits from BPS Bioscience or Active Motif were used for measuring HDAC2 activity. (See Materials and Methods, Sections 2.1 and 2.2 for details)

Compounds **2** and **3** showed HDAC2 IC<sub>50</sub> values of 19.4 and 4.8 nM respectively (**Table 1**). Both showed a significantly lower pan-HDAC IC<sub>50</sub> of 0.9 and 1.1 nM respectively. CN146 (**4**) was found to be less potent than compound **2** and **3** with an HDAC2 IC<sub>50</sub> value of 161 nM, and a pan-HDAC IC<sub>50</sub> value of 45.1 nM. Compound **7**, which carries a tropolone moiety, showed an HDAC2 IC<sub>50</sub> value of 87 μM. Although it was reported with a K<sub>i</sub> value of 0.81 nM against HDAC2 [231]. Compound **1** (SAHA) showed an IC<sub>50</sub> value of 84 and 59 nM for HDAC2 and pan-HDAC respectively.

The inhibitory activity of compounds **5** and **6** for HDAC2 were also found to be far less than reported in the literature (IC<sub>50</sub> of 0.119 and 3.5 nM respectively) [206]. Even at a concentration of 100 μM **5** was not able to completely block total HDAC or HDAC2 activity. Compound **6** showed an IC<sub>50</sub> value of 7.28 μM and 1.42 μM for HDAC2 and pan-HDAC respectively (**Table 1**).

Further compound **5** was chosen to study the concentration-response in detail, with compounds **1** and **8** as standards (**Figure 2**). We did not observe any effect of **5** under normal assay conditions (manufacturer's protocol), whereas **1** and **8** showed HDAC2 inhibition in agreement with literature values (**Figure 2**). As the observed absence of inhibitory activity of compound **5** was unexpected, several control experiments were conducted. Assays were run against HDAC2 where **5** was used in combination with either **1** or **8** (data not shown), in order to verify if **5** or its impurities (if present) would interfere with the assay. We found that the decrease in activity was solely attributed to either **1** or **8** and the contribution of **5** was negligible.

**Table 1:** Comparison of HDAC activities of compounds **1-10**.

Compound	Literature		<i>In silico</i> Docking Studies		<i>In Vitro</i> Present study	
	HDAC2 IC <sub>50</sub> (nM)	Pan-HDAC IC <sub>50</sub> (nM)	Binding Energy kcal/mol	Binding Affinity HDAC2 (nM)	HDAC2 IC <sub>50</sub> (nM)	Pan-HDAC IC <sub>50</sub> (nM)
<b>1</b>	85.8 [206]	ND	-7.92	1570	84.1 (290) <sup>‡</sup>	59.1
<b>2</b>	ND	1.1 [229]	-11.77	2.4	4.8	1.1
<b>3</b>	2.0 [230]	ND	-10.59	17.3	19.4	0.9
<b>4</b>	651 [189]	ND	-8.95	275.3	161	45.1
<b>5</b>	0.119 [206]	ND	-6.83	9810	8% <sup>§</sup>	11% <sup>§</sup>
<b>6</b>	3.5 [206]	ND	-7.34	4180	7280	1420
<b>7</b>	0.81* [231]	ND	-7.35	3990	87085	9650
<b>8</b>	1.3 [240]	1.8 [241]	-8.23	929.8	11 <sup>‡</sup>	ND
<b>9</b>	-	-	-7.10	6270	>10,000 <sup>‡</sup>	ND
<b>10</b>	-	-	-6.25	26240	>10,000 <sup>‡</sup>	ND

\*Reported in K<sub>i</sub>, inhibition constant. <sup>‡</sup>Results from Oslo, <sup>§</sup>inhibition at 100 μM (20 % inhibition at 50 μM). <sup>§</sup>inhibition at 100 μM. ND = Not determined.

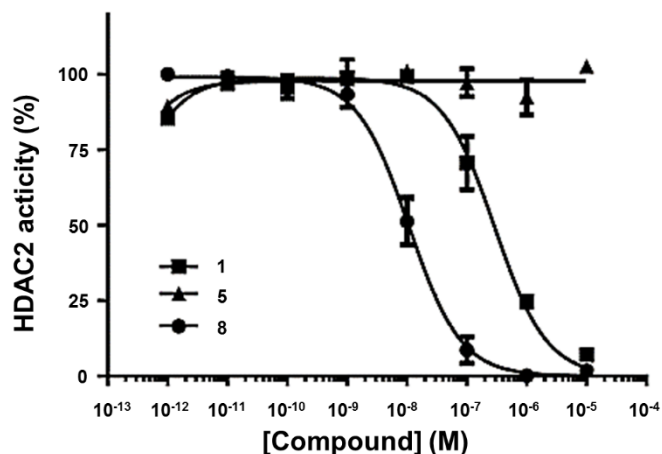


**Figure 2:** Activity-concentration curves of compound **1**, **5** and **8** using fluorogenic HDAC2 assay (BPS Bioscience, manufacturer's conditions).

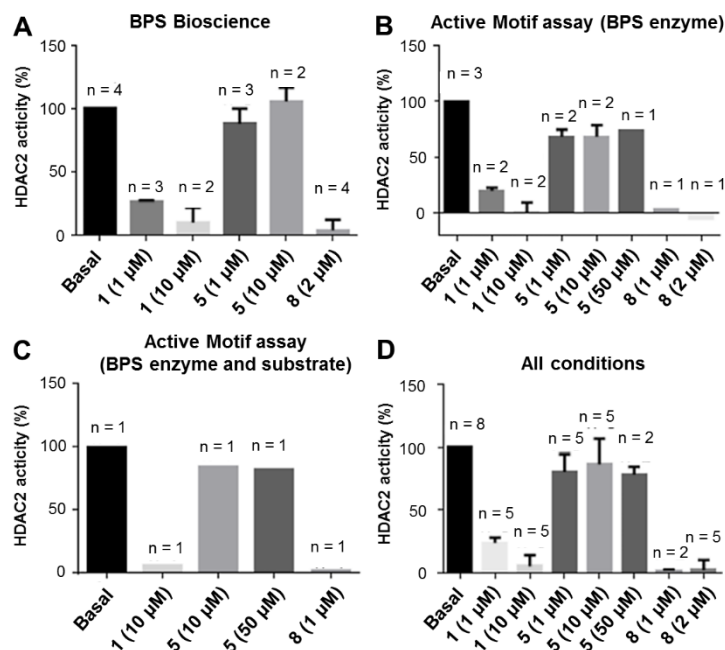


**Figure 3:** HDAC2 activity of **1**, **5** and **8** under different assay conditions. **A)** BPS Bioscience following the manufacturer's protocol. **B)** Active Motif assay following the manufacturer's protocol in presence of HDAC2 enzyme from BPS Bioscience. **C)** Active Motif assay with the enzyme and substrate (20  $\mu$ M) from BPS Bioscience. **D)** Results from **A-C** merged.

Santacruzamate A was reported as a potent HDAC2 inhibitor [206] which potentially can be used as a radiolabelled PET probe. In this respect, the synthesis of two bioisosteres of Santacruzamate A, **9** and **10** was performed and these compounds were tested in HDAC assays. An assay against HDAC2 for **9** and **10** produced no decrease in activity even at a concentration of 10  $\mu$ M (**Table 1**). Equally no inhibitory effect was observed for other class I HDACs (HDAC1 and 3, data not shown).

We further investigated whether assay conditions could explain the lack of activity of Santacruzamate A. As shown in **Figure 3**, compound **5** was tested against recombinant HDAC2 enzymes under different assay conditions (HDAC fluorogenic assay from Active Motif vs BPS Bioscience). However, none of these assay conditions could reproduce the subnanomolar affinity reported by Pavlik *et al.* [206]. Thus different assay conditions could not explain the observed lack of effect of **5** on HDAC2 activity.

Results for compounds, **5**, **6** and **7** indicate marked inconsistencies with the results published by Pavlik *et al.* and Ononye *et al.* [206,231,232]. Hence, those results should be reconsidered and looked at with caution.

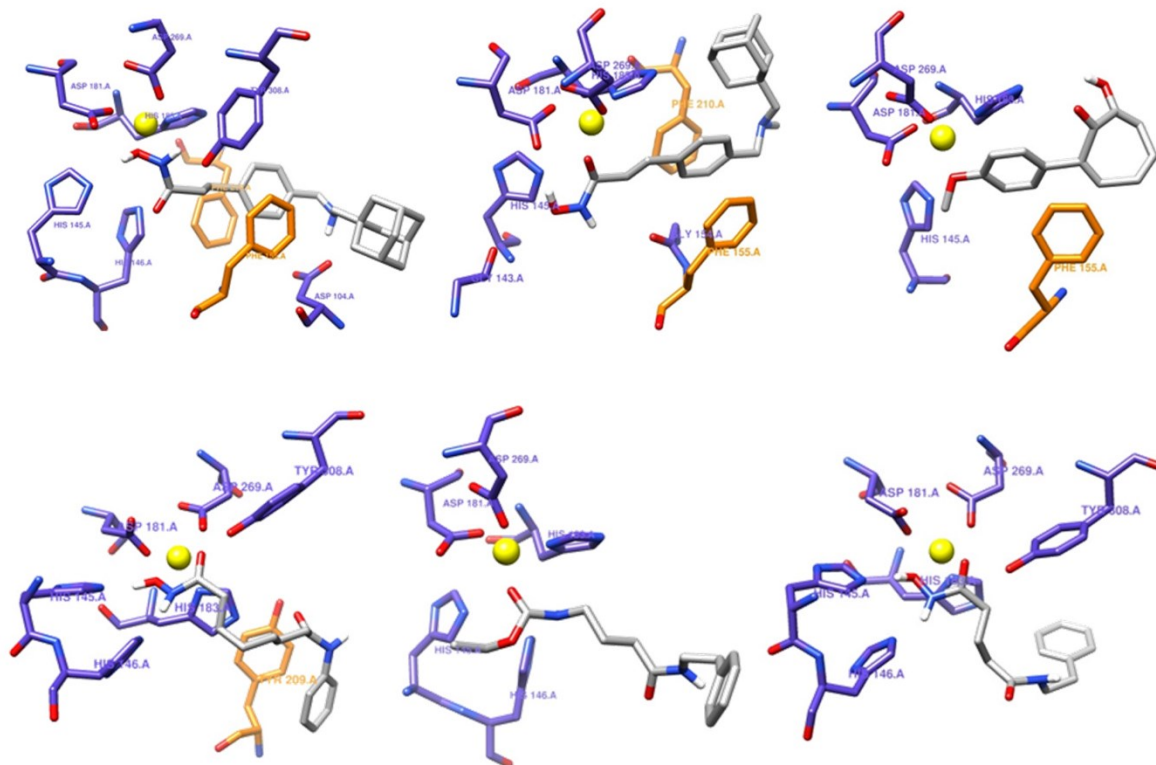
### 3.3. Molecular docking studies

To further investigate the interactions of these compounds with the HDAC2 enzyme binding pocket and to predict the *in silico* binding energy and binding affinity, molecular docking studies were performed. Rational drug design involves investigating new molecules that complement their biological target in shape and charge, and effectively bind to the active site [242]. Molecular docking is an *in silico* modeling method which attempts to predict non-covalent interactions usually between a macromolecule and a small molecule, and is widely used as a computational tool in academia and industry for rapid identification of potential drugs with minimal expense and effort [243].

Docking studies were performed using Autodock 4.2.6 in a Cygwin-Linux environment. Following ligand and target preparation in Autodock Tools 1.5.6, the energy minimized compounds were docked into the binding pocket of the HDAC2 crystal structure [244], which was obtained from the Research Collaboratory for Structural Bioinformatics Protein Data Bank ((RCSB-PDB) ID: 4lxz). For receptor preparation, water molecules were removed, polar hydrogen atoms were added, and Kollman united atom partial charges were assigned to HDAC2 using Autodock Tools at pH 7.4. For the ligand preparation, the 3D structure was generated with the use of ChemBioOffice Version 11.0 and the mm<sup>2</sup> energy of the molecule was minimized to minimum root mean square (RMS)-gradient of 0.050 for each ligand. To understand the importance of the Zn<sup>2+</sup>-binding site in HDAC2, docking was performed by setting the grid box size at 60 x 60 x 60 units of 0.375 Å spacing along the x, y, and z axes, and centered on atom ZN401. Cygwin Terminal was used to run AutoGrid to generate the grid map of the various ligand and receptor atoms. After the grid map was generated, the Lamarckian genetic algorithm implemented in AutoDock was applied to estimate the possible conformations of the ligand–protein complex. AutoDock simulations were performed 50 times to be sure to cover all possible binding possibilities. The result with the lowest docking energy analysis in cluster rank 1 was used for further analysis. For visualisation of the docked conformations, the Chimera 1.10.1 software package was used.

Docking studies indicated that compounds **2-4** fit well in the HDAC2 binding pocket and showed calculated HDAC2 binding affinity values of 2.4, 17.3 and 275 nM respectively. Further, these three compounds can chelate the Zn<sup>2+</sup>-ion, with a measured distance from the Zn<sup>2+</sup>-ion of 1.78 Å (**2** (C=O)), 1.72 Å (**3** (C=O)) and 1.75 Å (**4** (C=O)). Additionally, all three compounds showed two  $\pi$ - $\pi$  interactions with Phe155A and Phe210A, which attributes to the favourable interaction with HDAC2. A similar  $\pi$ - $\pi$  stacking interaction was also observed for class I HDAC inhibitor, Chidamide

[245]. Key interactions in the catalytic pocket occurred with His183, Asp181 and Tyr308. Additionally, compound **2** formed a key hydrogen bond with Asp104 (See **Table S2**, Supporting Information for more details).



**Scheme 2:** 3D representation of predicted binding models of **2**, **3**, **7** (top row, left to right) and **1**, **5**, **6** (bottom row, left to right) respectively in the binding pocket of HDAC2. Key interactions between the protein residues (blue) and the ligand (grey) are shown and the zinc ion is shown as a yellow sphere (rest of the protein residues omitted for clarity). Residues shown in orange are involved in  $\pi$ - $\pi$  stacking.

Further, an *in silico* binding affinity value of 3.99  $\mu$ M was obtained for compound **7**. Surprisingly, the methoxy group was observed to interact with the  $Zn^{2+}$ -ion (1.90 Å) instead of the anticipated hydroxyl ketone moiety. Compound **7** makes one  $\pi$ - $\pi$  interaction with Phe155A and only one hydrogen bonding contact with His145A in the binding pocket, explaining its low binding affinity. For compounds **5** and **6**, *in silico* binding affinity values of 9.8 and 4.2  $\mu$ M were obtained and no  $\pi$ - $\pi$  contacts were observed as anticipated. Potentially explaining the lower binding energy for **5** and **6** in these simulations. Similarly compounds **9** and **10** showed *in silico* binding affinity values of 6.3 and 26.2  $\mu$ M, respectively. Although, *in silico* results have to be interpreted with caution due to their inconsistencies, performed *in vitro* assays for compounds **1–4**, **5**, **6**, **9** and **10** generally agree with the data obtained in the *in silico* simulation studies.

## 4. CONCLUSION

In summary we have studied selected potent HDAC inhibitors for their HDAC2 and pan-HDAC inhibitory activity in order to identify potential HDAC2 PET tracers. Observed IC<sub>50</sub> values of compounds **1-4**, and **8** are in agreement with literature values. However, major differences in the IC<sub>50</sub> values for Santacruzamate A (**5**), Santacruzamate A-SAHA hybrid (**6**) and  $\alpha$ -aryl tropolone (**7**), were found compared to literature reports. We further carefully, 1) studied the inhibitory effect of Santacruzamate A (**5**) by using different assay conditions and different concentrations against control compounds **1** and **8**. But, the reported literature affinity values could not be reproduced. 2) Molecular docking studies were performed, which were also in agreement with the gathered *in vitro* assay results. Additionally the docking studies showed key interactions of the potent compounds (**2** and **3**) in the HDAC2 binding pocket. These, key  $\pi$ - $\pi$  interactions and additional hydrogen bonding, contributing to higher affinity, were not observed for compounds **5**, **6** and **7**. These results suggests that the presence of an aryl group for  $\pi$ - $\pi$  interactions, a hydrogen bond donor and an appropriate bulky cap group can be helpful for achieving selectivity when designing new HDAC2 inhibitors. In line with the results obtained with Santacruzamate A (**5**), the fluorinated bioisosteres of Santacruzamate A, **9** and **10** did not show any HDAC2 inhibition even at a concentration of 10  $\mu$ M. In this respect, literature inhibitory activities reported for compounds **5**, **6** and **7** have to be reconsidered and read with caution.



### EVALUATION OF [<sup>11</sup>C]KB631 AS A PET TRACER FOR *IN VIVO* VISUALISATION OF HDAC6 IN B16.F10 MELANOMA

---

**Koen Vermeulen**<sup>1</sup>, Muneer Ahamed<sup>2</sup>, Kaat Luyten<sup>1,3</sup> and Guy Bormans<sup>1</sup>

<sup>1</sup> Laboratory for Radiopharmaceutical Research, Department of Pharmaceutical and Pharmacological Sciences, KU Leuven, Leuven, Belgium

<sup>2</sup> Centre for Advanced Imaging, University of Queensland, Brisbane, Australia

<sup>3</sup> Switch Laboratory, VIB-KU Leuven Center for Brain & Disease Research, KU Leuven, Leuven, Belgium



## Abstract

**Introduction:** HDAC6, a structural and functional distinct member of the HDAC-family, shows great promise as a target to treat several cancers and neurodegenerative diseases. Several clinical trials are evaluating HDAC6 inhibitors in solid tumours and haematological malignancies, but so far no HDAC6 inhibitor has received marketing authorisation. The availability of an HDAC6-specific PET tracer can potentially aid in cancer diagnosis, select patients for HDAC6 inhibitor treatment and accelerate HDAC6 drug development. We have evaluated the HDAC6 PET tracer [<sup>11</sup>C]KB631, *in vitro* and *in vivo* in B16.F10 melanoma inoculated mice.

**Materials and methods:** *In vitro* binding specificity was evaluated by autoradiography studies on rodent brain, B16.F10 melanoma and PC3 prostate carcinoma cryosections. Biodistribution and quantification of plasma radio-metabolites was determined in NMRI-mice in control conditions and after blocking with KB631, Ricolinostat and SAHA. Tracer tumour uptake was evaluated in B16.F10 melanoma inoculated C57BL/6 mice.

**Results:** *In vitro* autoradiography studies showed HDAC6-selective binding to rodent brain, B16.F10 melanoma and PC3 prostate carcinoma tissue slices. Tracer binding in several organs of interest could be partially blocked in NMRI-mice pre-treated with KB631, Ricolinostat or SAHA, indicating specific tracer binding. A biodistribution and 90-min dynamic  $\mu$ PET study on B16.F10 melanoma mice, pre-treated with vehicle or Ricolinostat (50 mg/kg), indicated HDAC6-specific tumour uptake.

**Conclusions:** [<sup>11</sup>C]KB631 shows HDAC6-selective binding in mouse B16.F10 melanoma tumours *in vitro* and *in vivo*. [<sup>11</sup>C]KB631 PET can be used for *in vivo* investigation of the expression of HDAC6 in tumours.

**Advances in Knowledge:** [<sup>11</sup>C]KB631 shows increased expression of HDAC6 in mouse B16.F10 melanoma tumours and can be used to visualise target engagement of HDAC6 inhibitors.

## 1. INTRODUCTION

The alternate acetylation state of evolutionarily conserved lysine residues located at the N-terminal tails of histones contributes to the general transcriptional regulation of underlying genes. This process, controlled by the opposing actions of histone acetyl transferases (HATs) and histone deacetylases (HDACs), is part of a broader network of epigenetic post-translational modifications (PTMs) [246], contributing to the histone homeostasis which in turn influences cellular homeostasis. Aberrant levels of HAT/HDAC can lead to various pathologies, ranging from oncological malignancies to cardiac diseases and even neurophysiological anomalies [9,11].

Currently 18 HDAC isoforms are known, divided into 4 classes based on their sequence homology to yeast HDAC: Class I (HDAC1, 2, 3, 8), class II (HDAC4, 5, 6, 7, 9, 10), class III (sirtuins) and class IV (HDAC11). The various classes differ in protein structure, substrate specificity, subcellular localization and tissue expression patterns [11]. All classes except class III are known to use  $Zn^{2+}$  as a catalysing agent to facilitate the deacetylation reaction. Class III HDACs use nicotinamide adenine dinucleotide ( $NAD^+$ ) to hydrolyse the acetyl-moiety [16].

Observation of the disruption of HAT/HDAC homeostasis in several malignancies led to the identification of HDAC as a drug target. However, because of the high similarity between different HDACs, e.g. HDAC1 and 2 have 85% sequence homology, pan-inhibition of HDACs can lead to serious adverse effects. Consequently, research has focussed on developing isoform-selective inhibitors. For HDAC3, 6 and 8, selective inhibitors have already been reported [37].

Inhibitors of  $Zn^{2+}$ -dependent HDACs typically, contain (1) a 'cap' group, which interacts with the surface of the catalytic pocket of the HDAC enzyme, (2) a linker, which can contain different aromatic rings and/or alkyl chains, connected to (3) the  $Zn^{2+}$ -binding moiety. Chelation of the  $Zn^{2+}$ -ion can be accomplished with multiple functional groups, such as carboxylic acids, benzamides, thiol groups or hydroxamates [30]. FDA approved HDAC inhibitors, depicted in **Figure 1A** include pan-HDAC inhibitors Vorinostat (Zolinza<sup>®</sup> also known as suberoylanilide hydroxamic acid (SAHA)) [240] and Romidepsin, (Istodax<sup>®</sup>) [247] both used for the treatment of cutaneous T-cell lymphoma (CTCL). In addition, Belinostat (Beleodaq<sup>®</sup>) [248], applied for the treatment of peripheral T-cell lymphoma (PTCL) and Panobinostat (Farydak<sup>®</sup>) [240] used to combat multiple myeloma (MM) are available on the market.  $IC_{50}$  values are presented in **Table 1**.

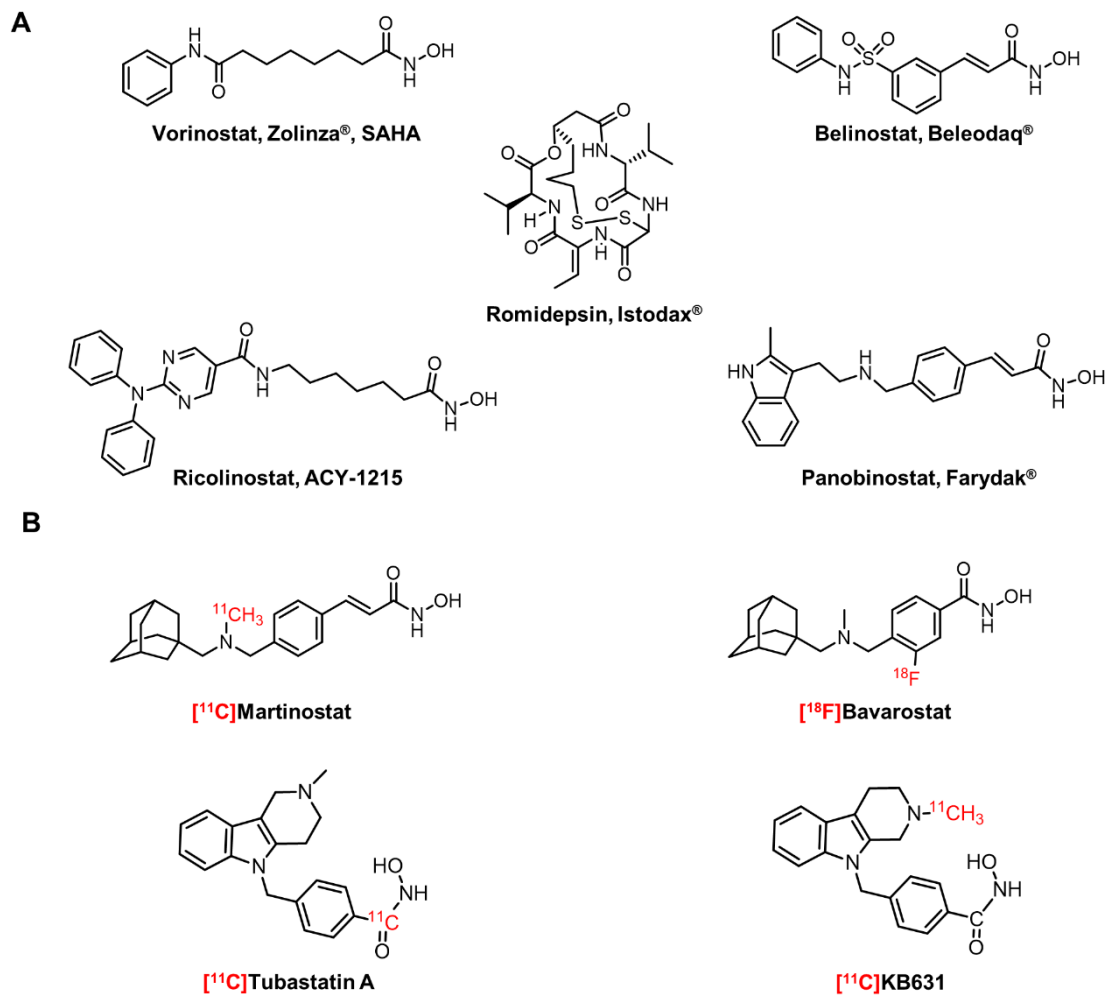


**Figure 1: Chemical structures.** A) Market authorised pan-HDAC inhibitors and HDAC6 inhibitor Ricolinostat. B) HDAC PET tracers with affinity for HDAC6.

**Table 1:** IC<sub>50</sub> values of market authorised pan-HDAC inhibitors and HDAC6 inhibitor Ricolinostat.

Compound	HDAC1 (nM)	HDAC2 (nM)	HDAC3 (nM)	HDAC6 (nM)
<b>SAHA</b> [240]	2.6	3.5	10	3.2
<b>Romidepsin</b> [247]	36	48	/	14000
<b>Belinostat</b> [248]	27	27	27	82
<b>Panobinostat</b> [240]	2	1.3	2.2	3
<b>Ricolinostat</b> [249]	58	48	51	5

HDAC6 is a unique HDAC isoform as it contains two homologous catalytic deacetylase domains. Both domains function individually and participate in the global deacetylase activity of the enzyme.

Contrary to class I HDACs, HDAC6 is predominantly localized in the cytoplasm and subsequently targets cytosolic acetylated proteins. Mainly  $\alpha$ -tubulin, heat shock protein 90 (Hsp90) and cortactin are targeted and deacetylated by HDAC6. Deacetylation of  $\alpha$ -tubulin and cortactin is implied in cytoskeleton dynamics and cell motility and deacetylation of the molecular chaperone Hsp90 is necessary to activate a cellular response to misfolded proteins and stress [42,43]. Expression of HDAC6 was reported in several organs, including: heart, liver, kidney, brain and pancreas [51]. HDAC6 is a key regulator of multiple cellular signalling and downstream transduction pathways. The regulation of different cellular processes including cell migration and the degradation of misfolded proteins, are not solely attributed to the deacetylation process, as HDAC6 also contains a C-terminal, zinc finger containing, ubiquitin binding domain (BUZ-domain) that is equally important in the control of these processes [46]. The BUZ-domain is able to bind free ubiquitin or ubiquitinated proteins destined for proteasomal degradation [47]. Misfolded or damaged proteins will be marked with a poly-ubiquitin tag after which different degradation pathways can be followed. The most prominent degradation route is the transport of misfolded proteins to the proteasome. However, if the proteasome becomes oversaturated or inhibited, another process is required to remove the cytotoxic, misfolded or damaged proteins. This process, known as the aggresome-autophagy pathway, is initially cytoprotective and induces accelerated degradation of mutant proteins. The pathway is initiated and regulated by high affinity binding of HDAC6 to poly-ubiquitinated proteins [48,49].

HDAC6 was found to play a role in cancer and neurodegenerative diseases [51,52]. HDAC6 is overexpressed in a variety of human cancers and is required for oncogenic cell transformation [51,71]. The HDAC6-gene is estrogen-regulated and increased HDAC6 mRNA and protein expression was observed in estrogen receptor  $\alpha$ -positive breast cancer MCF-7 cells treated with estradiol. In the same study, a fourfold increase in cell motility and cellular morphological changes caused by the deacetylation of  $\alpha$ -tubulin was observed [250]. Expression levels of HDAC6 were also increased in ovarian cancer, specifically in non-benign tumours, where HDAC6 potentially can be used as a prognostic marker [57]. In prostate and kidney cancer, upregulation of HDAC6 was mediated by oncogenic retrovirus-associated DNA sequences (Ras) [54]. Overexpression was also found in oral squamous cell carcinoma, melanoma and several hematopoietic cancers [40,251,252]. Importantly, it has been observed that HDAC6 inhibition sensitises cancerous cells to chemotherapeutics, but not normal untransformed cells [63]. Deletion or downregulation of HDAC6 decreased programmed death ligand 1 (PD-L1) in B16.F10 melanoma, an important activator of inhibitory pathways in T-cells. Further, HDAC6 abrogation mediated several immune responses, inducing several tumour antigens [62]. In another study, inhibition or genetic abrogation of HDAC6 decreased proliferation and induced G1 arrest in B16.F10 and human melanoma cells [61].

Several clinical trials are evaluating the use of selective HDAC6 inhibitors in the treatment of oncological malignancies as monotherapy or in combination with monoclonal antibodies or small molecules [71]. One of these, Ricolinostat, (ACY-1215, **Figure 1A**), is an HDAC6-selective inhibitor which shows promise in combination with Bortezomib (proteasome inhibitor) for the treatment of MM [253]. Ricolinostat has IC<sub>50</sub> values of 5 nM for HDAC6 and 58 nM, 48

nM, and 51 nM for respectively class I HDACs 1, 2, 3 (**Table 1**) [249]. Recently it was reported that overexpression of HDAC6 in A375 melanoma cells mediated the resistance against Vemurafenib, an inhibitor of the BRAF serine/threonine kinase. Ricolinostat was observed to inhibit the proliferation of A375 melanoma cells and sensitised the cells against Vemurafenib [254]. Further, Ricolinostat is being evaluated in monotherapy or in combination with Lenalidomide or Dexamethasone for the treatment of MM and lymphoma and together with Nab-paclitaxel in metastatic breast cancer. ACY-241 (Citarinostat) is evaluated in combination with Nivolumab for the treatment of non-small cell lung cancer. HDAC6 inhibitor KA2507 is evaluated in patients with various solid tumours overexpressing PD-L1 which have relapsed or are refractory to prior treatment [71].

In Alzheimer's disease (AD) it has been postulated that the HDAC6-tau interaction mediates the formation of hyperphosphorylated tau. Furthermore, HDAC6 protein expression increased with 52% in cortex and 91% in the hippocampus of AD patients [52]. HDAC6 has also been implied as a regulator in Parkinson's disease, Huntington's disease and amyotrophic lateral sclerosis. A common feature of these degenerative diseases is the accumulation of misfolded proteins, subsequent formation of aggregates, discrepancies in macroautophagy pathways and disposition of inclusion bodies. All of which can be maintained or regulated by HDAC6 and its substrate proteins like Hsps [68]. HDAC6 has also been studied in depression as two HDAC6-selective inhibitors (ACY-738 and ACY-775) were shown to have antidepressant-like properties upon acute and chronic administration to mice, as determined in a tail suspension test and social defeat study [29]. The full function of HDAC6 in the central nervous system (CNS) has to be elucidated further as both neuroprotection and neurodegeneration properties have been attributed to HDAC6 [69,255,256]. This may be explained by the bi-functionality of HDAC6 as a deacetylation agent and its involvement in the aggresome pathway via the BUZ-domain [69]. One hypothesis states that initially the formation of aggresomes is beneficial for cell survival, but over an extended time period this accumulation can become detrimental for cell survival. [48]. Clinical studies with HDAC6 inhibitors in CNS have yet to be performed.

Positron emission tomography (PET) is a non-invasive, specific and highly sensitive diagnostic imaging modality. PET utilizes short-lived radionuclides (e.g. carbon-11  $T_{1/2}$  20 min, fluorine-18  $T_{1/2}$  110 min) which are incorporated in compounds with high binding affinity and selectivity for the molecular target to be visualised *in vivo* such as an enzyme, receptor or transporter. PET studies provide *in vivo* quantification of the expression levels of the molecular target contributing to basic scientific understanding of the role of the target in health and disease. In addition PET can be applied for biomarker quantification allowing for diagnosis and follow up of disease progression [145]. Implementation of PET in the general drug development stream can accelerate the development of potential drugs against a specific target. PET is the only molecular imaging modality that allows determination of pharmacodynamic parameters such as the dose-occupancy relation for CNS targets in man.

Several PET tracers targeting HDACs in cancer and neurodegenerative diseases were developed and evaluated in preclinical trials on rodents or non-human primates (NHP) [170]. However, only one HDAC PET tracer, [<sup>11</sup>C]Martinostat advanced to clinical trials and was evaluated as a HDAC tracer in brain. [<sup>11</sup>C]Martinostat (**Figure 1B**),

is an adamantyl-based hydroxamic acid compound with low nanomolar affinity for HDAC1, 2, 3 and 6. HDAC-specific brain retention in rats and a NHP was observed [185]. In clinical studies, [ $^{11}\text{C}$ ]Martinostat PET revealed lower HDAC expression in the dorsolateral prefrontal cortex of schizophrenic and schizoaffective patients compared to healthy individuals [187,188]. Although initial reports suggested high affinity of [ $^{11}\text{C}$ ]Martinostat for HDAC6 [185], later on it was established, in a thermal shift assay on human brain homogenate, that Martinostat was unable to efficiently bind HDAC6 [187] and thus the main proteins that were visualised by [ $^{11}\text{C}$ ]Martinostat PET in brain are the class I HDACs, HDAC1, 2 and 3.

[ $^{18}\text{F}$ ]Bavarostat (**Figure 1B**) is another adamantyl-based HDAC inhibitor with high HDAC6 affinity and selectivity ( $\text{IC}_{50}$  = 60 nM, > 80-fold selectivity over other HDACs). Fluorine-18 labelling was accomplished using a novel deoxyfluorination method involving a ruthenium complex catalyst. [ $^{18}\text{F}$ ]Bavarostat allowed visualisation and quantification of brain HDAC6 levels in rat and baboon where it exhibited high brain uptake, with specificity for grey over white matter as assessed by homologous blocking studies with Bavarostat [190].

In 2012 Butler *et al.* reported Tubastatin A, a tryptoline-based hydroxamic acid compound with potential beneficial neuroprotective properties based on potent and selective inhibition of HDAC6 ( $\text{IC}_{50}$  = 15 nM) as assessed against purified human HDAC protein. In the same paper, a derivative, KB631 was reported to have an even higher affinity ( $\text{IC}_{50}$  = 1.4 nM) and selectivity for HDAC6 (> 3500 vs HDAC1) [191]. The radiosynthesis of [ $^{11}\text{C}$ ]Tubastatin A (**Figure 1B**) was first reported by Lu *et al.* in which [ $^{11}\text{C}$ ]CO was inserted in the hydroxamic acid moiety *via* a Pd-mediated pathway [192]. However, this compound was not further evaluated *in vivo*. The isomer [ $^{11}\text{C}$ ]KB631 (**Figure 1B**), also reported by Lu *et al.* [193], was synthesized by conventional [ $^{11}\text{C}$ ]CH $_3$ I radioalkylation of the tryptoline moiety. This compound was evaluated as a potential tracer for HDAC6 in brain. However,  $\mu\text{PET}$  studies performed on rats and NHP showed only limited brain uptake of the compound and a full report of this tracer was not published. To our knowledge, an HDAC6 PET tracer for imaging of cancer has not yet been explored. As several reports pointed to an increased expression of HDAC6 in melanoma [40,61–63], we have evaluated [ $^{11}\text{C}$ ]KB631 as a tracer to visualise tumour HDAC6 in a B16.F10 melanoma mouse model.

## 2. MATERIALS AND METHODS

### 2.1. High performance liquid chromatography (HPLC) analysis

HPLC was performed on a LaChrom Elite system (Hitachi, Darmstadt, Germany) connected to a Waters 2487 UV-VIS detector and a 3-inch NaI(Tl) scintillation detector connected to a single channel analyser (Gabi, Raytest, Straubenhardt, Germany). Registration and integration of the HPLC chromatograms was performed with GINA Star (Raytest) or RaChel (Lablogic, Sheffield, UK) software. The chemical and radiochemical purity (RCP) was assessed using reversed phase (RP)-HPLC X-bridge C $_{18}$  column, 3.5  $\mu\text{m}$ , 3.0 x 100 mm) eluted with Na $_2$ HPO $_4$  0.01M pH



6.5/ethanol (EtOH) 65/35 with a flow rate of 0.3 mL/min. The column effluent passed a UV detector (254 nm) and a NaI(Tl) scintillation detector. Identity of the tracer was determined by co-elution with cold reference compound on the same HPLC system.

## **2.2. Quantification of radioactivity in biological samples.**

Quantification was performed with an automated gamma counter, equipped with a 3-inch NaI(Tl) well crystal coupled to a multichannel analyser (Wallac 1480 Wizard, Wallac, Turku, Finland). The results were corrected for background radiation, physical decay during counting and detector dead time.

## **2.3. Animal experiments.**

Animals were kept in a thermoregulated (22 °C) and humidity-controlled environment, in a 12 h/12 h light dark cycle, in individual ventilated cages and had free access to food and water. All animal experiments were conducted after approval of the local University Ethics Committee for Animals and according to the Belgian code of practice for the care and use of animals. Female C57BL/6 mice, 5 weeks of age (body mass 20-25 g), 7-8 weeks old BALB/c nu/nu mice (body mass 20-25 g) were purchased from Janvier (La Genest-Saint Isle, France). Naval Medical Research Institute (NMRI)-mice (body mass 30-40 g) and Female Wistar rats (170-200 g) were purchased from Envigo (Venray, The Netherlands).

## **2.4. LC-MS analysis**

Elucidation of intermediate reaction products was accomplished using a Dionex Ultimate 3000 LC system (Thermo Fisher Scientific, Sunnyvale, USA) coupled to a time-of-flight high-resolution mass spectrometer (TOF-HRMS) (MaXis impact, Bruker, Bremen, Germany), equipped with an orthogonal electrospray (ESI) interface. Acquisition and processing of data were done using Compass IsotopePattern (version 3.2, Bruker).

## **2.5. NMR analysis**

Proton nuclear magnetic resonance (<sup>1</sup>H NMR) spectra were acquired at 400 MHz on a Bruker AVANCE 400 MHz spectrometer (5 mm probe, Bruker AG, Fällanden, Switzerland). Chemical shifts are reported in parts per million (ppm) relative to tetramethylsilane (TMS,  $\delta = 0$ ), carbon nuclear magnetic resonance (<sup>13</sup>C NMR) spectra were acquired at 101 MHz on the same spectrometer.

## **2.6. Statistical analysis**

Quantitative data are expressed as mean  $\pm$  SD. Conventional statistics, Student's T-test and two-way analysis of variance (ANOVA) were calculated using Graphpad Prism 7.04 (Graphpad Software). Significance was accepted at the 95 % probability level.

Topological polar surface area (tPSA) and LogD values were calculated using MarvinSketch (Marvin 14.10.13.0, 2014, ChemAxon (<http://www.chemaxon.com>)).

## 2.7. Reagents and chemicals

All used chemicals and reagents were purchased from commercial available sources (Aldrich, TCI Europe, Acros) and used without further purification. HDAC inhibitors, SAHA, Ricolinostat and PCI34051 were purchased from Selleckchem or MedChem Express and used without further purification. CAY1063 [257] and a hydroxamic acid compound with low HDAC affinity (compound **6** in **Chapter II**) were synthesized as previously reported.

## 2.8. Chemistry

KB631 and precursor compound KB674 were synthesized following reported procedures [191].

**KB631** <sup>1</sup>H NMR (400 MHz, CDCl<sub>3</sub>) δ 7.95 (d, *J* = 2.6 Hz, 2H), 7.55 (s, 1H), 7.20 – 7.02 (m, 5H), 5.24 (s, 2H), 3.89 (s, 3H), 3.53 (s, 2H), 2.91 (s, 2H), 2.81 (s, 2H), 2.51 (s, 3H). <sup>13</sup>C NMR (101 MHz, CDCl<sub>3</sub>) δ 166.8, 143.00, 136.9, 133.2, 130.2, 129.5, 127.2, 126.1, 121.4, 119.4, 118.3, 109.1, 108.2, 52.9, 52.2, 51.6, 46.4, 45.9, 21.7. HRMS (ESI) *m/z* calculated for C<sub>20</sub>H<sub>21</sub>N<sub>3</sub>O<sub>2</sub> 336.1706 [M + H]<sup>+</sup>: found 336.1707.

**KB674** <sup>1</sup>H NMR (400 MHz, MeOD) δ 7.93 (dd, *J* = 8.3, 1.8 Hz, 2H), 7.55 (d, *J* = 7.8 Hz, 1H), 7.34 (s, 1H), 7.23 – 7.16 (m, 1H), 7.12 (dt, *J* = 6.1, 2.8 Hz, 3H), 5.44 (s, 2H), 4.31 (s, 2H), 3.54 (t, *J* = 6.1 Hz, 2H), 3.10 (t, *J* = 6.0 Hz, 2H), 1.97 (dd, *J* = 24.2, 1.6 Hz, 1H). <sup>13</sup>C NMR (101 MHz, MeOD) δ 168.2, 144.6, 138.9, 131.2, 130.9, 128.5, 127.7, 123.9, 121.2, 119.5, 110.8, 108.4, 52.7, 47.4, 43.7, 41.8, 19.9. HRMS (ESI) *m/z* calculated for C<sub>19</sub>H<sub>19</sub>N<sub>3</sub>O<sub>2</sub> 322.1550 [M + H]<sup>+</sup>: found 322.1545.

## 2.9. Radiosynthesis

Carbon-11 was produced by proton irradiation of a N<sub>2</sub> + H<sub>2</sub> (5%) gas mixture in a Cyclone 18/9 cyclotron (IBA Louvain-la-Neuve, Belgium) as [<sup>11</sup>C]CH<sub>4</sub> by a <sup>14</sup>N(p,α)<sup>11</sup>C nuclear reaction. [<sup>11</sup>C]CH<sub>4</sub> was converted to [<sup>11</sup>C]CH<sub>3</sub>I in a home-built gas phase recirculation module. [<sup>11</sup>C]KB631 was synthesized by N-methylation of the precursor KB674, by bubbling [<sup>11</sup>C]CH<sub>3</sub>I with a helium flow through a solution of the precursor (200–300 μg) dissolved in anhydrous DMSO (150–200 μL). After the transfer of the radioactivity was completed, the reaction vial was heated to 100 °C for 4 minutes. After cooling down, the crude mixture was diluted with 1.2 mL of mobile phase (Na<sub>2</sub>HPO<sub>4</sub> 0.01M pH 6.5/EtOH 69/31). The tracer was purified by HPLC on a RP-C<sub>18</sub> column (XBridge C<sub>18</sub> column, 5 μm, 4.6 mm x 150 mm; Waters, Milford, USA) eluted with Na<sub>2</sub>HPO<sub>4</sub> 0.01M pH 6.5/EtOH 69/31 at a flow rate of 1 mL/min. The corresponding product peak was collected and diluted with saline to obtain a final EtOH concentration < 10%. The solution was filtered through a sterile 0.22 μm membrane filter (Millex GV 13 mm; Millipore, Billerica, MA).

## 2.10. Generation of tumour bearing mice

Tumour cell lines cells were obtained from the American Type Culture Collection. B16.F10 cells were maintained in Dulbecco's Modified Eagle's Medium supplemented with 10% fetal bovine serum.  $5 \times 10^5$  cells per mouse were implanted subcutaneously in the right dorsal flank of 8-week-old C57BL/6 mice (body mass 20-25 g). The tumours were allowed to grow for 10-15 days until they reached  $\sim 0.5$ - $0.75 \text{ cm}^3$  in size as determined using a caliper.

$10 \times 10^6$  PC3 cells per mouse in 50% Matrigel (VWR, Radnor, U.S.A.) were subcutaneously inoculated into the right shoulder of 7–8-week-old BALB/c nu/nu mice (body mass 20-25 g). The tumours were allowed to grow for 4-5 weeks until they reached  $\sim 0.5$ - $0.75 \text{ cm}^3$  in size as determined using a caliper.

## 2.11. Cryotome sectioning

Brain tissue was derived from female Wistar rats (170-200 g) or NMRI-mice (20-25 g). Mice or rats were anesthetized with isoflurane 2.5% in O<sub>2</sub> at a flow rate of 1 L/min after which they were sacrificed by decapitation. Tumour or brain was excised, rinsed with saline to remove blood and rapidly frozen in 2-methylbutane ( $-40 \text{ }^\circ\text{C}$ ). Next, 20- $\mu\text{m}$  sections were obtained using a cryotome (Shandon cryotome FSE; Thermo Fisher, Waltham, MA) and these were mounted on adhesive microscope slides (Superfrost Plus; Thermo Fisher Scientific) and stored at  $-20 \text{ }^\circ\text{C}$ .

## 2.12. *In vitro* autoradiography

Before incubating, the frozen slices were air-dried and preincubated in phosphate buffered saline (PBS) for 10 min at room temperature. To assess specificity of binding, slices were incubated with 7.4 kBq/100  $\mu\text{L}$  of [<sup>11</sup>C]KB631 dissolved in PBS + 0.3% bovine serum albumin (BSA) in the presence of DMSO (10%) or 100  $\mu\text{M}$  (final concentration) of either KB631, Ricolinostat, SAHA, CAY10603, PCI34051 or compound **6** (Chapter II), dissolved in DMSO (10%). The slices were washed for 1 min in PBS + 0.3% BSA followed by a 2 min wash in a mixture of PBS + 0.3% BSA/EtOH (70/30) followed by a 1 min wash in PBS + 0.3% BSA/EtOH (90/10) with a final washing step encompassing a 1 min wash with PBS + 0.3% BSA, after which the slices were dried. Next, autoradiograms were obtained by exposing the slices to a phosphor storage screen (super-resolution screen; Perkin Elmer, Waltham, MA) overnight. The screens were read using a Cyclone Plus system (Perkin Elmer) and the images were analysed using Optiquant software (Perkin Elmer). The radioactivity distribution in the slides was expressed as digital light units/ $\text{mm}^2$  (DLU/ $\text{mm}^2$ ) corrected for background. Percentage block vs control was calculated as (DLU/ $\text{mm}^2$  in the presence of 100  $\mu\text{M}$  blocker) / (DLU/ $\text{mm}^2$  tracer only) on 3-4 tissue sections from the same experiment.

## 2.13. Biodistribution studies

The biodistribution of [<sup>11</sup>C]KB631 was examined in healthy NMRI-mice (30-40 g) The rodents were anesthetized with 2.5% isoflurane in O<sub>2</sub> at a flow rate of 1 L/min and sacrificed by decapitation after 2, 10, 30 or 60 min post injection (p.i.) (n = 3 per time point). To study binding specificity of the tracer, a pre-treatment biodistribution study (10 min

post tracer injection) was conducted on healthy NMRI-mice. Mice were injected intraperitoneally (i.p.) 30-45 min before tracer injection with vehicle (DMSO (5%), 40%  $\beta$ -cyclodextrin in H<sub>2</sub>O (95%)) or a blocking agent (KB631 10 mg/kg, SAHA 10 or 100 mg/kg, Ricolinostat 10 or 50 mg/kg) dissolved in the vehicle (n = 3 per pre-treatment). A similar experiment was conducted on C57BL/6 mice inoculated with B16.F10 melanoma that were pre-treated with either vehicle or Ricolinostat (50 mg/kg, dissolved in vehicle) (n = 3 per pre-treatment). Mice were anesthetized with 2.5% isoflurane in O<sub>2</sub> at a flow rate of 1 L/min and injected with about 5.5 MBq of tracer intravenously (i.v.) *via* a tail vein. After 10 min the animals were sacrificed by decapitation. For all experiments, blood and organs of interest were collected in tared tubes and weighed. The radioactivity in the different organs was counted in an automated gamma counter, as described above. For the calculation of the total radioactivity in blood, muscle and bone, the masses were assumed to be respectively 7%, 40% and 12% of the total body mass [258–260]. Data were expressed as percentage of injected dose (%ID, Supplementary data) or standardized uptake value (SUV). %ID was calculated as (counts per minute (cpm) in organ / total cpm recovered) x 100. SUV was calculated as (radioactivity in cpm in organ / weight of organ) / total cpm recovered / body weight) or Bq/g in organ / average body Bq/g. Data are expressed as mean  $\pm$  SD.

### 2.14. Plasma radio-metabolites

Healthy NMRI-mice were anesthetized with 2.5% isoflurane in O<sub>2</sub> at a flow rate of 1 L/min and injected with about 11 MBq of [<sup>11</sup>C]KB631 *via* a tail vein. Mice were sacrificed by decapitation at 10 or 60 min p.i. (n = 3 per time point). Blood was collected in K<sub>2</sub>EDTA containing, tubes (BD vacutainer, BD, Franklin Lakes, NJ, U.S.A.) and stored on ice. The blood was centrifuged for 10 min at 2330  $\times g$  to separate the plasma. Plasma (~350  $\mu$ L) was spiked with 20  $\mu$ L authentic reference compound (100  $\mu$ g/mL in DMSO) weighed and counted in a gamma counter. Subsequently, individual plasma samples were injected and analysed by RP-HPLC on a Chromolith RP-C<sub>18</sub> column (3 mm x 100 mm, Merck, Darmstadt, Germany) eluted with gradient mixtures of CH<sub>3</sub>CN (A) and 0.05 M NaOAc pH 5.5 (B) (0-4 min: 1% A flow rate 0.5 mL/min; 4-9 min: linear gradient 1% A to 90%, flow rate 1 mL/min; 9-12 min: 90% A, flow rate 1 mL/min; 12-15 min: linear gradient 90% A to 1% A, flow rate 0.5 mL/min). After passing through an in-line UV detector, (254 nm), coupled to a 3-inch NaI(Tl) scintillation detector connected to a single channel analyser, 15 fractions in total per plasma sample were collected. Radioactivity in the fractions was determined in an automated gamma counter.

### 2.15. $\mu$ PET

Small animal whole-body PET scans were performed using a FOCUS™ 220  $\mu$ PET scanner (Concorde Microsystems, Knoxville, U.S.A.). B16.F10 melanoma bearing mice (C57BL/6, n = 3) were anesthetized using 2.5% isoflurane in O<sub>2</sub> (2 L/min) and kept under anaesthesia during the entire scan period. Mice were injected i.p. with vehicle or 50 mg/kg Ricolinostat dissolved in vehicle 30-45 min before tracer injection. About 7.5 MBq of [<sup>11</sup>C]KB631 was injected *via* a tail vein after which the mice were subjected to a 90-min dynamic PET scan. Acquisition data were Fourier rebinned

in 24 time frames (4 x 15 s, 4 x 60 s, 5 x 180 s, 8 x 300 s, 3 x 600 s). Time activity curves (TACs) were generated using PMOD software (v3.3, PMOD Technologies, Zürich, Switzerland).

### 3. RESULTS

#### 3.1. Radiosynthesis

KB674, dissolved in DMSO, was reacted with [<sup>11</sup>C]CH<sub>3</sub>I for 4 min at 100 °C to yield [<sup>11</sup>C]KB631 (**Figure 2**). At end of synthesis, radiochemical yields (as determined by area under the curve (AUC) on prep HPLC) ranged from 50-60% with a RCP of > 97% and a molar activity of about 71 ± 34 GBq/μmol (n = 6).

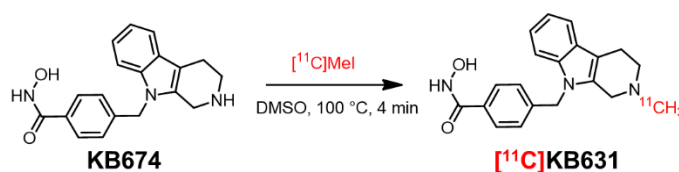


**Figure 2:** Radiosynthesis of [<sup>11</sup>C]KB631.

#### 3.2. *In vitro* autoradiography

*In vitro* autoradiography experiments were performed on rat and mouse brain and murine grown tumour sections (**Figure 3**). To assess specificity of binding, slices were incubated with the tracer in presence of KB631, Ricolinostat or SAHA. Tracer binding was heterogeneous in brain with highest binding in subcortical areas, rhinal cortex and cerebellum as observed on rat brain sections. Up to 90% of the tracer binding in the rhinal cortex and 70% in the cerebellum was blocked by co-incubation of KB631, Ricolinostat or SAHA. In the tumour sections, almost double the amount of added radioactivity was retained on the B16.F10 melanoma compared to the PC3 sections. Moreover, in these sections regional, focal tracer binding was observed. Blocking with Ricolinostat in B16.F10 melanoma tissue was moderate, as only 50% of the tracer binding could be blocked. Up to 75% of the tracer binding was blocked in the PC3 tumour sections. Incubation of the tumour slices with pan-HDAC inhibitor SAHA decreased the tracer binding in brain and tumour sections only moderately. However, blocking with the different inhibitors was more pronounced in regions which exhibited highest tracer binding. This indicates that [<sup>11</sup>C]KB631 binding is saturable, but its specificity is tissue dependent. Additional *in vitro* autoradiography studies were conducted with CAY10603, another structural unrelated HDAC6 selective inhibitor, on PC3 and B16.F10 melanoma sections. CAY10603 was able to block tracer binding in these sections as efficiently as Ricolinostat (**Figure S1 A-B**). Selective HDAC8 inhibitor PCI34051 and

compound **6** (Chapter II), a hydroxamic acid compound with low HDAC affinity, were not able to efficiently block [ $^{11}\text{C}$ ]KB631 binding to B16.F10 melanoma or rat brain sections (Figure S1 C-D).

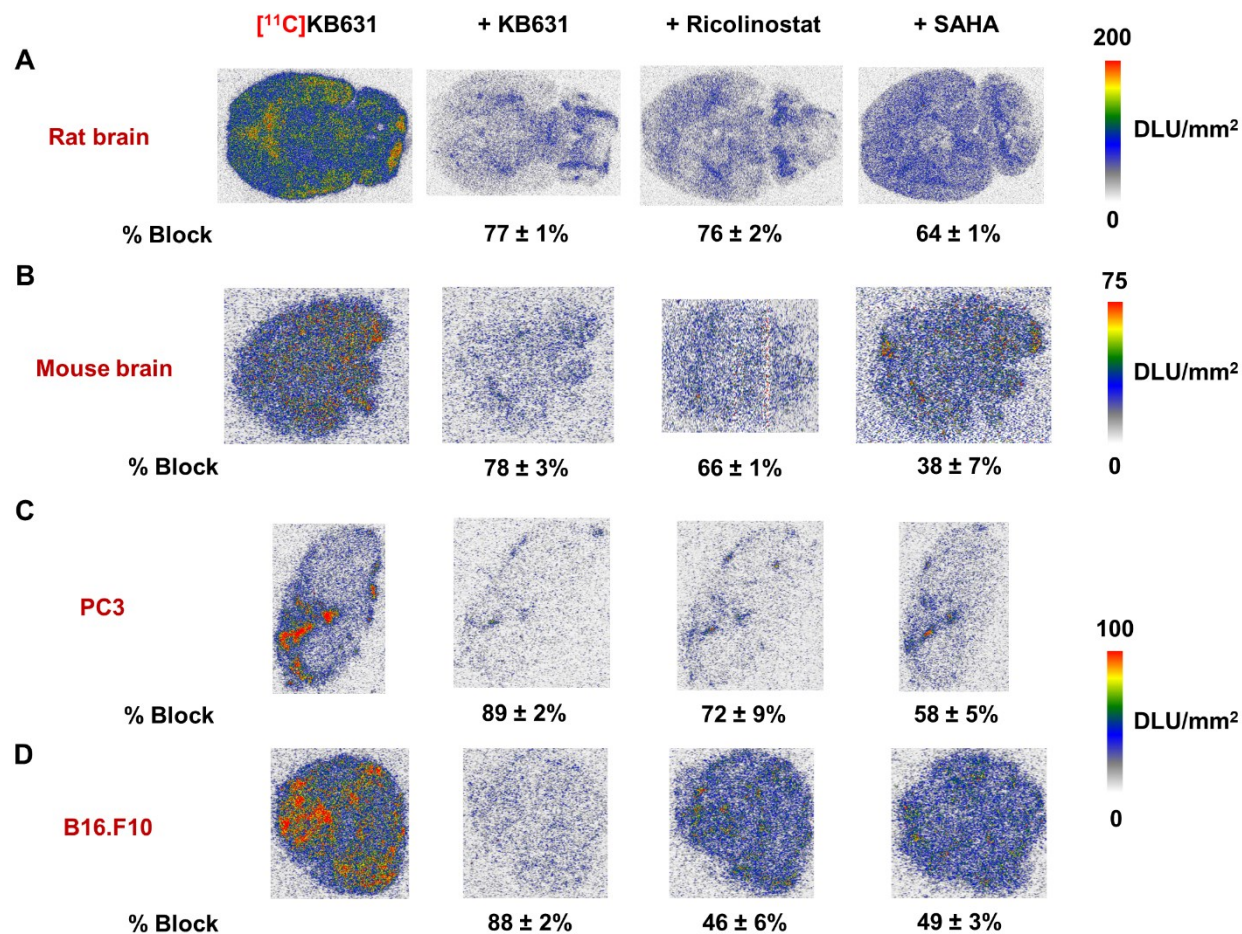


**Figure 3: *In vitro* autoradiography study on different tissue sections.** A) Rat brain B) Mouse brain C) PC3 prostate carcinoma D) Murine B16.F10 melanoma. Sections were incubated with [ $^{11}\text{C}$ ]KB631 (74 kBq/mL) in presence of vehicle, KB631, Ricolinostat or SAHA (100  $\mu\text{M}$  of blocking agents). Intensity is depicted as DLU/mm<sup>2</sup>. n = 3-4 sections per group. % Block was calculated as (average DLU/mm<sup>2</sup> in tissue slice in the presence of 100  $\mu\text{M}$  blocker) / (average DLU/mm<sup>2</sup> in tissue slice, tracer only) and presented as mean  $\pm$  SD.

### 3.3. Biodistribution studies

The biodistribution of [ $^{11}\text{C}$ ]KB631 was studied in male NMRI-mice (n = 3 per time point). Data are expressed as %ID (Table S1) and SUV in Table 2. The tracer is cleared primarily *via* the hepatobiliary route. Blood radioactivity levels decrease fairly rapid with a SUV 2/60 min ratio of 3.0. Not more than SUV = 0.1 was detected in the brain in any of the 4 studied time points.

**Table 2:** Biodistribution data of [<sup>11</sup>C]KB631 in male NMRI-mice at 2, 10, 30 and 60 min after tracer injection, presented as SUV.

	SUV			
	2 min	10 min	30 min	60 min
<b>Blood</b>	0.9 ± 0.0	0.5 ± 0.1	0.4 ± 0.1	0.3 ± 0.1
<b>Bone</b>	0.4 ± 0.0	0.4 ± 0.0	0.3 ± 0.0	0.2 ± 0.0
<b>Brain</b>	0.1 ± 0.0	0.1 ± 0.0	0.0 ± 0.0	0.1 ± 0.0
<b>Heart</b>	2.5 ± 0.3	1.3 ± 0.2	0.7 ± 0.1	0.3 ± 0.1
<b>Kidneys</b>	9.0 ± 1.1	5.4 ± 1.0	3.1 ± 0.5	1.4 ± 0.2
<b>Liver</b>	6.3 ± 1.0	5.0 ± 0.2	4.4 ± 0.4	2.6 ± 0.5
<b>Lungs</b>	3.8 ± 0.5	2.3 ± 0.1	1.5 ± 0.1	0.8 ± 0.1
<b>Muscle</b>	0.7 ± 0.1	0.6 ± 0.1	0.4 ± 0.0	0.2 ± 0.0
<b>Pancreas</b>	1.7 ± 0.2	1.5 ± 0.1	1.0 ± 0.1	0.6 ± 0.2
<b>Spleen</b>	2.5 ± 0.6	0.9 ± 0.1	0.9 ± 0.2	0.3 ± 0.2

SUV = Standardized uptake value. Data expressed as mean ± SD; n = 3 per time point.

**Table 3:** Biodistribution data of [<sup>11</sup>C]KB631 in male NMRI-mice 10 min after tracer injection. Mice were pre-treated with vehicle, KB631 (10 mg/kg), SAHA (10-100 mg/kg) or Ricolinostat (10-50 mg/kg).

	SUV					
	Control	KB631	SAHA	SAHA	Ricolinostat	Ricolinostat
			10 mg/kg	100 mg/kg	10 mg/kg	50 mg/kg
<b>Blood</b>	0.5 ± 0.0	0.9 ± 0.1	0.6 ± 0.1	1.2 ± 0.3	0.9 ± 0.0	1.6 ± 0.4
<b>Bone</b>	0.4 ± 0.0	0.4 ± 0.0	0.4 ± 0.1	0.5 ± 0.2	0.6 ± 0.1	0.6 ± 0.1
<b>Brain</b>	0.1 ± 0.0	0.1 ± 0.0	0.1 ± 0.0	0.1 ± 0.0	0.1 ± 0.0	0.1 ± 0.0
<b>Heart</b>	1.4 ± 0.0	1.4 ± 0.2	1.6 ± 0.2	1.8 ± 0.2	2.0 ± 0.1	2.0 ± 0.1
<b>Kidneys</b>	4.4 ± 0.3	9.4 ± 1.2	9.0 ± 1.9	8.5 ± 3.1	5.6 ± 1.0	9.5 ± 3.0
<b>Liver</b>	4.5 ± 0.6	4.4 ± 0.7	4.5 ± 0.6	4.0 ± 1.3	6.2 ± 1.4	4.4 ± 0.6
<b>Lungs</b>	2.1 ± 0.3	2.6 ± 0.3	2.1 ± 0.2	3.0 ± 1.6	4.2 ± 1.5	3.4 ± 0.8
<b>Muscle</b>	0.5 ± 0.1	0.7 ± 0.1	0.7 ± 0.0	0.7 ± 0.3	0.8 ± 0.1	0.8 ± 0.1
<b>Pancreas</b>	1.4 ± 0.1	1.6 ± 0.2	1.5 ± 0.0	1.3 ± 0.5	2.3 ± 0.1	1.8 ± 0.2
<b>Spleen</b>	1.0 ± 0.2	1.4 ± 0.2	1.5 ± 0.3	1.2 ± 0.2	1.5 ± 0.1	1.6 ± 0.2

Calculated as (SUV organ/SUV blood) Data expressed as mean ± SD; n = 3 per pre-treatment.

The biodistribution study 10 min after tracer injection was repeated after pre-treatment with KB631 (10 mg/kg), SAHA (10 or 100 mg/kg) or Ricolinostat (10 or 50 mg/kg) injected i.p. 30-45 min before i.v. injection of [<sup>11</sup>C]KB631. Data are presented as %ID (**Table S2**) and SUV in **Table 3**. Blocking with KB631 and the higher doses of SAHA and Ricolinostat increased blood radioactivity levels, hence to correctly assess potential blocking effects, organ/blood

ratios were calculated and are depicted in **Figure 4**. A significant effect of KB631 blocking was observed in all the organs of interest except for kidneys and spleen. Pre-treatment with 10 mg/kg SAHA or Ricolinostat did not influence the biodistribution of [ $^{11}\text{C}$ ]KB631 (**Table 3**). The higher doses of Ricolinostat (50 mg/kg) and SAHA (100 mg/kg), commonly used in clinical trials yielded a significant blocking effect in all the organs of interest (**Figure 4**). Brain uptake of [ $^{11}\text{C}$ ]KB631 was low ( $\text{SUV} \leq 0.1$ ), but was partially, but significantly blocked by KB631 and the higher doses of SAHA and Ricolinostat.

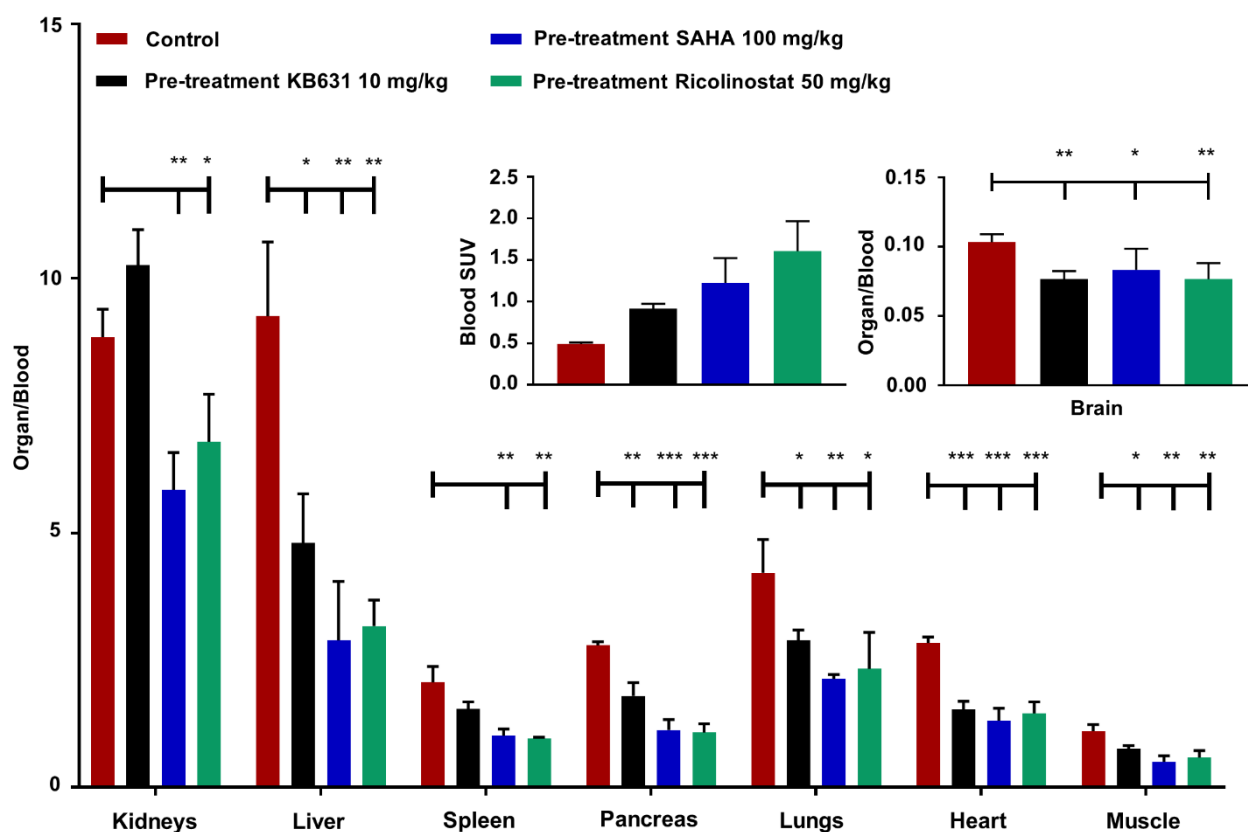


**Figure 4: Pre-treatment biodistribution of [ $^{11}\text{C}$ ]KB631 in NMRI-mice.** Animals were anesthetized with 2.5% isoflurane in  $\text{O}_2$  at a flow rate of 1 L/min. KB631 (10 mg/kg), SAHA (100 mg/kg) or Ricolinostat (50 mg/kg) was administered i.p. 30-45 min before i.v. tracer injection (5.5 MBq). Mice were sacrificed 10 min p.i. ( $n = 3$  per pre-treatment). Organs of interest are shown. Data is expressed as organ to blood SUV ratio. Blood values are shown as SUV. \* $P \leq 0.05$ , \*\* $P \leq 0.01$  \*\*\* $P \leq 0.001$  calculated with two-way ANOVA.

Biodistribution studies in B16.F10 melanoma bearing mice (**Table 4**, **Table S3**) showed a low uptake of tracer in the tumour ( $\text{SUV} = \sim 0.5$ , **Figure 5**). Pre-treatment with 50 mg/kg Ricolinostat induced an increase of radioactivity in the blood conform to the *ex vivo* biodistribution study on healthy NMRI-mice (**Table 3**, **Figure 4**). When comparing organ/blood ratios, it was observed that tracer binding could be significantly blocked with pre-treatment of



Ricolinostat ( $P < 0.01$ ) and was reduced by half (tumour/blood control = 0.5 vs block = 0.25) (**Figure 5**). These results suggest HDAC6-specific binding of [<sup>11</sup>C]KB631 to B16.F10 melanoma.

**Table 4:** Biodistribution data of [<sup>11</sup>C]KB631 in B16.F10 melanoma inoculated C57BL/6 mice 10 min after tracer injection. Mice were pre-treated with vehicle or Ricolinostat (50 mg/kg).

	SUV	
	Control	Ricolinostat
<b>Blood</b>	0.9 ± 0.1	1.9 ± 0.1
<b>Bone</b>	0.4 ± 0.0	0.6 ± 0.2
<b>Brain</b>	0.1 ± 0.0	0.1 ± 0.0
<b>Heart</b>	1.6 ± 0.1	1.5 ± 0.1
<b>Kidneys</b>	7.9 ± 0.0	5.8 ± 1.2
<b>Liver</b>	4.7 ± 0.3	3.6 ± 0.3
<b>Lungs</b>	2.5 ± 0.4	2.7 ± 0.3
<b>Muscle</b>	0.5 ± 0.1	0.7 ± 0.0
<b>Pancreas</b>	1.6 ± 0.0	1.7 ± 0.1
<b>Spleen</b>	1.2 ± 0.1	1.3 ± 0.1
<b>Tumour</b>	0.4 ± 0.1	0.5 ± 0.1

SUV = Standardized uptake value. Data expressed as mean ± SD; n = 3 per pre-treatment.

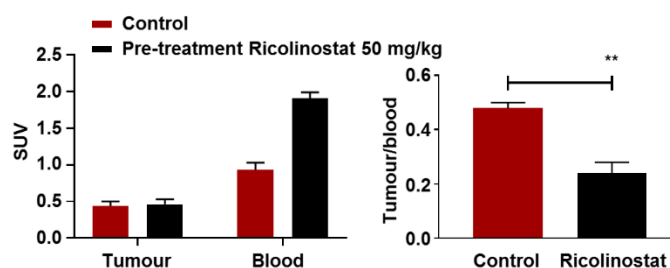


**Figure 5: Biodistribution of [<sup>11</sup>C]KB631 in B16.F10 melanoma bearing mice after Ricolinostat pre-treatment.** Animals were anesthetized with 2.5% isoflurane in O<sub>2</sub> at a flow rate of 1 L/min. Vehicle or Ricolinostat (50 mg/kg) was administered i.p. 30-45 min before tracer injection (5.5 MBq). Mice were sacrificed 10 min p.i. (n = 3 per pre-treatment). SUV values of tumour and blood are shown besides the tumour blood ratio. \*\* $P \leq 0.01$ , calculated by unpaired T-test with Welch's correction.

### 3.4. Plasma radio-metabolite study

The results of the plasma radio-metabolite study conducted in healthy NMRI-mice at 10 and 60 min injection p.i. (n = 3 per time point) are presented in **Figure 6**. The tracer remained fairly stable in plasma over the 60-min time course, as 84% of the radioactivity corresponded to intact tracer. The remaining 16% eluted earlier on RP-HPLC.

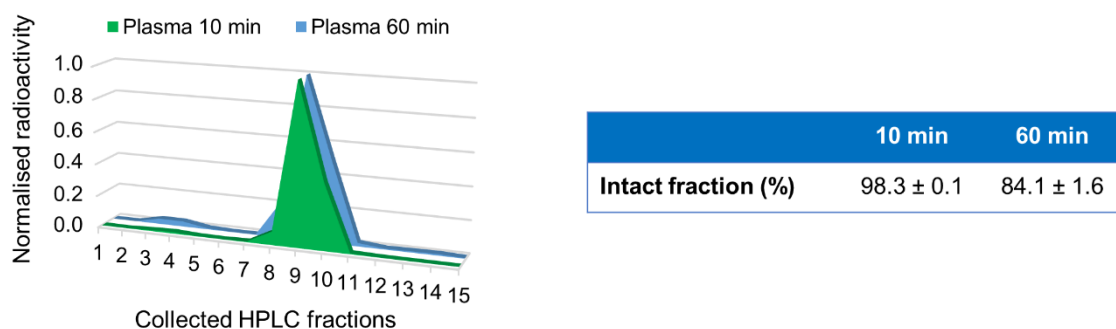


**Figure 6: Plasma radio-metabolite study.** Animals were anesthetized with 2.5% isoflurane in O<sub>2</sub> at a flow rate of 1 L/min. Mice were injected i.v. with 11 MBq and sacrificed 10 or 60 min p.i. (n = 3 per pre-treatment) Up to 85% the of intact tracer was found in plasma 60 min after tracer injection.

### 3.5. $\mu$ PET

B16.F10 inoculated C57BL/6 mice (n = 3) were treated on consecutive days with respectively vehicle and Ricolinostat (i.p. 50 mg/kg) (**Figure 7A-B**). In baseline conditions, tracer concentration in the tumour increased to SUV = 0.7 at 10 min p.i. followed by slow tracer wash out over the 90-min course of the scan. After pre-treatment with Ricolinostat tracer uptake in the tumour continued to increase as a function of time, reaching a max at SUV = 0.8 at 55 min p.i. In control conditions, a steady muscle wash out of radioactivity was observed (SUV<sub>20</sub>/SUV<sub>90</sub> = 2.0) (**Figure 7D, blue**), whereas after blocking with Ricolinostat, (**Figure 7D, green**) the SUV curve shifted upwards to reach a maximum after 23 min p.i., from then on a slow wash-out was observed. A significant decrease of the tumour/muscle SUV ratios, was observed after blocking P < 0.0001 (**Figure 7E**), suggesting HDAC6-specific tracer binding.

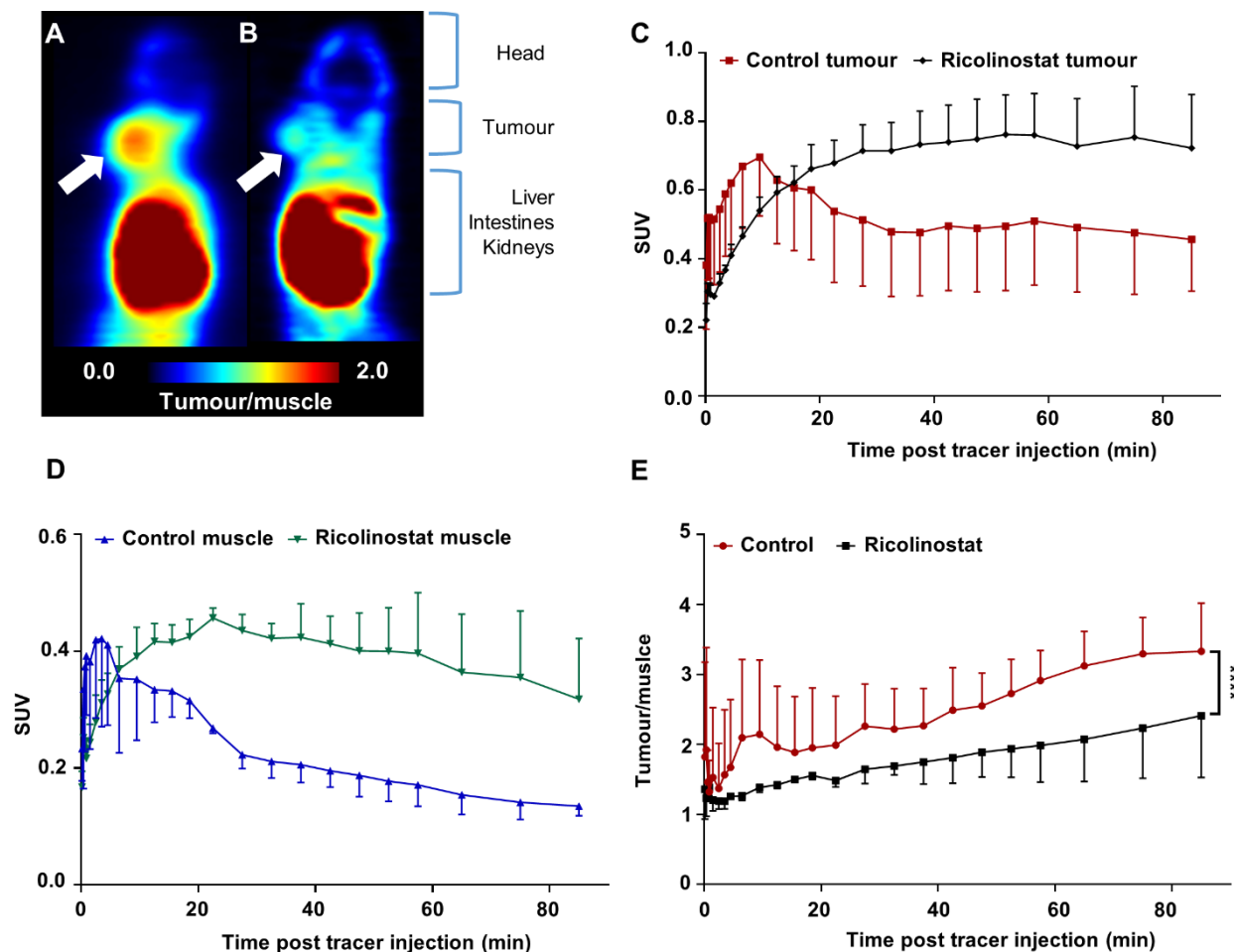


**Figure 7:  $\mu$ PET study on C57BL/6 mice inoculated with B16.F10 melanoma.** Animals were anesthetized using 2.5% isoflurane in O<sub>2</sub> (2 L/min) and kept under anaesthesia during the entire scan period. **A)** Tumour/muscle ratio averaged baseline image of 90-min dynamic scan after injection of [<sup>11</sup>C]KB631 (7.5 MBq, n = 3). **B)** Tumour/muscle ratio averaged image of 90-min dynamic scan after blocking with 50 mg/kg Ricolinostat administered i.p. 30-45 min before [<sup>11</sup>C]KB631 injection. **A-B)** White arrows indicate tumour site. **C)** Averaged tumour TACs derived from baseline and blocking. **D)** Averaged TACs derived from baseline and blocking studies in muscle **E)** Tumour/muscle ratio as a function of time (\*\*\*\*P < 0.0001, calculated by paired T-test on averaged SUV<sub>0-90 min</sub> tumour/muscle ratios of control vs Ricolinostat).

#### 4. DISCUSSION

Compared to other members of the HDAC-family, HDAC6 has 2 functional deacetylation domains, an ubiquitin binding domain and is localised predominantly in the cytosol. Its main targets also reside in the cytosol, including Hsp90, cortactin and  $\alpha$ -tubulin. As HDAC6 is involved directly and indirectly in multiple cellular pathways *via* the deacetylation of regulators of cell homeostasis and degradation of proteins *via* the aggresome pathway, there is increasing evidence that aberrant expression of this HDAC isoform contributes to progression and maintenance of various diseases [48,51].

The role of HDAC6 in cancer and neurodegenerative diseases has been well documented, yet no HDAC6 inhibitors have been approved for clinical use. Interesting results are obtained in clinical studies with Ricolinostat in combination with Bortezomib to combat MM [252]. Further, treatment of melanoma cells with Ricolinostat induced accelerated cell death of the malignant cells [254]. Pharmacological inhibition of HDAC6 in B16.F10 cells was observed to downregulate PD-L1 in malignancies, which is an activator of the PD-1 mediated inhibitory pathway in T-cells. Furthermore, a reduction of tumour growth was observed in *in vivo* experiments on B16.F10 melanoma inoculated mice after treatment with HDAC6 inhibitors, Nexturastat or Tubastatin A [62]. Ricolinostat was chosen as structural unrelated HDAC6 inhibitor to assess the binding specificity of [<sup>11</sup>C]KB631 in *in vitro* and *in vivo* experiments on B16.F10 melanoma.

Efforts are being made, and several clinical trials are running to evaluate potential new, isoform-selective HDAC inhibitors for the treatment of both solid and non-solid malignancies [261]. In this regard, development of PET probes, enabling visualisation and quantification of HDAC6 or other HDAC isoforms *in vivo* can accelerate the drug development stream.

The original reported synthesis of [<sup>11</sup>C]KB631 where precursor compound KB674 was reacted with [<sup>11</sup>C]CH<sub>3</sub>I in presence of KOH for 4 min at 80 °C was adapted. As the base form of the precursor was used, KOH was omitted from the reaction mixture and the reaction temperature was increased to 100 °C. Reaction yields up to 60%, based on prep-HPLC AUCs were obtained compared to reported yields, which varied around 8% decay corrected to initial [<sup>11</sup>C]CO<sub>2</sub>.

Even though it was determined that [<sup>11</sup>C]KB631 only sparsely permeated the blood-brain barrier (BBB), an *in vitro* autoradiography experiment was performed to assess tracer binding to brain. *In vitro* autoradiography has the advantage that radioactivity can be applied to the tissue of interest and bypass passive diffusion over the BBB. Further, potential metabolism is omitted. Expression of HDAC6 in brain was reported in the cortex, caudate putamen, hippocampus, amygdala, substantia nigra compacta and the locus coeruleus [52], in neurons but not in oligodendrocytes [65]. Furthermore, HDAC6 is highly expressed in raphe nuclei in the brain stem and more specifically in the serotonergic neurons of mice brain. This data was confirmed in *post-mortem* human brain [66]. [<sup>11</sup>C]KB631 binding in brain tissue was heterogeneous with highest binding in subcortical areas, rhinal cortex and parts of the cerebellum as determined in rat brain. Blocking with KB631, Ricolinostat or SAHA decreased tracer binding up to 70 or 90% in respectively cerebellum and rhinal cortex.

[<sup>18</sup>F]Bavarostat was reported to specifically bind to rat and baboon brain *in vivo*, with predominant uptake in subcortical areas. In *in vitro* autoradiography studies, 40% of [<sup>18</sup>F]Bavarostat binding to rat cerebellum was blocked by co-incubation with 100 µM Tubastatin A [190] which was similar to blocking with Bavarostat.

Heterogeneous binding of [<sup>11</sup>C]KB631 on the tumour sections was observed. Both B16.F10 melanoma and PC3 prostate cancer cells are known to be highly metastatic, a characteristic that requires highly dynamic microtubules

and localized polymerization of actin filaments which can be mediated by deacetylation of respectively  $\alpha$ -tubulin and cortactin by HDAC6. Further it was reported that HDAC6 overexpression in cancer cells increased chemotactic cell motility, an effect that could be counteracted by inhibition with HDAC6 selective inhibitor, Tubacin [51,262]. Incubation of B16.F10 melanoma and PC3 prostate carcinoma tumour tissues with [<sup>11</sup>C]KB631 in presence of Ricolinostat yielded varying results with high block in PC3 but only moderate block in B16.F10 melanoma sections. But in areas of higher tracer binding, the blocking was more pronounced. The highly localised tracer binding can be indicative of HDAC6-rich protrusions of tumour cell migration, motility or invasion [13]. However further research is required to elucidate the observed phenomenon. Saturable binding, with low non-specific binding was observed in both tumour types as investigated by incubation of the tracer with KB631. SAHA was only able to moderately challenge the tracer binding in the tumour sections. Although it was reported that pan-HDAC inhibitor SAHA also has nanomolar affinity for HDAC6 and class I HDACs [240], its binding kinetics may be slower compared to those of KB631.

Initial biodistribution studies conducted on healthy male NMRI-mice at 4 different time points showed a steady blood clearance, hepatobiliary excretion with secondary renal clearance and low brain uptake ( $SUV \leq 0.1$ ) in agreement with literature reports. Passive BBB permeation can occur for compounds with a logD value of 1.5-3, a *t*PSA lower than 90 Å<sup>2</sup> and a molecular weight under 500 Da. KB631 has a molecular weight of 335.4 Da, a calculated *t*PSA value of 57 and a calculated logD value of 2.7. These parameters combined suggest free diffusion of the compound over the BBB [161]. It was postulated that the lack of brain penetrance of [<sup>11</sup>C]KB631 was attributed to the unfavourable properties of the hydroxamate moiety [193]. However, recently it was shown that hydroxamic acid containing tracers ([<sup>11</sup>C]Martinostat, [<sup>18</sup>F]Bavarostat) targeting HDACs have high brain exposure [263]. The exact reason for the low BBB permeation of [<sup>11</sup>C]KB631 remains elusive.

In a biodistribution study, NMRI-mice were pre-treated with different HDAC inhibitors, and again, low brain uptake of [<sup>11</sup>C]KB631 was observed. However, the low uptake in brain was partially blocked by pre-treatment of KB631, and higher doses of SAHA and Ricolinostat (**Figure 4**). This is surprising as SAHA is not able to cross the BBB efficiently [264] and was classified as a class IV drug in the biopharmaceutics classification system [265]. Nevertheless, the high administered dose of 100 mg/kg, may impart some brain uptake. In a study where [<sup>18</sup>F]FAHA was used to determine distribution of HDACs in rat brain, it was observed that increasing doses of SAHA up to 100 mg/kg yielded effective block of tracer binding in brain [266]. Ricolinostat has predominantly been evaluated in cancer and data regarding its brain uptake is lacking.

Pre-treatment with KB631 and the higher doses of SAHA and Ricolinostat, increased blood radioactivity levels, likely induced by saturation of peripheral HDAC6. This increases the free fraction of [<sup>11</sup>C]KB631 in blood in turn increasing the uptake of [<sup>11</sup>C]KB631 in different tissues and organs. In this respect, organ/blood values were evaluated to assess blocking effects.

Expression of HDAC6 was reported in several organs including heart, liver, kidney, brain and pancreas [51]. Tracer blocking is observed in these organs with the higher doses of SAHA and Ricolinostat, blocking with KB631 was

effective in the studied organs except for kidneys and spleen. Conversely, the lower doses of SAHA and Ricolinostat were unable to block tracer binding in any of the studied tissues. The effect observed for the higher doses of SAHA and Ricolinostat is in accordance with reported literature where 50 mg/kg of Ricolinostat is used to achieve sufficient plasma and organ levels [252] and administration between 50 to 150 mg/kg of SAHA is easily tolerated [264]. This indicates that the lower doses are likely insufficient to induce full HDAC6 saturation.

In *in vivo* [<sup>11</sup>C]KB631  $\mu$ PET studies, B16.F10 melanoma bearing mice were subjected to a two-day experiment where vehicle pre-treatment was compared with Ricolinostat (50 mg/kg). After baseline scans, an averaged tumour SUV<sub>20-90 min</sub> of 0.5 was measured. Although tumour uptake was rather low, tumour-to-background contrast was high enough to delineate the position of the tumour (**Figure 7A**). After pre-treatment with Ricolinostat, an increase of tumour SUV<sub>20-90 min</sub> to 0.8 was noticed. A similar effect was observed in muscle tissue, possibly attributed to increased radioactivity levels in blood in accordance with the *ex vivo* biodistribution. Here, a reduction of tumour/blood ratio with 50% after pre-treatment with Ricolinostat was observed. Blood sampling on tumour mice undergoing  $\mu$ PET scanning is challenging, and decreases survival chances drastically. As the same three mice were scanned on consecutive days and to reduce the strain placed upon the rodents, it was opted to omit blood sampling. In this respect, organ/muscle ratios were calculated and used to evaluate the specificity of binding. The muscle wash out in control conditions is more rapid compared to blocking conditions and thus a more prominent blocking effect of Ricolinostat is observed at later time points. Combined with the *ex vivo* biodistribution data it can be concluded that [<sup>11</sup>C]KB631 binds specifically to HDAC6 in the B16.F10 melanoma and other HDAC6 expressing organs.

Preliminary results obtained in the B16.F10 melanoma inoculated mice show promise to use this tracer in oncological malignancies. Further studies can focus on the heterogeneous intra-tumoural localisation of HDAC6 and complementary tracer binding as observed in *in vitro* autoradiography studies. Subsequent research is warranted to explore the potential of [<sup>11</sup>C]KB631 in other solid tumours and potentially other peripheral diseases including inflammation and cardiovascular diseases [249].

## 5. CONCLUSION

In this proof of concept study, [<sup>11</sup>C]KB631 was evaluated *in vitro* and *in vivo* in healthy tissues, where clinical relevant doses of SAHA and Ricolinostat were able to block the tracer binding. *In vitro* autoradiography studies showed that [<sup>11</sup>C]KB631 binds HDAC6-specific to different types of tissue including rodent brain and murine grown tumours. In  $\mu$ PET studies in a B16.F10 melanoma mouse model, [<sup>11</sup>C]KB631 showed limited but specific tumour binding, as indicated by *in vivo* blocking studies with Ricolinostat. Further research is warranted, extending the use of this tracer to other tumour types or inflammatory or cardiovascular diseases.

---

### EVALUATION OF [<sup>11</sup>C]NMS-E973 AS A PET TRACER FOR *IN VIVO* VISUALISATION OF HSP90

---

**Koen Vermeulen<sup>1\*</sup>**, Evelyne Naus<sup>2\*</sup>, Muneer Ahamed<sup>3</sup>, Bala Attili<sup>1</sup>, Maxime Siemons<sup>1,2</sup>, Kaat Luyten<sup>1,2</sup>, Sofie Celen<sup>1</sup>, Joost Schymkowitz<sup>2</sup>, Frederic Rousseau<sup>2</sup> and Guy Bormans<sup>1</sup>

<sup>1</sup> Laboratory for Radiopharmaceutical Research, Department of Pharmaceutical and Pharmacological Sciences, KU Leuven, Leuven, Belgium

<sup>2</sup> Switch Laboratory, VIB-KU Leuven Center for Brain & Disease Research, KU Leuven, Leuven, Belgium

<sup>3</sup> Centre for Advanced Imaging, University of Queensland, Brisbane, Australia

\*These authors contributed equally to this manuscript.

Manuscript published in Theranostics 2019; 9(2):554-572

Supplementary information: <http://www.thno.org/v09/p0554/thnov09p0554s1.pdf>





## Abstract

Heat shock protein 90 is an ATP-dependent molecular chaperone important for folding, maturation and clearance of aberrantly expressed proteins and is abundantly expressed (1-2% of all proteins) in the cytosol of all normal cells. In some tumour cells, however, strong expression of Hsp90 is also observed on the cell membrane and in the extracellular matrix and the affinity of tumoural Hsp90 for ATP domain inhibitors was reported to increase over 100-fold compared to that of Hsp90 in normal cells. Here, we explore [<sup>11</sup>C]NMS-E973 as a PET tracer for *in vivo* visualisation of Hsp90 and as a potential tool for *in vivo* quantification of occupancy of Hsp90 inhibitors.

**Materials and methods:** Hsp90 expression was biochemically characterized in a panel of established cell lines including the melanoma line B16.F10. B16.F10 melanoma xenograft tumour tissue was compared to non-malignant mouse tissue. NMS-E973 was tested *in vitro* for Hsp90 inhibitory activity in several tumour cell lines. Hsp90-specific binding of [<sup>11</sup>C]NMS-E973 was evaluated in B16.F10 melanoma cells and B16.F10 melanoma, prostate cancer LNCaP and PC3, SKOV-3 xenograft tumour slices and *in vivo* in a B16.F10 melanoma mouse model.

**Results:** Strong intracellular upregulation and abundant membrane localisation of Hsp90 was observed in the different tumour cell lines, in the B16.F10 tumour cell line and in B16.F10 xenograft tumours compared to non-malignant tissue. NMS-E973 showed Hsp90-specific inhibition and reduced proliferation of cells. [<sup>11</sup>C]NMS-E973 showed strong binding to B16.F10 melanoma cells, which was inhibited by 200 μM of PU-H71, a non-structurally related Hsp90 inhibitor. Hsp90-specific binding was observed by *in vitro* autoradiography of murine B16.F10 melanoma, LNCaP and PC3 prostate cancer and SKOV-3 ovary carcinoma tissue slices. Further, B16.F10 melanoma-inoculated mice were subjected to a μPET study, where the tracer showed fast and persistent tumour uptake. Pre-treatment of B16.F10 melanoma mice with PU-H71 or Ganetespib (50 mg/kg) completely blocked tumour accumulation of [<sup>11</sup>C]NMS-E973 and confirmed *in vivo* Hsp90 binding specificity. Hsp90-specific binding of [<sup>11</sup>C]NMS-E973 was observed in blood, lungs and spleen of tumour-bearing animals but not in control animals.

**Conclusion:** [<sup>11</sup>C]NMS-E973 is a PET tracer for *in vivo* visualisation of tumour Hsp90 expression and can potentially be used for quantification of Hsp90 occupancy. Further translational evaluation of [<sup>11</sup>C]NMS-E973 is warranted.

## **1. INTRODUCTION**

The heat shock protein (Hsp) family is part of a big cluster of molecular chaperones important for folding, maturation and clearance of aberrantly expressed proteins. Hsps facilitate cellular signalling processes and control the general maintenance of cell homeostasis. Hsps occur in all cellular compartments of eukaryotic cells as well as in all prokaryotes [74]. They are classified into a number of functionally and structurally distinct families that are named after the molecular mass of well-characterised members, ranging from 10 to 100 kDa. The 90 kDa members of the eukaryotic Hsp-family (Hsp90) are ATP-dependent proteins that can predominantly be found in the cytosol, although they also occur in the nucleus bound to obligate substrates, such as the nuclear receptors (glucocorticoid and androgen receptors) [75]. Hsp90 occurs as two major isoforms: the inducible Hsp90AA1 (Hsp90 $\alpha$ ) and the constitutively expressed Hsp90AB1 (Hsp90 $\beta$ ). Other paralogues exist that are restricted to the endoplasmic reticulum (ER) and mitochondria; 94 kDa glucose-regulated protein (Grp94) and tumour necrosis factor receptor-associated protein 1 (TRAP1), respectively. In a stress-free environment, these 90 kDa chaperones make up 1-2% of all the soluble cellular proteins, whereas their fraction increases to 6-7% in cancer cells and up to 10% during cellular stress [79–81].

Hsp90-mediated processes function with the help of a complex of co-chaperones (chaperone machinery), which consist of different cofactors with different binding preferences for specific Hsp90 conformations. Several cofactors regulate the ATPase activity of Hsp90; others modulate/maturate substrate processing. Moreover, the Hsp90 complex is regulated by post-translational modifications such as acetylation, nitrosylation and phosphorylation [72]. The client proteins processed by the Hsp90 machinery are abundant; over 400 have been reported, encompassing kinases, transcription factors, E3-ubiquitin ligases, steroid hormone receptors and other essential signalling proteins [83,84]. Many of these client proteins contribute to the six hallmarks of cancer [115].

Hsp90 is found to be upregulated in many types of cancer ranging from hematopoietic to solid tumours. Furthermore, some cancer cells are addicted to and exploit the Hsp90 complex, keeping oncogenic proteins from being degraded by the proteasome, elevating the survival chances of the tumour cells and maintaining the malignant state [6,11]. Not only expression levels were found to be higher but Hsp90 was also found to adopt a tumour-specific conformation in multi-chaperone complexes in tumours, resulting in a 100-fold increase in affinity for the ATP site binding inhibitor 17-allylamino-17-demethoxy-geldanamycin (17-AAG, **Figure 4, Quinone in Chapter I**) [92]. In normal cells, Hsp90 is confined to the intracellular space; but, in tumour cells (fibrosarcoma [98], melanoma [99], breast cancer [100]), vast expression of Hsp90 was also observed on the cell surface or secreted to the extracellular matrix (ECM), consensually referred to as extracellular Hsp90 (eHsp90) [101].

Currently, several Hsp90 inhibitors are being developed and some are being evaluated in oncological clinical trials [268]. The mechanism of action of most Hsp90 inhibitors is based on disrupting the interaction between ATP and the N-terminal ATP-binding domain (ND) of the enzyme. Inhibition of the ATP pocket will restrain Hsp90 in the ADP-

bound state and client proteins will be ubiquitinated and probed for subsequent degradation by the proteasome [267]. However, C-terminal domain (CD) inhibitors are also currently under investigation. These inhibitors destabilize the chaperone complex, leading to release of co-chaperones and substrates and subsequent degradation of client proteins [115].

First-generation Hsp90 inhibitors encompass derivatives of natural products such as Geldanamycin and Radicicol. Although Geldanamycin is a potent ND Hsp90 inhibitor, its use was limited due to solubility issues, limited *in vivo* stability and hepatotoxicity in animal models. This led to the development of Geldanamycin analogues (Alvespimycin, Tanespimycin, Retaspimycin HCl, **Figure 4, Quinone in Chapter I**) with more favourable pharmacokinetics and less toxicity. Newer, synthetic inhibitors, include molecules based on purine (PU-H71, **Figure 1E**), resorcylic pyrazole/isoxazole (Ganetespib, **Figure 1D**, NMS-E973, **Figure 1F**) and benzamide scaffolds. However, this list is not limitative and new chemical entities with affinity for Hsp90 are continued to be discovered [115]. Although over 15 Hsp90 inhibitors are being evaluated in clinical trials and initial preclinical results look promising, many of the compounds have not lived up to expectations. Frequent adverse effects (gastrointestinal problems, reversible night blindness) limit the further use or evaluation of these compounds. Moreover, Hsp90 inhibition *via* the ATP-containing ND induces a heat shock response (HSR) *via* heat shock factor 1 (HSF1), which upregulates transcription of pro-survival Hsps, Hsp27, Hsp40 and Hsp70 [131]. The use of a combinatorial approach to target Hsp90 and Hsp70 or HSF1 can bypass this compensatory effect, increasing the effectiveness of drug treatment. The development of CD inhibitors, where the HSR is less pronounced, can also be an alternative [132]. Research has also taken an interest in targeting eHsp90. Where Tsutsumi et al. observed an absence of internalisation of the cell-impermeable Hsp90 inhibitor DMAG-N-oxide in melanoma cells [103], Crowe et al. demonstrated eHsp90-specific active internalisation of their fluorescent probes HS-27 and HS-131 (**Figure 1B**) and radiolabelled [<sup>125</sup>I]HS-111 (**Figure 1C**) in mammary tumour cells [269]. Furthermore, internalisation of the HS probes was blocked using an antibody against the CD of Hsp90 [270]. Imaging studies with HS-131 showed increased expression levels and internalisation of eHsp90 in aggressive malignant cells. Following this, it was concluded that eHsp90 can be a valuable target of cancer cell metastasis and invasiveness and can play a defined role as a biomarker of malignant cell behaviour.

The radiosynthesis of a small molecule Hsp90 inhibitor [<sup>124</sup>I]PU-H71 (**Figure 1E**) was recently reported [195], and the biodistribution of this positron emission tomography (PET) tracer was studied in MDA-MB-468/ASPC1 mouse xenografts, two different tumour types with different abundancies of the Hsp90 chaperone complex. The tracer showed relatively slow kinetics but tracer uptake in the Hsp90-high MDA-MB-468 tumour persisted over 48 h, whereas tracer uptake in the Hsp90-low ASPC1 tumour gradually decreased over 48 h. Furthermore, patients harbouring different types of cancers (breast cancer, lymphoma, gynaecologic malignancies) were subjected to PET-CT scans 24 h after injection of [<sup>124</sup>I]PU-H71 to identify PU-PET responsive tumours as part of a clinical study NCT01393509. [93]. An early phase I clinical trial is recruiting patients for PET imaging studies with this tracer (clinical trial identifier: NCT01269593).

A copper-64-labelled dimeric Sansalvamide A decapeptide (**Figure 14 in Chapter I**) was used to evaluate Hsp90 expression in pancreatic cancer. The tracer showed *in vivo* uptake in PL45 tumours that could be efficiently blocked by pre-treatment of the animals with 17-AAG at 4 h post tracer injection. Tumour-to-muscle ratios showed adequate tumour uptake; however, substantial hepatobiliary uptake was observed [197].

Recently, Brasca *et al.* reported NMS-E973, a potent and selective Hsp90 inhibitor that showed great promise in several *in vitro* cellular assays against numerous tumour cell lines [207]. NMS-E973 (**Figure 1F**) was reported with a half maximal depolymerisation concentration ( $DC_{50}$ ) of 10 nM and a dissociation constant ( $K_D$ ) of 0.35 nM for Hsp90 $\alpha$  and 4.5 nM and 670 nM for Grp94 and TRAP1, respectively. NMS-E973 was tested against a panel of 52 protein kinases, where it showed high selectivity towards Hsp90. In several *in vivo* studies, the compound induced a decrease in tumour growth and was effective against intracranially implanted melanoma [208]. The efficacy of NMS-E973 was also confirmed in a glioblastoma xenograft mouse model, where p53 upregulated modulator of apoptosis (PUMA) was induced following treatment of NMS-E973, leading to a reduction in tumour volume [271].

In this work, we report the radiosynthesis, *in vitro* and *in vivo* evaluation of [ $^{11}C$ ]NMS-E973 as a PET probe for *in vivo* visualisation of Hsp90 in B16.F10 melanoma-inoculated mice.

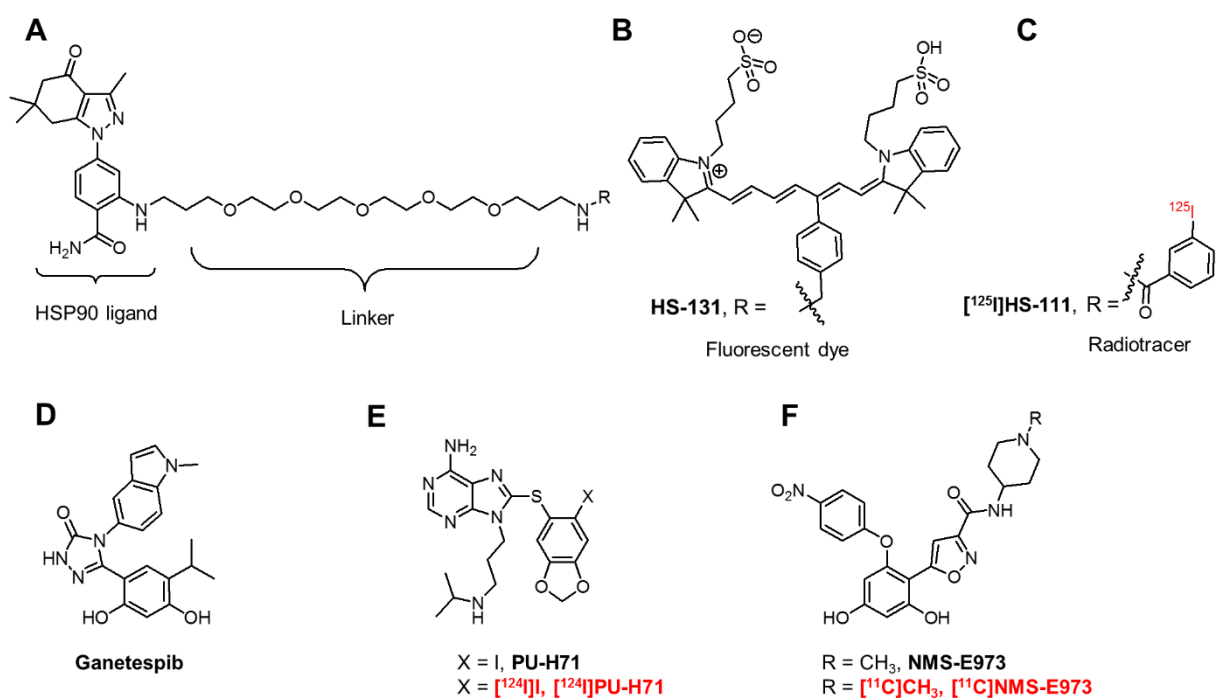


**Figure 1:** Chemical structures of fluorescent probes and nuclear imaging probes targeting Hsp90. **A)** Core structure of HS compounds. **B)** Fluorescent dye HS-131. **C)** Radiotracer [ $^{125}I$ ]HS-111. **D)** Potent Hsp90 inhibitor Ganetespib. **E)** PU-H71 and its [ $^{124}I$ ]-labelled radiotracer. **F)** NMS-E973 and its radiolabelled version [ $^{11}C$ ]NMS-E973.

## 2. MATERIALS AND METHODS

### 2.1. High-performance liquid chromatography (HPLC) analysis

HPLC was performed on a LaChrom Elite HPLC system (Hitachi, Darmstadt, Germany) connected to a Waters 2487 UV-VIS detector and a 3-inch NaI(Tl) scintillation detector connected to a single channel analyser (Gabi, Raytest, Straubenhardt, Germany). Registration and integration of the HPLC chromatograms was performed with GINA Star (Raytest) or RaChel (Lablogic, Sheffield, UK) software. The chemical and radiochemical purity (RCP) was assessed using reversed phase (RP)-HPLC (BDS Hypersil C<sub>18</sub>, 100 × 3 mm, 5 μm) eluted with 80%/20% Na<sub>2</sub>HPO<sub>4</sub> 0.01 M pH 9.3/CH<sub>3</sub>CN at a flow rate of 0.6 mL/min. The column effluent passed a UV detector (254 nm) and a NaI(Tl) scintillation detector. The identity of the tracer was determined by co-elution with cold reference compound on the same HPLC system.

### 2.2. Quantification of radioactivity in biological samples

Quantification was performed with an automated gamma counter equipped with a 3-inch NaI(Tl) well crystal coupled to a multichannel analyser (Wallac 1480 Wizard, Wallac, Turku, Finland). The results were corrected for background radiation, physical decay during counting and detector dead time.

### 2.3. Animal experiments

Animals were kept in a thermoregulated (22 °C) and humidity-controlled environment with a 12 h/12 h light/dark cycle in individual ventilated cages and had free access to food and water. All animal experiments were conducted with approval of the local University Ethics Committee for Animals and according to the Belgian code of practice for the care and use of animals. Female C57BL/6 mice, 8 weeks of age (body mass 20-25 g) and female Wistar rats (body mass 170-200 g) were purchased from Janvier (La Genest-Saint Isle, France). Naval Medical Research Institute (NMRI)-mice (body mass 30-40 g) were purchased from Envigo (Venray, The Netherlands).

### 2.4. LC-MS analysis

Elucidation of intermediate reaction products was accomplished using a Dionex Ultimate 3000 LC system (Thermo Fisher Scientific, Sunnyvale, USA) coupled to a high-resolution time-of-flight mass spectrometer (TOF-HRMS) (MaXis impact, Bruker, Bremen, Germany) equipped with an orthogonal electrospray (ESI) interface. Acquisition and processing of data were done using Compass IsotopePattern (version 3.2, Bruker).

### 2.5. NMR analysis

NMR was performed using proton nuclear magnetic resonance (<sup>1</sup>H NMR) at 400 MHz. Chemical shifts are reported in parts per million (ppm) relative to tetramethylsilane (TMS, δ = 0). Carbon nuclear magnetic resonance (<sup>13</sup>C NMR)

spectra were acquired at 101 MHz on a Bruker AVANCE 400 MHz spectrometer (5 mm probe, Bruker AG, Fällanden, Switzerland).

### 2.6. Statistical analysis

Quantitative data are expressed as mean  $\pm$  SD. Conventional statistics, repeated one-way analysis of variance (ANOVA) with Dunnett's post hoc test or one-way ANOVA/Tukey (HSD) test were calculated using Graphpad Prism 7.04 (Graphpad Software). Significance was accepted at the 95% probability level. High content data are represented as boxplots with Kruskal-Wallis test with Dunnett's correction.

### 2.7. Reagents and chemicals

Synthesis of the precursor compound **7**, 5-[2,4-Dihydroxy-6-(4-nitrophenoxy) phenyl]-N-(piperidin-4-yl)-isoxazole-3-carboxamide was performed as described by Brasca *et al.* [207] and a detailed synthetic protocol and characterization is provided in Supplementary Material (**Figure S1**). Hsp90 inhibitors, Ganetespib, PU-H71, Pifithrin- $\mu$ , PU-WS13, and authentic reference compound NMS-E973 were purchased from Selleckchem or MedChem Express and used without further purification. Topological polar surface area (tPSA) and LogD values were calculated using MarvinSketch (Marvin 14.10.13.0, 2014, ChemAxon, <http://www.chemaxon.com>).

### 2.8. Cell culture

All analysed cell lines including MCF-7, PC3, B16.F10, OVCAR-3, BT-474 and MDA-MB-415 were obtained from the American Type Culture Collection (ATCC). All lines were grown according to the supplier's instruction in medium (F-16 or Dulbecco's Modified Eagle's Medium (DMEM)) supplemented with 10% fetal bovine serum, non-essential amino acids and glutamine (Life Technologies, USA).

### 2.9. Inhibitory concentration (IC<sub>50</sub>) analysis

Cells were plated in 96-well plates at 2000 cells/well at day 0. At day 1, cells were treated with compound for 24 h at a concentration range of 0-1 mM. Cells were subsequently fixed with 4% PFA for 20 min. Subsequent 4, 6-diamidino-2-phenylindole (DAPI) staining of nuclei and imaging by high-content analysis allowed counting of remaining nuclei after treatment with different concentrations. Statistical analysis to calculate half-maximal inhibitory concentration (IC<sub>50</sub>)-values was performed using GraphPad Prism 7.04. Data were fitted to a non-linear regression curve and three-parameter model.

### 2.10. Immunofluorescent staining of cells and high-content screening

Cells were plated in 96-well plates (Greiner) at a density of 8000-10000 cells/well. At day 1, cells were treated with vehicle (DMSO; 0.001% final concentration), or with a compound (NMS-E973 or Ganetespib) at its IC<sub>50</sub> concentration for 16 h. At day 2, cells were washed with phosphate buffered saline (PBS) and fixed with 4% paraformaldehyde

(Thermo Scientific, 16% PFA diluted in PBS) for 30 min and either permeabilised or not by adding 0.2% Triton-X100 to blocking buffer (1% bovine serum albumin (BSA) in PBS) for 60 min. Primary antibodies were added to the cells in blocking buffer at a dilution of 1:500 (Anti-Hsp90, AC88, Abcam, anti-protein kinase B (AKT), C67E7, CST and anti-Hsp70 6B3,CST), and incubated overnight at 4 °C with gentle shaking. Cells were washed 3 times for 5 min in PBS and subsequently incubated with DAPI (0.1 µg/mL and/or secondary antibody (1:1000; goat-anti mouse, goat anti rabbit, goat anti rat, Alexa 549, Alexa 477, CY5; PROMEGA) in blocking buffer for 60 min. Imaging was performed on an IN Cell Analyser 2000 (GE Healthcare). The IN Cell Developer package (v1.9.2) allows visualisation, imaging, and quantification of staining intensity and quantification of inclusions in cells following immunofluorescent staining. Statistical analyses are done on a minimum of 1000 single cells per condition by R-studio (version 0.97.55) using R (3.0.1) software.

### 2.11. Immunofluorescent staining of tumour section slices

Slices were fixed with 4% paraformaldehyde (Thermo Scientific, 16% PFA diluted in PBS) for 30 min and antigen retrieval at pH 9 (EnVision FLEX Target Retrieval Solution, Dako) was executed according to the manufacturer's guidelines. To eliminate fixation-caused autofluorescence, tissue sections were incubated in 1 mg/mL sodium borohydride 3 times for 10 min at room temperature. Slides were then blocked with 10% goat serum, 1% (w/v) BSA and 0.3 M glycine in tris(hydroxymethyl)aminomethane (tris)-buffered saline (TBS) for 1 h. The primary antibodies (Hsp90 AC88, Abcam) were incubated in blocking buffer overnight at 4 °C at 1/200 dilution. The secondary antibody was diluted in blocking buffer (1/500 dilution, goat-anti mouse Alexa-594; PROMEGA) and incubated for 1 h together with DAPI (0.1 µg/mL). After several washing steps in TBS, the tissue sections were mounted with antifade reagent (ProLong Gold, Invitrogen) and kept in the dark for 24 h. Negative control slides (no primary antibody addition) were included in every batch. The screening was performed using a Nikon Eclipse TE-2000S inverted microscope at 60× magnification.

### 2.12. Radiosynthesis

Carbon-11 was produced by proton irradiation of a N<sub>2</sub> + H<sub>2</sub> (5%) gas mixture in a Cyclone 18/9 cyclotron (IBA Louvain-la-Neuve, Belgium) as [<sup>11</sup>C]CH<sub>4</sub> by a <sup>14</sup>N(p,α)<sup>11</sup>C nuclear reaction. [<sup>11</sup>C]CH<sub>4</sub> was converted to [<sup>11</sup>C]CH<sub>3</sub>I in a home-built gas phase recirculation module. [<sup>11</sup>C]NMS-E973 was synthesized by N-methylation of the precursor, 5-[2,4-Dihydroxy-6-(4-nitrophenoxy) phenyl]-N-(piperidin-4-yl)-isoxazole-3-carboxamide by bubbling [<sup>11</sup>C]CH<sub>3</sub>I with a helium flow through a solution of the precursor (400-500 µg) dissolved in anhydrous Dimethylsulfoxide (DMSO) (200-250 µL) in the presence of Cs<sub>2</sub>CO<sub>3</sub> (1-3 mg). After the transfer of the radioactivity was completed, the reaction vial was heated to 100 °C for 4 min. After cooling down, the crude mixture was diluted with 1.2 mL of water and the reaction mixture was purified by HPLC on a C<sub>18</sub> column (XBridge C<sub>18</sub> column, 5 µm, 4.6 mm × 150 mm; Waters, Milford, USA) eluted with 69%/31% Na<sub>2</sub>HPO<sub>4</sub> 0.01 M pH 9.3/ethanol (EtOH) at a flow rate of 1 mL/min. The corresponding

product peak was collected and diluted with saline to obtain a final EtOH concentration < 10%. The solution was filtered through a sterile 0.22  $\mu\text{m}$  membrane filter (Millex GV 13 mm; Millipore, Billerica, MA).

### 2.13. Confirmation of N-methylation

*Tert*-butyl-4-[[{5-[2,4-bis(methoxymethoxy)-6-(4-nitrophenoxy)phenyl]-isoxazole-3-yl}carbonyl]amino]piperidin-1-carboxylate ( $3.5 \times 10^{-4}$  mmol) was weighed and dissolved in 200  $\mu\text{L}$   $\text{CH}_3\text{CN}$  in a reaction vial with septum containing 2.87 mg  $\text{Cs}_2\text{CO}_3$ .  $\text{CH}_3\text{I}$  ( $3.09 \times 10^{-5}$  mmol) dissolved in 10  $\mu\text{L}$   $\text{CH}_3\text{CN}$ , was transferred with a  $\text{N}_2$  stream over a silver triflate column heated to 225  $^\circ\text{C}$ , to form methyl triflate, and bubbled through the reaction mixture. After a 10 min reaction at room temperature, the crude mixture was treated with 1 M of HCl overnight to remove the BOC protecting group. The mixture was injected on LC-MS and the QC HPLC system (BDS Hypersil  $\text{C}_{18}$ , 100  $\times$  3 mm, 5  $\mu\text{m}$ ; eluted with 80%/20%  $\text{Na}_2\text{HPO}_4$  0.01 M pH 9.3/ $\text{CH}_3\text{CN}$ ). The crude mixture was co-injected on HPLC with 10  $\mu\text{L}$  of 10  $\mu\text{g}/\text{mL}$  NMS-E973.

### 2.14. Biodistribution studies

The biodistribution of [ $^{11}\text{C}$ ]NMS-E973 was studied in healthy female Wistar rats (body mass 170-200 g) and healthy NMRI-mice (body mass 30-40 g). The animals were anesthetized with 2.5% isoflurane in  $\text{O}_2$  at a flow rate of 1 L/min and injected with  $\sim 18.5$  MBq (rats) or 5.5 MBq (mice) of tracer *via* a tail vein. The rodents were sacrificed by decapitation after 2, 10, 30 or 60 min p.i. ( $n = 3$  per time point). To assess Hsp90-specific binding in healthy tissue, NMRI-mice were injected intraperitoneally (i.p.) 45 min before tracer injection with either vehicle, NMS-E973 (25 mg/kg) or PU-H71 (50 mg/kg) dissolved in an aqueous solution of 5% DMSO and 40% (2-hydroxypropyl)- $\beta$ -cyclodextrin. Pre-treatment solutions were sterile filtered through a 0.22  $\mu\text{m}$  membrane filter (Millex-GV, Millipore). Blood and organs of interest were collected in tared tubes and weighed. The radioactivity in the different organs was counted in an automated gamma counter, as described above. For the calculation of the total radioactivity in blood, muscle and bone, the masses were assumed to be respectively 7%, 40% and 12% of the total body mass [258–260]. Data were expressed as percentage of injected dose (%ID) and standardized uptake value (SUV). %ID was calculated as (counts per min (cpm) in organ / total cpm recovered)  $\times$  100%. SUV was calculated as (radioactivity in cpm in organ / weight of organ in g) / (total cpm recovered / total body weight in g). Data are expressed as mean  $\pm$  SD;  $n = 3$  per time point. Of note, %ID of urine takes into account the excreted urine as well as the whole bladder.

### 2.15. Plasma radio-metabolite studies

Healthy male NMRI-mice were anesthetized with 2.5% isoflurane in  $\text{O}_2$  at a flow rate of 1 L/min and injected with about 11 MBq of the tracer *via* a tail vein. Mice were sacrificed by decapitation at 2, 10 or 30 min p.i. ( $n = 3$  per time point). Blood was collected in  $\text{K}_2\text{EDTA}$ -containing tubes (BD vacutainer, BD, Franklin Lakes, NJ, U.S.A.) and stored on ice. The blood was centrifuged for 10 min at (2330  $\times g$ ) to separate the plasma. Plasma (350  $\mu\text{L}$ ) was spiked with 20  $\mu\text{L}$  authentic reference compound (100  $\mu\text{g}/\text{mL}$  in DMSO), weighed and counted in a gamma counter. Subsequently,



individual plasma samples (300-350 µL) were analysed by RP-HPLC on a Chromolith RP C<sub>18</sub> column (3 mm × 100 mm, Merck, Darmstadt, Germany) eluted with gradient mixtures of CH<sub>3</sub>CN (A) and 0.05 M NaOAc pH 5.5 (B) (Table S1). After passing through an in-line UV detector (254 nm) coupled to a 3-inch NaI(Tl) scintillation detector connected to a single channel analyser, the HPLC eluent was collected in 1 mL fractions with 15 fractions in total per plasma sample, radioactivity was measured in an automated gamma counter.

### 2.16. Murine-grown tumour and muscle tissue slices

10×10<sup>6</sup> LNCaP, SKOV-3, or PC3 cells per mouse in 50% Matrigel (VWR, Radnor, U.S.A.) were subcutaneously inoculated into the right shoulder of 7–8-week-old BALB/c nu/nu mice (body mass 20-25 g) obtained from Janvier (La Genest-Saint Isle, France). The tumours were allowed to grow for 4-5 weeks until they reached ~0.5-0.75 cm<sup>3</sup> in size as determined using a caliper. 5×10<sup>5</sup> B16.F10 cells per mouse were implanted subcutaneously in the right dorsal flank of 8-week-old C57BL/6 mice (body mass 20-25 g). The tumours were allowed to grow for 10-15 days until they reached ~0.5-0.75 cm<sup>3</sup> in size as determined using a caliper. Subsequently, the mice were anesthetized with 2.5% isoflurane in O<sub>2</sub> at a flow rate of 1 L/min after which they were sacrificed by decapitation. Tumour or muscle tissue was excised, rinsed with saline to remove blood and rapidly frozen in 2-methylbutane (-40 °C). Next, 20 µm sections were obtained using a cryotome (Shandon cryotome FSE; Thermo Fisher, Waltham, MA) and these were mounted on adhesive microscope slides (Superfrost Plus; Thermo Fisher Scientific) and stored at -20 °C.

### 2.17. *In vitro* autoradiography of tumour, muscle and myocardium tissue slices

Frozen slices were air-dried and preincubated in PBS for 10 min at room temperature. After drying, the slices were incubated with 74 kBq/mL of the tracer in 200-250 µL PBS + 0.3% BSA per section for 10 min at room temperature. To assess binding specificity, slices were incubated with 74 kBq/mL of tracer (200-250 µL PBS + 0.3% BSA) in the presence of DMSO (10%) or 100 µM of either authentic NMS-E973, PU-H71, Ganetespib, PU-WS13 or Hsp70 inhibitor Pifithrin-µ in DMSO (10%). Incubation solutions were removed, after which the tumour slices were washed twice for 5 min in PBS + 0.3% BSA at 4 °C with a final washing step encompassing a quick dip in water at 4 °C, after which the slices were dried. Autoradiograms were obtained by exposing the slices to a phosphor storage screen (super-resolution screen; Perkin Elmer, Waltham, MA) overnight. The screens were read using a Cyclone Plus system (Perkin Elmer) and the images were analysed using Optiquant software (Perkin Elmer). Results are expressed as digital light units per square mm (DLU/mm<sup>2</sup>). Percentage block vs control was calculated as (DLU/mm<sup>2</sup> in the presence of 100 µM blocker) / (DLU/mm<sup>2</sup> tracer only) on 3-4 tissue sections from the same experiment.

### 2.18. *Ex vivo* autoradiography of B16.F10 melanoma, heart and muscle tissue

A B16.F10 melanoma-inoculated mouse, generated as mentioned above, and a healthy C57BL/6 mouse were injected with 4.5-5.5 MBq of [<sup>11</sup>C]NMS-E973. After 30 min, an overdose of pentobarbital (200 mg/kg i.p. Doléthal, Vetoquinol N.V. Aartselaar, Belgium) was administered followed by perfusion with saline *via* the left ventricle, followed by

opening of the right atrium, until the liver turned pale. Organs of interest were quickly excised and snap frozen in 2-methylbutane (-40 °C). Next, 60 µm sections were obtained using a cryotome (Shandon cryotome FSE; Thermo Fisher, Waltham, MA) and these were mounted on adhesive microscope slides (Superfrost Plus; Thermo Fisher Scientific) after which they were exposed to a phosphor storage screen (super-resolution screen; Perkin Elmer, Waltham, MA) overnight. The remaining excised tissue was further sectioned in 20 µm slices and stored at -20 °C.

### **2.19. Cell binding studies**

B16.F10 melanoma cells were seeded (200,000 cells/well) in 24-well plates and incubated at 37 °C for 24 h in the presence of 5% CO<sub>2</sub>. After washing with PBS, the cells were incubated with 555 kBq of [<sup>11</sup>C]NMS-E973 dissolved in DMEM in the presence of 2% DMSO, or 200 µM of NMS-E973, PU-H71 or Pifithrin-µ dissolved in DMSO (2%) for 60 min at 37 °C and 5% CO<sub>2</sub>. After incubation, cells were washed three consecutive times with 250 µL of ice-cold PBS. The cells were then incubated twice with 500 µL glycine-HCl in PBS (50 mM, pH 2.8) for 5 min at room temperature to remove radioactivity bound to the cell surface. Cells were washed again three consecutive times with ice-cold PBS and subsequently lysed using 250 µL of lysis buffer (reagent A100, Chemometec, Allerød, Denmark). After 5 min incubation, 250 µL neutralization buffer (reagent B, Chemometec, Allerød, Denmark) was added to quench the lysing of the cells. Glycine wash and lysed fractions were collected and radioactivity was counted with an automated gamma counter. The number of cells per well was counted using an automated counting device (NucleoCounter® NC-200™, Chemometec). Results were expressed as percentage of applied radioactivity bound to 1×10<sup>6</sup> cells. Radiotracer experiments with live cells potentially allow for quantification of Hsp90-specific binding in extracellular and intracellular compartments. We initially tried to quantify the eHsp90-bound fraction by applying an acidic glycine wash [272] but in subsequent autoradiography experiments we observed that the acidic wash did not result in complete dissociation of [<sup>11</sup>C]NMS-E973 from tissue slices and hence we only used total cell binding data in this study.

### **2.20. µPET imaging studies on B16.F10-inoculated C57BL/6 mice**

Ten days after inoculation, mouse (n = 3) whole-body PET scans were acquired on 3 consecutive days using a FOCUS™ 220 µPET scanner (Concorde Microsystems, Knoxville, U.S.A.). Before the start of the PET scan, mice were anesthetized using 2.5% isoflurane in oxygen (2 L/min) and kept under anaesthesia during the entire scan period. The experimental setup is presented in **Table 1**. At day one and three, mice were pre-treated i.p. 45 min before tracer injection with either vehicle (day 1-1) or PU-H71 (50 mg/kg) (day 3-1) dissolved in an aqueous solution of 5% DMSO and 40% (2-hydroxypropyl)-β-cyclodextrin. A similar study was conducted comparing vehicle-pre-treated mice (n = 4-6) with Ganetespib (50 mg/kg) dissolved in the same vehicle (**Table 1**, day 1-2, 2-2) Pre-treatment solutions were filtered through a 0.22 µm membrane filter (Millex-GV, Millipore). Immediately after intravenous (i.v.) injection of 11 MBq [<sup>11</sup>C]NMS-E973 *via* a tail vein, mice were scanned dynamically for a duration of 90 min. Following day 1-1 scans, the mice (n = 3) were subjected to an overnight fasted state with only access to water. Following the abstinence period (day 2-1), mice were anesthetized using 2.5% isoflurane in oxygen (2 L/min) and injected i.p. with 11 MBq 2-

[<sup>18</sup>F]fluoro-2-deoxy-D-glucose ([<sup>18</sup>F]FDG). The mice were allowed to recover consciousness during the uptake period of [<sup>18</sup>F]FDG. 60 min p.i. mice were anesthetized (2.5% isoflurane in oxygen 2 L/min) and submitted to a 10-min static PET scan. Acquisition data of the dynamic scans were Fourier rebinned in 24 time frames (4 × 15 s, 4 × 60 s, 5 × 180 s, 8 × 300 s, 3 × 600 s). Time activity curves (TACs) of the tumours were generated using PMOD software (v3.3, PMOD Technologies, Zürich, Switzerland).

**Table 1:** Experimental setup of  $\mu$ PET imaging studies of B16.F10-inoculated C57BL/6 mice.

Day	Number of animals	Tracer	Experiment	Route of administration	Blocking 45 min pre tracer injection	Type of scan	Duration of scan
1-1	3	[ <sup>11</sup> C]NMS-E973	Baseline	i.v.	Vehicle	Dynamic	0-90 min
2-1	3	[ <sup>18</sup> F]FDG	Baseline	i.p.	/	Static	10 min, 60-70 min p.i.
3-1	3	[ <sup>11</sup> C]NMS-E973	Block	i.v.	PU-H71 (50 mg/kg)	Dynamic	0-90 min
1-2	4	[ <sup>11</sup> C]NMS-E973	Baseline	i.v.	Vehicle	Dynamic	0-90 min
2-2	6	[ <sup>11</sup> C]NMS-E973	Block	i.v.	Ganetespiib (50 mg/kg)	Dynamic	0-90 min

### 3. RESULTS

#### 3.1. Biochemical characterization of Hsp90, Hsp70 and AKT protein expression in a panel of established cancer cell lines

We selected 6 established cancer cell lines of different origin including breast (MCF-7, MDA-MB-415 and BT-474), ovarian (OVCAR-3), prostate (PC3) and murine melanoma (B16.F10). By performing immunofluorescent staining analysis and subsequent high-content imaging analysis, endogenous protein expression of Hsp90, Hsp70 and AKT in all these lines was characterized. AKT, a client protein of Hsp90, was included as its stability is dependent on Hsp90. Additionally, extracellular expression of Hsp90 was determined by employing a non-permeabilization staining method. While permeabilization lead to a more diffuse staining of Hsp90 throughout the whole cell including the nucleus, non-permeabilization resulted in diffuse membrane staining and excluded nucleus staining. Hsp90 is thus expressed on the cell membrane, in the cytoplasm and in the nucleus. We observed different expression levels of Hsp70, eHsp90 and AKT throughout these cell lines (**Figure 2**).

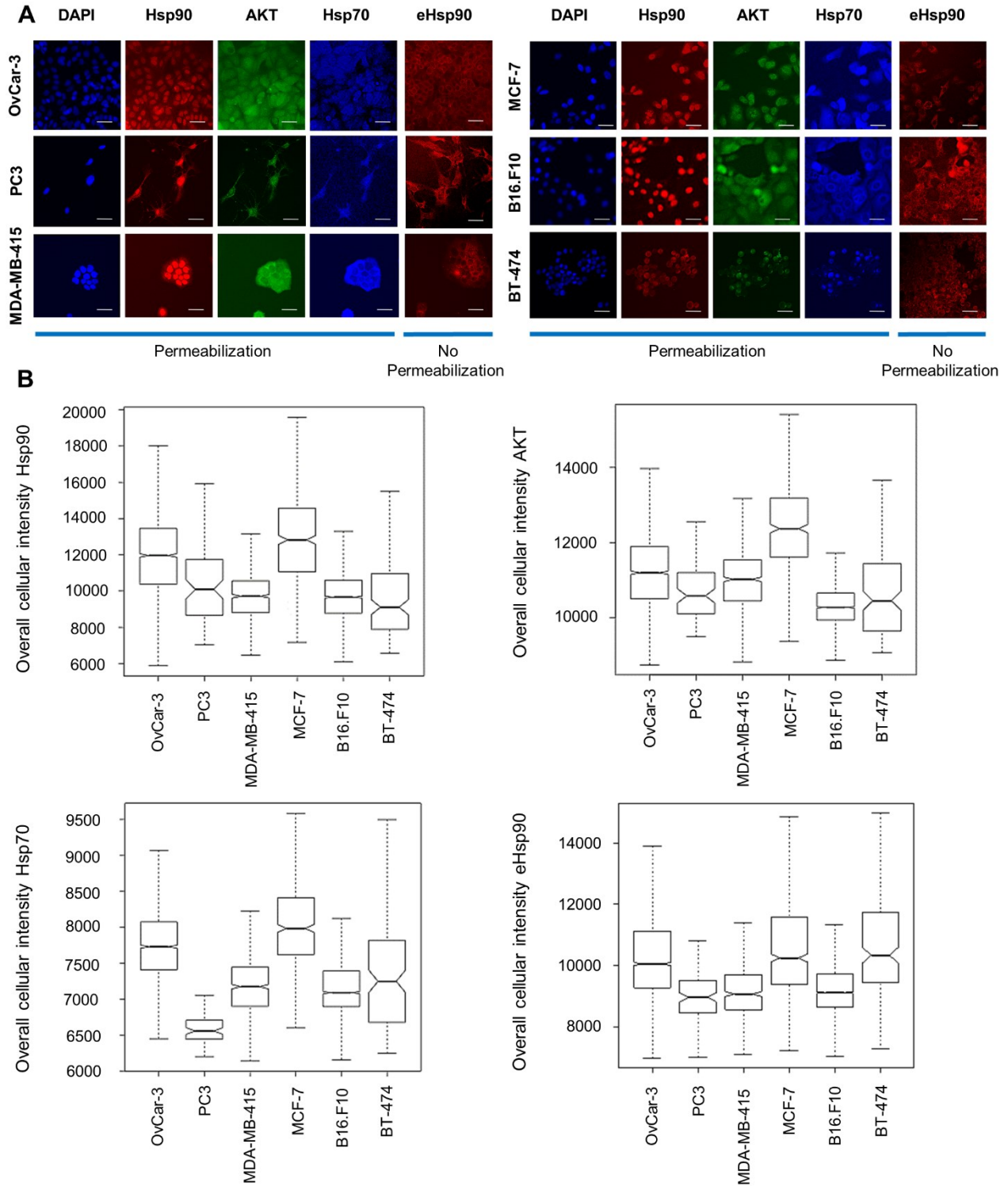


**Figure 2: Immunocytochemical staining and protein expression levels of Hsp70, Hsp90 and AKT in different cancer cell lines. A)** Immunofluorescent staining of cellular baseline Hsp90, AKT, Hsp70 and eHsp90 protein in different cell lines with DAPI as reference nuclear staining. Scale bar, 100  $\mu$ m. **B)** Immunofluorescence intensity measurements by high-content imaging represented as boxplots. Boxplots represent the median of  $n > 1000$  cells.

### 3.2. *In vitro* biochemical characterization of NMS-E973 vs Ganetespib activity in cancer cell

#### lines

Throughout this study, Ganetespib was used as a positive control for Hsp90 inhibition and its activity is compared with that of NMS-E973. Therefore, IC<sub>50</sub> values were determined for NMS-E973 and Ganetespib after 24 h incubation in all cell lines by a dose dependence response assay and subsequent nuclei counting by high-content imaging analysis (**Table 2**). Inhibition of Hsp90 by NMS-E973 or Ganetespib lead to fast and significant reduction in the number of cells after 24 h in most lines, with the exception of the MCF-7 cell line, which shows a stronger resistance to both drugs and probably needs a longer incubation time to see significant cell death. Similarly, the IC<sub>50</sub> of PU-H71 in B16.F10 cells was determined to be 108 ± 86 nM.

**Table 2:** IC<sub>50</sub> determination of NMS-E973 and Ganetespib.

Cell line	IC <sub>50</sub> NMS-E973 (nM) ± SD	IC <sub>50</sub> Ganetespib (nM) ± SD
MCF-7	∞	∞
MDA-MB-415	174 ± 10	24 ± 9
BT-474	276 ± 25	412 ± 19
B16.F10	454 ± 35	321 ± 47
PC3	48 ± 21	138 ± 42
OvCar-3	677 ± 41	279 ± 39

As Hsp90 regulates the expression and stabilization of a number of client proteins, including AKT, inhibition of Hsp90 results in downregulation of these proteins' expression levels. Likewise, Hsp70 is upregulated as a result of Hsp90 inhibition, due to induction of a cellular HSR [267]. High-content imaging analysis after staining shows that treatment of the cell lines at their IC<sub>50</sub> concentration for 16 h with Ganetespib or NMS-E973 resulted in significantly lower expression of AKT and upregulated Hsp70 response in comparison to vehicle-treated controls (**Figure 3**). When quantifying expression levels of Hsp90, we observed that total Hsp90 expression in cells was slightly but significantly down after both treatments. The intensity of total Hsp90 expression levels is on average higher than the eHsp90 staining levels due to the nucleus exclusion. The effect of NMS-E973 and Ganetespib on the expression of Hsp90 and eHsp90 in the B16.F10 melanoma cell line was further investigated (**Figure S2**). These data show that treatment with both inhibitors did not visibly change the phenotype of the cells. Additionally, cyclin-dependent kinase 1 (CDK1) expression was characterized by SDS/Western blot of the B16.F10 melanoma line. Inhibition of Hsp90 by NMS-E973 and Ganetespib was confirmed as the CDK1 signal was reduced by the treatment. As a protein loading control, the Hsp90-independent protein glyceraldehyde 3-phosphate dehydrogenase (GAPDH) was used. (**Figure S3**). In conclusion, NMS-E973 shows a potent *in vitro* cell Hsp90 inhibitory activity comparable to that of Ganetespib.

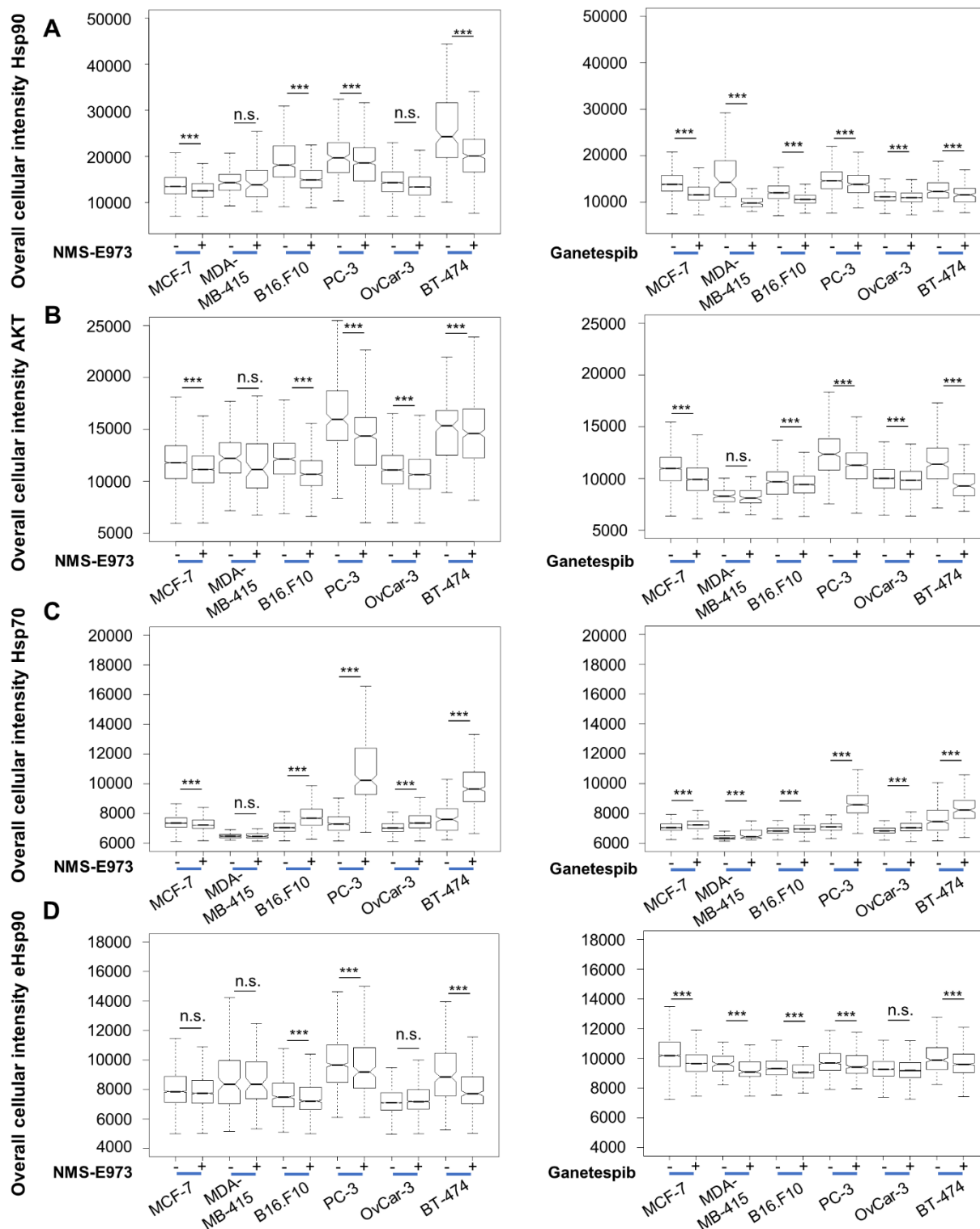


**Figure 3: Effect of NMS-E973 and Ganetespiib treatment on different cell lines.** Boxplot of high-content imaging results of Hsp90 A), AKT B), Hsp70 C) and eHsp90 D). Staining shows the effect on protein expression of overnight treatment with NMS-E973 or Ganetespiib, indicating the Hsp90 inhibitory activity of the compounds. Boxplots are of three independent experimental repeats with the number of cells analysed per condition > 1000 (\*\*\*)  $P < 0.001$ .

### 3.3. Biochemical characterization of Hsp90 protein expression in xenograft-derived tumour tissue

Hsp90 protein was biochemically characterized in both the B16.F10 melanoma cell line and corresponding derived xenograft tumour tissue by immunocytochemical and histofluorescent staining. Immunohistochemistry experiments were performed on tumour slices of xenograft-derived B16.F10 melanoma tissue, and diffuse Hsp90 staining patterns were observed that are comparable to the *in vitro* cell culture staining experiments (**Figure 4A**). Interestingly, healthy skin tissue and healthy muscle tissue were found to express low levels of Hsp90 in comparison to the melanoma tissue, indicating that Hsp90 is clearly upregulated in malignant tissue (**Figure 4B**). From these experiments, vast upregulation of Hsp90 expression in B16.F10 melanoma cells and tissue was confirmed.

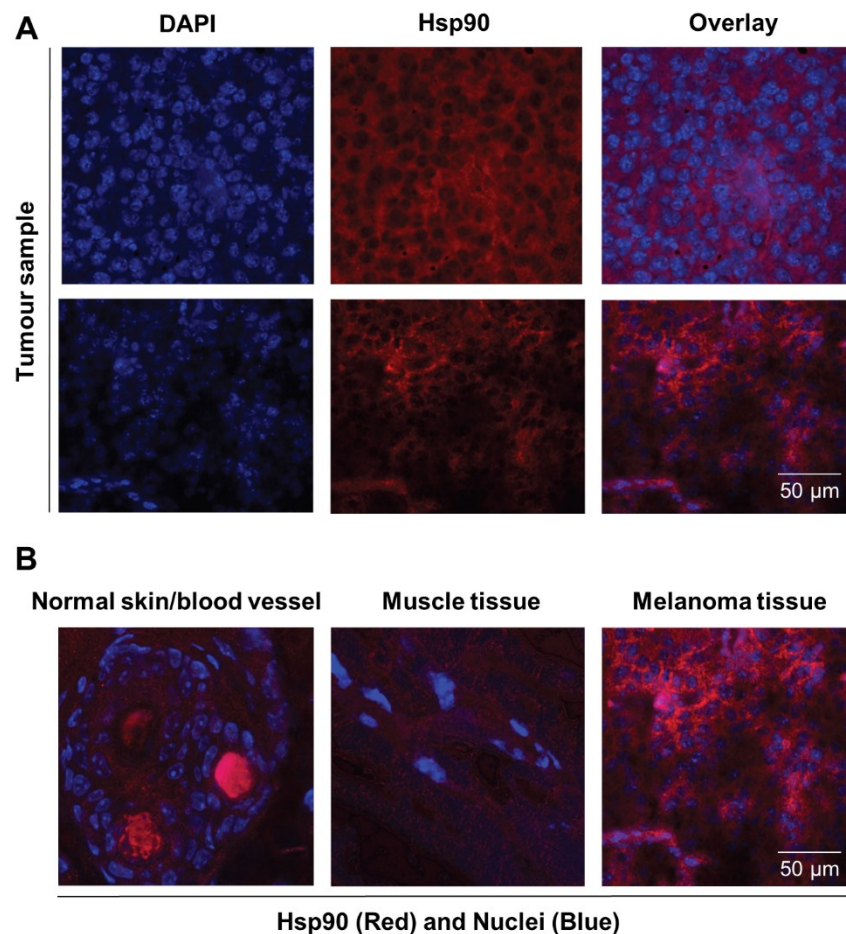


**Figure 4: Immunofluorescent staining of normal, healthy tissue and melanoma tissue. A)** Representative immunofluorescence images of tumour sections ( $n = 2$ ) stained for nuclei (DAPI, blue) and Hsp90 (Alexa 594, red) showing expression of Hsp90. Scale bar, 50  $\mu\text{m}$ . **B)** Immunofluorescence overlay images of nuclei (DAPI, blue) and Hsp90 (TexasRed, Red) staining showing that Hsp90 expression in skin and muscle tissue is low in comparison to that of malignant melanoma tissue. Strong red staining in blood vessels is caused by autofluorescence.

### 3.4. Radiosynthesis

Attempts to radiolabel the desmethyl radiolabeling precursor with  $[^{11}\text{C}]\text{CH}_3\text{I}$  or  $[^{11}\text{C}]\text{CH}_3\text{OTf}$  dissolved in Dimethylformamide (DMF) in the presence or absence of *N,N*-Diisopropylethylamine (DIPEA) were unsuccessful. However, successful radiochemical methylation was achieved by dissolving the precursor in anhydrous DMSO and reacting with  $[^{11}\text{C}]\text{CH}_3\text{I}$  in the presence of  $\text{Cs}_2\text{CO}_3$  (**Figure 5**). The reaction yielded 25-40% of the title compound relative to total recovered carbon-11 radioactivity on preparative HPLC. The title compound was easily purified by RP-HPLC to a radiochemical purity of >97% and a molar activity of  $\sim 85$  GBq/ $\mu\text{mol}$  at the end of synthesis (EOS) ( $n = 3$ ). A QC-chromatogram of  $[^{11}\text{C}]\text{NMS-E973}$  spiked with authentic reference compound NMS-E973 is depicted in **Figure S4**. Additional simulated labelling tests were performed to confirm methylation on the piperidine moiety (**Figures S5-S7**).

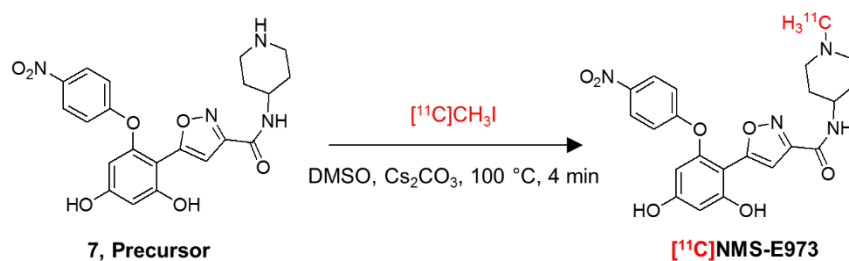


**Figure 5:** Radiosynthesis of  $[^{11}\text{C}]\text{NMS-E973}$ .

### 3.5. *In vitro* and *ex vivo* autoradiography

*In vitro* autoradiography experiments with  $[^{11}\text{C}]\text{NMS-E973}$  were conducted on sections of several different tumour tissues and compared to healthy murine muscle tissue. Regional binding heterogeneity of the tracer was observed in all tumour types (**Figure 6**). A tendency for higher radiotracer concentration at the edges of the tumour sections was noticed. To assess tracer Hsp90 binding specificity, tumour slices were incubated with  $[^{11}\text{C}]\text{NMS-E973}$  in the presence of 100  $\mu\text{M}$  NMS-E973, non-structurally related Hsp90 inhibitors PU-H71 and Ganetespib, the Hsp70 inhibitor Pifithrin- $\mu$ , or the Grp94 inhibitor PU-WS13. Tracer binding was quantified as DLU/ $\text{mm}^2$  in tumour tissues and compared to healthy muscle tissue. Blocking efficiencies are presented in **Table 3**. Co-incubation with Pifithrin- $\mu$  or PU-WS13 yielded no significant reduction in tracer binding to any of the studied tissues. Blocking with NMS-E973 (90% block), PU-H71 (82% block) and Ganetespib (85% block) was most effective in the PC3 tumour sections. The ovary carcinoma SKOV-3 showed similar potent blocking compared to the B16.F10 tumour sections. Roughly 75% of the tracer was blocked by incubation with NMS-E973 and approximately 60% with PU-H71 and Ganetespib. Incubation of muscle tissue resulted in significant tracer blocking that was, however, less pronounced compared to that of tumour tissue.



To study the difference between *in vitro* and *in vivo* tracer binding, an *ex vivo* autoradiography experiment was set up where uptake and distribution of the tracer was compared in tissues of a B16.F10 melanoma inoculated mouse. Sections of the organs of interest (tumour, heart and muscle) were further used on the following day (after decay of the injected carbon-11 activity) in an *in vitro* autoradiography study. Similar to the previous study, higher tracer binding to the outer edges of the sections was observed in the *in vitro* autoradiography for all the studied tissues, whereas *ex vivo* studies show a more homogenous distribution of the tracer. Furthermore, muscle tissue radioactivity concentration is clearly lower compared to that of myocardium and tumour tissue in *ex vivo* autoradiography; similar radioactivity concentrations were observed in *in vitro* autoradiography experiments of the same tissues.

In addition, the tissue radioactivity distribution pattern is remarkably different between *ex vivo* autoradiography (relatively homogeneous) and *in vitro* autoradiography (higher concentration at the outer edges of the section) for identical tissues.

**Table 3:** Percentage blocking of tracer binding in the presence of different Hsp90 inhibitors in several tumour types.

Tissue	Compound	% Block + SD <sup>a</sup>	Tissue	Compound	% Block + SD <sup>a</sup>
<b>PC3</b>	NMS-E973	90 ± 1 <sup>***</sup>	<b>B16.F10</b>	NMS-E973	74 ± 3 <sup>***</sup>
	PU-H71	84 ± 2 <sup>***</sup>		PU-H71	57 ± 3 <sup>***</sup>
	Ganetespib	85 ± 2 <sup>***</sup>		Ganetespib	59 ± 3 <sup>***</sup>
	PU-WS13	No block		PU-WS13	No block
	Pifitrhin-μ	No block		Pifitrhin-μ	No block
<b>SKOV-3</b>	NMS-E973	73 ± 9 <sup>***</sup>	<b>Muscle</b>	NMS-E973	74 ± 3 <sup>***</sup>
	PU-H71	55 ± 7 <sup>***</sup>		PU-H71	57 ± 3 <sup>***</sup>
	Ganetespib	62 ± 5 <sup>***</sup>		Ganetespib	59 ± 3 <sup>***</sup>
	PU-WS13	No block		PU-WS13	No block
	Pifitrhin-μ	No block		Pifitrhin-μ	No block
<b>LNCaP</b>	NMS-E973	63 ± 4 <sup>***</sup>			
	PU-H71	51 ± 5 <sup>***</sup>			
	Pifitrhin-μ	11 ± 14 <sup>n.s.</sup>			

<sup>a</sup> Calculated as (average DLU/mm<sup>2</sup> in tissue slice in the presence of 100 μM blocker) / (average DLU/mm<sup>2</sup> in tissue slice tracer only), \*\*\*P ≤ 0.001, n.s. = not significant. SD values are of 3-4 different slices from the same experiment.

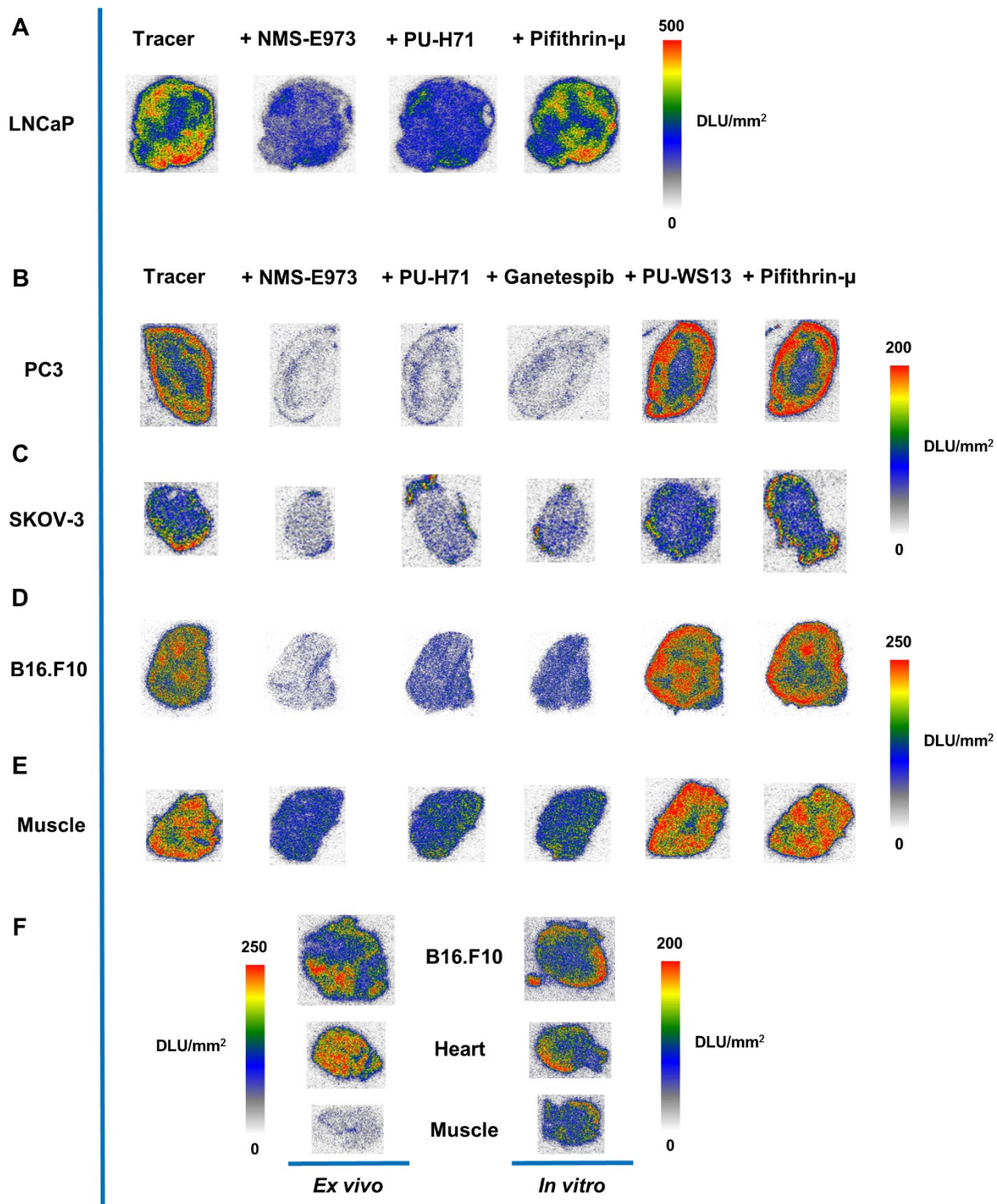


**Figure 6: Autoradiography studies.** *In vitro* autoradiography of **A)** LNCaP, **B)** PC3, **C)** SKOV-3, **D)** B16.F10 melanoma, and **E)** murine muscle tissue. Slices were incubated with tracer, tracer + NMS-E973, tracer + PU-H71, tracer + Pifithrin- $\mu$ , tracer + Ganetespib, tracer + PU-WS13, or tracer + Pifithrin- $\mu$  at 74 kBq/mL of [<sup>11</sup>C]NMS-E973 per slice and 100  $\mu$ M of blocking agents. **F)** *Ex vivo* vs *in vitro* autoradiography. Tissue was acquired from the same B16.F10 melanoma-bearing mouse. Intensity is depicted as DLU/mm<sup>2</sup>. n = 3-4 sections per group.

### 3.6. Cell binding studies

To study binding of [<sup>11</sup>C]NMS-E973 to Hsp90 in live cells, a cell binding study was performed on B16.F10 melanoma cells (**Figure 7**). The reduction of [<sup>11</sup>C]NMS-E973 cell binding in the presence of 200 μM PU-H71 (83%) was higher than that in the presence of 200 μM NMS-E973 (61%). The Hsp70 inhibitor Pifithrin-μ was used as a negative control for the blocking studies. A significant increase ( $P \leq 0.001$ ) in total binding (+21%) compared to that of control conditions was observed, suggesting increased Hsp90 expression resulting from Hsp70 inhibition.

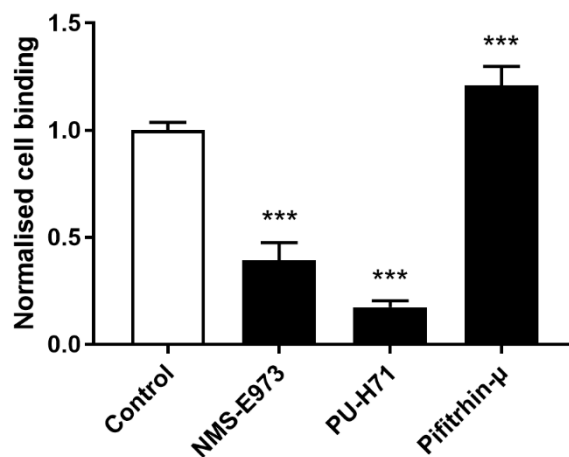


**Figure 7: Cell binding of [<sup>11</sup>C]NMS-E973 to B16.F10 melanoma cells.** Specific cell binding was assessed by blocking with NMS-E973, PU-H71 or Pifithrin-μ (200 μM) at 37 °C. Values are expressed as percentage of applied radioactivity bound to 1×10<sup>6</sup> cells normalised to the value for control cells. Data are expressed as mean ± SD (n = 3). Significance is calculated as control vs blocking (\*\*\*P ≤ 0.001).

### 3.7. Biodistribution studies and plasma radio-metabolite study

The biodistribution of [<sup>11</sup>C]NMS-E973 was studied in healthy female Wistar rats and healthy male NMRI-mice (**Tables S2-S3**). [<sup>11</sup>C]NMS-E973 was cleared from the plasma predominantly by the hepatobiliary system combined with a smaller fraction of renal clearance. Only limited brain and testes uptake (< 0.1 %ID) of the tracer was observed. The amount of intact tracer in the plasma was determined in male NMRI-mice at 2, 10 and 30 min p.i. At least 72% of recovered radioactivity corresponded to intact tracer at 30 min post tracer injection. The detected radio-metabolite was more polar than the title compound at all time points examined (**Figure S8**).

To assess tracer binding in healthy tissue, pre-treatment studies with NMS-E973 (25 mg/kg) and PU-H71 (50 mg/kg) were conducted in NMRI-mice. Mice were sacrificed 10 min after tracer injection. Data are expressed as %ID and SUV (**Table S4**). When comparing the vehicle-pre-treated and inhibitor-injected animals, only limited displacement of radioactivity in the organs of interest was observed. Significant blockage of tracer binding was seen after pre-

treatment with NMS-E973, but only in the lungs and blood. PU-H71 pre-treatment yielded no significant displacement, however, a shift of radioactivity from the hepatobiliary circuit to the blood occurred, suggesting slower hepatobiliary plasma clearance.

Additional biodistribution studies were performed 60 min after tracer injection on B16.F10 melanoma-inoculated tumour mice pre-treated with vehicle ( $n = 3$ ), PU-H71 (50 mg/kg, i.p.,  $n = 4$ ) or Ganetespib (50 mg/kg, i.p.,  $n = 3$ ). Data are shown in **Table S5**. A significant decrease in tumour uptake was observed after blocking with either PU-H71 or Ganetespib. A decrease in blood radioactivity was also observed after pre-treatment with PU-H71 and Ganetespib. Tumour/muscle SUV ratios are respectively,  $2.4 \pm 0.9$  in control conditions,  $1.2 \pm 0.2$  for blocking with PU-H71 and  $1.1 \pm 0.2$  for Ganetespib blocking.

### 3.8. $\mu$ PET studies in B16.F10-inoculated C57BL/6 mice

**Figure 8** shows the results of  $\mu$ PET studies conducted in C57BL/6 mice inoculated with B16.F10 melanoma cells. Mice were scanned on consecutive days and time-activity curves are shown as mean SUV  $\pm$  SD (**Figure 8F-G**). The averaged images of the baseline scan (0-90 min p.i., **Figure 8A-D**) revealed tumour-specific uptake of radioactivity, indicated by a high tumour-to-background contrast. TACs of baseline scans on separate days show highly reproducible tumour uptake of the tracer (**Figure 8F-G**). Tumour uptake of [ $^{11}\text{C}$ ]NMS-E973 was significantly blocked by pre-treatment with either PU-H71 or Ganetespib (averaged SUV<sub>0-90min</sub>  $P \leq 0.001$ ) whereas no blocking effect was observed in muscle tissue (averaged SUV<sub>0-90min</sub> n.s.) (**Figure 8B, E, F-G**), in line with the results of the B16.F10 melanoma-inoculated tumour mice biodistribution blocking study. Consistent with the *ex vivo* biodistribution (**Table S5**), both hepatobiliary and renal tracer clearance were observed.  $\mu$ PET studies also confirmed limited (if any) activity passing through the blood-brain barrier (BBB). High tumour-to-background contrast was observed in mice injected with [ $^{18}\text{F}$ ]FDG and subjected to a 10 min static scan (60-70 min after tracer injection). The distribution of radioactivity in the tumour suggests a highly active tumour with limited necrosis (**Figure 8C**).

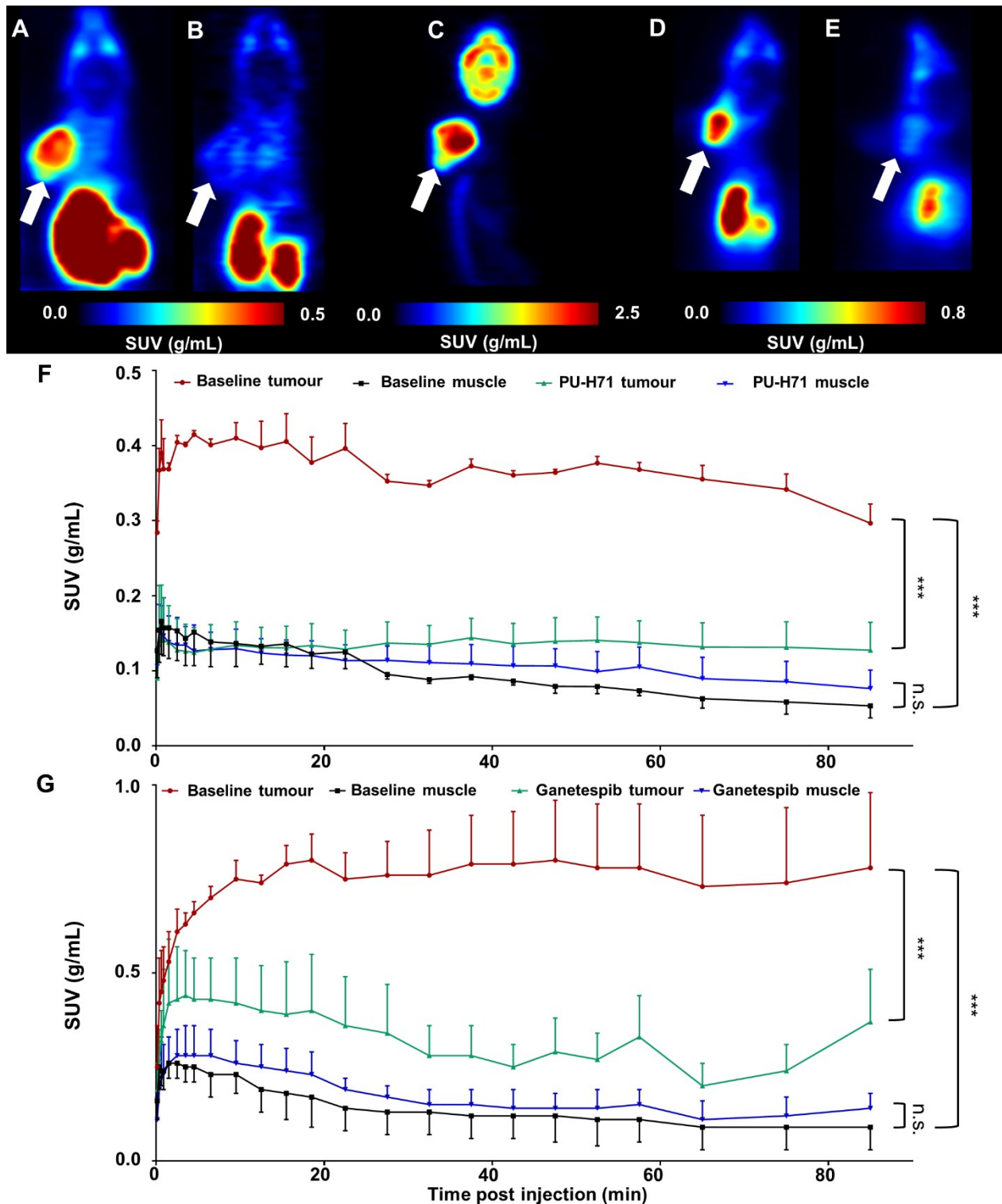


**Figure 8: Whole-body coronal  $\mu$ PET imaging of C57BL/6 mice inoculated with B16.F10 melanoma. A) Averaged baseline image of 90-min dynamic scan after injection of [<sup>11</sup>C]NMS-E973. B) Averaged image of 90-min dynamic scan after blocking with 50 mg/kg PU-H71 administered i.p. 45 min before [<sup>11</sup>C]NMS-E973 injection. C)  $\mu$ PET image derived from a 10-min static scan (60-70 min p.i.) after i.p. injection of 11 MBq of [<sup>18</sup>F]FDG. D) Averaged baseline image of 90-min dynamic scan after injection of [<sup>11</sup>C]NMS-E973. E) Averaged image of 90-min dynamic scan after blocking with 50 mg/kg Ganetespib administered i.p. 45 min before [<sup>11</sup>C]NMS-E973 injection. (A-E) White arrows indicate tumour site. F) Averaged TACs derived from baseline (red, tumour uptake; black,**

muscle uptake) and PU-H71 blocking (green, tumour uptake; blue, muscle uptake) studies (n = 3). **G**) Averaged TACs derived from baseline (red, tumour uptake; black, muscle uptake) and Ganetespib blocking (green, tumour uptake; blue, muscle uptake) studies (n = 4-6). Significance calculated on averaged  $SUV_{0-90 \text{ min}}$  of control vs blocking, (\*\*\*)  $P \leq 0.001$ , n.s. = not significant).

## 4. DISCUSSION

Hsp90 and its extracellular counterpart eHsp90 have gained attention as detrimental regulators of cancer maintenance in several tumour types, contributing to cell motility, invasion and metastasis [273]. Over 15 Hsp90 inhibitors are being evaluated in clinical trials [274]. Uncertainty about optimal treatment regimens remain and possible side effects such as reversible night blindness and gastrointestinal problems still occur [132]. Hence, elucidation of the optimal therapeutic potential of Hsp90 inhibitors is required. In an attempt to reveal the effect of Hsp90 inhibition on the downstream pathway, researchers have focused on imaging client proteins or regulated pathways after Hsp90 inhibition. In two separate studies, [ $^{18}\text{F}$ ]FDG was used in combination with Hsp90 inhibitors Retaspimycin HCl (IPI-504) or BIIB021 in patients with metastatic gastrointestinal stromal tumours. Reduced uptake of [ $^{18}\text{F}$ ]FDG was observed after treatment, implying metabolic changes in the tumour cells resulting from Hsp90 inhibitor treatment [203,204]. In another PET study, anti-EGFR antibody Cetuximab was radiolabelled with Iodine-124 to assess the efficacy of Hsp90 inhibitor Onalespib in mice xenografts of head-and-neck squamous cell carcinoma. Reduced uptake of radiolabelled antibody was observed in mice treated with Onalespib, implying a decreased expression of Hsp90 client protein EGFR [201]. [ $^{89}\text{Zr}$ ]Trastuzumab and [ $^{89}\text{Zr}$ ]Bevacizumab have been used to evaluate the effect of Hsp90 inhibitor Luminespib in, respectively, Human epidermal growth factor receptor 2 (HER2)-positive and estrogen receptor-positive metastatic breast cancer patients [205]. The use of Hsp90 as a PET biomarker could be key to understanding the role played by Hsp90 in health and disease and may enable rational optimisation of Hsp90 inhibitor administration regimens by quantification of tumour Hsp90 occupancy after Hsp90 inhibitor treatment. In this respect, we successfully radiolabelled and evaluated [ $^{11}\text{C}$ ]NMS-E973.

Extracellular Hsp90 is known to be expressed by highly active, metastatic tumours as is observed in several tumour lines ranging from breast cancer to melanomas [99,270]. Normal cells do not express eHsp90 except under conditions promoting cellular stress [273]. One example of eHsp90 appearance in healthy tissue has been observed in response to tissue damage and subsequent wound healing [275]. Translocation of Hsp90 to the cell surface or ECM occurs *via* an exosome trafficking pathway partially mediated by upstream regulators including p53 and hypoxia-inducible factor-1 $\alpha$  (HIF-1 $\alpha$ ) [101,276]. It was postulated that eHsp90 functions as a regulator of cell motility, angiogenesis and cell invasion processes in both malignant states and during tissue injury. Moreover eHsp90 is actively internalised by endocytic processes as shown in a study by Crowe *et al.* and it was suggested that this process occurs *via* multiple pathways [269]. In the same study, it was determined that many aggressive tumour cell lines actively internalise eHsp90 and this internalisation process was not influenced by fluorescent inhibitors targeting the ATP-binding pocket. Moreover, internalisation was inhibited using a C-terminal antibody [270].

We have characterized total and extracellular Hsp90 expressions in 6 cell lines *in vitro* using high-content screening (**Figure 2A-B**). High-content screening analysis is an imaging method to visualise, image and quantify protein expression levels in tumour cells, allowing analysis of a large number of cells in an automated manner. By subsequent quantification and morphometric analyses Hsp90, eHsp90, Hsp70 and AKT protein expression levels on a single cell level throughout different cell lines were quantified. All cell lines expressed eHsp90, some to a higher extent than other. Hsp90, Hsp70 and AKT are all expressed in the cytoplasm as well as in the nucleus in a diffuse manner. These cell lines thus provide a useful tool for compound activity analysis. We first determined the IC<sub>50</sub> for NMS-E973 and Ganetespib to determine treatment concentrations without excessive cell death. Next, we analysed protein expression levels upon treatment with NMS-E973 and compared its activity to Ganetespib as a control. When Hsp90 is functionally inhibited, client proteins such as AKT and CDK1 will fail to mature due to destabilized complex formation between client protein and chaperone, leading to increased ubiquitination and subsequent proteasomal degradation [12]. High-content imaging indeed showed a decrease in AKT expression in all the studied cell lines besides the MDA-MB-415 breast cancer line (where presumably a longer incubation time is needed) when incubated with inhibitors. Moreover, western blot studies indicated a significantly lowered expression of the Hsp90 client protein CDK1 (**Figure S3**) in the presence of Hsp90 inhibitors Ganetespib or NMS-E973. Furthermore, Hsp70 expression, which is induced *via* the heat shock response to compensate inhibited Hsp90 [88], was upregulated after treatment of cells with NMS-E973 (**Figure 3C**) or Ganetespib. The potency of NMS-E973 to affect Hsp90 function is thus in accordance with previous literature reports [207,267].

Experiments on B16.F10 melanoma cells (**Figure 7**) showed efficient blocking of [<sup>11</sup>C]NMS-E973 binding during co-incubation of the cells with NMS-E973 or PU-H71, indicating that cell binding is Hsp90 selective. PU-H71, a representative of the purine-bearing class of Hsp90 inhibitors, was chosen as a non-structurally related inhibitor and is known as an inhibitor of the epichaperome, a complex connectivity of Hsp90-Hsp70 and its co-chaperones [93,96]. Blocking with 200 μM PU-H71 was more efficient compared to 200 μM NMS-E973. Based on their respective *t*PSA and logD values, 151.20 Å<sup>2</sup> and 1.04 for NMS-E973 and 100.11 Å<sup>2</sup> and 0.70 for PU-H71, passive diffusion of NMS-E973 over the cell membrane may be more limited and exposure of the intracellular compartment to PU-H71 can be faster and more substantial, leading to higher blocking efficiency. Moreover, the IC<sub>50</sub> of NMS-E973 and PU-H71 were determined to be 454 nM and 108 nM, respectively, in the B16.F10 cell line, indicating a 4-fold higher activity of PU-H71 towards the B16.F10 melanoma cell line. Inhibition of Hsp70 with Pifithrin-μ, a p53 inhibitor with known activity against Hsp70 (IC<sub>50</sub> = 2.5-12.7 μM) [277], yielded a significant increase in tracer binding. Hsp70 is closely linked to Hsp90 and plays an important role in the Hsp90 machinery as a provider of client proteins [88]. Hsp90 inhibition induces Hsp70 transcription and upregulation [86,267] and Hsp70 ablation enhances Hsp90 inhibitor efficacy and induces apoptosis [278,279]. Inversely, it was reported that inhibition with Pifithrin-μ or knockdown of Hsp70 was unable to upregulate Hsp90 expression [280]. However, following the crosstalk and interplay between Hsp90 and Hsp70, high sensitivity detection of radioactivity by gamma counting can possibly enable quantification of the latter mechanism, mediated by an affinity increase rather than a change in expression. This may explain the increased total

binding of [<sup>11</sup>C]NMS-E973 in B16.F10 melanoma cells observed after co-incubation with Pifithrin- $\mu$  compared to the control conditions.

In an *in vitro* autoradiography experiment, slices of different tumour types were incubated with [<sup>11</sup>C]NMS-E973 in the presence or absence of 100  $\mu$ M NMS-E973, PU-H71, Ganetespib, PU-WS13 or Pifithrin- $\mu$ . Heterogeneous tracer distribution was observed and the border regions of the tumour sections showed the highest radioactivity concentration, which was particularly the case for the PC3 tissue (**Figure 6B**). The investigated tumours showed variable degrees of Hsp90-specific binding (**Table 3**) This may be attributed to the aggressiveness of the different tumour types as it was reported that tumours with higher metastatic potential had increased expression levels of eHsp90 and showed higher internalisation of the eHsp90 fluorescent probe HS-131 [269]. The highest Hsp90-specific binding was observed in the PC3 prostate cancer, which is described as a tumour with prominent metastatic potential [262] and high expression of Hsp90 and eHsp90 (**Figure 2**). Incubating the tumour sections in the presence of Ganetespib yielded similar results to blocking with PU-H71 in SKOV-3 and B16.F10 tissue. (**Figure 6C-D**). The androgen-dependent LNCaP and androgen-independent PC3 prostate carcinomas and SKOV-3 ovarian cancer are representatives of gonadal malignancies. Stabilisation and nuclear transfer of the agonist or antagonist-bound androgen receptor is mediated by Hsp90 [281]. It was observed that [<sup>11</sup>C]NMS-E973 shows Hsp90-specific binding to both PC3 and LNCaP tumour sections, independent of their reliance on the androgen receptor.

It has to be noted that most Hsp90 inhibitors are pan-selective, meaning that they exert activity against the different Hsp90 isoforms. PU-H71 has been determined to have a higher affinity, expressed as IC<sub>50</sub>, towards Grp94 (30 nM) compared to Hsp90 $\alpha$  (43 nM) [120]. Furthermore, Grp94 is known to be highly expressed in different kinds of cancers [282]. To discriminate [<sup>11</sup>C]NMS-E973 binding to Grp94 and Hsp90 $\alpha$ , PU-WS13, a purine-based Hsp90 inhibitor with highest potency towards Grp94 (EC<sub>50</sub> 220 nM) and 140-fold selectivity over Hsp90 $\alpha$  [283] was used as a blocking compound in an *in vitro* autoradiography experiment (**Figure 6**). No significant blocking in any of the studied tumour tissues (PC3, B16.F10, muscle) was observed. This further emphasizes the tracer specificity for Hsp90. Similar to the cell binding study, the Hsp70 inhibitor Pifithrin- $\mu$  was unable to challenge [<sup>11</sup>C]NMS-E973 in any of the investigated tissue sections.

We found intriguing differences when comparing *ex vivo* autoradiography (resulting from *in vivo* physiological tracer distribution) with *in vitro* autoradiography (tracer distribution on post mortem tissues) of adjacent sections of identical muscle, myocardium and tumour tissue samples. Higher tracer concentrations were observed at the edges of the tissue sections in *in vitro* autoradiography, whereas a more homogenous uptake was observed for *ex vivo* autoradiography. In addition, the tracer concentration was lower for skeletal muscle compared to myocardium and tumour tissue in *ex vivo* autoradiography experiments (in line with biodistribution results), whereas tracer concentration was comparable for the three studied tissues in the *in vitro* autoradiography experiments. We hypothesize that Hsp90 expression and/or affinity changes due to processes associated with sacrificing the animal



causing cell stress and cell death lead to the observed differences between *ex vivo* and *in vitro* autoradiography [284], but further studies will be required to examine this hypothesis.

*Ex vivo* biodistribution studies conducted on two rodent species (**Tables S2-S3**), indicated preferential hepatobiliary excretion of [<sup>11</sup>C]NMS-E973. This excretion can limit the detection of tumours in the abdominal region. Efforts can be made to develop more polar Hsp90 tracers that are mainly excreted *via* the renal tract. The plasma concentration of the tracer decreased steadily over time. The 2/60 min ratio of blood activity was similar for rats and mice; however, rat blood radioactivity levels (%ID) were twice as high as those of mice. More than 70% of radioactivity in mouse plasma corresponded to intact tracer at 30 min p.i. (**Figure S8**).

Biodistribution experiments on B16.F10 melanoma mice confirmed Hsp90-specific tumour binding as it could also be blocked by pre-treatment with either PU-H71 or Ganetespib. In addition, we also observed a blocking effect in blood and blood-rich organs (lungs, spleen), indicating Hsp90-specific binding that was not observed in healthy mice. This interesting observation may be related to tumour shedding of Hsp90 [54-55].

The literature reports ubiquitous and high (2% of total proteins) expression of Hsp90 in all cells. Based on an estimated average protein mass per unit of cell volume of 0.2 g/mL, we calculated the total mass of protein in a 2000 μm<sup>3</sup> cell to be 4×10<sup>-10</sup> g [287]. As Hsp90 comprises 2% of this mass, an estimated total density of receptors (B<sub>max</sub>) of 222 pmol/mg protein for HSP90 in unstressed conditions could be calculated, corresponding to 30 μM per tissue. In comparison, the well-known dopamine 2 receptor (D<sub>2</sub>R), which is efficiently visualised by [<sup>11</sup>C]Raclopride PET [159,288], has a B<sub>max</sub> in the striatum ranging from 290-360 fmol/mg protein. It is hence remarkable that generally low uptake of [<sup>11</sup>C]NMS-E973 is observed in *in vivo* healthy tissue. More so in an *in vivo* biodistribution study on healthy NMRI-mice, blocking with NMS-E973 or PU-H71 did not result in significant tracer concentration decrease in healthy tissues (**Table S4**).

Rats were included in the biodistribution studies to study the reported brain permeability of [<sup>11</sup>C]NMS-E973. However, in our study, [<sup>11</sup>C]NMS-E973 showed only limited, if any, brain uptake of the tracer (< 0.1 %ID) (**Tables S2-S3**) in 2 rodent species. It has been postulated that passive diffusion through the BBB occurs for compounds with a *t*PSA value under 90 Å<sup>2</sup> and a logD value ranging from 2.0 to 3.5 [161]. Calculated *t*PSA and LogD values for NMS-E973 (151.20 Å<sup>2</sup> and 1.04) are far from the assumed optimal *t*PSA and logD values that allow significant brain penetration. Moreover, μPET images (**Figure 8A, D**) confirm the low brain uptake of [<sup>11</sup>C]NMS-E973. Nevertheless NMS-E973 may still have an effect on intracranial tumours, such as glioma, as in these conditions the BBB may be damaged.

Tumour targeting of [<sup>11</sup>C]NMS-E973 was clearly established in μPET studies on C57BL/6 mice inoculated with B16.F10 melanoma cells. Hsp90 binding specificity of [<sup>11</sup>C]NMS-E973 was confirmed *in vivo* by pre-treatment studies with PU-H71 and Ganetespib. [<sup>11</sup>C]NMS-E973 tumour binding was significantly reduced throughout the whole scan period. When comparing [<sup>11</sup>C]NMS-E973 and [<sup>18</sup>F]FDG μPET, a similar intratumoural distribution of the tracer was observed.

The reason(s) for the specific tumour targeting of [<sup>11</sup>C]NMS-E973 still remain to be determined. Malignant cells have significantly increased Hsp90 levels but an increased affinity or relocalisation of Hsp90 from intracellular to more accessible surface-bound sites could also contribute to the increased tracer concentration in the tumour. Recent studies also suggest a role of the epichaperome, a network of different Hsps and their co-chaperones, as an important factor in cancer dynamics. The interplay and connectivity between Hsps and their co-chaperones determines the resistance to and effectiveness of Hsp90 inhibitors [96].

Our results suggest that [<sup>11</sup>C]NMS-E973 PET enables quantification of Hsp90 expression in tumours, possibly identifying patients that may respond to treatment with Hsp90 inhibitors. Furthermore, Hsp90 PET with [<sup>11</sup>C]NMS-E973 can potentially be used to quantify Hsp90 occupancy in tumours after treatment with Hsp90 inhibitors, contributing to rational optimisation of dose regimens for treatment of patients with Hsp90 inhibitors. However, to fully optimize its use as an occupancy measuring tool, translation to the clinic will be required. The limitations of this study are that visualisation of Hsp90 will be difficult in the abdominal region due to hepatobiliary and renal clearance of [<sup>11</sup>C]NMS-E973. Further, the tracer shows relatively low SUV values in the tumour, but this uptake was highly Hsp90 specific. Although carbon-11 has its advantages as it enables multiple injections each day, its half-life of 20.38 min limits its use in studies where steady-state conditions are required. A switch to a fluorine-18 compound can resolve this matter.

## 5. CONCLUSIONS

We efficiently radiolabelled and evaluated [<sup>11</sup>C]NMS-E973 *in vitro* and *in vivo* as an Hsp90-specific PET tracer. Evaluation of NMS-E973 confirmed its Hsp90 inhibitory activity. Cell binding studies in B16.F10 melanoma cells showed specific binding of [<sup>11</sup>C]NMS-E973. Biodistribution studies showed low brain uptake and preferential hepatobiliary clearance, and an absence of observable Hsp90-specific binding in healthy tissues. However, clear tumour binding that was blocked by pre-treatment with PU-H71 and Ganetespib was observed in *in vitro* and *in vivo* experiments. These pre-clinical results indicate that [<sup>11</sup>C]NMS-E973 PET can be used to quantify Hsp90 expression *in vivo* in tumours and may allow quantification of target occupancy after treatment with Hsp90-targeted drugs.

## CHAPTER V

---

### DEVELOPMENT OF [<sup>11</sup>C]YC-72-AB85 AS A PET PROBE FOR VISUALISATION OF HSP90 IN BRAIN AND CANCER

---

**Koen Vermeulen**<sup>1</sup>, Emmanuelle Briard<sup>2</sup>, Yves Auberson<sup>2</sup>, Joseph Schöfer<sup>2</sup>, Christopher Cawthorne<sup>3</sup> and Guy Bormans<sup>1</sup>

<sup>1</sup> Laboratory for Radiopharmaceutical Research, Department of Pharmaceutical and Pharmacological Sciences, KU Leuven, Leuven, Belgium

<sup>2</sup> Novartis, Basel, Switzerland

<sup>3</sup> Nuclear Medicine & Molecular Imaging & MoSAIC, Department of Imaging & Pathology KU Leuven, Leuven, Belgium



## Abstract

Hsp90 has been implicated in multiple life changing diseases including cancer and neurodegenerative disorders. Many Hsp90 inhibitors reached the stage of clinical evaluation. However, all of them are targeting cancer and promising results observed in preclinical trials on xenograft animal models could not be reproduced in the clinic. Different lines of research also focus on Hsp90 as a drug target for CNS disorders. The development of a suitable Hsp90 PET probe can provide *in vivo* quantification of the expression levels of Hsp90 as a biomarker for diagnosis and follow up of cancer and CNS progression. In addition, Hsp90 PET can be used to quantify target occupancy of new inhibitors targeting Hsp90. In this respect, [<sup>11</sup>C]YC-72-AB85 was developed and evaluated as an Hsp90 PET probe in B16.F10 melanoma bearing mice and its brain uptake was determined in rats.

**Materials and Methods:** *In vitro* binding of [<sup>11</sup>C]YC-72-AB85 to tissue slices of mouse B16.F10 melanoma, PC3 prostate carcinoma and rodent brain was evaluated using autoradiography. Biodistribution of [<sup>11</sup>C]YC-72-AB85 was evaluated in healthy and B16.F10 melanoma mice. *In vivo* brain uptake was assessed by  $\mu$ PET studies in rats.

**Results:** *In vitro* binding of [<sup>11</sup>C]YC-72-AB85 to brain and tumour cryosections was efficiently blocked by the presence of non-structurally related Hsp90 inhibitors, Onalespib and SNX-0723 indicating Hsp90-specific binding. Saturable Hsp90 binding in blood and blood rich organs was increased in tumour mice compared to control mice. *In vivo*, tumour/muscle ratios increased after blocking with YC-72-AB85 and Onalespib, indicating Hsp90-specific tracer binding. Only a limited fraction of radio-metabolites was observed in mice (8-15% polar metabolites 60 min p.i.) whereas in rats the fraction of radio-metabolites was higher (25% at 30 min p.i.). Pre-treatment with Onalespib (30 mg/kg i.p.) in rats doubled the tracer concentration in plasma and resulted in an increased brain uptake. In combined pre-treatment and displacement studies, reversible and specific binding of [<sup>11</sup>C]YC-72-AB85 was observed in rat brain as assessed by studies with Onalespib (30 mg/kg), YC-72-AB85 (2-5 mg/kg) and SNX-0723 (5-6 mg/kg).

**Conclusion:** [<sup>11</sup>C]YC-72-AB85 is a promising PET tracer for *in vivo* visualisation of Hsp90 in tumours and brain. Increased Hsp90-specific tracer binding in blood and blood-rich organs was observed in tumour mice vs control mice. Further studies in animal tumour models and fully quantitative PET studies with arterial sampling in rhesus monkeys are warranted.

## 1. INTRODUCTION

The molecular chaperone heat shock protein 90 kDa (Hsp90) interacts with a multitude of co-chaperones, other Hsps and cofactors and is part of a transient, dynamic complex, termed the chaperome. The Hsp90 sub-family is divided into constitutively expressed Hsp90 $\beta$ , inducible Hsp90 $\alpha$ , both residing primarily in cytosol, and 2 paralogues, 94 kDa glucose regulated protein (Grp94) and tumour necrosis factor receptor associated protein 1 (TRAP1) respectively found in the endoplasmic reticulum (ER) and mitochondria [289]. Hsp90 is ATP-dependent and together with the chaperone machinery, it stabilizes, matures and refolds misfolded proteins and regulates protein trafficking [290]. It has been found that Hsp90 is highly selective towards client proteins, as predominantly proteins that acquired near native state (tertiary structure) are recognised and processed [76]. Over 400 proteins are known to be processed by Hsp90 with major substrates encompassing kinases, transcription factors and hormone receptors [290].

The Hsp90 protein structure consists of an N-terminal domain (ND) which binds ATP, a middle domain (MD), important in substrate recognition and hydrolysis of ATP which further connects the ND to the C-terminal domain (CD). The CD functions as a recognition site for co-chaperones and initiates dimerization of two Hsp90 protomers, required for proper Hsp90 function [291]. Many (proto-)oncoproteins are Hsp90 client proteins, and depend on intervention of Hsps to reach their native conformation. Together with other Hsps such as Hsp70 and Hsp40, Hsp90 functions as a barrier against cellular stresses, and is thus abundantly expressed (2% of total cellular protein count) throughout all eukaryotic cells. Several cellular stressors such as reactive oxygen species, heat, gamma-irradiation but also pathological effectors can increase Hsp90 levels up to 10% of the total cellular protein count [80]. Transcriptional induction of Hsp90 is typically mediated by heat shock factor 1 (HSF1), the predominant regulator of the heat shock response (HSR) and itself a client protein of Hsp90 [292]. Furthermore, Hsp90 is actively secreted *via* an exosome dependent pathway to the cell membrane and extracellular matrix (ECM). Interestingly, this is only observed in malignant cells but not in untransformed cells, except in tissue damage and subsequent wound healing [275].

In cancer, different subsets of the chaperome are frequently found upregulated and the involvement of Hsps and its 90 kDa member herein has been well documented [293]. Overexpression of Hsp90 has been observed in a plethora of human cancers not limited to breast, ovary, prostate, head and neck, melanoma, hepatocarcinoma and hematopoietic carcinomas [289]. Induced by hypoxia-inducible factor-1 $\alpha$  (HIF-1 $\alpha$ ) or cytokines such as tumour growth factor- $\alpha$  (TGF- $\alpha$ ), extracellular Hsp90 (eHsp90), has been found to facilitate cell invasion and metastasis, where it interacts with metalloproteinase 2 (MMP2) or human epidermal growth factor receptor 2 (HER2) [100,104]. Moreover, cancer associated Hsp90 has been observed to occur in a 'stress state', which is abundantly (> 100-fold) more sensitive towards Hsp90 inhibitors [92]. Recent studies indicate that oncological Hsp90 is embedded in a multichaperone network, termed the epichaperome, a biochemically altered chaperome of predominantly Hsp90 and Hsp70 and their respective co-chaperones, designated for cell survival. Different degrees of chaperome members connectivity were observed in different cancer cells and 60-70% of the tested cell lines had medium to high levels of

epichaperome complexes. The degree of connectivity depends on the total cellular stress level, where increased connectivity or even hyperconnectivity of the different chaperome members is often observed in chronic stress situations, such as cancer [93,96].

Hsp90 is expressed in all neurons but only limited expression was observed in glial cells [107]. Hsp90 $\alpha$ - $\beta$  have been found to localise on the cell surface of developing central nervous system (CNS) cells, where it aids cell migration, as assessed in rat brain. Further, Hsp90 is upregulated in Schwann cells after sciatic nerve damage, where it regulates cytoskeleton reorganization important for post trauma lamellipodia formation [108]. Hsp90 has also been observed to regulate  $\alpha$ -amino-3-hydroxy-5-methyl-4-isoxazolepropionic acid (AMPA) receptor trafficking where it is important in delivery of AMPA receptors to synapses and synaptic cycling of the receptor [294]. Hsp90 also has been implied as a regulator of membrane deformation and exosome release [295]. Neurodegenerative diseases are in essence proteinopathies [296], a disease state where a continuous strain is put on the cells of the CNS by abundantly expressed and misfolded proteins. A major factor in the propagation of these diseases is aging as here protein quality control is diminished [110]. Cellular insults, mediated by misfolded or aggregated proteins induce a broad range of counteracting, cytoprotective pathways as observed in Alzheimer's disease (AD), Parkinson's disease (PD) and Huntington's disease (HD) [297]. Molecular chaperones are able to diminish aggregation of misfolded proteins, processing them for degradation by the proteasome [298]. Upregulation of Hsp90 in CNS disorders has been reported to occur similarly to cancer pathology [297]. Induction of Hsp90 in the CNS stabilizes defective proteins, preventing their degradation by the proteasome, but increasing their aggregation propensity. Furthermore, in human pluripotent stem cell derived midbrain dopaminergic neurons, a shift of Hsp90 to a stress state was observed, as well as a change of chaperome interaction strength [95]. Abrogation of Hsp90 induces a compensatory HSR and leads to subsequent elevated levels of cytoprotective chaperones, Hsp40 and Hsp70 [299]. In PD, Hsp90 was observed to co-localize with  $\alpha$ -synuclein filaments of Lewy bodies in brain slices of PD patients [113]. Furthermore, it was observed that Hsp90 inhibition, rescued striatal dopamine levels in rats, but not in neurons already affected by  $\alpha$ -synuclein deposition [300]. In a study conducted on the rTg4510 AD mouse model, which overexpresses the microtubule associated protein Tau (also a client protein of Hsp90), occupancy of Hsp90 with the Hsp90 inhibitor HSP990, was correlated with induction of Hsp70. In this mouse model, inhibition of Hsp90 normalised synaptic function, as assessed by measuring synaptic plasticity mediated paired-pulse facilitation [86]. Hsp90 also indirectly elevates hyperphosphorylated tau levels by chaperoning of kinases such as cyclin-dependent protein kinase 5 (CDK5) and glycogen synthase kinase-3 beta (GSK3 $\beta$ ) [299]. Both mutant and wild type Huntingtin are client proteins of Hsp90. Decreasing Hsp90 proteins levels reduced the expression of HD phenotypes and disease progression [301]. Interestingly, increased levels of Hsp90 were also observed in the hippocampus of epileptic patients [302].

Over 15 small molecule inhibitors of Hsp90 have been evaluated in clinical trials, all of them are competitive inhibitors of the ATP binding domain. These studies mainly target Hsp90 in different cancers (melanoma, breast cancer, ovarian cancer, head and neck cancer, gastrointestinal cancer, prostate cancer and others) [274]. Although generally well

tolerated, revolutionary clinical breakthroughs as observed in preclinical tumour xenograft rodent models, have yet to be observed [194]. Also, the compensatory HSR, mediated by HSF1 and induced by Hsp90 inhibition limits the effectiveness of anti-Hsp90 therapy. Development of CD inhibitors or treatment with combination therapy, targeting other members of the chaperome, can offer relief [303]. Further, disruption of Hsp90/co-chaperone engagement is less prone to activate HSF1 and can be an applicable strategy [292].

Interesting results in CNS disorders were obtained with two Hsp90 inhibitors. SNX-0723 (**Figure 1**) was used in a study aiming to treat a PD mouse model, where brain uptake was demonstrated *via* induction of brain Hsp70. Further, treatment of cells with SNX-0723 decreased  $\alpha$ -synuclein oligomerization and ameliorated  $\alpha$ -synuclein induced toxicity in a rat model of PD [300,304]. Onalespib (**Figure 1**), a potent Hsp90 inhibitor currently under evaluation in oncological clinical trials for different cancers, was also tested in a murine glioma model. Onalespib was reported to cross the blood-brain barrier (BBB), with long lasting effects against glioma. Pharmacokinetics of this compound were assessed in healthy mice where 24 h after i.v. injection, a brain concentration of 100 nM was observed [305]. Physicochemical parameters (molecular weight (Mw), LogD, topological polar surface area (tPSA) and number of hydrogen bond donors (HBD)) and the affinity (half-maximal inhibitory concentration (IC<sub>50</sub>)) for Hsp90 of these compounds are presented in **Table 1**.

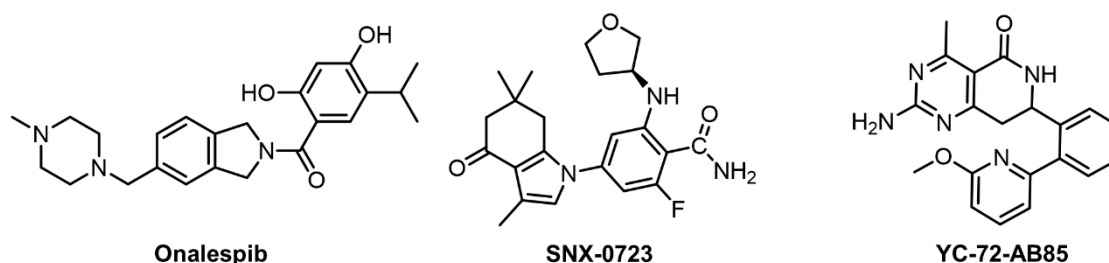


**Figure 1:** Hsp90 inhibitors used in this study.

**Table 1:** Physicochemical parameters of Hsp90 inhibitors.

Compound	Mw	LogD	tPSA (Å <sup>2</sup> )	HBD	IC <sub>50</sub> (nM)
<b>Onalespib</b>	409.5	2.8	67.2	2	18 [124]
<b>SNX-0723</b>	399.4	3.1	86.4	3	14 [304]
<b>YC-72-AB85</b>	361.4	2.2	103.0	3	19 [209]

Positron emission tomography (PET) is a non-invasive, specific and highly sensitive molecular imaging technique, which allows visualisation and quantification of molecular events. Rather short-lived positron emitting radioisotopes ( $T_{1/2}$  = 20-110 min) are incorporated into pharmaceuticals, which are further administered at 'tracer' doses ( $\mu$ g scale) to the subject. Hence, pharmacological effects are omitted. PET allows investigation of the pharmacodynamics of a



drug, demonstration of its target engagement and establishment of the dose occupancy relation which can accelerate drug development. PET allows to detect alterations of molecular pathways at a significantly earlier time point before structural or morphological changes occur. Depending on the binding characteristics of the labelled vector molecule, different receptors, enzymes, transporters or protein aggregates, relevant for a variety of diseases (cancer, inflammation, CNS disorders) can be visualised and quantified and their expression levels can be compared to healthy conditions [154]. Recent studies imply a role for Hsp90 as a potential biomarker in cancer initiation and progression or for identification of patients that are anticipated to respond to Hsp90-targeted therapy. In this respect, several PET probes targeting Hsp90 were developed.

[<sup>124</sup>I]PU-H71 (**Figure 2**) was determined to be an inhibitor of the epichaperome. This compound was tested in a xenograft tumour mouse model inoculated with MDA-MB-468 and ASPC1 tumours, representatives of respectively high and low connectivity networks of the epichaperome. Radioactivity was initially detected in all organs, but 48 h post injection (p.i.) radioactivity was only retained in the MDA-MB-468 tumour. Furthermore, this tracer was subjected to clinical trials on patients exhibiting different tumours (breast, lymphoma) [93]. A copper-64 labelled derivative of Sansalvamide A (**Figure 2**), was tested in mice harbouring PL45 pancreatic tumours wherein the tracer showed Hsp90-specific binding as assessed by heterologous blocking with the well-known Hsp90 inhibitor 17-AAG (**Figure 4, Quinone in Chapter I**) [197]. A fluorine-18 labelled derivative of Ganetespib (**Figure 2**) was developed and synthesized *via* click chemistry and evaluated in breast cancer MDA-MB-231 and MC7 cells where specific binding was observed after blocking with Ganetespib (**Figure 4, Resorcinol in Chapter I**). However, *in vivo*  $\mu$ PET studies on MDA-MB-231 inoculated tumour mice were discouraging as only low tumour uptake was observed compared to other organs [196].

Recently, a highly Hsp90-selective PET tracer, [<sup>11</sup>C]NMS-E973 (**Figure 2 and Chapter IV**) was developed by our lab. [<sup>11</sup>C]NMS-E973 shows Hsp90 specific binding to B16.F10 melanoma cells and to tissue slices of murine B16.F10 melanoma, LNCaP and PC3 prostate cancer and SKOV-3 ovary carcinoma. In a  $\mu$ PET study, fast and persistent *in vivo* tumour binding of [<sup>11</sup>C]NMS-E973 to B16.F10 melanoma inoculated mice was observed as assessed by heterologous blocking with PU-H71 and Ganetespib. Hsp90-specific binding of [<sup>11</sup>C]NMS-E973 was also observed in blood, lungs and spleen of tumour-bearing animals but not in control animals. This suggests that Hsp90 is shedded from the tumour and spreads to the whole body [306].

Although NMS-E973 was reported to enter brain [208], significant brain uptake of [<sup>11</sup>C]NMS-E973 was not observed. In this report we describe the development and *in vivo* evaluation of a carbon-11 analogue of YC-72-AB85 (**Figure 1**) [209], amenable for radiolabelling as reported in patent WO 2008/132211 [307], as a first PET probe for visualisation of Hsp90 in brain. Its physicochemical parameters are described in **Table 1**.

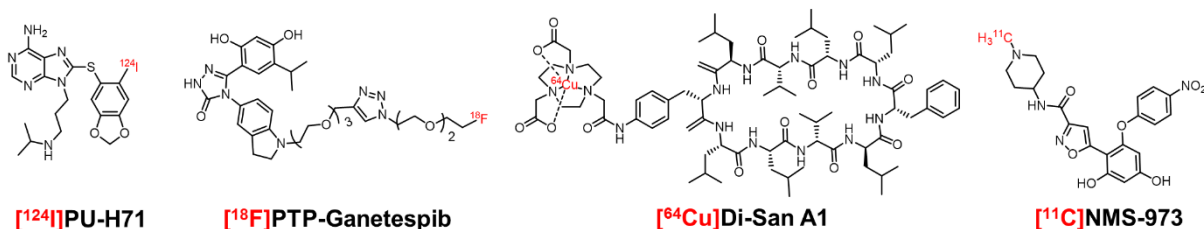


Figure 2: Hsp90 PET tracers.

## 2. MATERIALS AND METHODS

### 2.1. High-performance liquid chromatography (HPLC) analysis

HPLC was performed on a LaChrom Elite HPLC system (Hitachi, Darmstadt, Germany) connected to a Waters 2487 UV-VIS detector and a 3-inch NaI(Tl) scintillation detector connected to a single channel analyser (Gabi, Raytest, Straubenhardt, Germany). Registration and integration of the HPLC chromatograms was performed with GINA Star (Raytest) or RaChel (Lablogic, Sheffield, UK) software. The chemical and radiochemical purity (RCP) was assessed using reversed phase (RP)-HPLC (BDS Hypersil C<sub>18</sub>, 100 × 3 mm, 5 μm eluted with 77/23 NaOAc 0.05 M pH 4.6/ CH<sub>3</sub>CN at a flow rate of 0.7 mL/min). The column effluent was passed over a UV detector (254 nm) and a NaI(Tl) scintillation detector. The identity of the tracer was determined by co-elution with authentic reference compound, YC-72-AB85 on the same HPLC system.

### 2.2. Quantification of radioactivity in biological samples

Quantification of radioactivity was performed with an automated gamma counter equipped with a 3-inch NaI(Tl) well crystal coupled to a multichannel analyser (Wallac 1480 Wizard, Wallac, Turku, Finland). The results were corrected for background radiation, physical decay during counting and detector dead time.

### 2.3. Animal experiments

Animals were kept in a thermoregulated (22 °C) and humidity-controlled environment with a 12 h/12 h light/dark cycle in individual ventilated cages and had free access to food and water. All animal experiments were conducted after approval of the local University Ethics Committee for Animals and according to the Belgian code of practice for the care and use of animals. Female C57BL/6 mice, 8 weeks of age (body mass 20-25 g) and female Wistar rats (body mass 200-250 g) were purchased from Janvier (La Genest-Saint Isle, France). Naval Medical Research Institute (NMRI)-mice (body mass 30-40 g) were purchased from Envigo (Venray, The Netherlands).

## 2.4. LC-MS analysis

Elucidation of intermediate reaction products was accomplished using a Dionex Ultimate 3000 LC system (Thermo Fisher Scientific, Sunnyvale, USA) coupled to a high-resolution time-of-flight mass spectrometer (TOF-HRMS) (MaXis Impact, Bruker, Bremen, Germany) equipped with an orthogonal electrospray (ESI) interface. Acquisition and processing of data were done using Compass IsotopePattern (version 3.2, Bruker).

## 2.5. NMR analysis

NMR was performed using proton nuclear magnetic resonance (<sup>1</sup>H NMR) at 400 MHz. Chemical shifts are reported in parts per million (ppm) relative to tetramethylsilane (TMS,  $\delta = 0$ ). Carbon nuclear magnetic resonance (<sup>13</sup>C NMR) spectra were acquired at 101 MHz on a Bruker AVANCE 400 MHz spectrometer (5 mm probe, Bruker AG, Fällanden, Switzerland).

## 2.6. Statistical analysis

Quantitative data are expressed as mean  $\pm$  SD. Conventional statistics, Student's T-test and two-way analysis of variance (ANOVA) were calculated using Graphpad Prism 7.04 (Graphpad Software). Significance was accepted at the 95% probability level. Topological polar surface area (tPSA) and LogD values were calculated using MarvinSketch (Marvin 14.10.13.0, 2014, ChemAxon (<http://www.chemaxon.com>)).

## 2.7. Reagents and chemicals

Onalespib was purchased from Bio-Connect Life Sciences and used without further purification. SNX-0723 was synthesized as previously reported [308].

## 2.8. Chemistry

The synthesis of the precursor compound is depicted in **Figure 3**.

**2-(benzyloxy)-6-(tributylstannyl)pyridine.** 2-(benzyloxy)-6-bromopyridine (1 g, 3.8 mmol) was dissolved in dry tetrahydrofuran (THF) (7.5 mL) and flushed with N<sub>2</sub>. The mixture was cooled to -78 °C after which *n*-butyllithium (2.5 M in hexanes, 2.3 mL, 5.7 mmol) was added dropwise and the mixture was stirred for 1 h. Next, tributyltin chloride (1 mL, 3.8 mmol) was added dropwise. The reaction mixture was stirred for 10 min at -78 °C and further 3 h at ambient temperature. The reaction was quenched with saturated NH<sub>4</sub>Cl, and extracted with ethylacetate (EtOAc). The organic layers were washed with brine, dried (Na<sub>2</sub>SO<sub>4</sub>), filtered, and evaporated. The compound was purified on Al<sub>2</sub>O<sub>3</sub> with 0.5-1% EtOAc in heptane to afford the title compound (1.260 g, 70%): <sup>1</sup>H NMR (400 MHz, CDCl<sub>3</sub>)  $\delta$  7.50 – 7.45 (m, 2H), 7.44 – 7.39 (m, 1H), 7.39 – 7.34 (m, 2H), 7.31 (d,  $J = 7.4$  Hz, 1H), 7.04 – 6.98 (m, 1H), 6.68 – 6.60 (m, 1H), 5.45 (s, 2H), 1.64 – 1.55 (m, 6H), 1.36 (dd,  $J = 14.7, 7.3$  Hz, 6H), 1.14 – 1.05 (m, 6H), 0.91 (t,  $J = 7.3$  Hz, 9H). <sup>13</sup>C NMR (101 MHz,

CDCl<sub>3</sub>)  $\delta$  171.0, 163.2, 138.7, 136.5, 128.8, 128.5, 128.0, 126.6, 110.0, 67.6, 29.5, 27.7, 14.1, 10.4. HRMS (ESI)  $m/z$  calculated for C<sub>24</sub>H<sub>37</sub>NOSn, 476.1974 [M + H]<sup>+</sup>: found 476.1996.

**(R)-2-amino-7-((R)-2-(6-(benzyloxy)pyridin-2-yl)phenyl)-7,8-dihydro-4-methylpyrido[4,3-d]pyrimidin-5(6H)-one.**

2-(benzyloxy)-6-(tributylstannyl)pyridine (50 mg, 0.15 mmol), SA-34-PA68 (80 mg 0.17 mmol), synthesized as reported [209] and provided by Novartis and K<sub>2</sub>CO<sub>3</sub> (23 mg, 0.17 mmol) were dissolved in dioxane (2 mL) in a closed vial. The mixture was heated to reflux, after which siliacat-DPP-Pd® (10 mol %, 60 mg) was added. The reaction was stirred at reflux temperature for 3 days. After completion, the catalyst was filtered off and rinsed with water and dioxane. The filtrate was evaporated, re-dissolved in EtOAc and washed with water. The organic layers were dried (Na<sub>2</sub>SO<sub>4</sub>), filtered and evaporated. The crude was purified *via* silica gel chromatography using 2% CH<sub>3</sub>OH in dichloromethane (DCM) to afford the title compound (30 mg, 54%): <sup>1</sup>H NMR (400 MHz, CDCl<sub>3</sub>)  $\delta$  7.67 – 7.58 (m, 2H), 7.46 - 7.32 (m, 8H), 6.87 (d,  $J$  = 7.3 Hz, 1H), 6.78 (d,  $J$  = 8.3 Hz, 1H), 6.26 (s, 1H), 5.61 (s, 2H), 5.36 (d,  $J$  = 12.2 Hz, 1H), 5.21 (d,  $J$  = 12.2 Hz, 1H), 5.13 (dd,  $J$  = 11.5, 4.2 Hz, 1H), 3.19 (dd,  $J$  = 16.3, 4.0 Hz, 1H), 2.85 (dd,  $J$  = 16.4, 11.6 Hz, 1H), 2.68 (s, 3H). <sup>13</sup>C NMR (101 MHz, CDCl<sub>3</sub>)  $\delta$  171.2, 169.2, 166.0, 162.9, 162.7, 156.6, 139.9, 139.5, 138.9, 137.3, 130.6, 129.3, 128.5, 128.2, 128.0, 126.8, 117.4, 111.5, 110.2, 68.2, 50.4, 40.1, 28.0, 25.5, 24.6, 17.7. HRMS (ESI)  $m/z$  calculated for C<sub>26</sub>H<sub>23</sub>N<sub>5</sub>O<sub>2</sub>, 438.1924 [M + H]<sup>+</sup>: found 438.1952.

**(R)-2-amino-7,8-dihydro-7-((R)-2-(6-hydroxypyridin-2-yl)phenyl)-4-methylpyrido[4,3-d]pyrimidin-5(6H)-one.** (R)-

2-amino-7-((R)-2-(6-(benzyloxy)pyridin-2-yl)phenyl)-7,8-dihydro-4-methylpyrido[4,3-d]pyrimidin-5(6H)-one (33 mg, 0.07 mmol) was added together with Pd/C (22 mg), Pd(OH<sub>2</sub>)/C (22 mg) and HCOONH<sub>4</sub> (30 mg, 0.4 mmol) and was dissolved in CH<sub>3</sub>OH (10 mL). The reaction was refluxed for 16 h. The crude reaction was filtered over a celite, rinsed with CH<sub>3</sub>OH. The filtrate was evaporated and purified with silica gel chromatography with 3-5% CH<sub>3</sub>OH in DCM to afford the precursor compound (17.3 mg, 67%): <sup>1</sup>H NMR (300 MHz, MeOD)  $\delta$  7.66 (d,  $J$  = 8.5 Hz, 1H), 7.62 (dd,  $J$  = 9.3, 6.9 Hz, 1H), 7.57 (td,  $J$  = 7.6, 1.4 Hz, 1H), 7.45 (td,  $J$  = 7.5, 1.3 Hz, 1H), 7.36 (dd,  $J$  = 7.6, 1.3 Hz, 1H), 6.52 (dd,  $J$  = 9.2, 0.9 Hz, 1H), 6.40 (dd,  $J$  = 6.8, 0.8 Hz, 1H), 4.86 – 4.82 (m, 1H), 2.98 – 2.79 (m, 2H), 2.62 (s, 3H). <sup>13</sup>C NMR (101 MHz, MeOD)  $\delta$  171.9, 170.0, 167.7, 166.0, 164.3, 147.4, 143.3, 140.2, 135.0, 131.6, 131.1, 129.5, 128.2, 119.5, 111.3, 109.6, 51.2, 39.9, 24.6. HRMS (ESI)  $m/z$  calculated for C<sub>19</sub>H<sub>17</sub>N<sub>5</sub>O<sub>2</sub>, 348.1455 [M + H]<sup>+</sup> found 348.1488.

Reference compound YC-72-AB85 was synthesized as reported [209] and provided by Novartis and was used without further purification.

## 2.9. Radiosynthesis

Carbon-11 was produced by proton irradiation of a N<sub>2</sub> + H<sub>2</sub> (5%) gas mixture in a Cyclone 18/9 cyclotron (IBA Louvain-la-Neuve, Belgium) and obtained as [<sup>11</sup>C]CH<sub>4</sub> by a <sup>14</sup>N(p, $\alpha$ )<sup>11</sup>C nuclear reaction. [<sup>11</sup>C]CH<sub>4</sub> was converted in a home-built gas phase recirculation module to [<sup>11</sup>C]CH<sub>3</sub>I which was further converted to [<sup>11</sup>C]CH<sub>3</sub>OTf by passing over a silver triflate column (3 x 150 mm) heated to 220 °C. [<sup>11</sup>C]YC-72-AB85 was synthesized by O-methylation of the precursor, by bubbling [<sup>11</sup>C]CH<sub>3</sub>OTf with a helium flow through a solution of the precursor (250-300  $\mu$ g) and Cs<sub>2</sub>CO<sub>3</sub> (2.5-3 mg)

dissolved in anhydrous CH<sub>3</sub>CN (200-250 μL). After the transfer of the radioactivity was completed, the reaction vial was heated to 50 °C for 4 min. After cooling down, the crude mixture was diluted with 1.8 mL of water and the reaction mixture was purified by HPLC on a RP-C<sub>18</sub> column (XBridge C<sub>18</sub> column, 5 μm, 4.6 mm × 150 mm; Waters, Milford, USA) eluted with 67/33 NaOAc 0.05 M pH 4.6/ethanol (EtOH) at a flow rate of 1 mL/min. The corresponding product peak was collected and diluted with saline to obtain a final EtOH concentration < 10%. The solution was filtered through a sterile 0.22 μm membrane filter (Millex GV 13 mm; Millipore, Billerica, MA).

## 2.10. Generation of B16.F10 tumour bearing mice

Tumour cell lines cells were obtained from the American Type Culture Collection (ATCC). B16.F10 cells were maintained in Dulbecco's Modified Eagle's Medium (DMEM) supplemented with 10% fetal bovine serum. 5×10<sup>5</sup> cells per mouse were implanted subcutaneously in the right dorsal flank of 8-week-old C57BL/6 mice (body mass 20-25 g). The tumours were allowed to grow for 10-15 days until they reached ~0.5-0.75 cm<sup>3</sup> in size as determined using a caliper.

10×10<sup>6</sup> PC3 cells per mouse in 50% Matrigel (VWR, Radnor, U.S.A.) were subcutaneously inoculated into the right shoulder of 7–8-week-old BALB/c nu/nu mice (body mass 20-25 g). The tumours were allowed to grow for 4-5 weeks until they reached ~0.5-0.75 cm<sup>3</sup> in size as determined using a caliper.

## 2.11. Cryotome sectioning

Brain tissue was obtained from female Wistar rats or NMRI-mice. The rodents were anesthetized with 2.5% isoflurane in O<sub>2</sub> at a flow rate of 1 L/min after which they were sacrificed by decapitation. Tumour or brain tissue was excised, rinsed with saline to remove blood and rapidly frozen in 2-methylbutane (-40 °C). Next, 20 μm sections were obtained using a cryotome (Shandon cryotome FSE; Thermo Fisher, Waltham, MA) and these were mounted on adhesive microscope slides (Superfrost Plus; Thermo Fisher Scientific) and stored at -20 °C.

## 2.12. *In vitro* autoradiography studies

Frozen slices were air-dried and preincubated in tris(hydroxymethyl)aminomethane (tris).HCl 50 mM pH 7.4 for 10 min at room temperature. After drying, the slices were incubated with 74 kBq/mL of the tracer in 200-300 μL tris.HCl 50 mM pH 7.4 + 0.3% bovine serum albumin (BSA) per section for 10 min at room temperature. To assess binding specificity, slices were incubated with 200-300 μL tris.HCl 50 mM pH 7.4 + 0.3% BSA supplemented with dimethylsulfoxide (DMSO) (10%) or 10 μM of either YC-72-AB85, Onalespib or SNX-0723 dissolved in DMSO (10%) for 10 min. Incubation solutions were removed, after which the sections were subjected to a quick dip in tris.HCl 50 mM pH 7.4 + 0.3% BSA at 4 °C. Hereafter slices were air-dried and incubated with [<sup>11</sup>C]YC-72-AB85 (74 kBq/mL in 200-300 μL tris.HCl 50 mM pH 7.4 + 0.3% BSA) for 10 min. Slices were washed twice for 5 min in tris.HCl 50 mM pH 7.4 + 0.3% BSA at 4 °C with a final washing step encompassing a quick dip in water at 4 °C, after which the slices were dried. Autoradiograms were obtained by exposing the slices to a phosphor storage screen (super-resolution screen;

Perkin Elmer, Waltham, MA) overnight. The screens were read using a Cyclone Plus system (Perkin Elmer) and the images were analysed using Optiquant software (Perkin Elmer). Results are expressed as digital light units per square mm (DLU/mm<sup>2</sup>). Percentage block vs control was calculated as (DLU/mm<sup>2</sup> in the presence of 100 µM blocker) / (DLU/mm<sup>2</sup> tracer only) on 3-4 tissue sections within the same experiment.

### **2.13. Biodistribution studies**

The biodistribution of [<sup>11</sup>C]YC-72-AB85 was studied in healthy NMRI-mice (body mass 30-40 g). The animals were anesthetized with 2.5% isoflurane in O<sub>2</sub> at a flow rate of 1 L/min and injected with ~5.5 MBq of tracer *via* a tail vein. The rodents were sacrificed by decapitation after 10 or 60 min p.i. (n = 3 per time point).

A similar experiment was conducted on healthy C57BL/6 mice and C57BL/6 mice inoculated with B16.F10 melanoma cells. To assess Hsp90-specific binding, healthy and tumour mice were injected intraperitoneally (i.p.) 30-45 min before tracer injection with either 250-300 µl vehicle, YC-72-AB85 (15 mg/kg) or Onalespib (30 mg/kg) dissolved in 250-300 µl of an aqueous solution of 5% DMSO, (5% Tween 80 for YC-72-AB85) and 90-95% (2-hydroxypropyl)-β-cyclodextrin (40%) in H<sub>2</sub>O. Pre-treatment solutions were sterile filtered through a 0.22 µm membrane filter (Millex-GV, Millipore). Blood and organs of interest were collected in tared tubes and weighed. The radioactivity in the different organs was counted in an automated gamma counter. For the calculation of the total radioactivity in blood, muscle and bone, the masses were assumed to be respectively 7%, 40% and 12% of the total body mass [258,259]. Data were expressed as percentage of injected dose (%ID) and standardized uptake value (SUV). %ID was calculated as (counts per min (cpm) in organ / total cpm recovered) × 100%. SUV was calculated as (radioactivity in cpm in organ / weight of organ in g) / (total cpm recovered / total body weight in g). Data are expressed as mean ± SD, n = 3 per pre-treatment.

### **2.14. Radio-metabolite studies**

Healthy male NMRI-mice were anesthetized with 2.5% isoflurane in O<sub>2</sub> at a flow rate of 1 L/min and injected with ~11 MBq of the tracer *via* a tail vein. Mice were sacrificed by decapitation at 10 or 60 min p.i. (n = 3 per time point). Healthy rats (n = 3) anesthetized with 2.5% isoflurane in O<sub>2</sub> at a flow rate of 1 L/min, were pre-treated i.p. with either 700-800 µl of vehicle (5% DMSO and 95% (2-hydroxypropyl)-β-cyclodextrin (40%) in H<sub>2</sub>O) or Onalespib (30 mg/kg) dissolved in 700-800 µl of vehicle, and injected with ~37 MBq of the tracer *via* a tail vein. 30 min p.i., ~1 mL of whole blood was withdrawn *via* a contralateral tail vein. Blood was collected in K<sub>2</sub>EDTA-containing tubes (BD vacutainer, BD, Franklin Lakes, NJ, USA) and stored on ice. The blood was centrifuged for 5 min at 2330 ×g to separate the plasma. Plasma was spiked with authentic reference compound (5 µl of 860 µg/mL solution in DMSO), weighed and counted in a gamma counter. Subsequently, individual plasma samples were analysed by RP-HPLC on a Chromolith RP-C<sub>18</sub> column (3 mm × 100 mm, Merck, Darmstadt, Germany) eluted with gradient mixtures of CH<sub>3</sub>CN (A) and 0.05 M NaOAc pH 5.5 (B) (0-4 min: 1% A flow rate 0.5 mL/min; 4-9 min: linear gradient 1% A to 90%, flow rate 1 mL/min; 9-12 min: 90% A, flow rate 1 mL/min; 12-15 min: linear gradient 90% A to 1% A, flow rate 0.5 mL/min). After passing through

an in-line UV detector (254 nm) coupled to a 3-inch NaI(Tl) scintillation detector connected to a single channel analyser, the HPLC eluent was collected, 15 fractions in total per plasma sample, and radioactivity was measured in an automated gamma counter.

Healthy male NMRI-mice (n = 3) were anesthetized with 2.5% isoflurane in O<sub>2</sub> at a flow rate of 1 L/min and injected with ~15 MBq of the tracer *via* a tail vein and sacrificed by an overdose of Dolethal® (200 mg/mL pentobarbital, vetoquinol, UK) at 60 min p.i. followed by cardiac perfusion with saline, until liver turned pale. Brains were isolated and homogenized in 3 mL CH<sub>3</sub>CN. The homogenate was centrifuged (2330 ×g), 1 mL of supernatant was collected and diluted with 1 mL H<sub>2</sub>O and filtered through a 0.22 μm filter (Millex-GV, Millipore). 0.5 mL of the filtrate was further diluted with 0.5 mL H<sub>2</sub>O and spiked with 5 μL of authentic reference compound solution (860 μg/mL in DMSO). The samples were injected on HPLC, consisting of a BDS Hypersil RP C<sub>18</sub> column (100 x 3 mm, 5 μm) eluted with NaOAc 0.05 M pH 4.6 / CH<sub>3</sub>CN 77/23 v/v. at a flow rate of 0.7 mL/min. The HPLC eluate was passed through an in-line UV detector (254 nm) coupled to a 3-inch NaI(Tl) scintillation detector connected to a single channel analyser and was collected as 1 mL fractions, 15 fractions in total. The collected fractions were measured in an automated gamma counter.

## 2.15. Determination of plasma protein binding

Rat blood was collected in K<sub>2</sub>EDTA-containing tubes *via* a tail vein 30 min after tracer injection and centrifuged (2330 ×g) for 5-10 min. Rats were pre-treated as described above (vehicle or Onalespib) (n = 3 per pre-treatment). Plasma (100 μl) was added to a tarred Microcon® centrifugal filter device (Amicon® Bioseparations, Merck, Millipore), weighed, counted in an automated gamma counter (radioactivity concentration in plasma) and centrifuged (4436 ×g) for 10 min. The acquired ultra-filtrate was weighed and counted in an automated gamma counter (radioactivity concentration in protein free plasma (PFP)).

To determine non-specific binding (NSB) to the Amicon®-filter material, blood was collected before tracer injection and centrifuged at 2330 ×g for 10 min. The plasma was transferred to a tarred Microcon® centrifugal filter device (Amicon® Bioseparations, Merck, Millipore) (n = 3 per experiment), centrifuged (4436 ×g) for 20 min after which the ultra-filtrate was stored on ice. 150 μL of this PFP was incubated for 2 min with 370 kBq of [<sup>11</sup>C]YC-72-AB85 at 37 °C after which the samples were weighed, counted in an automated gamma counter (radioactivity concentration in supernatant) and centrifuged (4436 ×g) for 10 min. After centrifugation, the filtrate was weighed and counted in an automated gamma counter (radioactivity concentration filtrate). NSB was calculated as 100% - % recovery; %recovery = (radioactivity concentration in filtrate / radioactivity concentration in supernatant) x 100.

Plasma free fraction was calculated as ((radioactivity concentration in PFP, corrected for NSB / radioactivity concentration in plasma) x 100%).

## 2.16. *In vivo* $\mu$ PET study

Wistar rats ( $n = 3$ ) were subjected to multiple  $\mu$ PET scans. Scanning was performed with a FOCUS™ 220  $\mu$ PET scanner (Concorde Microsystems, Knoxville, U.S.A.). Before the start of the PET scan, rats were anesthetized using 2.5% isoflurane in O<sub>2</sub> (2 L/min) and kept under anaesthesia during the entire scan period. The study setup is presented in **Table 2**. Baseline scans were conducted by pre-treatment (i.p.) of animals with 700-800  $\mu$ l of vehicle (5% DMSO, 5% Tween 80, 90% (2-hydroxypropyl)- $\beta$ -cyclodextrin (40%) in H<sub>2</sub>O) 30-45 min before injection of  $\sim$ 45 MBq of [<sup>11</sup>C]YC-72-AB85. Blocking studies were performed by administration (i.p.) of 700-800  $\mu$ l of either a solution of YC-72-AB85 (5 mg/kg) in 5% DMSO, 5% Tween 80, 90% (2-hydroxypropyl)- $\beta$ -cyclodextrin (40%) in H<sub>2</sub>O; a solution of Onalespib (30 mg/kg) dissolved in 5% DMSO, 90% (2-hydroxypropyl)- $\beta$ -cyclodextrin (40%) in H<sub>2</sub>O or a solution of SNX-0723 in 5% N-methyl 2-pyrrolidone (NMP), 5% Tween, 90% (2-hydroxypropyl)- $\beta$ -cyclodextrin (40%) in H<sub>2</sub>O, 30-45 min before tracer injection ( $\sim$ 45 MBq). In a displacement study, rats were pre-treated with Onalespib (30 mg/kg, i.p., dissolved in 5% DMSO, 90% (2-hydroxypropyl)- $\beta$ -cyclodextrin (40%) in H<sub>2</sub>O) 30-45 min before tracer injection ( $\sim$ 45 MBq) and 20 min p.i., YC-72-AB85 (2 mg/kg dissolved in 5% DMSO, 5% Tween 80, 90% (2-hydroxypropyl)- $\beta$ -cyclodextrin (40%)) or SNX-0723 (5 mg/kg dissolved in 5% NMP, 5% Tween, 90% (2-hydroxypropyl)- $\beta$ -cyclodextrin (40%)) was administered intravenously (i.v.). The animal heads were positioned in the centre of the field of view of the  $\mu$ PET scanner. Rats were scanned dynamically over a course of 90 min. Acquisition data of the dynamic scans were Fourier rebinned in 24 time frames (4  $\times$  15 s, 4  $\times$  60 s, 5  $\times$  180 s, 8  $\times$  300 s, 3  $\times$  600 s). Time activity curves (TACs) of the brain were generated using PMOD software (v3.3, PMOD Technologies, Zürich, Switzerland).

**Table 2:** Experimental setup of  $\mu$ PET imaging studies with [<sup>11</sup>C]YC-AB85 on healthy female Wistar rats.

Day	Number of animals	Experiment	Route of administration	Blocking 30-45 min pre tracer injection	Type of scan	Duration of scan
1-1	3	Baseline	i.p.	Vehicle	Dynamic	90 min
1-2	3	Block	i.p.	YC-72-AB85 (5 mg/kg)	Dynamic	90 min.
2-1	3	Block	i.p.	Onalespib (30 mg/kg)	Dynamic	90 min
2-2	3	Block Displacement	i.p. i.v.	Onalespib (30 mg/kg) YC-72-AB85 (2 mg/kg)	Dynamic	90 min
3-1	3	Block	i.p.	SNX-0723 (6 mg/kg)	Dynamic	90 min
3-2	3	Block Displacement	i.p. i.v.	Onalespib (30 mg/kg) SNX-0723 (5 mg/kg)	Dynamic	90 min



### 3. RESULTS

#### 3.1. Radiosynthesis

[<sup>11</sup>C]YC-72-AB85 (**Figure 3**) was synthesized by O-alkylation of the corresponding lactim precursor. The compound was obtained with radiochemical yields of 10-40% based on integration of area's under the curve (AUC) of the peaks observed on the prep-HPLC chromatogram, a molar activity of  $430 \pm 150$  GBq/ $\mu$ mol ( $n = 4$ ) at end of synthesis and a RCP of > 99%.

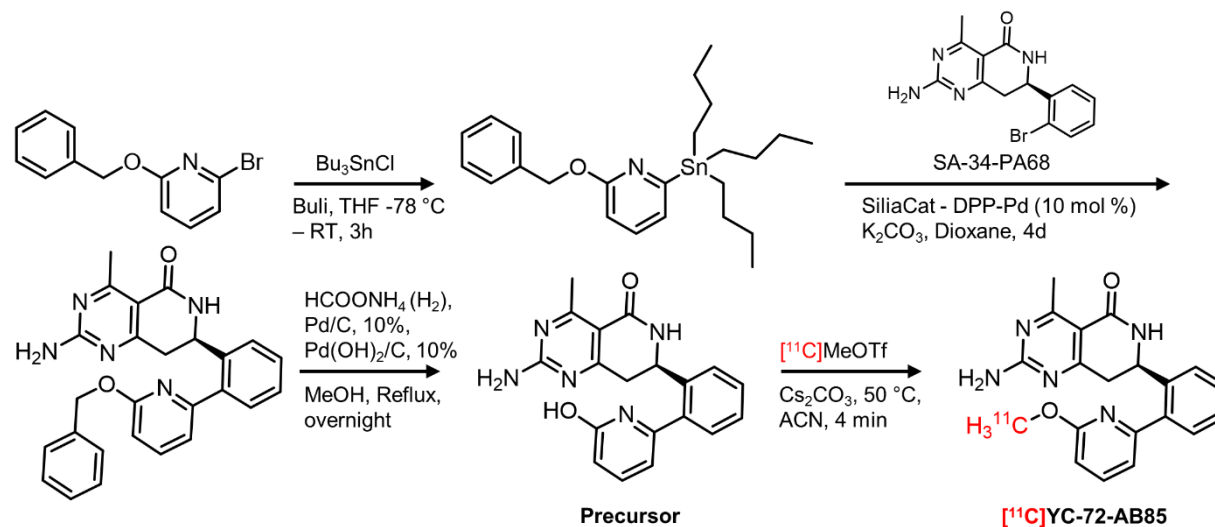


**Figure 3:** Synthesis of precursor and radiosynthesis of [<sup>11</sup>C]YC-72-AB85.

#### 3.2. *In vitro* autoradiography

[<sup>11</sup>C]YC-72-AB85 shows consistent heterogeneous binding in brain of rat and mouse (**Figure 4A-B**). The tracer was most prominently retained in cortex, cerebellum and caudate putamen. The observed binding was highly Hsp90-specific as assessed by blocking with YC-72-AB85 and Onalespib (10  $\mu$ M). Blocking with these structurally unrelated Hsp90 inhibitors, determined on whole brain sections, resulted in an almost complete block of tracer binding. High Hsp90-specific binding was also observed in 2 different tumour tissues (B16.F10 melanoma and PC3 prostate carcinoma) where heterogeneous binding was observed with a propensity to bind outer regions of the tumour sections (**Figure 4C-D**).

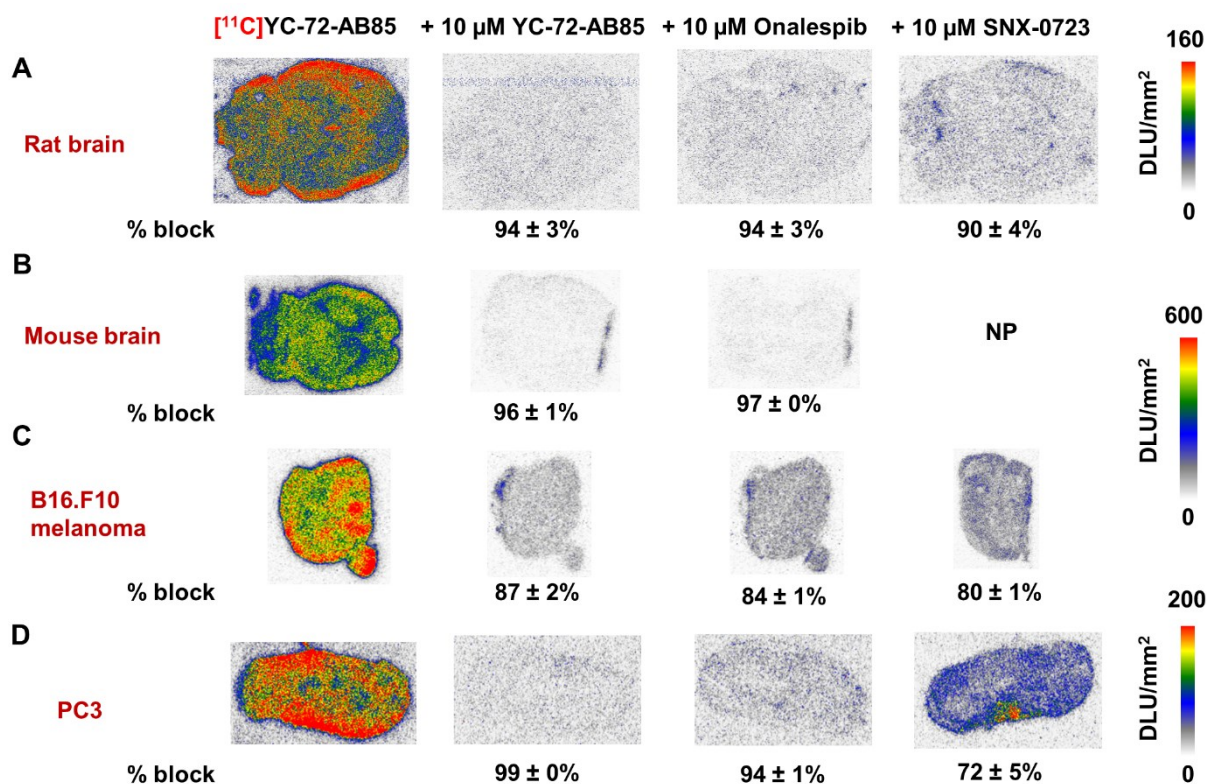


**Figure 4: *In vitro* autoradiography.** A) Rat brain B) Mouse brain C) B16.F10 melanoma D) PC3 prostate carcinoma. Slices were incubated with [<sup>11</sup>C]YC-72-AB85 (74 kBq/mL). Binding specificity was assessed by blocking studies with YC-72-AB85, Onalespib and SNX-0723 (10 μM). Intensity is depicted as DLU/mm<sup>2</sup>. n = 3 sections per group. % Block was calculated as (average DLU/mm<sup>2</sup> in tissue slice in the presence of 10 μM blocker) / (average DLU/mm<sup>2</sup> in tissue slice, tracer only) and presented as mean ± SD. NP = not performed.

### 3.3. Biodistribution and radio-metabolite studies in mice

The biodistribution of [<sup>11</sup>C]YC-72-AB85 was studied in healthy NMRI-mice at 10 and 60 min p.i. (n = 3 per time point). Blood levels remained fairly stable over the studied time points (SUV<sub>10 min</sub> = 0.7, SUV<sub>60 min</sub> = 0.5). High brain uptake was observed, which remained stable (SUV<sub>10 min</sub> = 1.8, SUV<sub>60 min</sub> = 1.6) over the studied time points (**Table 3**). A plasma radio-metabolite study was conducted 10 and 60 min after tracer injection on healthy NMRI-mice. The fraction of polar radio-metabolites was lower than 15% at 10 min after tracer injection, and remained at the same level at the 60 min time point. The fraction of radio-metabolites in brain was negligible (< 4%) at 60 min p.i in mice brain (**Table 4**).

**Table 3:** Biodistribution data of [<sup>11</sup>C]YC-72-AB85 in male NMRI-mice at 10 and 60 min after tracer injection.

	%ID <sup>a</sup>		SUV <sup>b</sup>	
	10 min	60 min	10 min	60 min
Blood	5.1 ± 0.3	3.7 ± 0.4	0.7 ± 0.0	0.5 ± 0.1
Bone	10.3 ± 2.3	10.6 ± 0.6	0.9 ± 0.2	0.9 ± 0.1
Brain	1.9 ± 0.1	1.7 ± 0.1	1.8 ± 0.1	1.6 ± 0.1
Carcass	48.7 ± 1.7	47.9 ± 1.5		
Heart	0.8 ± 0.1	0.6 ± 0.1	1.9 ± 0.1	1.2 ± 0.2
Intestines	15.1 ± 1.1	21.3 ± 2.0		
Kidneys	4.6 ± 0.3	3.4 ± 0.4	2.9 ± 0.2	2.2 ± 0.3
Liver	17.9 ± 0.3	14.9 ± 0.5	3.4 ± 0.2	3.0 ± 0.2
Lungs	1.4 ± 0.2	0.9 ± 0.2	2.3 ± 0.4	1.7 ± 0.3
Muscle	27.9 ± 6.7	22.8 ± 2.2	0.7 ± 0.2	0.6 ± 0.1
Pancreas	2.2 ± 0.6	1.4 ± 0.3	2.7 ± 0.3	2.0 ± 0.3
Spleen	1.4 ± 0.2	0.9 ± 0.1	4.7 ± 0.2	3.3 ± 0.4
Stomach	1.6 ± 0.2	1.4 ± 0.2		
Testes	0.4 ± 0.0	0.6 ± 0.0	0.5 ± 0.1	0.8 ± 0.0
Urine	0.5 ± 0.1	2.4 ± 0.8		

<sup>a</sup> Percentage of injected dose calculated as (cpm in organ/total cpm recovered) x 100. <sup>b</sup> SUV = Standardized uptake value. Calculated as (radioactivity in cpm in organ/weight of organ in grams) / total cpm recovered/body weight). Data expressed as mean ± SD, n = 3 per time point.

**Table 4:** Brain and plasma radio-metabolite study in male NMRI-mice.

	Plasma	Brain
	Intact tracer (%)	
10 min p.i.	87 ± 2	ND
60 min p.i.	89 ± 4	96 ± 0

ND = not determined, Data expressed as mean ± SD, n = 3 per time point.

A biodistribution study 10 min p.i. was performed on healthy C57BL/6 mice (**Table 5**) and compared with C57BL/6 mice bearing B16.F10 melanoma (**Table 6**) (n = 3 per pre-treatment). To assess the binding specificity of the tracer in the different organs of interest, blocking studies were performed with YC-72-AB85 (15 mg/kg) and Onalespib (30 mg/kg). In tumour mice, a significant increase of blood radioactivity concentration was observed compared to control conditions, (SUV<sub>blood-control</sub> = 0.6 vs SUV<sub>blood-melanoma</sub> = 1.9). This increase was also determined to be Hsp90-specific as a significant part of the blood associated radioactivity was blocked by pre-treatment of tumour mice with YC-72-AB85 or Onalespib (**Figure 5A**). In healthy mice, the blocking effect in blood of Onalespib was less pronounced and blocking

with YC-72-AB85 slightly increased blood radioactivity levels (**Table 5**). Brain uptake in healthy and tumour bearing mice was similar and blocking with YC-72-AB85 decreased brain uptake. However, after Onalespib pre-treatment, radioactivity in the brain increased (**Table 5-6**). Further, a moderate tumour tracer uptake was observed (SUV = 0.6) which only slightly decreased after pre-treatment with YC-72-AB85 or Onalespib (**Table 6, Figure 5A**). Blocking resulted in increased SUV tumour/blood ratios (Control = 0.3, YC-72-AB85 block = 0.6, Onalespib block = 0.7) highlighting the dominant blocking effect in blood (**Figure 5B**). However, when comparing SUV tumour/muscle ratios (Control = 1.2, YC-72-AB85 block = 0.6, Onalespib block = 0.7) a significant decrease ( $P \leq 0.05$ ) was observed after blocking with YC-72-AB85 (**Figure 5C**).

**Table 5:** Biodistribution data of [ $^{11}\text{C}$ ]YC-72-AB85 in female C57BL/6 mice 10 min after tracer injection. Mice were pre-treated with vehicle, YC-72-AB85 (15 mg/kg) or Onalespib (30 mg/kg).

	%ID <sup>a</sup>			SUV <sup>b</sup>		
	Control	YC-72-AB85	Onalespib	Control	YC-72-AB85	Onalespib
<b>Blood</b>	4.5 ± 0.8	5.8 ± 2.1	2.9 ± 0.2	0.6 ± 0.1	0.8 ± 0.3	0.4 ± 0.0
<b>Bone</b>	12.4 ± 1.7	5.7 ± 2.6	8.8 ± 5.0	1.0 ± 0.1	0.5 ± 0.2	0.7 ± 0.4
<b>Brain</b>	4.3 ± 0.4	2.7 ± 0.4	6.5 ± 2.6	1.8 ± 0.2	1.1 ± 0.1	2.8 ± 1.0
<b>Carcass</b>	47.8 ± 3.1	51.2 ± 2.0	40.3 ± 0.7			
<b>Heart</b>	0.9 ± 0.2	1.0 ± 0.3	0.7 ± 0.0	1.7 ± 0.4	1.7 ± 0.6	1.3 ± 0.0
<b>Intestines</b>	18.7 ± 1.1	16.8 ± 1.3	19.6 ± 2.2			
<b>Kidneys</b>	3.3 ± 0.6	3.2 ± 0.5	3.3 ± 0.4	2.3 ± 0.3	2.3 ± 0.3	2.3 ± 0.4
<b>Liver</b>	15.1 ± 0.9	17.2 ± 1.4	21.3 ± 0.6	2.9 ± 0.2	3.1 ± 0.4	3.9 ± 0.2
<b>Lungs</b>	2.1 ± 0.7	1.4 ± 0.5	1.5 ± 0.2	2.6 ± 0.5	1.7 ± 0.5	2.0 ± 0.6
<b>Muscle</b>	27.2 ± 3.6	25.6 ± 13.7	20.1 ± 4.6	0.7 ± 0.1	0.6 ± 0.3	0.5 ± 0.1
<b>Pancreas</b>	1.5 ± 0.3	1.1 ± 0.3	1.1 ± 0.4	2.5 ± 0.2	1.5 ± 0.2	1.4 ± 0.3
<b>Spleen</b>	1.0 ± 0.1	0.4 ± 0.1	0.5 ± 0.2	3.0 ± 0.1	1.3 ± 0.3	1.7 ± 0.5
<b>Stomach</b>	1.7 ± 0.2	0.7 ± 0.6	1.4 ± 0.1			
<b>Urine</b>	0.4 ± 0.1	0.1 ± 0.1	0.2 ± 0.1			

<sup>a</sup> Percentage of injected dose calculated as (cpm in organ/total cpm recovered) x 100. <sup>b</sup> SUV = Standardized uptake value. Calculated as (radioactivity in cpm in organ/weight of organ in grams) / total cpm recovered/body weight). Data expressed as mean ± SD, n = 3 per pre-treatment.

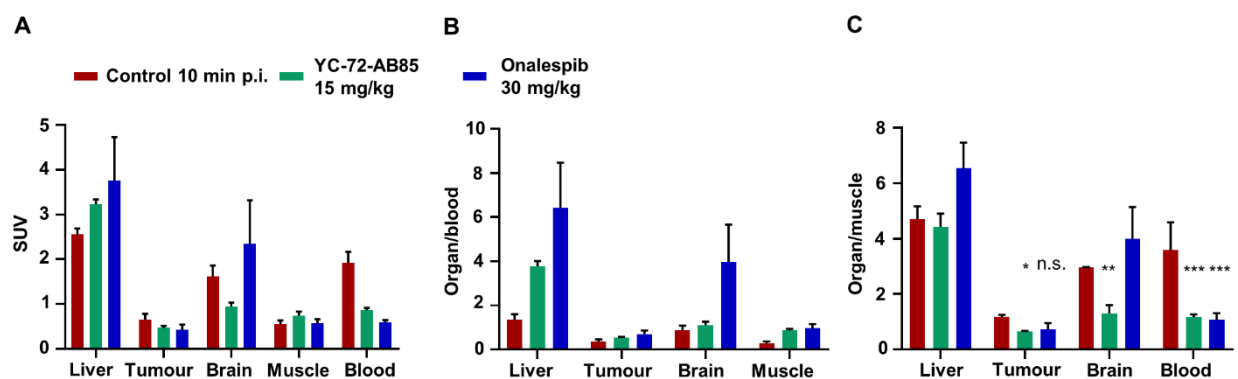


**Figure 5: Pre-treatment biodistribution of [<sup>11</sup>C]YC-72-AB85 in B16.F10 melanoma inoculated mice 10 min p.i. A)** SUV values of selected organs. **B)** SUV organ/blood ratios. **C)** SUV organ/muscle ratios. Significance is calculated as control vs blocking (n.s. = not significant, \*P ≤ 0.05, \*\*P ≤ 0.01, \*\*\*P ≤ 0.001) calculated with two-way ANOVA. Data expressed as mean ± SD, n = 3 per pre-treatment.

**Table 6: Biodistribution data of [<sup>11</sup>C]YC-72-AB85 in B16.F10 melanoma inoculated female C57BL/6 mice 10 min after tracer injection. Mice were pre-treated with vehicle, YC-72-AB85 (15 mg/kg) or Onalespib (30 mg/kg).**

	%ID <sup>a</sup>			SUV <sup>b</sup>		
	Control	YC-72-AB85	Onalespib	Control	YC-72-AB85	Onalespib
Blood	13.4 ± 1.7	6.0 ± 0.4	4.2 ± 0.3	1.9 ± 0.2	0.9 ± 0.1	0.6 ± 0.0
Bone	12.8 ± 4.1	4.9 ± 0.8	5.0 ± 1.4	1.1 ± 0.3	0.4 ± 0.1	0.4 ± 0.1
Brain	3.0 ± 0.5	1.8 ± 0.2	4.7 ± 2.0	1.6 ± 0.2	0.9 ± 0.1	2.3 ± 1.0
Carcass	45.4 ± 1.0	50.3 ± 1.1	48.6 ± 9.8			
Heart	0.9 ± 0.1	0.8 ± 0.0	0.6 ± 0.0	2.0 ± 0.3	1.5 ± 0.1	1.3 ± 0.0
Intestines	16.0 ± 1.0	15.2 ± 0.6	16.1 ± 4.6			
Kidneys	3.4 ± 0.5	3.1 ± 0.1	2.7 ± 0.5	2.7 ± 0.1	2.2 ± 0.1	2.1 ± 0.3
Liver	14.3 ± 0.2	17.2 ± 0.3	18.1 ± 3.3	2.6 ± 0.1	3.2 ± 0.1	3.8 ± 1.0
Lungs	2.5 ± 0.0	1.2 ± 0.1	1.1 ± 0.0	3.4 ± 0.0	1.6 ± 0.0	1.4 ± 0.1
Muscle	21.8 ± 3.3	29.5 ± 3.7	22.8 ± 3.7	0.5 ± 0.1	0.7 ± 0.1	0.6 ± 0.1
Pancreas	1.6 ± 0.4	1.3 ± 0.1	0.8 ± 0.1	2.3 ± 0.3	1.8 ± 0.1	1.2 ± 0.2
Spleen	1.9 ± 0.6	0.6 ± 0.1	0.5 ± 0.1	4.1 ± 0.3	1.4 ± 0.1	1.4 ± 0.2
Stomach	1.4 ± 0.2	1.1 ± 0.3	1.5 ± 0.8			
Tumour	3.9 ± 2.4	2.1 ± 0.6	2.3 ± 1.8	0.6 ± 0.1	0.5 ± 0.0	0.4 ± 0.1
Urine	0.4 ± 0.0	0.3 ± 0.1	0.2 ± 0.1			

<sup>a</sup> Percentage of injected dose calculated as (cpm in organ/total cpm recovered) x 100. <sup>b</sup> SUV = Standardized uptake value. Calculated as (radioactivity in cpm in organ/weight of organ in grams)/total cpm recovered/body weight). Data expressed as mean ± SD, n = 3 per pre-treatment.

### 3.4. *In vivo* $\mu$ PET studies on rats reveal high and sustained brain uptake of [ $^{11}\text{C}$ ]YC-72-AB85

In  $\mu$ PET studies conducted on three Wistar rats, high brain uptake was observed which was sustained over the 90 min dynamic scan period (**Figure 6A, 5C dark red**). Blocking with YC-72-AB85 (5 mg/kg) decreased brain tracer binding (**Figure 6A, 6C black**), indicating saturable binding. To assess binding specificity and potential off-target binding in brain, rats were pre-treated with non-structural related Hsp90 inhibitor, Onalespib (30 mg/kg) and SNX-0723 (6 mg/kg). Surprisingly, treatment with both Hsp90 inhibitors increased tracer uptake in brain (**Figure 6C blue, brown**). Brain/muscle ratios (**Figure 6D**) show a clear blocking effect of YC-72-AB85 and a moderate blocking effect of SNX-0723. Pre-treatment with Onalespib however resulted in increasing radioactivity levels in brain, indicating that Onalespib does not permeate the BBB and only displaces the tracer from peripheral binding sites increasing the amount of available tracer that can bind to brain. Further, a two-fold increase of free tracer in plasma was observed in blocking conditions (**Table 7**), as assessed on blood of Wistar rats pre-treated with vehicle or Onalespib (30 mg/kg) 30 min before tracer injection. In a follow up experiment, rats were again pre-treated with Onalespib (30 mg/kg, i.p.) 30-45 min before tracer injection. 20 min after tracer injection YC-72-AB85 (2 mg/kg) or SNX-0723 (5 mg/kg) was injected *via* a tail vein. This resulted in a rapid wash-out of activity from brain to baseline levels (**Figure 6E green, orange**) which was faster for displacement with YC-72-AB85. This observation indicates reversible and Hsp90-specific tracer binding. The fraction of plasma radio-metabolites in rats 30 min p.i. amounted to ~25% in baseline conditions and ~15% in blocking conditions (Onalespib (30 mg/kg) (**Table 7**).

**Table 7:** Plasma radio-metabolite and plasma protein binding study (determination of tracer free fraction in plasma) in Wistar rats (n = 3) pre-treated with vehicle or Onalespib (30 mg/kg).

	Baseline 30 min p.i.	Onalespib 30 min p.i. (30 mg/kg)
Intact tracer (%)	73 $\pm$ 4	84 $\pm$ 6
Plasma free fraction (%)	12 $\pm$ 5	24 $\pm$ 5

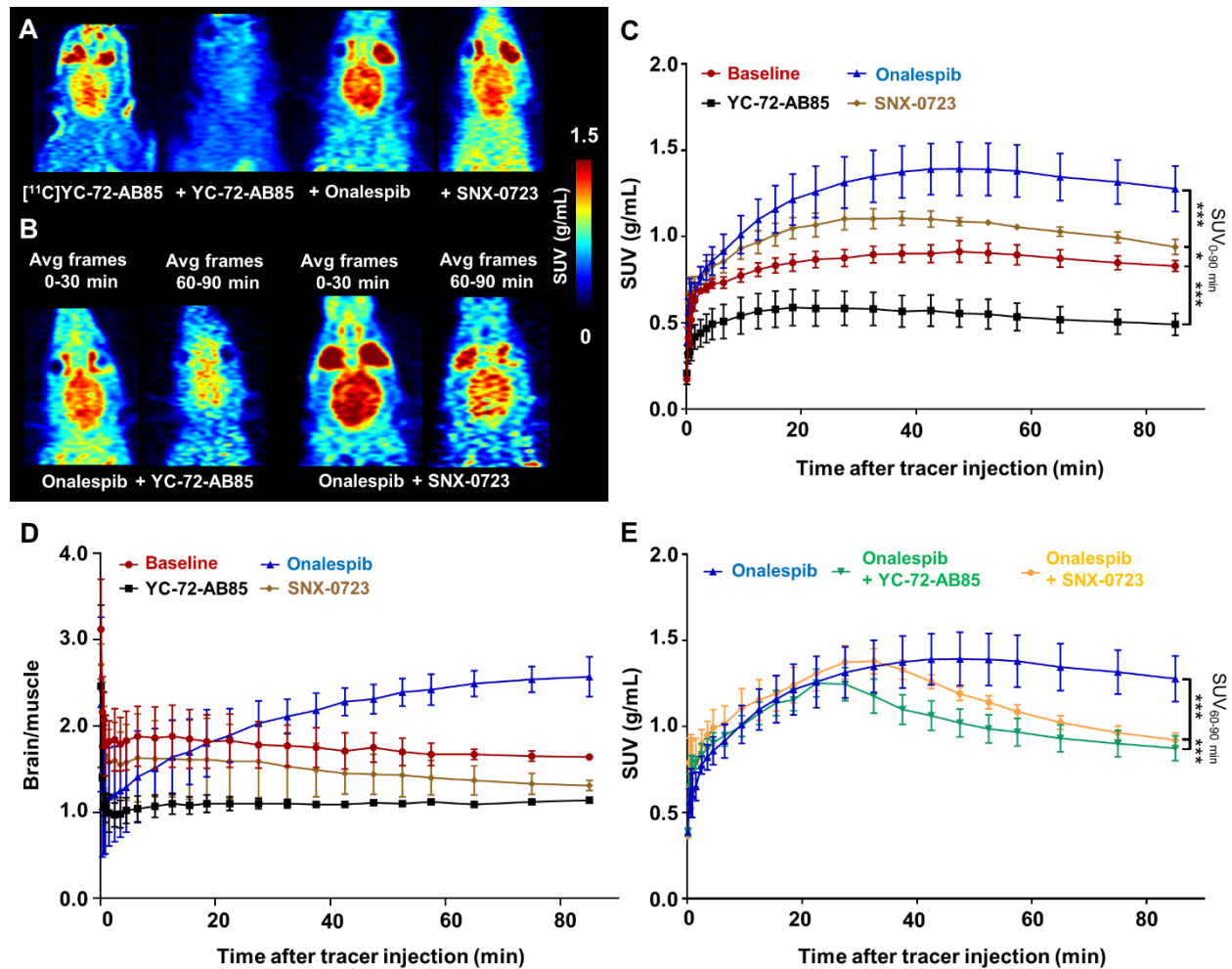


**Figure 6:  $\mu$ PET studies on Wistar rats.** **A)** Averaged images of 90-min dynamic scan after injection of [<sup>11</sup>C]YC-72-AB85 (45 MBq, n = 3). Rats were pretreated with an i.p. injection of vehicle, YC-72-AB85 (5 mg/kg), Onalespib (30 mg/kg) or SNX-0723 (6 mg/kg). **B)** Averaged images of 0-30 min and 60-90 min of 90 min dynamic scan of rats pre-treated with Onalespib (30 mg/kg) and injected with [<sup>11</sup>C]YC-72-AB85 (45 MBq, n = 3). 20 min after start of the scan, 2 mg/kg YC-72-AB85 or 5 mg/kg SNX-0723 was injected *via* a tail vein. **C)** Averaged TACs (SUV) of  $\mu$ PET studies with [<sup>11</sup>C]YC-72-AB85, rats were pre-treated with vehicle (dark red), YC-72-AB85 (black, \*\*\*P  $\leq$  0.001), Onalespib (blue, \*\*\*P  $\leq$  0.001) and SNX-0723 (brown, \*P  $\leq$  0.05). Significance calculated as baseline vs block (averaged SUV<sub>0-90 min</sub>). **D)** Averaged TACs (brain/muscle) of  $\mu$ PET studies with [<sup>11</sup>C]YC-72-AB85, rats were pre-treated with vehicle (dark red), YC-72-AB85 (black), Onalespib (blue) and SNX-0723 (brown). **E)** Averaged TACs (SUV) of  $\mu$ PET studies with [<sup>11</sup>C]YC-72-AB85, rats were pre-treated with, Onalespib (blue, 30 mg/kg). 20 min after start of scan 2 mg/kg YC-72-AB85 (green, \*\*\*P  $\leq$  0.001) or 5 mg/kg SNX-0723 (orange, \*\*\*P  $\leq$  0.001) was injected *via* a tail vein. Significance was calculated as Onalespib pre-treatment vs displacement agent (averaged SUV<sub>60-90 min</sub>). Significance was calculated with paired T-test.

#### 4. DISCUSSION

Frequently occurring CNS disorders (AD, PD, HD) share a common progressive degeneration of neurons. Affected cells tend to lose the ability to effectively degrade the increasing amount of misfolded proteins consequently leading to oligomerization of misfolded protein and formation of plaques or inclusion bodies. Hence, these diseases are generally recognized as protein folding disorders [110]. It has been observed that aging can alter Hsp90 levels in the

brain, however both decreased and increased Hsp90 levels have been observed, depending on the brain region and cell type. Similar results were obtained for other chaperones and co-chaperones [309]. Importantly, these results should be looked at with caution as clear discrepancies were observed between *ex vivo* and *in vitro* autoradiography Hsp90 binding assessed with [<sup>11</sup>C]NMS-E973 [306]. This can potentially be attributed to acute changes of Hsp90 expression and post-translational modifications, *ante*- and *post*-mortem, where differences in biosampling procedures can present varying results [310].

Several factors such as cellular stress and gene mutations can lead to an altered protein structure (e.g. decreased solubility or higher propensity to aggregate). When this is coupled to a decreased capacity to remove cytotoxic entities due to changes in expression or function of chaperome members, a degenerative state can be induced and preserved [297]. Current drugs targeting CNS disorders offer symptomatic relief but therapeutic cures which alter or reverse disease progression are unavailable. In this regard, molecular imaging with PET can enable *in vivo* quantification of target expression, demonstrate target engagement and allows establishment of a dose-occupancy relation for new CNS drug candidates in man [154,311]. Hsp90 inhibitors have been extensively studied in preclinical and clinical oncology trials. However, inhibition of Hsp90 for treatment of CNS disorders and its involvement in diseases such as PD, AD and HD has been studied less intensively.

In *in vitro* autoradiography studies on brain sections of rodents, high tracer binding in cortex, cerebellum and caudate putamen was observed. Homologous (YC-72-AB85) and heterologous (Onalespib, SNX-0723) blocking proved to be very effective, indicating *in vitro* Hsp90-specific binding of [<sup>11</sup>C]YC-72-AB85 in brains of rats and mice. Binding of [<sup>11</sup>C]YC-72-AB85 was also determined to be Hsp90-specific in two different tumour types, B16.F10 melanoma and PC3 prostate carcinoma. Here, tracer binding was more pronounced at the outer edges of the section, similarly to previous *in vitro* autoradiography studies with [<sup>11</sup>C]NMS-E973 [306].

In *ex vivo* biodistribution studies a predominant hepatobiliary clearance was observed with minimal urinary excretion. Blood clearance, as assessed in healthy NMRI-mice, was rather slow. %ID of brain at the 10 min time point was twice as high for C57BL/6 mice compared to NMRI-mice (~4% vs ~2%). This can be explained by the brain/total body weight, which was also twice as high for C57BL/6 mice. Radioactivity levels in blood of B16.F10 melanoma bearing mice were significantly higher compared to healthy mice. Moreover, tracer binding in blood was significantly blocked by pre-treatment with YC-72-AB85 or Onalespib in tumour mice, whereas this effect was not observed in healthy control mice. The same phenomenon was also observed with [<sup>11</sup>C]NMS-E973, in blood and blood-rich organs (spleen, lungs) [306]. Blocking of [<sup>11</sup>C]YC-72-AB85 in spleen and lungs of tumour mice was also clearly observed after pre-treatment with YC-72-AB85 and Onalespib indicating that in oncological malignancies Hsp90 levels in blood are altered, possibly by shedding of Hsp90 from the tumour [101]. The B16.F10 melanoma cell type is often used to study metastasis, increased binding of tracer in blood can therefore also be attributed to binding to circulating B16.F10 metastatic melanoma cells [312]. Another explanation can be binding of [<sup>11</sup>C]YC-72-AB85 to peripheral blood mononuclear cells (PBMCs). These cells express elevated levels of Hsp90 as observed in studies concerning exercise-



heat acclimation in humans [313], systemic Lupus Erythematosus [314] and B-cell malignancies [315]. Tumour uptake of [<sup>11</sup>C]YC-72-AB85 was moderate to low and at first glance not Hsp90-specific. However, the significant blocking effect in blood and other peripheral organs (spleen, lung) increases the availability of the tracer to bind to the tumour (**Figure 5, Table 6**). When comparing tumour/muscle ratios a clear blocking effect after pre-treatment of the tumour bearing mice with YC-72-AB85 and Onalespib was observed, which was only significant for YC-72-AB85 treatment (**Figure 5C**).

In this study, two non-structurally related Hsp90 inhibitors were used to assess binding specificity of [<sup>11</sup>C]YC-72-AB85 in brain. Pre-treatment of mice with 30 mg/kg Onalespib i.p. increased brain uptake of [<sup>11</sup>C]YC-72-AB85 in healthy C57BL/6 mice, B16.F10 melanoma bearing mice and also in rats. This suggests that Onalespib only passes the BBB to a limited extent. This is surprising as physicochemical parameters (**Table 1**) are in agreement with free diffusion over the BBB [161]. Further investigation of blood of rats showed that radioactivity levels in plasma doubled after pre-treatment with Onalespib.

Pre-treatment with YC-72-AB85 effectively blocked binding of [<sup>11</sup>C]YC-72-AB85 to brain and the blocking effect was even more pronounced when comparing brain/muscle ratios. In a pre-treatment study with SNX-0723 in rats, increased brain uptake of the tracer was observed, possibly mediated by a dominant blocking effect in peripheral tissues. Which potentially increased available tracer in plasma, similarly to pre-treatment with Onalespib, but this remains to be assessed. Brain/muscle ratios indicate a relatively small blocking effect of SNX-0723. To assess binding specificity in brain of rats, it was opted to pre-treat rats with Onalespib to saturate peripheral Hsp90 binding sites. Intravenous administration of brain permeable Hsp90 inhibitors YC-72-AB85 and SNX-0723, 20 min after tracer injection resulted in a decrease in brain activity indicating Hsp90-specific and reversible binding (**Figure 6E-green, red**). However, the doses injected were not sufficient to completely block tracer binding. Higher doses of YC-72-AB85 may be needed to induce full target occupancy. Blocking studies with 15 mg/kg YC-72-AB85 administered i.p. in healthy C57BL/6 mice decreased brain uptake from SUV = 1.8 to SUV = 1.1. However, blood radioactivity levels were also increased. When comparing brain/blood ratios the blocking effect was even more pronounced, respectively 3.0 (baseline) vs 1.4 (YC-72-AB85).

Plasma radio-metabolite studies indicate a fairly low fraction of radio-metabolites in plasma of mice (15% at 60 min p.i.) and rats (25% at 30 min p.i.) The fraction of radio-metabolites in brain of mice at 60 min p.i. was negligible.

The observed Hsp90-specific binding in blood is interesting but also complicates the interpretation of blocking effects and it will be interesting to identify the cells that are responsible for Hsp90 specific binding in the blood cell fraction. The blood associated Hsp90 seems to work as a sink for circulating tracer resulting in a relatively constant plasma concentration mimicking constant infusion. Additional  $\mu$ PET studies, preferably in rhesus monkeys with arterial blood sampling, need to be performed to determine the optimal kinetic model and Hsp90 quantification method, as a last step towards first-in-man evaluation of the tracer. Whole body PET experiments can also be performed to study the distribution of [<sup>11</sup>C]YC-72-AB85 in peripheral organs and to interpret effects of blocking in these organs.

Additional studies have to be performed, to identify the cells which are responsible for Hsp90 specific binding in blood and to verify the hypothesis of Hsp90 shedding from the tumour. The good brain penetration of [<sup>11</sup>C]YC-72-AB85 potentially allows for visualisation and quantification of Hsp90 in glioma, a tumour type in which Hsp90 inhibitor treatment is extensively studied [305].

## 5. CONCLUSIONS

[<sup>11</sup>C]YC-72-AB85 shows high Hsp90-specific tracer binding in brain and tumour sections *in vitro*. In biodistribution studies, tumour/muscle ratios indicate Hsp90-specific tumour binding as assessed by blocking studies with YC-72-AB85 and Onalespib. In tumour mice, increased Hsp90 specific binding in blood and blood rich organs was observed by blocking studies with YC-72-AB85 and Onalespib. In  $\mu$ PET studies on rats, high tracer binding in brain was observed, which could be blocked by pre-treatment with YC-72-AB85. Pre-treatment with Onalespib increased radioactivity levels in the brain, which could be displaced by i.v. injection of YC-72-AB85 or SNX-0723. Taken together, [<sup>11</sup>C]YC-72-AB85 shows great promise as an imaging agent for visualisation of Hsp90 in brain. However, further studies are warranted to determine the most appropriate kinetic model and quantification method.

## **CHAPTER VI**

---

### **GENERAL DISCUSSION AND FUTURE PERSPECTIVES**

---



## 1. PET IMAGING OF HDACS

The histone deacetylase (HDAC) family has gained attention as mediators of various diseases [19]. HDACs however have isoform-specific roles in diverging cellular pathways in health and disease. Therefore medicinal chemistry research has focussed on the development of isoform-selective HDAC inhibitors. Although a lot of resources have been invested on the development of HDAC inhibitors, only four are currently available as market-authorized drugs. Furthermore, these four are pan-HDAC inhibitors that are only applicable for treatment of a subset of haematological cancers [20]. In this respect, positron emission tomography (PET) with isoform-specific HDAC tracers can aid in HDAC drug development by identification of HDAC subtypes overexpressed in various cancers, which can be potentially used as prognostic markers or to identify patients that likely may benefit from HDAC-inhibitor therapy. This approach can be expanded to cardiac, inflammatory and central nervous system (CNS) disorders, in which HDACs have also been observed to play a detrimental role [19].

Identification of a new PET imaging target generally starts by searching for an unmet clinical diagnostic need in which the expression and/or ligand binding affinity of a protein (such as receptor, transporter, enzyme) is altered compared to the healthy state. Here, the biological function and the localization of the aberrant entity is important [316]. Next, literature can be explored to identify (a library of) compounds or scaffolds with high affinity for the target. This library can be screened *in vitro* against recombinant protein, cell lysate or tissue homogenate in which affinity of the compound for the target can be determined [240]. Affinity is indeed a crucial parameter for PET ligands since the bound-to-unbound ratio, depends on the maximum density of receptors/dissociation constant ( $B_{max}/K_D$ ) ratio. If the target resides at an intracellular location or is surrounded by a blood barrier with tight junctions, often additional structural modifications need to be made to increase membrane permeation. Even if these requirements are met, PET tracers can still fail as imaging agents as other parameters, such as efflux transporter affinity, high non-specific binding (NSB), off-target binding or undesirable kinetics (too slow or too fast) can limit the applicability. To maximize chances of lead identification, *in silico* molecular docking studies can be implemented in the high-throughput screening of potential scaffolds, with an additional benefit that it is very cost friendly [243]. The use of predictive *in vitro* and *in silico* algorithms is also implied in CNS PET tracer development [317]. These *in silico* and *in vitro* assays are based on molecular and physicochemical parameters, including LogP, LogD, molecular weight (Mw), topological polar surface area (tPSA), number of hydrogen bond donors (HBD) and pKa, defined as CNS PET multiple parameter optimization (MPO). Generally, a score of CNS PET MPO > 3 is advised. Further, passive permeability assays can be conducted on cells harbouring efflux transporters (P-glycoprotein (P-gp) or multi-drug resistance protein 1 (MDR1)) to identify substrates for these receptors. The development of *in silico* absorption, distribution, metabolism and excretion (ADME) calculation algorithms can further aid in lead identification of CNS PET tracers [317,318].

In this PhD research project, we initially focused on development of HDAC2-specific PET tracers for CNS PET imaging (**Chapter II**). HDAC2 has been implied as a detrimental factor in multiple diseases, especially in CNS disorders [7]. Molecular docking studies were implemented in the search for potential HDAC2 tracers based on Santacruzamate A

(compound **5** in **Chapter II**), which supposedly expressed very high affinity towards HDAC2 [206]. These compounds, as well as new derivatives thereof were screened *in silico* and evaluated *in vitro* in two different labs using different assay conditions. Disappointedly, the high affinity of Santacruzamate A for HDAC2 was not confirmed in our assays. Furthermore, this discrepancy was also observed by an independent research group [233]. Later on, the research group that first reported Santacruzamate A as well as other groups published reports in which the initially reported high affinity values of Santacruzamate A for HDAC2 could not be reproduced [319,320].

The reasons for the discrepancies between original reported results and our findings remain elusive. The group which first described Santacruzamate A, state in a follow up article, that errors in their affinity assays can be attributed to numerous factors including enzyme origin, temperature, pH, solvents, substrates and many more [319]. We identified key features for high affinity HDAC binding. Firstly, a proper Zn<sup>2+</sup>-binding group, prototypically represented by the hydroxamic acid moiety, is required. Santacruzamate A possess an ethyl-carbamate moiety which is unable to efficiently coordinate the catalytic Zn<sup>2+</sup>-ion. Compound **6** in **Chapter II** (Santacruzamate A-SAHA hybrid) does possess a hydroxamic acid moiety, but also proves ineffective in inhibiting HDAC activity. Potentially explained by the lack of a second requirement, an aromatic functional group present in the linker region of the HDAC inhibitor which can mediate  $\pi$ - $\pi$  stacking interactions with phenylalanine residues in the HDAC active site. Thirdly, both compounds did not express key hydrogen bonds, which were present in high affinity compounds **1** (SAHA) and **3** (Martinostat).

Our *in silico* docking study results were highly in line with *in vitro* results. Limitations in *in silico* studies remain, as computerised simulations often exhibit inconsistencies in acquired data compared to *in vitro* or *in vivo* assays. Hence, obtained results should always be interpreted with care, although they can be a good starting point for lead identification [243]. HDAC *in vitro* affinity assays, typically performed on recombinant or purified protein [321], also need to be interpreted with caution as *in vivo*, HDACs are embedded in multi-complex structures, which influences affinity, accessibility and target engagement of HDAC inhibitors [321]. Up till now, no HDAC2-selective inhibitors have been reported, probably due to the high similarity between HDAC1 and 2 who share 85% sequence homology [37].

Conversely, multiple selective HDAC6 inhibitors are (being) developed and reported, of which three are currently evaluated in clinical trials as monotherapy or in combination with other drugs [71]. In recent years, many PET tracers targeting HDACs were developed either to study HDACs in cancer or CNS disorders [170]. Many of them also exhibit similar pan-HDAC inhibition properties as their unlabelled, therapeutic counterparts. However, three HDAC6-selective PET tracers have been reported (**Table 1**) (**Figure 13 in Chapter I**). Initially, all of them were developed for visualisation of HDAC6 in CNS [190,191] but only [<sup>18</sup>F]Bavarostat was able to efficiently permeate the BBB, where high specific binding in grey matter was observed [190]. Tubastatin A and KB631 are structural analogues with the same Mw, LogD, tPSA and HBD values which suggest free diffusion over the BBB [161]. However this is not observed *in vivo*, in our study and in other reports [193]. A detailed report concerning [<sup>11</sup>C]KB631 PET brain imaging has not yet been published and neither *in vitro* nor *in vivo* evaluation of [<sup>11</sup>C]Tubastatin A has been reported [192].

All three tracers in **Table 1** constitute a hydroxamic acid group directly coupled to a phenyl ring and further linked to a bulky capping group. The hydroxamic acid moiety is used to chelate the Zn<sup>2+</sup>-ion in the catalytic domain of HDAC6. Whereas the bulky and rigid capping groups, respectively adamantane (Bavarostat) and tryptoline (KB631) interact with the rim of the entrance of the HDAC6 pocket, which is wider compared to other HDAC isoforms. These features imply HDAC6-selectivity as was previously reported [190,191]. [<sup>18</sup>F]Bavarostat possesses an adamantane moiety, frequently used in CNS drug development [322]. Further, methylation of the secondary amine was key for good brain uptake as was determined in previous research on the development of fluorine-18 analogues of Martinostat [189]. Tryptoline based compounds able to pass the BBB are reported [323,324] and physicochemical parameters of KB631 imply free diffusion over the BBB. Further, in  $\mu$ PET studies in rats pre-treated with a P-gp inhibitor, brain uptake of [<sup>11</sup>C]KB631 remained unaltered [193]. Hence, the lack of brain uptake of [<sup>11</sup>C]KB631 remains elusive.

**Table 1:** Physicochemical properties of HDAC6 PET tracers.

Compound	Mw	LogD	tPSA (Å <sup>2</sup> )	HBD	HDAC6 IC <sub>50</sub> (nM)	Selectivity over HDAC1
[ <sup>11</sup> C]Tubastatin A	335.4	2.6	57	2	15	> 1000
[ <sup>11</sup> C]KB631	335.4	2.6	57	2	1.4	> 3700
[ <sup>18</sup> F]Bavarostat	346.4	2.3	53	2	60	> 16000

However, [<sup>11</sup>C]KB631 is a first selective HDAC6 PET tracer evaluated in oncological conditions (**Chapter III**). In a proof-of-concept study, this tracer was evaluated *in vitro* and *in vivo* in B16.F10 melanoma. B16.F10 cells exhibit high metastasis propensity, which can be mediated by deacetylation of cortactin and  $\alpha$ -tubulin by HDAC6, enhancing cytoskeleton remodelling and cell invasion [51]. In *in vitro* autoradiography studies on B16.F10 melanoma and PC3 sections, highly focal retention of radioactivity is observed, which can indicate a leading edge of cell motion. This was however not observed in *in vivo*  $\mu$ PET studies, which can be explained by the resolution limit of PET. Another explanation can be that this focal retention of the tracer is due to *post-mortem* molecular changes. Further investigation of this phenomenon is warranted. *In vitro* autoradiography on brain sections show heterogeneous distribution of [<sup>11</sup>C]KB631, with high tracer binding in subcortical areas and cerebellum similar to what was reported for [<sup>18</sup>F]Bavarostat [190]. *Ex vivo* biodistribution studies on healthy and diseased mice, show specific binding in organs and tissues where HDAC6 is reported to be expressed including heart, liver, kidney, brain, pancreas and melanoma [51,62]. In Ricolinostat (**Figure 1A in Chapter III**) blocking studies, a clear increase of blood radioactivity levels was observed, attributed to blocking of HDAC6 in peripheral organs. The increased plasma concentration results in higher tracer delivery to other tissues, including tumour and muscle. Tumour/muscle ratios were decreased by pretreatment with Ricolinostat suggesting HDAC6-specific tumour binding.

This study indicates the importance of conducting multiple experiments, combining *ex vivo* biodistribution experiments with *in vivo*  $\mu$ PET studies. In *ex vivo* biodistribution studies, where resolution limitations and spill-over effects inherent to  $\mu$ PET studies are absent, blood radioactivity levels and fraction of radio-metabolites can be

assessed. However,  $\mu$ PET studies allow acquisition of the dynamic biodistribution over the whole scan period. Further, multiple scans on the same animals can be conducted, enabling head-to-head comparison between baseline and blocking studies and between different tracers. In conclusion, [ $^{11}\text{C}$ ]KB631 shows promise as a PET tracer for visualisation of tumour HDAC6, but further studies in other tumour models and ultimately in patients are required to explore its full potential. Alternatively, [ $^{11}\text{C}$ ]KB631 can also be tested in other disease models such as cardiovascular or inflammatory diseases [19]. It would also be interesting to evaluate [ $^{18}\text{F}$ ]Bavarostat in different disease models, where head-to-head studies with [ $^{11}\text{C}$ ]KB631 can indicate the tracer of choice for current HDAC6 imaging in peripheral diseases.

## **2. PET IMAGING OF HSP90**

B16.F10 melanoma bearing mice were used in HDAC6 experiments and heat shock protein (Hsp)90 PET tracer evaluation. This murine cell line has a high potency for metastasis [312], is easily maintained and tumour growth is rapid where adequate tumour sizes are obtained 10-15 days after inoculation. Moreover, melanoma cells can be inoculated in healthy C57BL/6 mice and do not require immune deficient (athymic) mice. However, because of the rapid growth, inoculated mice need to be monitored frequently as tumours tend to become haemorrhagic and necrotic.

Important changes with regard to Hsp90 in healthy conditions compared to tumour environment have been reported. Firstly, Hsp90, already comprises 2% of the total cellular protein count in healthy conditions, but this fraction further increases to 6-7% in cancer [80]. Of note, increased levels of other molecular chaperones (Hsp70, Hsp110) were also observed but Hsp90 co-chaperones (p23, ATPase homologue 1 (AHA1)) were upregulated to a lesser extent (10-20 less abundant). Secondly, Hsp90 in a stressed environment (such as cancer) shifts to a stress state, facilitates connectivity between other members of the chaperome, ultimately forming pro-cell survival chaperome complexes (epichaperome) [94]. Thirdly, oncogenic Hsp90 will be actively translocated to the cell membrane or the extracellular compartment (eHsp90), where it influences cell motility, invasion and metastasis [275]. Taken together, Hsp90, eHsp90 or Hsp90 embedded in the epichaperome, can be used as a biomarker to study cell stress in malignant transformation, allowing identification of Hsp90 responsive tumours and follow up of disease progression. Stress-activated Hsp90 has also been implied in CNS disorders such as Alzheimer's disease (AD), Parkinson's disease (PD) [95], epilepsy [302], cardiac disease, inflammation and other diseases where the heat shock response (HSR) is activated [325]. In this respect, Hsp90 PET can have multiple applications.

In **Chapter IV**, the development of a highly selective Hsp90 PET tracer, [ $^{11}\text{C}$ ]NMS-E973 (**Figure 1F in Chapter IV**) is reported. NMS-E973, first reported by Brasca et al [207] is a potent (Hsp90 $\alpha$  half-maximal depolymerisation concentration ( $\text{DC}_{50}$ ) = 10 nM) and selective Hsp90 inhibitor, which showed strong cytostatic effects in various tumour cell lines [208]. [ $^{11}\text{C}$ ]NMS-E973 shows strong binding to B16.F10 melanoma cells that could be inhibited by



PU-H71 (200  $\mu$ M), a non-structurally related Hsp90 inhibitor. *In vitro* autoradiography studies showed Hsp90-specific binding on tissue slices of murine B16.F10 melanoma, LNCaP and PC3 prostate cancer and SKOV-3 ovary carcinoma. In a  $\mu$ PET study, fast and persistent *in vivo* tumour binding of [ $^{11}$ C]NMS-E973 to B16.F10 melanoma-inoculated mice was observed. Pretreatment of B16.F10 melanoma mice with PU-H71 or Ganetespiib (50 mg/kg) completely blocked tumour accumulation of [ $^{11}$ C]NMS-E973 and confirmed *in vivo* Hsp90 binding specificity. Hsp90-specific binding of [ $^{11}$ C]NMS-E973 was also observed in blood, lungs and spleen of tumour-bearing animals but not in control animals. This may suggest that Hsp90 is shedded from the tumour and spreads to the whole body in agreement with earlier reports demonstrating secretion of truncated and phosphorylated Hsp90 $\alpha$ , promoting tumour invasiveness through activation of metalloproteinase 2 (MMP2) or the human epidermal growth factor receptor 2 (HER2) [100,104].

Although NMS-E973 was reported to enter brain, we did not observe significant brain uptake of [ $^{11}$ C]NMS-E973. Other Hsp90 inhibitors with physicochemical characteristics compatible with efficient brain uptake were therefore explored. [ $^{11}$ C]YC-72-AB85 (**Figure 3 in Chapter V**) was identified as a potential tracer for *in vivo* visualisation of Hsp90 in brain (**Chapter V**). A comparison between [ $^{11}$ C]NMS-E973 and [ $^{11}$ C]YC-72-AB85 regarding physicochemical properties is presented in **Table 2**. [ $^{11}$ C]YC-72-AB85 was observed to bind specifically to B16.F10 melanoma as studied in an *ex vivo* biodistribution study. Elevated Hsp90-specific binding of [ $^{11}$ C]YC-72-AB85 was detected in blood of tumour mice compared to healthy counterparts. [ $^{11}$ C]YC-72-AB85 binding to brain slices of mice and rats is highly Hsp90-specific as observed in *in vitro* autoradiography studies. Hsp90-specific binding of [ $^{11}$ C]YC-72-AB85 was further confirmed *in vivo* in rats.

**Table 2:** Physicochemical properties of [ $^{11}$ C]NMS-E973 and [ $^{11}$ C]YC-72-AB85.

Compound	Mw	LogD	tPSA ( $\text{\AA}^2$ )	HBD	Hsp90 $\alpha$ activity (nM)	Brain SUV 60 min p.i.*	Blood clearance (SUV) 10/60 min p.i.*
[ $^{11}$ C]NMS-E973	454.4	1.0	151.2	3	10 (DC <sub>50</sub> ) [207]	1.6	3.5
[ $^{11}$ C]YC-72-AB85	361.4	2.2	103.0	3	19 (IC <sub>50</sub> ) [209]	< 0.1	1.4

\*Determined in NMRI-mice.

NMS-E973 and YC-72-AB85 are both Hsp90 inhibitors targeting the N-terminal ATP binding site. The resorcinol moiety of NMS-E973 interacts with the adenosine pocket [207]. Whereas YC-72-AB85 mediates this interaction *via* its aminopyrimidine functional group [209]. This nicely illustrates the diversity of moieties that can be used to target Hsp90. Another resorcinol containing compound, Onalespiib (**Figure 4, Resorcinol in Chapter I**), was used in studies with [ $^{11}$ C]YC-72-AB85. This compound was successfully evaluated in preliminary studies on a murine glioma model [305]. However, in our studies, only low BBB permeation of Onalespiib was observed. Although physicochemical parameters (**Table 1 in Chapter V**) imply free diffusion over the BBB [161]. NMS-E973 was previously reported to reduce the tumour volume of intracranial implanted melanoma. One explanation for the effectiveness of NMS-E973 and Onalespiib against brain cancers can be that implantation of the tumour cells induces BBB damage leading to

leaky vessels and increased passive diffusion. Ganetespib (**Figure 4, Resorcinol in Chapter I**), also a resorcinol bearing Hsp90 inhibitor, was successfully used to assess specific binding of [ $^{11}\text{C}$ ]NMS-E973  $\mu\text{PET}$  studies on B16.F10 melanoma bearing mice. However, reports regarding the effectiveness of Ganetespib in brain disorders are lacking. Resorcinol based compounds targeting the CNS cannabinoid receptors are described [326]. Hence it is not unthinkable that this structural class can be applied to target Hsp90 in CNS.

Based on physicochemical parameters (**Table 2**), [ $^{11}\text{C}$ ]YC-72-AB85 should more easily pass cellular membranes compared to [ $^{11}\text{C}$ ]NMS-E973. This is also observed *in vivo*, as [ $^{11}\text{C}$ ]YC-72-AB85 easily enters brain whereas almost no brain uptake of [ $^{11}\text{C}$ ]NMS-E973 was observed (**Chapter IV**). The blood clearance ( $\text{SUV}_{\text{blood}} 10/60 = 3.5$ ) of [ $^{11}\text{C}$ ]NMS-E973 as determined in NMRI-mice was more than double compared to that of [ $^{11}\text{C}$ ]YC-72-AB85 ( $\text{SUV}_{\text{blood}} 10/60 = 1.4$ ). This can also be attributed to the physicochemical properties of YC-72-AB85, which allow easier diffusion into blood cells with subsequent binding to intracellular Hsp90, which can lead to slower blood clearance.

All three blocking compounds used in **Chapter V** were assessed in a permeability assay on Madin-Darby Canine Kidney – MDR1 (MDCK-MDR1) cells in Novartis, Basel. The data is presented in **Table 3** under the form of personal communication. Permeability of YC-72-AB85 in the cells was highest followed by Onalespib and SNX-0723. However, Onalespib showed substantial efflux from the cells (efflux > 2 indicates P-gp affinity). YC-72-AB85 and SNX-0723 did not show substantial efflux by the P-gp receptor. Additionally, all compounds were administered to healthy mice *via* the i.v. route. After which blood and brain concentrations were determined (**Table 3**). Brain uptake was highest for YC-72-AB85 which was also sustained after 60 min. The brain concentration of SNX-0723 was lower than YC-72-AB85, but substantial. Whereas Onalespib was not able to permeate into brain. These data are clearly in line with  $\mu\text{PET}$  experiments conducted with [ $^{11}\text{C}$ ]YC-72-AB85.

**Table 3:** MDCK-MDR1 permeability assay of YC-72-AB85, SNX-0723 and Onalespib and blood and brain concentrations of these inhibitors as assessed by i.v. injection in healthy mice.

	MDCK-MDR1		Blood (ng/mL)*		Brain (ng/g)*		Brain/blood	
	Permeability	Efflux	5 min	60 min	5 min	60 min	5 min	60 min
	$10^{-6} \text{ cm.s}^{-1}$							
<b>YC-72-AB85</b>	13.8	0.9	420.5	113.6	1416.9	605.3	3.4	5.3
<b>SNX-0723</b>	7.1	1.0	205.1	42.9	955.3	324.5	4.7	7.6
<b>Onalespib</b>	11.7	4.5	142.4	14.7	< 5	< 5	NA	NA

\*Blood and brain concentrations determined in female CD1 mice following single 1 mg/kg dose by i.v. injection. NA = not applicable. *Data provided by Dr. E. Briard, Novartis, Basel.*

For both Hsp90 tracers, elevated blood tracer levels were detected in tumour mice which could be significantly blocked with different non-structurally related Hsp90 inhibitors (PU-H71, Ganetespib and Onalespib). Blocking studies were also conducted in healthy mice. However, here the blocking effect was less pronounced. The site of

specific binding in blood remains elusive. We hypothesize that this can be either free Hsp90, shed from the tumour [100,104], metastatic B16.F10 melanoma cells [312] or peripheral blood mononuclear cells (PBMCs) which are reported to express elevated Hsp90 levels in different circumstances, as observed in studies in humans regarding exercise-heat acclimation [313], systemic Lupus Erythematosus [314] and B-cell malignancies [315].

Further research is needed to identify the cells that are responsible for the observed Hsp90-specific binding. This may be achieved by fluorescence-activated cell sorting (FACS) using a cell permeable fluorescent derivative of NMS-E973 or YC-72-AB85. Similar experiments were carried out with PU-FITC, which was able to permeate the cell membrane and was used to determine epichaperome levels in human blood tumours [94,327].

*In vitro* autoradiography studies on tumour and muscle (skeletal muscle and myocardium) sections, showed an interesting binding pattern of [<sup>11</sup>C]NMS-E973 with higher tracer concentration at the edges of the sections. However, in *ex vivo* autoradiography studies, tracer binding was more homogenous. Furthermore, binding of the tracer to muscle tissue was significantly lower in *ex vivo* experiments, suggesting the occurrence of changes of Hsp90 expression, distribution and/or inhibitor binding affinity in dying/hypoxic tissue [285]. This experiment is in a sense unique as it allows the assessment of Hsp90 in the same tissue, but in different conditions (*in vitro* vs *ex vivo*). It has been postulated that the interpretation of data acquired from biosampling highly depends on the followed procedures (e.g. tissue sampling can induce hypoxia or hypothermia). In the particular case of Hsp90, which is mediated by different stress factors, interpretation of molecular data can highly depend on the time and procedure of tissue sampling and clear differences in *ante*- and *post*-mortem conditions have been observed (e.g. hypoxia is a regulator of translocation of Hsp90 to the cell membrane and extracellular matrix (ECM)) [275,306,310]. In this respect, Hsp90 PET provides a unique tool to study Hsp90 *in vivo*.

[<sup>11</sup>C]NMS-E973 was extensively evaluated in B16.F10 melanoma bearing mice in  $\mu$ PET studies and in an *ex vivo* biodistribution study 60 min p.i. Although absolute tracer uptake in the tumour was relatively low, it was determined to be highly Hsp90-specific. A limitation of this study was the comparison of *ex vivo* blocking study data acquired in B16.F10 inoculated C57BL/6 mice with healthy NMRI-mice, two different mouse species. Similar studies were conducted with [<sup>11</sup>C]YC-72-AB85 where tracer uptake in B16.F10 melanoma inoculated mice was compared with healthy mice of the identical strain. At this point, head-to-head comparison of [<sup>11</sup>C]NMS-E973 with [<sup>11</sup>C]YC-72-AB85 is not possible as B16.F10 melanoma uptake was only assessed with [<sup>11</sup>C]YC-72-AB85 in an *ex vivo* biodistribution study 10 min p.i. Preferentially, [<sup>11</sup>C]YC-72-AB85 needs to be evaluated in  $\mu$ PET studies on B16.F10 melanoma bearing mice to correctly compare [<sup>11</sup>C]NMS-E973 with [<sup>11</sup>C]YC-72-AB85. Later on, this can be extended to other tumour models or other disease models (inflammation, cardiac diseases [328,329]).

Based on preliminary data obtained with [<sup>11</sup>C]NMS-E973, researchers of the EU-funded EUDARIO clinical trial which investigate Hsp90 in patients harbouring metastatic ovarian cancer are interested in introducing Hsp90 PET in a sub-study on a small patient population (n = 6). Before engaging in a clinical study, head-to-head  $\mu$ PET studies with

[<sup>11</sup>C]NMS-E973 and [<sup>11</sup>C]YC-72-AB85 need to be conducted in an ovarian cancer mouse model to select the best tracer for further studies.

Although specificity of binding in different organs and tumour tissue was determined for both Hsp90 tracers, still questions remain concerning the exact cellular (tumour cells, blood cells, neurons, glial cells) subcellular (cytoplasm, mitochondria, nucleus) or molecular (Hsp90 $\alpha$ , Hsp90 $\beta$ , 94 kDa glucose regulated protein (Grp94), tumour necrosis factor receptor associated protein 1 (TRAP1) or eHsp90) localisation and binding of the saturable Hsp90 pool. Because of limitations of PET resolution, these questions could not be answered in the performed studies. Of note, fluorescence microscopy studies with Hsp90 antibodies in **Chapter IV** indicated the presence of Hsp90 in the nucleus and the cell membrane of different tumour cells and tissue. In this regard, fluorescent probes, based on small molecule Hsp90 inhibitors (NMS-E973 or YC-72-AB85) can aid in the elucidation of the exact (sub)cellular location of tracer binding in tumour, brain and blood.

All the PET tracers evaluated in this thesis were radiolabelled with carbon-11. The  $T_{1/2}$  of 20.4 min limits patient exposure to radioactivity and allows multiple scans in the same subject even within the same day. Due to presence of stable carbon in all small molecules, carbon-11 can be integrated in many drug structures, with some (radio)chemical limitations, without altering biological activity. Carbon-11 is also the radionuclide of choice in initial, preliminary research and lead identification as radiosynthesis is quick and mostly straightforward. However, the short  $T_{1/2}$  is also a disadvantage as only a limited number of experiments/scans can be performed with one produced batch, which is not cost-efficient. When advancing to larger clinical studies, fluorine-18 labelled derivatives are preferred. The  $T_{1/2}$  of 109.8 min allows multiple patients to be scanned with one production batch and to extended scanning periods, which is favourable in case of slow tracer kinetics. To allow for a broader application and more cost efficient translation to the clinic, fluorine-18 derivatives of NMS-973/YC-72-AB85 will need to be developed.

HDAC6 and Hsp90 are closely related as discussed throughout this dissertation. Both proteins are essential in general homeostasis but detrimental overexpression of both entities is observed and implied in multiple diseases (cancer, CNS disorders). Moreover, Hsp90 is essential for the proper folding of HDAC6 and activation of Hsp90 is mediated by HDAC6 [48,51]. Research is also focussing on the development of HDAC6-Hsp90 dual inhibitors [143]. [<sup>11</sup>C]KB631 and Hsp90 PET tracers, [<sup>11</sup>C]NMS-E973 and [<sup>11</sup>C]YC-72-AB85 were evaluated in *in vitro* autoradiography studies on B16.F10 melanoma and PC3 prostate carcinoma sections where specific and heterogeneous binding was observed for all of the tracers (**Chapter III, Chapter IV, Chapter V**). All tracers showed low but specific tumour binding in  $\mu$ PET studies conducted on B16.F10 melanoma bearing mice. HDAC6 and Hsp90 are also essential in folding, maturation and activation of nuclear hormone receptors (androgen receptors (AR), glucocorticoid receptor (GR)), enabling nuclear transfer, and ultimately leading to transcription of target genes such as prostate specific antigen (PSA), which is an important marker in prostate carcinoma [138]. The Hsp90-HDAC6 regulating network is also involved in (triple negative) breast cancer where single and combined anti-Hsp90/HDAC6 therapy yielded beneficial results [330]. In this respect, Hsp90 and HDAC6 PET can be used in gynaecological malignancies, to monitor Hsp90 and/or HDAC6

inhibitor treatment. A good starting point can be to extend the evaluation of [<sup>11</sup>C]KB631, [<sup>11</sup>C]NMS-E973 and [<sup>11</sup>C]YC-72-AB85 to prostate, breast or ovarian carcinoma xenograft mouse models.

### 3. FUTURE PERSPECTIVES

#### Further preclinical evaluation and tracer selection for clinical evaluation

[<sup>18</sup>F]Bavarostat can be evaluated in preclinical oncological studies and compared head-to-head with [<sup>11</sup>C]KB631 in the B16.F10 tumour model. This can later be extended to other tumour models (SKOV-3 or PC3).

Future perspectives for experiments with [<sup>11</sup>C]NMS-E973 and [<sup>11</sup>C]YC-72-AB85 are depicted in **Figure 1**.

Head-to-head studies with [<sup>11</sup>C]NMS-E973, and [<sup>11</sup>C]YC-72-AB85 in tumour models (B16.F10 melanoma and SKOV-3 ovarian cancer) can be conducted. The most promising tracer can advance to the EUDARIO sub-study. If [<sup>11</sup>C]YC-72-AB85 outperforms [<sup>11</sup>C]NMS-E973 it will be used as a multiple purpose tracer in CNS and malignant conditions.

Development and evaluation of fluorine-18 Hsp90 tracer analogues which can be used for quantification of tumour or brain Hsp90 occupancy of clinically used Hsp90 inhibitors such as Ganetespib, PU-H71 or Onalespib in different tumour or brain disease models (AD, PD, glioma).

Carbon-11, and at a later stage, [<sup>18</sup>F]YC-72-AB85 brain Hsp90 PET studies (control and blocking) can be performed in rhesus monkeys with arterial sampling according to an earlier reported protocol [331] to verify whether results in rats and mice can be translated to non-human primate as a last step towards first-in-man evaluation of the tracer.

#### Clinical studies

Implementation of [<sup>11</sup>C]NMS-E973 or [<sup>11</sup>C]YC-72-AB85 PET in the EUDARIO sub-study in patients harbouring ovarian cancer. Hsp90 inhibitor (Ganetespib) therapy can be followed up and dose occupancy studies can be conducted.

First-in-man evaluation of carbon-11 and/or [<sup>18</sup>F]YC-72-AB85 in CNS of healthy patients or patients with CNS disorders (neurodegenerative diseases, epilepsy).

#### *In vitro* studies

NMS-E973 and YC-72-AB85 can be evaluated in binding assays in which the affinity and selectivity for the different Hsp90 paralogues can be determined head-to-head.

Identification of the (sub)cellular location or molecular form of Hsp90 (Hsp90 $\alpha$  Hsp90 $\beta$ , eHsp90, Grp94, TRAP1, epichaperome,...) tracer binding with fluorescent Hsp90 probes, based on NMS-E973 or YC-72-AB85.

Tritium labelled derivatives of studied compounds allow high-throughput competition binding studies to determine  $K_i$  values or  $B_{max}$  of new candidate Hsp90 PET tracers. This will also allow high-throughput *in vitro* characterization of Hsp90 expression in cells and tumour sections from animal models or patients.

### Other disease areas

Hsp90 PET imaging can be expanded to inflammation and wound healing or cardiovascular diseases [328,329].

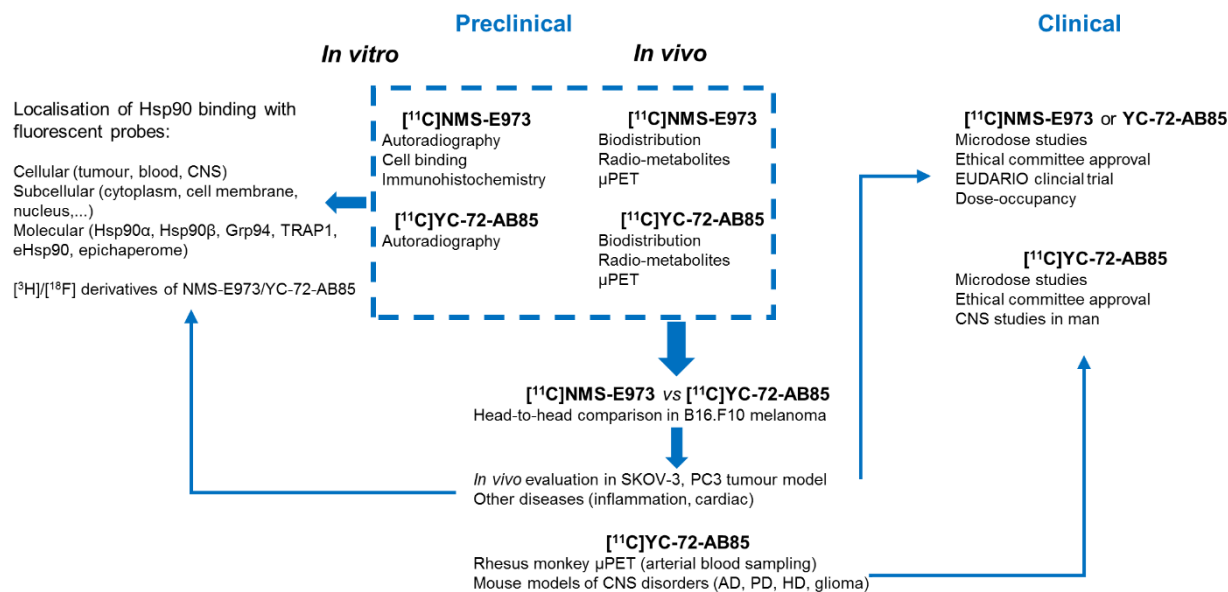


**Figure 1:** Future perspectives of *in vitro* and *in vivo* studies with Hsp90 tracers [ $^{11}C$ ]NMS-E973 and [ $^{11}C$ ]YC-72-AB85. Dashed box indicates performed *in vitro* and *in vivo* experiments. Thickness of arrow is indicative for the time span at which experiments can be conducted. Thicker arrows indicate experiments in the near future.

## SUMMARY

Positron emission tomography (PET) is a translational, highly sensitive, *in vivo* molecular imaging technique that visualizes the dynamic biodistribution of positron-emitting radiotracers. The specific high-affinity interaction of PET radiopharmaceuticals thereby allows quantification of the expression of their target biological molecules. Which can serve as *in vivo* biomarkers for molecular processes in health and disease. Other imaging modalities such as Magnetic resonance imaging (MRI) or X-ray imaging provide mostly high-resolution anatomic information but limited information on specific molecular events.

PET radiotracers can be radiolabelled with positron-emitting isotopes of biologically relevant elements such as C, N, O and F. These are frequently found in biomolecules and medicinal compounds that exhibit high affinity interactions with disease relevant biomarkers. It is thus possible to radiolabel these molecules without compromising the affinity. The resulting radiotracer is administered for a PET scan in 'tracer' amounts, avoiding pharmacological or toxicological effects.

*In vivo* visualisation of disease relevant biomarkers with PET allows to select patients that are likely to respond to a specific therapy. Further, the effect of the disease treatment can be closely monitored in-line with the "personalized medicine" approach. Aberrancies in cellular homeostasis reflected in altered expression of the biomarker can be detected with PET in considerably earlier stages, before morphological changes occur. Furthermore, PET can be applied in drug development to demonstrate *in vivo* pharmacodynamics of new drug candidates, demonstrate their target engagement and quantify their dose-occupancy relation.

Epigenetics is the study of the changes in gene expression that are unrelated to the DNA sequence itself. Post-translational modifications (PTMs) of histones play an important role as epigenetic modulators in chromatin remodelling and DNA transcription. One of the most studied epigenetic PTMs is the acetylation of evolutionarily conserved lysine residues located at the N-termini of histone tails, controlled by the opposing forces of histone acetyltransferase (HAT) and histone deacetylases (HDAC). An acetylated histone lysine leads to an uncondensed, active chromatin state, whereas the deacetylated histone lysine yields a higher degree of interaction between the negatively charged DNA and positively charged histone amino acid sequences, forming a condensed, mostly inactive, chromatin state. This forward and backward catalysis of acetylation contributes to the acetylated histone homeostasis which in turn influences the cellular homeostasis. Epigenetic modifications are thus determinant factors in the control of downstream gene expression and gene expression variability. HDAC activity is not limited to histones, as cytosolic proteins (heat shock proteins (Hsp), cortactin,  $\alpha$ -tubulin) have acetyl binding regions and can be targeted by HDACs. There are 18 HDACs described in literature, divided in 4 classes, each with distinct or

overlapping molecular functions. Their role in cancer is well documented with additional findings in other diseases including neurodegenerative disorders and cardiac diseases.

Hsp90 is a predominantly cytosolic, ATP-dependent, molecular chaperone important for folding, maturation and clearance of over 400 proteins. In a stress-free environment, Hsp90 makes up 1-2% of all the soluble cellular proteins, whereas this fraction can increase to 6-10% in cancer cells. Many of its client proteins are involved in oncogenic pathways and contribute to several hallmarks of cancer. Oncogenic Hsp90 adopts a tumour-specific conformation in multi-chaperone complexes with a 100-fold affinity increase for Hsp90 inhibitors. Further, high Hsp90 cell surface (eHsp90) levels are observed in different tumour cells (fibrosarcoma, melanoma, breast cancer) and this has been related to tumour metastasis. Over 15 Hsp90 inhibitors, targeting the ATP-binding pocket, have been evaluated in clinical trials. The role of Hsp90 in cancer is well documented in literature, however recent publications also inquire a role of Hsp90 in neurodegenerative diseases.

In our search for selective HDAC2 PET tracers, we evaluated *in vitro* and *in silico* activities of Santacruzamate A and candidate radiotracer derivatives thereof, reported as potent HDAC2-selective inhibitors. *In silico* docking studies were highly in line with *in vitro* affinity assays but marked discrepancies between reported activity values and the values obtained in our assays were observed for these compounds. To understand the structural basis of the activity of some of these inhibitors, molecular docking studies were performed to elucidate their interaction patterns and binding modes with HDAC2. Here, key  $\pi$ - $\pi$  interactions in the HDAC2 binding pocket were observed with high affinity HDAC inhibitors (Martinostat, SAHA and TSA) which did not occur for Santacruzamate A and derivatives. It was further observed in affinity assays that reported IC<sub>50</sub>-values could not be reproduced invalidating Santacruzamate A and derivatives for further development as PET tracers for visualisation of HDAC2.

Further we evaluated [<sup>11</sup>C]KB631, as a selective and high-affinity HDAC6 tracer in melanoma. HDAC6-specific binding was evaluated in *in vitro* autoradiography studies on tumour and brain sections and in *ex vivo* biodistribution studies in mice. Further, a pre-treatment biodistribution, with KB631, HDAC6-selective inhibitor Ricolinostat and Pan-HDAC inhibitor SAHA, was performed to assess the specificity of [<sup>11</sup>C]KB631 binding in healthy and B16.F10 melanoma bearing mice. The same mouse model was also used in *in vivo*  $\mu$ PET studies. In this proof of concept study, [<sup>11</sup>C]KB631 showed HDAC6-specific binding *in vitro* to PC3 and B16.F10 melanoma tumour sections and brain sections. In control and blocking *ex vivo* biodistribution studies in healthy and tumour mice, low brain uptake of the tracer was observed. *In vivo* HDAC6-specific binding of [<sup>11</sup>C]KB631 was also found in different organs of interest. In  $\mu$ PET studies in B16.F10 melanoma inoculated mice, rather low tumour uptake was observed, however this uptake was HDAC6-specific as it could be blocked by pre-treatment with Ricolinostat. Further research is needed to explore the full potential of [<sup>11</sup>C]KB631 to study the role of HDAC6 *in vivo* in cancer.

Brasca *et al.* reported the potent and selective Hsp90 inhibitor NMS-E973, which showed strong cytostatic effects in tumour cell lines. We developed and evaluated [<sup>11</sup>C]NMS-E973 as a PET tracer for *in vivo* visualisation of Hsp90. [<sup>11</sup>C]NMS-E973 shows strong binding to B16.F10 melanoma cells which can be inhibited with PU-H71 (200  $\mu$ M), a



non-structurally related Hsp90 inhibitor. [ $^{11}\text{C}$ ]NMS-E973 *in vitro* autoradiography showed Hsp90-specific binding on tissue slices of murine B16.F10 melanoma, LNCaP and PC3 prostate cancer, SKOV-3 ovary carcinoma and muscle tissue. *Ex vivo* autoradiography experiments were also conducted on muscle (skeletal muscle and myocardium) and B16.F10 melanoma tissue. Remarkable discrepancies were observed compared to *in vitro* data as in *in vitro* studies tracer binding to muscle was severely increased compared to the *in vivo* binding visualized by *ex vivo* autoradiography. This indicates the occurrence of changes in Hsp90 behaviour in dying/hypoxic and dead tissue. In a  $\mu\text{PET}$  study, fast and persistent *in vivo* tumour binding of [ $^{11}\text{C}$ ]NMS-E973 in B16.F10 melanoma was observed. Pre-treatment of B16.F10 melanoma mice with PU-H71 or Ganetespib completely blocked tumour accumulation of [ $^{11}\text{C}$ ]NMS-E973 and confirmed *in vivo* Hsp90 binding specificity. Hsp90-specific binding of [ $^{11}\text{C}$ ]NMS-E973 was also observed in blood, lungs and spleen of tumour-bearing animals but not in control animals. This suggests that Hsp90 is shedded from the tumour and spreads to the whole body, but this hypothesis needs to be evaluated further.

Although NMS-E973 was reported to enter brain, we did not observe significant brain uptake of [ $^{11}\text{C}$ ]NMS-E973. Therefore other Hsp90 inhibitors with physicochemical characteristics compatible with efficient brain uptake were explored. In cooperation with researchers from Novartis we identified [ $^{11}\text{C}$ ]YC-72-AB85 as a potential tracer for *in vivo* visualisation of brain Hsp90. [ $^{11}\text{C}$ ]YC-72-AB85 shows Hsp90-specific and saturable tumour binding, similar to [ $^{11}\text{C}$ ]NMS-E973 in B16.F10 melanoma mice. Hsp90-specific tracer binding is however also observed in brain *in vitro* (autoradiography) in rats and mice and *in vivo* ( $\mu\text{PET}$ ) in rats. Compared to control conditions, a clear increase of [ $^{11}\text{C}$ ]YC-72-AB85 rat brain uptake was observed after blocking with the non-brain permeable and non-structurally related Hsp90 inhibitor Onalespib. This increase was induced by tracer displacement from peripheral binding sites, resulting in a higher fraction of tracer available to bind brain Hsp90. Pre-treatment with Onalespib followed by i.v. injection of YC-72-AB85 or SNX-0723 resulted in tracer displacement from brain, indicating Hsp90-specific tracer binding in brain.

In conclusion, in the search for a selective HDAC2 PET tracer based on Santacruzamate A and derivatives we found remarked differences between our *in silico* and *in vitro* assays and reported literature concerning activity/affinity towards HDAC2. Hence, it was concluded that Santacruzamate A and derivatives could not be used as HDAC2 PET tracers. However, we developed and evaluated PET tracers, which enabled visualisation of HDAC6 and Hsp90 in oncological malignancies. Furthermore, [ $^{11}\text{C}$ ]YC-72-AB85 allows Hsp90 imaging in brain. All of these tracers were evaluated in *in vitro* autoradiography studies on tumour and/or rodent brain sections where they expressed specific binding. Specific binding was also observed for all tracers *in vivo* in a B16.F10 melanoma mouse model as assessed by blocking studies with HDAC6 or Hsp90 structural unrelated inhibitors. Further, elevated Hsp90 levels could be detected with both Hsp90 tracers in blood of tumour mice, which was not observed in healthy counterparts. These pre-clinical results indicate that these PET tracers show promise to be used to quantify HDAC6 or Hsp90 expression *in vivo* in tumours or brain and may allow quantification of target occupancy after treatment with HDAC6 or Hsp90 inhibitors in a clinical setting.

## SAMENVATTING

Positron emissie tomografie (PET) is een translationele, sensitieve *in vivo* moleculaire beeldvormingstechniek die de dynamische lichaamsverdeling van positron emitter speurstoffen in kaart kan brengen. De specifieke hoge affiniteitsinteractie van de PET-speurstof laat toe om de expressie van hun biologische doelwitmoleculen te kwantificeren. Andere beeldvormingsmodaliteiten zoals kernspin tomografie of Röntgen beeldvorming geven veelal een hoge resolutie anatomische weergave van het lichaam met beperkte informatie over moleculaire processen.

PET-speurstoffen kunnen radioactief gemerkt worden met positron emitter isotopen van biologisch relevante elementen zoals C, N, O en F. Deze elementen komen vaak voor in biomoleculen of geneesmiddelen die hoge affiniteitsinteracties hebben met ziekte-relevante biomerkers. Het is theoretisch mogelijk om deze moleculen radioactief te merken zonder de biomarker affiniteit te compromitteren. De radioactieve speurstof wordt bij een PET-onderzoek toegediend in uiterst kleine massahoeveelheden waardoor farmacologische of toxicologische (neven)werkingen worden vermeden.

*In vivo* beeldvorming van ziekte-relevante biomerkers met PET laat toe om patiënten te selecteren die waarschijnlijk zullen beantwoorden aan een specifieke therapie. Daarnaast is het ook mogelijk om de respons van de therapie te monitoren in lijn met de “gepersonaliseerde geneeskunde” benadering.

Afwijkingen van de cellulaire homeostase, die gereflecteerd worden in een gewijzigde expressie van de biomarker, kunnen met PET in een vroegtijdig stadium gedetecteerd worden, voorafgaand aan morfologische wijzigingen. Verder kan PET toegepast worden in geneesmiddelenontwikkeling voor de *in vivo* bepaling van farmacodynamische parameters, het aantonen van binding aan het doelwit en het bepalen van de dosis-bezettingsgraad relatie van het kandidaat geneesmiddel.

Epigenetica beschrijft de studie van wijzigingen in genexpressie die niet gerelateerd zijn aan de DNA sequentie van het gen. Dit wordt gemedieerd door posttranslationele modificaties (PTMs) op histonen, die leiden tot structurele wijzigingen van chromatine met verandering van DNA transcriptie tot gevolg. Eén van de meest bestudeerde PTMs is de acetylatie van lysine residu's op de zogenaamde histonstaarten. De acetylatie en de-acetylatie wordt gemedieerd door respectievelijk histon acetyltransferase (HAT) en histon deacetylase (HDAC). Geacetyleerd lysine, leidt tot een veelal open chromatinestructuur, waarop DNA transcriptie kan plaatsvinden. Gede-acetyleerd lysine daarentegen laat interacties toe tussen de positief geladen basische aminozuren (lysine, arginine) en het negatief geladen DNA. Dit gaat gepaard met de condensatie van de chromatinestreng waardoor DNA transcriptie wordt bemoeilijkt. Deze wisselwerking tussen acetylatie en de-acetylatie beïnvloedt de geacetyleerde chromatinehomeostase die een effect heeft op de algemene celhomeostase. Epigenetische modificaties zijn dus belangrijke regulatoren van de genexpressie en genexpressie variabiliteit. Niet enkel histonen zijn substraten van HDAC, cytosolaire eiwitten (heat shock proteins (Hsp), cortactin en  $\alpha$ -tubuline), alsook verschillende

transcriptiefactoren kunnen acetyl bindingsdomeinen bezitten. Tot nu toe zijn 18 HDACs beschreven in de literatuur, met specifieke maar ook overlappende moleculaire functies. Algemeen is de rol van HDACs in kanker goed gedocumenteerd, maar HDACs spelen ook een rol in onder andere neurodegeneratie en hart- en vaatandoeningen.

Het moleculaire chaperon Hsp90, vooral terug te vinden in het cytosol van cellen, is afhankelijk van ATP voor het vouwen, matureren en verwijderen van meer dan 400 proteïnen. Hsp90 maakt tot 2% uit van de totale cellulaire eiwitpopulatie. Deze fractie kan stijgen tot 6-10% in kankercellen door blootstelling aan cellulaire stress. Veel van de "cliënt"-eiwitten die gevouwen worden door Hsp90 zijn betrokken in moleculaire processen die kanker veroorzaken. In een tumorcel bevindt Hsp90 zich in een stresstoestand waardoor Hsp90 een functioneel netwerk vormt met andere chaperones. Hierdoor zal de affiniteit voor Hsp90-inhibitoren met een factor 100 toenemen. In tumorcellen en bij wondheling wordt Hsp90 ook actief getransporteerd naar de celmembranen en de extracellulaire matrix (ECM). Hoge expressie van extracellulair Hsp90 (eHsp90) werd waargenomen bij verschillende kankers (fibrosarcoom, melanoom, borstkankers) en in verband gebracht met het metastaseringsproces.

Meer dan 15 Hsp90-inhibitoren werden reeds geëvalueerd in klinische studies. De rol van Hsp90 in kanker is goed gedocumenteerd en recente publicaties suggereren ook een rol van Hsp90 bij neurodegeneratieve aandoeningen.

In onze zoektocht naar een selectieve HDAC2-PET-speurstof werden verschillende moleculen uit de literatuur, gebaseerd op Santacruzamate A, *in vitro* en *in silico* geëvalueerd. Deze moleculen werden beschreven als potente en selectieve HDAC2-inhibitoren. De resultaten van de *in silico* studies lagen in lijn met resultaten verkregen met *in vitro* affiniteitsbepalingen. Echter, markante discrepanties werden opgemerkt ten opzichte van de eerder gerapporteerde affiniteitswaarden. Moleculaire dockingstudies werden uitgevoerd om een beter beeld te krijgen van de belangrijkste moleculaire interacties van de gesynthetiseerde verbindingen met het HDAC2-enzyme. In controle dockingstudies met referentiemoleculen (Martinostat, SAHA, TSA) werden belangrijke  $\pi$ - $\pi$  interacties opgemerkt, die niet aanwezig waren bij Santacruzamate A en derivaten. De affiniteit van de verschillende moleculen voor HDAC2 werd bepaald in 2 onafhankelijke laboratoria aan de hand van twee verschillende bepalingmethoden. Hieruit bleek dat de gerapporteerde waarden niet gereproduceerd konden worden en dat deze moleculen geen affiniteit voor HDAC2 vertoonden. Santacruzamate A en derivaten zijn dus niet geschikt als HDAC2-inhibitoren en worden ook niet verder ontwikkeld als HDAC2-PET-speurstof.

Verder hebben we [<sup>11</sup>C]KB631, een selectieve en potente HDAC6-speurstof, gebruikt om HDAC6-expressie in melanomen op te sporen. Deze spurstof werd gevalideerd in *in vitro* autoradiografiestudies op hersen- en tumorcoups en in *ex vivo* biodistributiestudies in muizen. B16.F10-melanoom geïnculeerde en gezonde muizen werden voorbehandeld met KB631, HDAC6-selectieve inhibitor Ricolinostat of pan-HDAC-inhibitor SAHA, om de bindingsspecificiteit te bepalen in gezond weefsel en tumorweefsel. Verder werd ook een  $\mu$ PET-studie uitgevoerd, waar de weefselverdeling van de spurstof in controlecondities werd vergeleken na voorbehandeling van muizen met Ricolinostat, om zo *in vivo* de bindingsspecificiteit te evalueren. In *in vitro* studies bleek de spurstof specifiek te binden aan hersenweefsel, PC3-prostaatcarcinoom en B16.F10-melanoomsecties. In tumorweefsel werd een eerder

heterogeen bindingspatroon vastgesteld. In de *ex vivo* biodistributie-experimenten werd slechts beperkte hersenopname van [<sup>11</sup>C]KB631 geobserveerd. Algemeen werd een relatief lage opname van de speurstof in de tumor opgemerkt, maar deze opname was wel HDAC6 specifiek. Verder onderzoek is nodig om het potentieel van [<sup>11</sup>C]KB631 als HDAC6-tumor-speurstof uit te klaren.

NMS-E973 werd gerapporteerd door Brasca *et al.* als een potente en selectieve Hsp90-inhibitor met cytotoxische eigenschappen in verscheidene types tumorcellen. We hebben [<sup>11</sup>C]NMS-E973 ontwikkeld en gevalideerd als een PET-speurstof, voor visualisatie van Hsp90 in melanoom. De bindingspecificiteit van [<sup>11</sup>C]NMS-E973 aan B16.F10-melanoomcellen werd onderzocht door voorbehandeling met PU-H71, een niet-structureel verwante Hsp90-inhibitor. In *in vitro* en *ex vivo* autoradiografie-experimenten werd binding van [<sup>11</sup>C]NMS-E973 getest op verschillende tumorcoupes (B16.F10-melanoom, PC3- en LNCaP-prostaatacarcinoom, SKOV-3-ovariumcarcinoom) en spierweefsel.

Duidelijke verschillen werden opgemerkt tussen *in vitro* en *in vivo* binding van dezelfde spierweefselcoupes, waarbij binding van de speurstof *in vivo* opmerkelijk lager was dan *in vitro*. Dit duidt op een gewijzigde expressie en/of activiteit van Hsp90 in stervend/hypoxisch en dood weefsel. [<sup>11</sup>C]NMS-E973 werd extensief gevalideerd in een  $\mu$ PET-experiment, waar de speurstofopname in B16.F10-melanoom geïnoculeerde muizen in controlecondities vergeleken werd met voorbehandeling met 2 niet-structureel verwante Hsp90-inhibitoren (PU-H71 en Ganetespib). [<sup>11</sup>C]NMS-E973-binding in de tumor kon bijna volledig geïnhibeerd worden door voorbehandeling met beide verbindingen waardoor de specificiteit van [<sup>11</sup>C]NMS-E973 bewezen werd. Verder werden de resultaten verkregen in de  $\mu$ PET-studies bevestigd in *ex vivo* biodistributiestudies. Hier werd een duidelijke toename van Hsp90 in het bloed en sterk doorbloed weefsel (longen en milt) waargenomen in tumormuizen in vergelijking met gezonde muizen. Dit wijst op afscheiding van Hsp90 vanuit de tumor naar het bloed en verspreiding hiervan naar de rest van het lichaam. Deze hypothese dient echter verder onderzocht te worden.

Eerdere publicaties stelden dat NMS-E973 door de bloed-hersenbarrière (BHB) kon permeëren maar dit werd niet waargenomen in onze studies met [<sup>11</sup>C]NMS-E973. Daarom zijn we op zoek gegaan naar Hsp90-inhibitoren met fysicochemische parameters die hersenopname wel toelaten. In samenwerking met Novartis, hebben we [<sup>11</sup>C]YC-72-AB85 geïdentificeerd als potentieel molecule dat hieraan voldoet. In een gelijkaardige *ex vivo* biodistributiestudie op B16.F10-melanoom geïnoculeerde muizen, zoals uitgevoerd met [<sup>11</sup>C]NMS-E973, werd waargenomen dat [<sup>11</sup>C]YC-72-AB85 ook specifiek bindt aan tumorweefsel. Verder werd er ook *in vitro* specifieke binding van [<sup>11</sup>C]YC-72-AB85 waargenomen op hersencoupes van rat en muis alsook *in vivo* in een  $\mu$ PET-studie bij ratten. Voorbehandeling van de ratten met Onalespib induceerde een verhoogde hersenopname van de speurstof, gemedieerd door verzadiging van perifeer Hsp90. Deze verhoogde hersenopname kon significant verlaagd worden door injectie van YC-72-AB85 of SNX-0723, 20 min na start van de  $\mu$ PET-scan. Hieruit kon ook geconcludeerd worden dat Onalespib slechts in beperkte mate de BHB permeëert.

In conclusie, in de zoektocht naar een selectieve HDAC2-PET-tracer, gebaseerd op Santacruzamate A en derivaten, werden markante verschillen opgemerkt tussen onze *in silico* en *in vitro* studies en de gerapporteerde literatuur met

betrekking tot activiteit/affiniteit voor HDAC2. Hieruit werd besloten dat Santacruzamate A en derivaten daarvan niet verder gebruikt kunnen worden als HDAC2-PET-tracers. Verder werden PET-tracers voor visualisatie van HDAC6 en Hsp90 in oncologische condities ontwikkeld en geëvalueerd. [<sup>11</sup>C]YC-72-AB85, kon verder ook gebruikt worden om Hsp90 in het centrale zenuwstelsel te visualiseren. Al de onderzochte tracers werden *in vitro* geëvalueerd met autoradiografiestudies op tumor- en/of hersencoupees van knaagdieren. In deze experimenten bleken de tracers specifiek te binden. Specifieke binding van de tracers werd ook vastgesteld in *in vivo* experimenten in een B16.F10-melanoom muismodel, onderzocht door voorbehandelingstudies met structureel onverwante HDAC6- of Hsp90-inhibitoren. In het bloed van tumormuizen konden verhoogde Hsp90-niveaus opgemerkt worden met beide Hsp90-PET-tracers. Deze opregulatie van Hsp90 werd echter niet opgemerkt in het bloed van gezonde muizen. De uitgevoerde preklinische resultaten geven aan dat de geëvalueerde PET-tracers potentieel gebruikt kunnen worden om de expressie van HDAC6 of Hsp90 te quantificeren *in vivo* in kanker of hersenen. Verder zouden deze tracers gebruikt kunnen worden om een dosis-effectrelatie op te stellen in therapieën met HDAC6- of Hsp90-geneesmiddelen in een klinische setting.

## REFERENCES

1. Banta J, Richards CL. Quantitative epigenetics and evolution. *Heredity*. 2018;121:210–24.
2. Margueron R, Reinberg D. Chromatin structure and the inheritance of epigenetic information. *Nat. Rev. Genet.* 2010;11:285–96.
3. Tessarz P, Kouzarides T. Histone core modifications regulating nucleosome structure and dynamics. *Nat. Rev. Mol. Cell Biol.* 2014;15:703–8.
4. Kouzarides T. Chromatin Modifications and Their Function. *Cell*. 2007;128:693–705.
5. Gräff J, Mansuy IM. Epigenetic codes in cognition and behaviour. *Behav. Brain Res.* 2008;192:70–87.
6. Latham J a, Dent SYR. Cross-regulation of histone modifications. *Nat. Struct. Mol. Biol.* 2007;14:1017–24.
7. Falkenberg KJ, Johnstone RW. Histone deacetylases and their inhibitors in cancer, neurological diseases and immune disorders. *Nat. Rev. Drug Discov.* 2014;2:673–91.
8. Meier K, Brehm A. Chromatin regulation: How complex does it get? *Epigenetics*. 2014;9:37–41.
9. Saha RN, Pahan K. HATs and HDACs in neurodegeneration: a tale of disconcerted acetylation homeostasis. *Cell Death Differ.* 2006;13:539–50.
10. Wagner T, Brand P, Heinzel T, Krämer OH. Histone deacetylase 2 controls p53 and is a critical factor in tumorigenesis. *Biochim. Biophys. Acta.* 2014;1846:524–38.
11. De Ruijter AJM, van Gennip AH, Caron HN, Kemp S, van Kuilenburg ABP. Histone deacetylases (HDACs): characterization of the classical HDAC family. *Biochem. J.* 2003;370:737–49.
12. Kelly RDW, Cowley SM. The physiological roles of histone deacetylase (HDAC) 1 and 2: complex co-stars with multiple leading parts. *Biochem. Soc. Trans.* 2013;41:741–9.
13. Dallavalle S, Pisano C, Zunino F. Development and therapeutic impact of HDAC6-selective inhibitors. *Biochem. Pharmacol.* 2012;84:756–65.
14. Clocchiatti A, Florean C, Brancolini C. Class IIa HDACs: From important roles in differentiation to possible implications in tumorigenesis. *J. Cell. Mol. Med.* 2011;15:1833–46.
15. Seidel C, Schnakenburger M, Dicato M, Diederich M. Histone deacetylase 6 in health and disease. *Epigenomics*. 2015;7:103–18.
16. North BJ, Verdin E. Sirtuins: Sir2-related NAD-dependent protein deacetylases. *Genome Biol.* 2004;5:224.
17. Sun L, Marin de Esvikova C, Bian K, Achille A, Telles E, Pei H, et al. Programming and Regulation of Metabolic Homeostasis by HDAC11. *EBioMedicine*. 2018;33:157–68.
18. Bhaskara S. Histone deacetylase 11 as a key regulator of metabolism and obesity. *EBioMedicine*. 2018;35:27–8.
19. Qiu X, Xiao X, Li N, Li Y. Histone deacetylases inhibitors (HDACis) as novel therapeutic application in various clinical diseases. *Prog. Neuro-Psychopharmacology Biol. Psychiatry*. 2017;72:60–72.
20. West AC, Johnstone RW. New and emerging HDAC inhibitors for cancer treatment. *J Clin Invest*. 2014;124:30–9.
21. Agents S, Emerging A, Strategy A, Singh AK. Targeting Histone Deacetylases with Natural and Synthetic Agents: An Emerging Anticancer Strategy. *Nutrients*. 2018;6:10:E731
22. Penney J, Tsai L-H. Histone deacetylases in memory and cognition. *Sci. Signal*. 2014;7:re12.
23. Broide RS, Redwine JM, Aftahi N, Young W, Bloom FE, Winrow CJ. Distribution of Histone Deacetylases 1–11 in the Rat Brain. *J. Mol. Neurosci.* 2007;31:281–7.
24. Volmar C-H, Wahlestedt C. Histone deacetylases (HDACs) and brain function. *Neuroepigenetics*. 2015;1:20–7.
25. Reolon GK, Maurmann N, Werenicz A, Garcia VA, Schröder N, Wood MA RR. Posttraining systemic administration of the histone deacetylase inhibitor sodium butyrate ameliorates aging-related memory decline in rats. *Behav. Brain Res.* 2011;221:329–32.
26. Gräff J, Tsai LH. The potential of HDAC inhibitors as cognitive enhancers. *Annu. Rev. Pharmacol. Toxicol.* 2013;53:311–30.
27. Morris MJ, Mahgoub M, Na ES, Pranav H, Monteggia LM. Loss of histone deacetylase 2 improves working memory and accelerates extinction learning. *J. Neurosci.* 2013;33:6401–11.
28. Covington HE, Maze I, LaPlant QC, Vialou VF, Ohnishi YN, Berton O, et al. Antidepressant actions of histone deacetylase inhibitors. *J. Neurosci.* 2009;29:11451–60.
29. Jochems J, Boulden J, Lee BG, Blendy J a, Jarpe M, Mazitschek R, et al. Antidepressant-Like Properties of Novel HDAC6-Selective Inhibitors with Improved Brain Bioavailability. *Neuropsychopharmacology*. 2013;39:389–400.

30. Balasubramanian S, Verner E, Buggy JJ. Isoform-specific histone deacetylase inhibitors: The next step? *Cancer Lett.* 2009;280:211–21.
31. Zwergel C, Stazi G, Valente S, Mai A. Histone Deacetylase Inhibitors: Updated Studies in Various Epigenetic-Related Diseases. *J. Clin. epigenetics.* 2016;2:1–15.
32. Marsh M, Narramore R, Chapple K, Lobo J, Wild JR, Corfe BM. Histone deacetylase inhibitors: Recent outcomes from clinical trials and the implications for oncology treatment approaches. *Clin. Investig.* 2013;3:571–94.
33. Suraweera A, O'Byrne KJ, Richard DJ. Combination Therapy With Histone Deacetylase Inhibitors (HDACi) for the Treatment of Cancer: Achieving the Full Therapeutic Potential of HDACi. *Front. Oncol.* 2018;8:1–15.
34. Ahmad Ganai S, Ramadoss M, Mahadevan V. Histone Deacetylase (HDAC) Inhibitors - emerging roles in neuronal memory, learning, synaptic plasticity and neural regeneration. *Curr. Neuropharmacol.* 2015;14:55–71.
35. Gupta P, C. Reid R, Iyer A, J. Sweet M, P. Fairlie D. Towards Isozyme-Selective HDAC Inhibitors For Interrogating Disease. *Curr. Top. Med. Chem.* 2012;12:1479–99.
36. Witt O, Deubzer HE, Milde T, Oehme I. HDAC family: What are the cancer relevant targets? *Cancer Lett.* 2009;277:8–21.
37. Wagner FF, Weiwler M, Lewis MC, Holson EB. Small molecule inhibitors of zinc-dependent histone deacetylases. *Neurotherapeutics.* 2013;10:589–604.
38. Heimburg T, Kolbinger FR, Zeyen P, Ghazy E, Herp D, Schmidtkunz K, et al. Structure-based design and biological characterization of selective histone deacetylase 8 (HDAC8) inhibitors with anti-neuroblastoma activity. *J. Med. Chem.* 2017;8:10188–204.
39. Wang X, Wan RZ, Liu ZP. Recent advances in the discovery of potent and selective HDAC6 inhibitors. *Eur. J. Med. Chem.* 2018;143:1406–18.
40. Tavares MT, Shen S, Knox T, Hadley M, Kutil Z, Bařinka C, et al. Synthesis and Pharmacological Evaluation of Selective Histone Deacetylase 6 Inhibitors in Melanoma Models. *ACS Med. Chem. Lett.* 2017;8:1031–6.
41. Verdel A, Khochbin. Identification of a New Family of Higher Eukaryotic Histone Deacetylases. *Biochemistry.* 1999;274:2440–5.
42. Bertos NR, Gilquin B, Chan GKT, Yen TJ, Khochbin S, Yang XJ. Role of the tetradecapeptide repeat domain of human histone deacetylase 6 in cytoplasmic retention. *J. Biol. Chem.* 2004;279:48246–54.
43. Verdel A, Curtet S, Brocard MP, Rousseaux S, Lemerrier C, Yoshida M, et al. Active maintenance of mHDA2/mHDAC6 histone-deacetylase in the cytoplasm. *Curr. Biol.* 2000;10:747–9.
44. Haggarty SJ, Koeller KM, Wong JC, Grozinger CM, Schreiber SL. Domain-selective small-molecule inhibitor of histone deacetylase 6 (HDAC6)-mediated tubulin deacetylation. *Proc. Natl. Acad. Sci. U. S. A.* 2003;100:4389–94.
45. Li Y, Shin D, Kwon SH. Histone deacetylase 6 plays a role as a distinct regulator of diverse cellular processes. *FEBS J.* 2013;280:775–93.
46. Seigneurin-Berny D, Verdel a, Curtet S, Lemerrier C, Garin J, Rousseaux S, et al. Identification of components of the murine histone deacetylase 6 complex: link between acetylation and ubiquitination signaling pathways. *Mol. Cell. Biol.* 2001;21:8035–44.
47. Hook SS, Orian A, Cowley SM, Eisenman RN. Histone deacetylase 6 binds polyubiquitin through its zinc finger (PAZ domain) and copurifies with deubiquitinating enzymes. *Proc. Natl. Acad. Sci. U. S. A.* 2002;99:13425–30.
48. Helleputte L Van, Benoy V, Bosch L Van Den. The role of histone deacetylase 6 ( HDAC6 ) in neurodegeneration. *Res. Rep. Biol.* 2014;5:1–13.
49. Boyault C, Sadoul K, Pabion M, Khochbin S. HDAC6, at the crossroads between cytoskeleton and cell signaling by acetylation and ubiquitination. *Oncogene.* 2007;26:5468–76.
50. Kawaguchi Y, Kovacs JJ, McLaurin A, Vance JM, Ito A, Yao TP. The deacetylase HDAC6 regulates aggresome formation and cell viability in response to misfolded protein stress. *Cell.* 2003;115:727–38.
51. Sakamoto KM, Aldana-Masangkay GI. The role of HDAC6 in cancer. *J. Biomed. Biotechnol.* 2011;2011:1–10.
52. Simões-Pires C, Zwick V, Nurisso A, Schenker E, Carrupt P-A, Cuendet M. HDAC6 as a target for neurodegenerative diseases: what makes it different from the other HDACs? *Mol. Neurodegener.* 2013;8:1–16.
53. Krämer OH, Mahboobi S, Sellmer A. Drugging the HDAC6-HSP90 interplay in malignant cells. *Trends Pharmacol. Sci.* 2014;35:501–9.
54. Lee YS, Lim KH, Guo X, Kawaguchi Y, Gao Y, Barrientos T, et al. The cytoplasmic deacetylase HDAC6 is required for efficient oncogenic tumorigenesis. *Cancer Res.* 2008;68:7561–9.
55. Kanno K, Kanno S, Nitta H, Uesugi N, Sugai T, Masuda T, et al. Overexpression of histone deacetylase 6 contributes to accelerated migration and invasion activity of hepatocellular carcinoma cells. *Oncol. Rep.* 2012;28:867–73.
56. Haakenson J, Zhang X. HDAC6 and Ovarian Cancer. *Int. J. Mol. Sci.* 2013;14:9514–35.

57. Bazzaro M, Lin Z, Santillan A, Lee MK, Wang MC, Chan KC, et al. Ubiquitin proteasome system stress underlies synergistic killing of ovarian cancer cells by bortezomib and a novel HDAC6 inhibitor. *Clin. Cancer Res.* 2008;14:7340–7.
58. Amengual JE, Johannet P, Lombardo M, Zullo K, Hoehn D, Bhagat G, et al. Dual targeting of protein degradation pathways with the selective HDAC6 inhibitor ACY-1215 and bortezomib is synergistic in lymphoma. *Clin. Cancer Res.* 2015;21:4663–75.
59. Hideshima T, Bradner JE, Wong J, Chauhan D, Richardson P, Schreiber SL, et al. Small-molecule inhibition of proteasome and aggresome function induces synergistic antitumor activity in multiple myeloma. *Proc. Natl. Acad. Sci. U. S. A.* 2005;102:8567–72.
60. Ding N, Ping L, Feng L, Zheng X, Song Y, Zhu J. Histone deacetylase 6 activity is critical for the metastasis of Burkitt's lymphoma cells. *Cancer Cell Int.* 2014;14:1–7.
61. Woan KV., Lienlaf M, Perez-Villarroel P, Lee C, Cheng F, Knox T, et al. Targeting histone deacetylase 6 mediates a dual anti-melanoma effect: Enhanced antitumor immunity and impaired cell proliferation. *Mol. Oncol.* 2015;9:1447–57.
62. Lienlaf M, Perez-Villarroel P, Knox T, Pabon M, Sahakian E, Powers J, et al. Essential role of HDAC6 in the regulation of PD-L1 in melanoma. *Mol. Oncol.* 2016;10:735–50.
63. Lernoux M, Schnekenburger M, Dicato M, Diederich M. Anti-cancer effects of naturally derived compounds targeting histone deacetylase 6-related pathways. *Pharmacol. Res.* 2018;129:337–56.
64. Fischer A, Sananbenesi F, Mungenast A, Tsai L-H. Targeting the correct HDAC(s) to treat cognitive disorders. *Trends Pharmacol. Sci.* 2010;31:605–17.
65. Southwood CM, Peppi M, Dryden S, Tainsky M a., Gow A. Microtubule deacetylases, SirT2 and HDAC6, in the nervous system. *Neurochem. Res.* 2007;32:187–95.
66. Fukada M, Hanai A, Nakayama A, Suzuki T, Miyata N, Rodriguiz RM, et al. Loss of deacetylation activity of Hdac6 affects emotional behavior in mice. *PLoS One.* 2012;7:e30924.
67. Leyk J, Goldbaum O, Noack M, Richter-Landsberg C. Inhibition of HDAC6 Modifies Tau Inclusion Body Formation and Impairs Autophagic Clearance. *J. Mol. Neurosci.* 2014;55:1031–46.
68. Richter-Landsberg C, Leyk J. Inclusion body formation, macroautophagy, and the role of HDAC6 in neurodegeneration. *Acta Neuropathol.* 2013;126:793–807.
69. d'Ydewalle C, Bogaert E, Van Den Bosch L. HDAC6 at the Intersection of Neuroprotection and Neurodegeneration. *Traffic.* 2012;13:771–9.
70. Espallergues J, Teegarden SL, Veerakumar A, Bouliden J, Jochems J, Chan M, et al. HDAC6 regulates GR signaling in serotonin pathways with critical impact on stress resilience. *J Neurosci.* 2012;32:4400–16.
71. Li T, Zhang C, Hassan S, Liu X, Song F, Chen K, et al. Histone deacetylase 6 in cancer. *J. Hematol. Oncol.* 2018;11:1–10.
72. Schopf Florian H., Biebl Maximilian M. BJ. The Hsp90 chaperone machinery. *Mol. Cell Biol.* 2017;18:345–60.
73. Finka A, Goloubinoff P. Proteomic data from human cell cultures refine mechanisms of chaperone-mediated protein homeostasis. *Cell Stress Chaperones.* 2013;18:591–605.
74. Jee H. Size dependent classification of heat shock proteins: a mini-review. *J. Exerc. Rehabil.* 2016;12:255–9.
75. Echeverría PC, Mazaira G, Erlejman A, Gomez-sanchez C, Pilipuk GP, Galigniana MD, et al. Nuclear import of the glucocorticoid receptor-hsp90 complex through the nuclear pore complex is mediated by its interaction with Nup62 and importin beta. *Mol. Cell Biol.* 2009;29:4788–97.
76. Zgajnar NR, Daneri-Becerra C, Galigniana MD, Mazaira GI, Lotufo CM. Gene expression regulation by heat-shock proteins: the cardinal roles of HSF1 and Hsp90. *Biochem. Soc. Trans.* 2017;46:51–65.
77. Dong H, Zou M, Bhatia A, Jayaprakash P, Hofman F, Ying Q, et al. Breast Cancer MDA-MB-231 Cells Use Secreted Heat Shock Protein-90alpha (Hsp90α) to Survive a Hostile Hypoxic Environment. *Sci. Rep.* 2016;6:1–9.
78. Wong KSK, Houry W. Hsp90 at the crossroads of genetics and epigenetics. *Cell Res.* 2006;16:742–9.
79. Chen B, Piel WH, Gui L, Bruford E, Monteiro A. The HSP90 family of genes in the human genome: Insights into their divergence and evolution. *Genomics.* 2005;86:627–37.
80. Erlejman AG, Lagadari M, Toneatto J, Piwien-Pilipuk G, Galigniana MD. Regulatory role of the 90-kDa-heat-shock protein (Hsp90) and associated factors on gene expression. *Biochim. Biophys. Acta - Gene Regul. Mech.* 2014;1839:71–87.
81. Whitesell L, Lindquist SL. HSP90 and the chaperoning of cancer. *Nat. Rev. Cancer.* 2005;5:761–72.
82. Pearl LH, Prodromou C. Structure and mechanism of the Hsp90 molecular chaperone machinery. *Annu. Rev. Biochem.* 2006;75:271–94.
83. Sidera K, Patsavoudi E. Extracellular HSP90. Conquering the cell surface. *Cell Cycle.* 2008;7:1564–8.
84. Barrott JJ, Haystead TJ. Hsp90, an unlikely ally in the war on cancer. *FEBS J.* 2013;280:1381–96.
85. Hanahan D, Weinberg R. Hallmarks of cancer: the next generation. *Cell.* 2011;144:646–74



86. Thirstrup K, Sotty F, Montezinho LCP, Badolo L, Thougard A, Kristjánsson M, et al. Linking HSP90 target occupancy to HSP70 induction and efficacy in mouse brain. *Pharmacol. Res.* 2016;104:197–205.
87. Bose S, Cho J. Targeting chaperones, heat shock factor-1, and unfolded protein response: Promising therapeutic approaches for neurodegenerative disorders. *Ageing Res. Rev.* 2017;35:155–75.
88. Buchner J, Li J. Structure, Function and Regulation of the Hsp90 Machinery. *Biomed. J.* 2013;36:106–17.
89. Siligardi G, Hu B, Panaretou B, Piper PW, Pearl LH, Prodromou C. Co-chaperone regulation of conformational switching in the Hsp90 ATPase cycle. *J. Biol. Chem.* 2004;279:51989–98.
90. Li J, Soroka J, Buchner J. The Hsp90 chaperone machinery: Conformational dynamics and regulation by co-chaperones. *Biochim. Biophys. Acta - Mol. Cell Res.* 2012;1823:624–35.
91. Jhaveri K, Taldone T, Modi S, Chiosis G. Advances in the clinical development of heat shock protein 90 (Hsp90) inhibitors in cancers. *Biochim. Biophys. Acta.* 2012;1823:742–55.
92. Kamal A, Thao L, Sensintaffar J, Zhang L, Boehm MF, Fritz LC, et al. A high-affinity conformation of Hsp90 confers tumour selectivity on Hsp90 inhibitors. *Nature.* 2003;425:407–10.
93. Rodina A, Wang T, Yan P, Gomes ED, Dunphy MPS, Pillarsetty N, et al. The epichaperome is an integrated chaperome network that facilitates tumour survival. *Nature.* 2016;538:397–401.
94. Wang T, Rodina A, Dunphy MP, Corben A, Modi S, Guzman ML, et al. Chaperome heterogeneity and its implications for cancer study and treatment. *J. Biol. Chem.* 2019;294:2162–79.
95. Kishinevsky S, Wang T, Rodina A, Chung SY, Xu C, Philip J, et al. HSP90-incorporating chaperome networks as biosensor for disease-related pathways in patient-specific midbrain dopamine neurons. *Nat. Commun.* 2018;9:4345.
96. Joshi S, Wang T, Araujo TLS, Sharma S, Brodsky JL. Adapting to stress - chaperome networks in Cancer. *Nat. Rev. Cancer.* 2018;18:562–75.
97. Speranza G, Anderson L, Chen AP, Do K, Eugeni M, Weil M, et al. First-in-human study of the epichaperome inhibitor PU-H71: clinical results and metabolic profile. *Invest. New Drugs.* 2018;36:230–9.
98. Eustace BK, Jay DG. Extracellular roles for the molecular chaperone, hsp90. *Cell Cycle.* 2004;3:1098–100.
99. Becker B, Multhoff G, Farkas B, Wild P-J, Landthaler M, Stolz W, et al. Induction of Hsp90 protein expression in malignant melanomas and melanoma metastases. *Exp. Dermatol.* 2004;13:27–32.
100. Sidera K, Gaitanou M, Stellas D, Matsas R, Patsavoudi E. A critical role for HSP90 in cancer cell invasion involves interaction with the extracellular domain of HER-2. *J. Biol. Chem.* 2008;283:2031–41.
101. Li W, Sahu D, Tsen F. Secreted heat shock protein-90 (Hsp90) in wound healing and cancer. *Biochim. Biophys. Acta - Mol. Cell Res.* 2012;1823:730–41.
102. Zou M, Bhatia a., Dong H, Jayaprakash P, Guo J, Sahu D, et al. Evolutionarily conserved dual lysine motif determines the non-chaperone function of secreted Hsp90 $\alpha$  in tumour progression. *Oncogene.* 2017;36:2160–71.
103. Tsutsumi S, Scroggins B, Koga F, Lee M-J, Trepel J, Felts S, et al. A small molecule cell-impermeant Hsp90 antagonist inhibits tumor cell motility and invasion. *Oncogene.* 2008;27:2478–87.
104. Eustace BK, Sakurai T, Stewart JK, Yimlamai D, Unger C, Zehetmeier C, et al. Functional proteomic screens reveal an essential extracellular role for hsp90 $\alpha$  in cancer cell invasiveness. *Nat. Cell Biol.* 2004;6:507–14.
105. Crowe LB, Hughes PF, Alcorta D a, Osada T, Smith AP, Totzke J, et al. A fluorescent Hsp90 probe demonstrates the unique association between extracellular Hsp90 and malignancy in vivo. *ACS Chem. Biol.* 2017;12:1047–55.
106. Xintong Wang, Dianzheng An, Xinlei Wang, Xiaomeng Liu BL. Extracellular Hsp90 $\alpha$  clinically correlates with tumor malignancy and promotes migration and invasion in esophageal squamous cell carcinoma. *Onco. Targets Ther.* 2019;12:1119–28.
107. Hideaki I, Yohtalou T, Yoshinobu E, Riki O. Localization of HSP90 in rat brain. *Int. J. Biochem.* 1993;25:93–9.
108. Sidera K, Samiotaki M, Yfanti E, Panayotou G, Patsavoudi E. Involvement of cell surface HSP90 in cell migration reveals a novel role in the developing nervous system. *J. Biol. Chem.* 2004;279:45379–88.
109. Thomaidou D, Yfanti E, Patsavoudi E. Expression of the 4C5 antigen during development and after injury of the rat sciatic nerve. *J. Neurosci. Res.* 1996;46:24–33.
110. Lackie RE, Maciejewski A, Ostapchenko VG, Marques-Lopes J, Choy W-Y, Duennwald ML, et al. The Hsp70/Hsp90 chaperone machinery in neurodegenerative diseases. *Front. Neurosci.* 2017;11:254:1–23.
111. Ebrahimi-Fakhari D, Wahlster L, Mclean PJ. Molecular Chaperones in Parkinson's Disease – Present and Future. *J. Park. Dis.* 2011;1:299–320.
112. Wang B, Liu Y, Huang L, Chen J, Li JJ, Wang R, et al. A CNS-permeable Hsp90 inhibitor rescues synaptic dysfunction and memory loss in APP-overexpressing Alzheimer's mouse model via an HSF1-mediated mechanism. *Mol. Psychiatry.* 2017;22:990–1001.

113. Uryu K, Richter-Landsberg C, Welch W, Sun E, Goldbaum O, Norris EH, et al. Convergence of heat shock protein 90 with ubiquitin in filamentous  $\alpha$ -synuclein inclusions of  $\alpha$ -synucleinopathies. *Am. J. Pathol.* 2006;168:947–61.
114. Kakimura J-I, Kitamura Y, Takata K, Umeki M, Suzuki S, Shibagaki K, et al. Microglial activation and amyloid-beta clearance induced by exogenous heat-shock proteins. *FASEB J.* 2002;16:601–3.
115. Sidera K, Patsavoudi E. HSP90 inhibitors: current development and potential in cancer therapy. *Recent Pat. Anticancer. Drug Discov.* 2014;9:1–20.
116. McCleese JK, Bear MD, Fossey SL, Mihalek RM, Foley KP, Ying W, et al. The novel HSP90 inhibitor STA-1474 exhibits biologic activity against osteosarcoma cell lines. *Int. J. Cancer.* 2009;125:2792–801.
117. Kim S, Bajji A, Tangallapally R, Markovitz B, Trovato R, Shenderovich M, et al. Discovery of (2S)-1-[4-(2-{6-Amino-8-[(6-bromo-1,3-benzodioxol-5-yl)sulfanyl]-9H-purin-9-yl]ethyl)piperidin-1-yl]-2-hydroxypropan-1-one (MPC-3100), a Purine-Based Hsp90 Inhibitor. *J. med. chem.* 2012;55:7480–501.
118. Lundgren K, Zhang H, Brekken J, Huser N, Powell RE, Timple N, et al. BIIB021, an orally available, fully synthetic small-molecule inhibitor of the heat shock protein Hsp90. 2009;8:921–9.
119. Bussenius J, Blazey CM, Aay N, Anand NK, Arcalas A, Baik T, et al. Discovery of XL888: A novel tropane-derived small molecule inhibitor of HSP90. *Bioorganic Med. Chem. Lett.* 2012;22:5396–404.
120. Patel HJ, Patel PD, Ochiana SO, Yan P, Sun W, Patel MR, et al. Structure-activity relationship in a purine-scaffold compound series with selectivity for the endoplasmic reticulum Hsp90 paralog Grp94. *J. Med. Chem.* 2015;58:3922–43.
121. Nakashima T, Ishii T, Tagaya H, Seike T, Nakagawa H, Kanda Y, et al. New molecular and biological mechanism of antitumor activities of KW-2478, a novel nonansamycin heat shock protein 90 inhibitor, in multiple myeloma cells. *Clin. Cancer Res.* 2010;16:2792–802.
122. Sydor JR, Normant E, Pien CS, Porter JR, Ge J, Grenier L, et al. Development of 17-allylamino-17-demethoxygeldanamycin hydroquinone hydrochloride (IPI-504), an anti-cancer agent directed against Hsp90. *Proc. Natl. Acad. Sci. U. S. A.* 2006;103:17408–13.
123. Huang KH, Veal JM, Fadden RP, Rice JW, Eaves J, Strachan JP, et al. Discovery of novel 2-aminobenzamide inhibitors of heat shock protein 90 as potent, selective and orally active antitumor agents. *J. Med. Chem.* 2009;52:4288–305.
124. Woodhead AJ, Angove H, Carr MG, Chessari G, Congreve M, Coyle JE, et al. Discovery of (2,4-dihydroxy-5-isopropylphenyl)-[5-(4-methylpiperazin-1-ylmethyl)-1,3-dihydroisoindol-2-yl]methanone (AT13387), a novel inhibitor of the molecular chaperone Hsp90 by fragment based drug design. *J. Med. Chem.* 2010;53:5956–69.
125. Ge J, Normant E, Porter JR, Ali J a., Dembski MS, Gao Y, et al. Design, synthesis, and biological evaluation of hydroquinone derivatives of 17-amino-17-demethoxygeldanamycin as potent, water-soluble inhibitors of Hsp90. *J. Med. Chem.* 2006;49:4606–15.
126. Lee K-H, Lee J-H, Han S-W, Im S-A, Kim T-Y, Oh D-Y, et al. Antitumor activity of NVP-AUY922, a novel heat shock protein 90 inhibitor, in human gastric cancer cells is mediated through proteasomal degradation of client proteins. *Cancer Sci.* 2011;102:1388–95.
127. Menezes DL, Taverna P, Jensen MR, Abrams T, Stuart D, Yu GK, et al. The novel oral Hsp90 inhibitor NVP-HSP990 exhibits potent and broad-spectrum antitumor activities in vitro and in vivo. *Mol. Cancer Ther.* 2012;11:730–9.
128. Ohkubo S., Kodama Y., Muraoka H., Hitotsumachi H., Yoshimura C., Kitade M., et al. TAS-116, a highly selective inhibitor of heat shock protein 90 $\alpha$  and  $\beta$ , demonstrates potent antitumor activity and minimal ocular toxicity in preclinical models. *Mol. Cancer Ther.* 2015;14:14–22.
129. Stenderup K, Rosada C, Gavillet B, Vuagniaux G, Dam TN. Debio 0932, a new oral Hsp90 inhibitor, alleviates psoriasis in a xenograft transplantation model. *Acta Derm. Venereol.* 2014;94:672–6.
130. Jaeger AM, Whitesell L. HSP90: enabler of cancer adaptation. *Annu. Rev. Cancer Biol.* 2018;3:275–97.
131. Piper PW, Millson SH. Mechanisms of resistance to Hsp90 inhibitor drugs: A complex mosaic emerges. *Pharmaceuticals.* 2011;4:1400–22.
132. Butler LM, Ferraldeschi R, Armstrong HK, Centenera MM. Maximizing the Therapeutic Potential of Hsp90 Inhibitors. *Mol Cancer Res.* 2015;13:1445–51.
133. Sawarkar R, Paro R. Hsp90@chromatin.nucleus: An emerging hub of a networker. *Trends Cell Biol.* 2013;23:193–201.
134. Zabinsky R a., Mason GA, Queitsch C, Jarosz DF. It's not magic – Hsp90 and its effects on genetic and epigenetic variation. *Semin. Cell Dev. Biol.* 2019;88:21–35.
135. Kijima T, Prince TL, Tigue ML, Yim KH, Schwartz H, Beebe K, et al. HSP90 inhibitors disrupt a transient HSP90-HSF1 interaction and identify a noncanonical model of HSP90-mediated HSF1 regulation. *Sci. Rep.* 2018;8:1–13.
136. Boyault C, Gilquin B, Zhang Y, Rybin V, Garman E, Meyer-Klaucke W, et al. HDAC6-p97/VCP controlled polyubiquitin chain turnover. *EMBO J.* 2006;25:3357–66.

137. Pernet L, Faure V, Gilquin B, Dufour-Guérin S, Khochbin S, Vourc'h C. HDAC6-ubiquitin interaction controls the duration of HSF1 activation after heat shock. *Mol. Biol. Cell.* 2014;25:4187–94.
138. Seidel C, Schnekenburger M, Mazumder A, Teiten M-H, Kirsch G, Dicato M, et al. 4-Hydroxybenzoic acid derivatives as HDAC6-specific inhibitors modulating microtubular structure and HSP90 $\alpha$  chaperone activity against prostate cancer. *Biochem. Pharmacol.* 2016;1:31–52.
139. Ai J, Wang Y, Dar J a, Liu J, Liu L, Nelson JB, et al. HDAC6 regulates androgen receptor hypersensitivity and nuclear localization via modulating Hsp90 acetylation in castration-resistant prostate cancer. *Mol. Endocrinol.* 2009;23:1963–72.
140. Kundrat L, Regan L. Balance between folding and degradation for Hsp90-dependent client proteins: A key role for CHIP. *Biochemistry.* 2010;49:7428–38.
141. Dickey C a., Kamal A, Lundgren K, Klosak N, Bailey RM, Dunmore J, et al. The high-affinity HSP90-CHIP complex recognizes and selectively degrades phosphorylated tau client proteins. *J. Clin. Invest.* 2007;117:648–58.
142. Cook C, Gendron TF, Scheffel K, Carlomagno Y, Dunmore J, DeTure M, et al. Loss of HDAC6, a novel CHIP substrate, alleviates abnormal tau accumulation. *Hum. Mol. Genet.* 2012;21:2936–45.
143. Ojha R, Huang H-L, HuangFu W-C, Wu Y-W, Nepali K, Lai M-J, et al. 1-Aroylindoline-hydroxamic acids as anticancer agents, inhibitors of HSP90 and HDAC. *Eur. J. Med. Chem.* 2018;150:667–77.
144. Liu H, Ren G, Miao Z, Zhang X, Tang X, Han P, et al. Molecular optical imaging with radioactive probes. *PLoS One.* 2010;5:e9470.
145. Ametamey SM, Honer M, Schubiger PA. Molecular imaging with PET. *Chem. Rev.* 2008;108:1501–16.
146. Passchier J, Gee A, Willemsen A, Vaalburg W, Van Waarde A. Measuring drug-related receptor occupancy with positron emission tomography. *Methods.* 2002;27:278–86.
147. Robson RE, Brunger MJ, Buckman SJ, Garcia G, Petrovic ZL, White RD. Positron kinetics in an idealized PET environment. *Sci. Rep.* 2015;5:1–10.
148. Conti M, Eriksson L. Physics of pure and non-pure positron emitters for PET: A review and a discussion. *EJNMMI Phys.* 2016;3:8:1-17.
149. Lancelot S, Zimmer L. Small-animal positron emission tomography as a tool for neuropharmacology. *Trends Pharmacol. Sci.* 2010;31:411–7.
150. Cherry SR, Jones T, Karp JS, Qi J, Moses WW, Badawi RD. Total-Body PET: maximizing sensitivity to create new opportunities for clinical research and patient care. *J. Nucl. Med.* 2018;59:3–12.
151. Bateman TM. Advantages and disadvantages of PET and SPECT in a busy clinical practice. *J. Nucl. Cardiol.* 2012;19:3–11.
152. Challapalli A, Aboagye EO. Positron emission tomography imaging of tumor cell metabolism and application to therapy response monitoring. *Front. Oncol.* 2016;6:1–20.
153. Mitterhauser M, Wadsak W. Imaging biomarkers or biomarker imaging? *Pharmaceuticals.* 2014;7:765–78.
154. Serdons K, Verbruggen A, Bormans GM. Developing new molecular imaging probes for PET. *Methods.* 2009;48:104–11.
155. Kitson S, Cuccurullo V, Ciarmiello A, Salvo D, Mansi L. Clinical applications of positron emission tomography (PET) imaging in medicine: oncology, brain diseases and cardiology. *Curr. Radiopharm.* 2009;2:224–53.
156. Declercq LD, Vandenberghe R, Van Laere K, Verbruggen A, Bormans G. Drug development in Alzheimer's disease: The contribution of PET and SPECT. *Front. Pharmacol.* 2016;7:1–27.
157. Cleeren F, Lecina J, Ahamed M, Raes G, Devoogdt N, Cavelliers V, et al. Al<sup>18</sup>F-labeling of heat-sensitive biomolecules for positron emission tomography imaging. *Theranostics.* 2017;7:2924–39.
158. Müller C, Zhernosekov K, Köster U, Johnston K, Dorner H, Hohn A, et al. A unique matched quadruplet of terbium radioisotopes for PET and SPECT and for  $\alpha$ - and  $\beta$ - radionuclide therapy: An in vivo proof-of-concept study with a new receptor-targeted folate derivative. *J. Nucl. Med.* 2012;53:1951–9.
159. Ikoma Y, Watabe H, Hayashi T, Miyake Y, Teramoto N, Minato K, et al. Measurement of density and affinity for dopamine D 2 receptors by a single positron emission tomography scan with multiple injections of [<sup>11</sup>C] raclopride. *J. Cereb. Blood Flow Metab.* 2010;30:663–73.
160. Uhl P, Fricker G, Haberkorn U, Mier W. Radionuclides in drug development. *Drug Discov. Today.* 2015;20:198–208
161. Pike VW. PET radiotracers: crossing the blood-brain barrier and surviving metabolism. *Trends Pharmacol. Sci.* 2009;30:431–40.
162. Wilhelm I, Krizbai I. In vitro models of the blood-brain barrier for the study of drug delivery to the brain. *Mol. Pharm.* 2014;11:1949–63.
163. Stanton PG. Regulation of the blood-testis barrier. *Semin. Cell. Dev. Biol.* 2016;59:166–73.

164. Wagner CC, Langer O. Approaches using molecular imaging technology - use of PET in clinical microdose studies. *Adv. Drug Deliv. Rev.* 2011;63:539–46.
165. Zanger UM, Schwab M. Cytochrome P450 enzymes in drug metabolism: Regulation of gene expression, enzyme activities, and impact of genetic variation. *Pharmacol. Ther.* 2013;138:103–41.
166. Lever SZ, Fan KH, Lever JR. Tactics for preclinical validation of receptor-binding radiotracers. *Nucl. Med. Biol.* 2017;44:4–30.
167. Zhang Y, Fox GB. PET imaging for receptor occupancy: Meditations on calculation and simplification. *J. Biomed. Res.* 2012;26:69–76.
168. Love TM, Stohler CS, Zubieta J-K. PET Measures of Endogenous Opioid Neurotransmission Predict Impulsiveness Traits in Humans. *Arch. Gen. Psychiatry.* 2009;66:1124–34.
169. EMA. Non-clinical safety studies for the conduct of human clinical trials and marketing authorization for pharmaceuticals. 2008 p. 1–22.
170. Tago T, Toyohara J. Advances in the Development of PET Ligands Targeting Histone Deacetylases for the Assessment of Neurodegenerative Diseases. *Molecules.* 2018;23:1-27.
171. Reid AE, Hooker J, Shumay E, Logan J, Shea C, Kim SW, et al. Evaluation of 6-([<sup>18</sup>F]fluoroacetamido)-1-hexanoic anilide for PET imaging of histone deacetylase in the baboon brain. *Nucl. Med. Biol.* 2009;36:247–58.
172. Bonomi R, Mukhopadhyay U, Shavrin A, Yeh H-H, Majhi A, Dewage SW, et al. Novel Histone Deacetylase Class IIa Selective Substrate Radiotracers for PET Imaging of Epigenetic Regulation in the Brain. *PLoS One.* 2015;10:e0133512
173. Hendricks JA, Keliher EJ, Marinelli B, Reiner T, Weissleder R, Mazitschek R. In vivo PET imaging of histone deacetylases by 18F-suberoylanilide hydroxamic acid (<sup>18</sup>F-SAHA). *J. Med. Chem.* 2011;54:5576–82.
174. Zeglis BM, Pillarsetty N, Divilov V, Blasberg R a., Lewis JS. The synthesis and evaluation of N1-(4-(2-[<sup>18</sup>F]-fluoroethyl)phenyl)-N8-hydroxyoctanediamide ([<sup>18</sup>F]-FESAHA), A PET radiotracer designed for the delineation of histone deacetylase expression in cancer. *Nucl. Med. Biol.* 2011;38:683–96.
175. Kim DH, Kim IS, Hwang H, Kim E-M, Jeong H-J, Lim ST, et al. Synthesis and Evaluation of 2-[<sup>18</sup>F]Fluoroethyltriazolesuberohydroxamine Acid for Histone Deacetylase in a Tumor Model as a Positron Emission Tomography Radiotracer. *Cancer Biother. Radiopharm.* 2018;33:52–9.
176. Wang C, Eessalu TE, Barth VN, Mitch CH, Wagner FF, Neelamegam R, et al. Design, synthesis, and evaluation of hydroxamic acid-based molecular probes for in vivo imaging of histone deacetylase (HDAC) in brain. 2014;4:29–38.
177. Kommidu H, Tosi U, Maachani UB, Guo H, Marnell CS, Law B, et al. 18F-Radiolabeled Panobinostat Allows for Positron Emission Tomography Guided Delivery of a Histone Deacetylase Inhibitor. *ACS Med. Chem. Lett.* 2018;9:114–9.
178. Wang Y, Zhang Y-L, Hennig K, Gale JP, Hong Y, Cha A, et al. Class I HDAC imaging using [<sup>3</sup>H]CI-994 autoradiography. *Epigenetics.* 2013;8:756–64.
179. Seo YJ, Kang Y, Muench L, Reid A, Caesar S, Jean L, et al. Image-guided synthesis reveals potent blood-brain barrier permeable histone deacetylase inhibitors. *ACS Chem. Neurosci.* 2014;5:588–96.
180. Hooker JM, Kim SW, Alexoff D, Xu Y, Shea C, Reid A, et al. Histone deacetylase inhibitor MS-275 exhibits poor brain penetration: Pharmacokinetic studies of [<sup>11</sup>C]MS-275 using positron emission tomography. *ACS Chem. Neurosci.* 2010;1:65–73.
181. Kim SW, Hooker JM, Otto N, Win K, Muench L, Shea C, et al. Whole-body pharmacokinetics of HDAC inhibitor drugs, butyric acid, valproic acid and 4-phenylbutyric acid measured with carbon-11 labeled analogs by PET. *Nucl. Med. Biol.* 2013;40:912–8.
182. Meng Q, Li F, Jiang S, Li Z. Novel <sup>64</sup>Cu-labeled CUDC-101 for in vivo PET imaging of histone deacetylases. *ACS Med. Chem. Lett.* 2013;4:858–62.
183. Bonomi R, Popov V, Laws MT, Gelovani D, Majhi A, Shavrin A, et al. Molecular Imaging of Sirtuin1 Expression-Activity in Rat Brain Using Positron-Emission Tomography-Magnetic-Resonance Imaging with [<sup>18</sup>F]-2-Fluorobenzoylamino-hexanoic anilide. *J. Med. Chem.* 2018;61:7116–30.
184. Mangner T, Laws M, Bonomi RE, Shavrin A, Popov V, Kamal S, et al. A Novel Substrate Radiotracer for Molecular Imaging of SIRT2 Expression and Activity with Positron Emission Tomography. *Mol. Imaging Biol.* 2018;20:594–604.
185. Wang C, Schroeder F, Wey HY, Borra R, Wagner FF, Reis S, et al. In Vivo Imaging of Histone Deacetylases (HDACs) in the Central Nervous System and Major Peripheral Organs. *J. Med. Chem.* 2014;57:7999–8009.
186. Wey HY, Wang C, Schroeder F., Logan J, Price JC, Hooker JM. Kinetic Analysis and Quantification of [<sup>11</sup>C]Martinostat for in vivo HDAC Imaging of the Brain. *ACS Chem. Neurosci.* 2015;6:708-15.
187. Wey HY, Gilbert TM, Zurcher NR, She A, Bhanot A, Taillon BD, et al. Insights into neuroepigenetics through human histone deacetylase PET imaging. *Sci. Transl. Med.* 2016;8:1–10.

188. Gilbert TM, Zürcher NR, Wu CJ, Bhanot A, Hightower BG, Kim M, et al. PET neuroimaging reveals histone deacetylase dysregulation in schizophrenia. *J. Clin. Invest.* 2018;129:364-72
189. Strebl MG, Wang C, Schroeder F a., Placzek MS, Wey H-Y, Van de Bittner GC, et al. Development of a Fluorinated Class-I HDAC Radiotracer Reveals Key Chemical Determinants of Brain Penetration. *ACS Chem. Neurosci.* 2015;7:528-33
190. Strebl MG, Campbell AJ, Zhao W-N, Schroeder F a., Riley MM, Chindavong PS, et al. HDAC6 Brain Mapping with [<sup>18</sup>F]Bavostat Enabled by a Ru-Mediated Deoxyfluorination. *ACS Cent. Sci.* 2017;3:1006-14
191. Butler KV., Kalin J, Brochier C, Vistoli G, Langley B, Kozikowski AP. Rational design and simple chemistry yield a superior, neuroprotective HDAC6 inhibitor, tubastatin A. *J. Am. Chem. Soc.* 2010;132:10842-6.
192. Lu S, Zhang Y, Kalin JH, Cai L, Kozikowski AP, Pike VW. Exploration of the labeling of [<sup>11</sup>C]tubastatin A at the hydroxamic acid site with [<sup>11</sup>C]carbon monoxide. *J. Label. Compd. Radiopharm.* 2016;59:9-13.
193. Shuiyu, L., Zhang, Y., Kalin, J., Liow, J.-S., Gladding, R., Li, R. B., Kozikowski, A. P., and Pike VW. Evaluation of [Methyl-<sup>11</sup>C]Kb631 – a Candidate Radioligand for Histone Deacetylase Isozyme 6 (Hdac6). *J. Label. Compd. Radiopharm.* 2013;56:1.
194. Schmid S, Götz M, Hugel T. Effects of Inhibitors on Hsp90's Conformational Dynamics, Cochaperone and Client Interactions. *ChemPhysChem.* 2018;19:1716-21.
195. Taldone T, Zatorska D, Ochiana SO, Smith-Jones P, Koziorowski J, Dunphy MP, et al. Radiosynthesis of the iodine-124 labeled Hsp90 inhibitor PU-H71. *J. Label. Compd. Radiopharm.* 2016;59:129-32.
196. Kang J, Young Lee J, Taş İ, More KN, Kim H, Park JH, et al. Radiosynthesis, biological evaluation and preliminary microPET study of 18F-labeled 5-resorcinolic triazolone derivative based on ganetespib targeting HSP90. *Bioorganic Med. Chem. Lett.* 2018;28:3658-64.
197. Wang X, Zhang J, Wu H, Li Y, Conti PS, Chen K. PET imaging of Hsp90 expression in pancreatic cancer using a new 64Cu-labeled dimeric Sansalvamide A decapeptide. *Amino Acids.* 2018;50:897-907.
198. Zhang C, Ma H, Chen X. Radioactive iodine labeling of monoclonal antibody against Hsp90  $\alpha$  and its use in diagnostic imaging in prostate cancer xenograft model. *Eur Rev Med Pharmacol Sci.* 2015;19:835-43.
199. Barrott JJ, Hughes PF, Osada T, Yang XY, Hartman ZC, Loiseau DR, et al. Optical and radioiodinated tethered Hsp90 inhibitors reveal selective internalization of ectopic Hsp90 in malignant breast tumor cells. *Chem. Biol.* 2013;20:1187-97.
200. Wang W, Zhao J, Wen X, Chun-Jen Lin C, Li J, Huang Q, et al. MicroPET/CT imaging of AXL downregulation by HSP90 inhibition in triple-negative breast cancer. *Contrast Media Mol. Imaging.* 2017;2017:1-11.
201. Spiegelberg D, Mortensen AC, Selvaraju RK, Eriksson O, Stenerlöw B, Nestor M. Molecular imaging of EGFR and CD44v6 for prediction and response monitoring of HSP90 inhibition in an in vivo squamous cell carcinoma model. *Eur. J. Nucl. Med. Mol. Imaging.* 2016;43:974-82.
202. Smith-Jones PM, Solit D, Afroz F, Rosen N LS. Early tumor response to Hsp90 therapy using HER2 PET: comparison with <sup>18</sup>F-FDG PET. *J Nucl Med.* 2006;47:793-6.
203. Wagner AJ, Chugh R, Rosen LS, Morgan J a., George S, Gordon M, et al. A phase I study of the HSP90 inhibitor retaspimycin hydrochloride (IPI-504) in patients with gastrointestinal stromal tumors or soft-tissue sarcomas. *Clin. Cancer Res.* 2013;19:6020-9.
204. Dickson M, Okuno SH, Keohan ML, Maki RG, D'Adamo DR, Akhurst TJ, et al. Phase II study of the HSP90-inhibitor BIIB021 in gastrointestinal stromal tumors. *Ann. Oncol.* 2013;24:252-7.
205. Gaykema SBM, Schroeder CP, Vitfell-Rasmussen J, Chua S, Munnink THO, Brouwers AH, et al. <sup>89</sup>Zr-trastuzumab and <sup>89</sup>Zr-bevacizumab PET to evaluate the effect of the HSP90 inhibitor NVP-AUY922 in metastatic breast cancer patients. *Clin. Cancer Res.* 2014;20:3945-54.
206. Pavlik CM, Wong CYB, Ononye S, Lopez DD, Engene N, McPhail KL, et al. Santacruzamate A, a potent and selective histone deacetylase inhibitor from the Panamanian marine cyanobacterium cf. *Symploca* sp. *J. Nat. Prod.* 2013;76:2026-33.
207. Brasca MG, Mantegani S, Amboldi N, Bindi S, Caronni D, Casale E, et al. Discovery of NMS-E973 as novel, selective and potent inhibitor of heat shock protein 90 (Hsp90). *Bioorganic Med. Chem.* 2013;21:7047-63.
208. Fogliatto G, Gianellini L, Brasca MG, Casale E, Ballinari D, Ciomei M, et al. NMS-E973, a novel synthetic inhibitor of Hsp90 with activity against multiple models of drug resistance to targeted agents, including intracranial metastases. *Clin. Cancer Res.* 2013;19:3520-32.
209. McBride CM, Levine B, Xia Y, Bellamacina C, Machajewski T, Gao Z, et al. Design, structure-activity relationship, and in vivo characterization of the development candidate NVP-HSP990. *J. Med. Chem.* 2014;57:9124-9.
210. Minucci S, Pelicci PG. Histone deacetylase inhibitors and the promise of epigenetic (and more) treatments for cancer. *Nat. Rev. Cancer.* 2006;6:38-51.

211. Bertrand P. Inside HDAC with HDAC inhibitors. *Eur. J. Med. Chem.* 2010;45:2095–116.
212. Seidel C, Florean C, Schneidenburger M, Dicato M, Diederich M. Chromatin-modifying agents in anti-cancer therapy. *Biochimie.* 2012;94:2264–79.
213. Folmer F, Orlikova B, Schneidenburger M, Dicato M, Diederich M. Naturally Occurring Regulators of Histone Acetylation/Deacetylation. *Curr. Nutr. Food Sci.* 2010;6:78–99.
214. Abend A, Kehat I. Histone deacetylases as therapeutic targets - From cancer to cardiac disease. *Pharmacol. Ther.* 2015;147:55-62
215. Florean C, Grandjennette C, Dicato M, Diederich M. Epigenomics of leukemia : from mechanisms to therapeutic applications. *Cell.* 2011;3:581–609.
216. Schneidenburger M, Dicato M, Diederich M. Epigenetic modulators from “The Big Blue”: A treasure to fight against cancer. *Cancer Lett.* 2014;351:182–97.
217. Kazantsev AG, Thompson LM. Therapeutic application of histone deacetylase inhibitors for central nervous system disorders. *Nat. Rev. Drug Discov.* 2008;7:854–68.
218. Seidel C, Schneidenburger M, Dicato M, Diederich M. Histone deacetylase modulators provided by Mother Nature. *Genes Nutr.* 2012;7:357–67.
219. Schneidenburger M, Florean C, Dicato M DM. Epigenetic alterations as a universal feature of cancer hallmarks and a promising target for personalized treatments. *Curr. Top. Med. Chem.* 2016;16:745–76.
220. Thaler F, Mercurio C. Towards selective inhibition of histone deacetylase isoforms: What has been achieved, where we are and what will be next. *ChemMedChem.* 2014;9:523–36.
221. Zhang L, Han Y, Jiang Q, Wang C, Chen X, Li X, et al. Trend of Histone Deacetylase Inhibitors in Cancer Therapy: Isoform Selectivity or Multitargeted Strategy. *Med. Res. Rev.* 2015;35:63–84.
222. Felice C, Lewis a, Armuzzi a, Lindsay JO, Silver A. Selective histone deacetylase isoforms as potential therapeutic targets in inflammatory bowel diseases. *Aliment. Pharmacol. Ther.* 2015;41:26–38.
223. Song J, Noh JH, Lee JH, Eun JW, Ahn YM, Kim SY, et al. Increased expression of histone deacetylase 2 is found in human gastric cancer. *APMIS.* 2005;113:264–8.
224. Zhu P, Martin E, Mengwasser J, Schlag P, Janssen KP, Göttlicher M. Induction of HDAC2 expression upon loss of APC in colorectal tumorigenesis. *Cancer Cell.* 2004;5:455–63.
225. Ravillah D, Mohammed A, Qian L, Brewer M, Zhang Y, Biddick L, et al. Chemopreventive effects of an HDAC2-selective inhibitor on rat colon carcinogenesis and APCmin/+ mouse intestinal tumorigenesis. *J. Pharmacol. Exp. Ther.* 2014;348:59–68.
226. Krämer OH. HDAC2: a critical factor in health and disease. *Trends Pharmacol. Sci.* 2009;30:647–55.
227. Gräff J, Rei D, Guan J-S, Wang W-Y, Seo J, Hennig KM, et al. An epigenetic blockade of cognitive functions in the neurodegenerating brain. *Nature.* 2012;483:222–6.
228. Eom GH, Kook H. Role of histone deacetylase 2 and its posttranslational modifications in cardiac hypertrophy. *BMB Rep.* 2015;48:131–8.
229. Gopalan B, Ponpandian T, Kachhadia V, Bharathimohan K, Vignesh R, Sivasudar V, et al. Discovery of adamantane based highly potent HDAC inhibitors. *Bioorganic Med. Chem. Lett.* 2013;23:2532–7.
230. Wang C, Schroeder FA, Wey H, Borra R, Wagner FF, Reis S, et al. In Vivo Imaging of Histone Deacetylases (HDACs) in the Central Nervous System and Major Peripheral Organs. *J. Med. Chem.* 2014;57:7999–8009.
231. Ononye SN, VanHeyst MD, Oblak EZ, Zhou W, Ammar M, Anderson AC, et al. Tropolones as lead-like natural products: the development of potent and selective histone deacetylase inhibitors. *ACS Med. Chem. Lett.* 2013;4:757–61.
232. Ononye SN, Vanheyst MD, Giardina C, Wright DL, Anderson AC. Studies on the antiproliferative effects of tropolone derivatives in Jurkat T-lymphocyte cells. *Bioorg. Med. Chem.* 2014;22:2188–93.
233. Liu Q, Lu W, Ma M, Liao J, Ganesan A, Hu Y, et al. Synthesis and biological evaluation of santacruzamate A and analogs as potential anticancer agents. *RSC Adv.* 2015;5:1109–12.
234. El Amrani M, Lai D, Debbab A, Aly AH, Siems K, Seidel C, et al. Protein kinase and HDAC inhibitors from the endophytic fungus *epicoccum nigrum*. *J. Nat. Prod.* 2014;77:49–56.
235. Seidel C, Schneidenburger M, Dicato M, Diederich M. Antiproliferative and proapoptotic activities of 4-hydroxybenzoic acid-based inhibitors of histone deacetylases. *Cancer Lett.* 2014;343:134–46.
236. Lee E, Hooker JM, Ritter T. Nickel-mediated oxidative fluorination for PET with aqueous [<sup>18</sup>F]fluoride. *J. Am. Chem. Soc.* 2012;134:17456–8.
237. Robert Weiss JS. Electrostatic Activation of Hypervalent Organo-Iodine Compounds: Bis(onio)-Substituted Aryliodine(III) Salts. *Angew. Chem. Int. Ed. Engl.* 1994;33:891–3.

238. Strebli MG, Wang C, Schroeder F, Placzek MS, Wey HY, Van de Bittner GC, et al. Development of a Fluorinated Class-I HDAC Radiotracer Reveals Key Chemical Determinants of Brain Penetration. *ACS Chem. Neurosci.* 2015;7:528-33
239. Li HD, Shen WS, Zou CX, Yuan L. Efficient and Clean Synthesis of N-Alkyl Carbamates by Transcarboxylation and O-Alkylation Coupled Reactions Using a DBU-CO<sub>2</sub> Zwitterionic Carbamic Complex in Aprotic Polar Media. *J. Ecol. Rural Environ.* 2010;26:25-30.
240. Shi P, Scott M, Ghosh B, Wan D, Wissner-Gross Z, Mazitschek R, et al. Synapse microarray identification of small molecules that enhance synaptogenesis. *Nat. Commun.* 2011;2:1-10.
241. Vigushin DM, Ali S, Pace PE, Mirsaidi N, Ito K, Adcock I, et al. Trichostatin A is a histone deacetylase inhibitor with potent antitumor activity against breast cancer in vivo. *Clin. Cancer Res.* 2001;7:971-6.
242. Nussinov R TC. The Different Ways through Which Specificity Works in Orthosteric and Allosteric Drugs. *Curr Pharm Des.* 2012;18:1311-6.
243. Alonso H, Bliznyuk A, Gready JE. Combining docking and molecular dynamic simulations in drug design. *Med. Res. Rev.* 2006;26:531-68.
244. Lauffer B, Mintzer R, Fong R, Mukund S, Tam C, Zilberley I, et al. Histone deacetylase (HDAC) inhibitor kinetic rate constants correlate with cellular histone acetylation but not transcription and cell viability. *J. Biol. Chem.* 2013;288:26926-43.
245. Pan DS, Yang QJ, Fu X, Shan S, Zhu JZ, Zhang K, et al. Discovery of an orally active subtype-selective HDAC inhibitor, chidamide, as an epigenetic modulator for cancer treatment. *Medchemcomm.* 2014;5:1789-96.
246. Delcuve GP, Khan DH, Davie JR. Roles of histone deacetylases in epigenetic regulation: emerging paradigms from studies with inhibitors. *Clin. Epigenetics.* 2012;4:1-13.
247. Furumai R, Matsuyama A, Kobashi N, Lee K, Nishiyama M, Nakajima H, et al. FK228 (Depsipeptide) as a Natural Prodrug That Inhibits Class I Histone deacetylase. *Sci. Technol.* 2002;228:4916-21.
248. Qian, X, LaRochelle WJ, Ara G, Wu F, Petersen KD, Thougard A, Sehested M, Lichenstein HS JM. Activity of PXD101, a histone deacetylase inhibitor, in preclinical ovarian cancer studies. *Mol. Cancer Ther.* 2006;5:2086-95.
249. Batchu SN, Brijmohan a. S, Advani a. The therapeutic hope for HDAC6 inhibitors in malignancy and chronic disease. *Clin. Sci.* 2016;130:987-1003.
250. Inoue A, Yoshida N, Omoto Y, Oguchi S, Yamori T, Kiyama R, et al. Development of cDNA microarray for expression profiling of estrogen-responsive genes. *J. Mol. Endocrinol.* 2002;29:175-92.
251. Surgery M, Surgery O. Aberrant expression of histone deacetylase 6 in oral squamous cell carcinoma. *Int. J. Oncol.* 2006;29:117-24.
252. Santo L, Hideshima T, Kung AL, Tseng JC, Tamang D, Yang M, et al. Preclinical activity, pharmacodynamic, and pharmacokinetic properties of a selective HDAC6 inhibitor, ACY-1215, in combination with bortezomib in multiple myeloma. *Blood.* 2012;119:2579-89.
253. Eckschlager T, Plch J, Stiborova M, Hrabeta J. Histone deacetylase inhibitors as anticancer drugs. *Int. J. Mol. Sci.* 2017;18:1-25.
254. Ueihuei P, Zhihao W, Pei S, Ou Y, Hu P, Liu W, et al. ACY-1215 accelerates vemurafenib induced cell death of BRAF-mutant melanoma cells via induction of ER stress and inhibition of ERK activation. *Oncol. Rep.* 2017;37:1270-6.
255. Pandey UB, Nie Z, Batlevi Y, McCray B a, Ritson GP, Nedelsky NB, et al. HDAC6 rescues neurodegeneration and provides an essential link between autophagy and the UPS. *Nature.* 2007;447:859-63.
256. Du G, Jiao R, Formation I. To prevent neurodegeneration HDAC6 uses different strategies for different challenges. *Commun. Integr. Biol.* 2011;4:139-42.
257. Kozikowski AP, Tapadar S, Luchini DN, Kim KH, Billadeau DD. Use of the nitrile oxide cycloaddition (NOC) reaction for molecular probe generation: A new class of enzyme selective histone deacetylase inhibitors (HDACIs) showing Picomolar activity at HDAC6. *J. med. chem.* 2008;51:4370-3
258. Horti AG, Fan H, Kuwabara H, Hilton J, Ravert HT, Holt DP, et al. [<sup>11</sup>C]-JHU75528: a radiotracer for PET imaging of CB1 cannabinoid receptors. *J. Nucl. Med.* 2006;47:1689-96.
259. Burns HD, Van Laere K, Sanabria-Bohórquez S, Hamill TG, Bormans G, Eng W, et al. [<sup>18</sup>F]MK-9470, a positron emission tomography (PET) tracer for in vivo human PET brain imaging of the cannabinoid-1 receptor. *Proc. Natl. Acad. Sci. U. S. A.* 2007;104:9800-5.
260. Frizberg AR, Whitney WP, Kuni CC. Biodistribution and renal excretion of <sup>99m</sup>Tc-N, N'-bis-(mercaptoacetamido) ethylenediamine. Effect of renal tubular transport inhibitors. *Int. J. Nucl. Med. Biol.* 1982;9:79-82.
261. Benedetti R, Conte M, Altucci L. Targeting Histone Deacetylases in Diseases: Where Are We? *Antioxid. Redox Signal.* 2015;23:99-126.

262. Tai S, Sun Y, Squires JM, Zhang H, Oh WK, Liang CZ, et al. PC3 is a cell line characteristic of prostatic small cell carcinoma. *Prostate*. 2011;71:1668–79.
263. Wang C, Schroeder F a, Hooker JM. Visualising epigenetics: current advances and advantages in HDAC PET imaging techniques. *Neuroscience*. 2014;264:186–97
264. Hanson JE, La H, Plise E, Chen YH, Ding X, Hanania T, et al. SAHA Enhances Synaptic Function and Plasticity In Vitro but Has Limited Brain Availability In Vivo and Does Not Impact Cognition. *PLoS One*. 2013;8:e69964
265. Konsoula R, Jung M. In vitro plasma stability, permeability and solubility of mercaptoacetamide histone deacetylase inhibitors. *Int. J. Pharm.* 2008;361:19–25.
266. Yeh HH, Tian M, Hinz R, Young D, Shavrin A, Mukhopadhyay U, et al. Imaging epigenetic regulation by histone deacetylases in the brain using PET/MRI with [<sup>18</sup>F]FAHA. *Neuroimage*. 2013;64:630–9.
267. Trepel J, Mollapour M, Giaccone G, Neckers L. Targeting the dynamic HSP90 complex in cancer. *Nat. Rev. Cancer*. 2010;10:537–49.
268. Neckers L, Trepel JB. Stressing the development of small molecules targeting HSP90. *Clin. Cancer Res*. 2014;20:275–7.
269. Crowe LB, Hughes PF, Alcorta D a, Osada T, Smith AP, Totzke J, et al. A fluorescent Hsp90 probe demonstrates the unique association between extracellular Hsp90 and malignancy in vivo. *ACS Chem. Biol*. 2017;12:1047–55.
270. Barrott JJ, Hughes PF, Osada T, Yang XY, Hartman ZC, Loiseau DR, et al. Optical and radioiodinated tethered Hsp90 inhibitors reveal selective internalization of ectopic Hsp90 in malignant breast tumor cells. *Chem. Biol*. 2013;20:1187–97.
271. Sun L, Yang S, Chi G, Jin X. Hsp90 inhibitor NMS-E973 exerts the anticancer effect against glioblastoma via induction of PUMA-mediated apoptosis. *Onco Targets Ther*. 2018;11:1583–93.
272. Eder M, Schäfer M, Bauder-Wüst U, Hull WE, Wängler C, Mier W, et al. <sup>68</sup>Ga-complex lipophilicity and the targeting property of a urea-based PSMA inhibitor for PET imaging. *Bioconjug. Chem*. 2012;23:688–97.
273. Li W, Tsen F, Sahu D, Bhatia A, Chen M, Multhoff G WD. Extracellular Hsp90 (eHsp90) as the Actual Target in Clinical Trials: Intentionally or Unintentionally. *Int Rev Cell Mol Biol*. 2013;303:203–35.
274. Wang H, Lu M, Yao M, Zhu W. Effects of treatment with an Hsp90 inhibitor in tumors based on 15 phase II clinical trials. *Mol. Clin. Oncol*. 2016;5:326–34.
275. Hance MW, Nolan KD, Isaacs JS. The double-edged sword: Conserved functions of extracellular Hsp90 in wound healing and cancer. *Cancers*. 2014;6:1065–97.
276. Yang C, Robbins PD. The roles of tumor-derived exosomes in cancer pathogenesis. *Clin. Dev. Immunol*. 2011;2011:1-11
277. Kaiser M, Kühnl a, Reins J, Fischer S, Ortiz-Tanchez J, Schlee C, et al. Antileukemic activity of the HSP70 inhibitor pifithrin- $\mu$  in acute leukemia. *Blood Cancer J*. 2011;1:e28.
278. Zhang L, Fok JLL, Mirabella F, Aronson LI, Fryer R a., Workman P, et al. Hsp70 inhibition induces myeloma cell death via the intracellular accumulation of immunoglobulin and the generation of proteotoxic stress. *Cancer Lett*. 2013;339:49–59.
279. Davenport EL, Zeisig A, Aronson LI, Moore HE, Hockley S, Gonzalez D, et al. Targeting heat shock protein 72 enhances Hsp90 inhibitor-induced apoptosis in myeloma. *Leukemia*. 2010;24:1804–7.
280. Sekihara K, Harashima N, Tongu M, Tamaki Y, Uchida N, Inomata T, et al. Pifithrin- $\mu$ , an inhibitor of heat-shock protein 70, can increase the antitumor effects of hyperthermia against human prostate cancer cells. *PLoS One*. 2013;8:1–11.
281. Georget V, Térouanne B, Nicolas JC, Sultan C. Mechanism of antiandrogen action: Key role of hsp90 in conformational change and transcriptional activity of the androgen receptor. *Biochemistry*. 2002;41:11824–31.
282. Khandelwal A, Crowley VM, Blagg BSJ. Resorcinol-based Grp94-Selective Inhibitors. *ACS Med. Chem. Lett*. 2017;8:1013–8.
283. Patel PD, Yan P, Seidler PM, Patel HJ, Sun W, Yang C, et al. Paralog-selective Hsp90 inhibitors define tumor-specific regulation of HER2. *Nat. Chem. Biol*. 2013;9:677–84.
284. Saito K, Dai Y, Ohtsuka K. Enhanced expression of heat shock proteins in gradually dying cells and their release from necrotically dead cells. *Exp. Cell Res*. 2005;310:229–36.
285. Zhang G, Liu Z, Ding H, Zhou Y, Doan HA, Sin KWT, et al. Tumor induces muscle wasting in mice through releasing extracellular Hsp70 and Hsp90. *Nat. Commun*. 2017;8:1–16.
286. Grammatikakis N, Vultur A, Ramana C V., Sigano A, Schweinfest CW, Watson DK, et al. The role of Hsp90N, a new member of the Hsp90 family, in signal transduction and neoplastic transformation. *J. Biol. Chem*. 2002;277:8312–20.
287. Milo R. What is the total number of protein molecules per cell volume? A call to rethink some published values. *BioEssays*. 2013;35:1050–5.
288. Hietala J, Nägren K, Lehtikoinen P, Ruotsalainen U, Syvälahti E. Measurement of striatal D<sub>2</sub> dopamine receptor density and affinity with [<sup>11</sup>C]-Raclopride in vivo: a test-retest analysis. *J. Cereb. Blood Flow Metab*. 1999;19:210–7.



289. Hoter A, El-Sabban M, Naim H. The HSP90 family: structure, regulation, function, and implications in health and disease. *Int. J. Mol. Sci.* 2018;19:2560.
290. Li T, Jiang H-L, Tong Y-G, Lu J-J. Targeting the Hsp90-Cdc37-client protein interaction to disrupt Hsp90 chaperone machinery. *J. Hematol. Oncol.* 2018;11:1–10.
291. Buchner J, Li J. Structure, Function and Regulation of the Hsp90 Machinery. *Biomed. J.* 2013;36:106.
292. Neckers L, Blagg B, Haystead T, Trepel JB, Whitesell L, Picard D. Methods to validate Hsp90 inhibitor specificity , to identify off-target effects , and to rethink approaches for further clinical development. *Cell Stress chaperones.* 2018;23:467–82.
293. Wu J, Liu T, Rios Z, Mei Q, Lin X, Cao S. Heat Shock Proteins and Cancer. *Trends Pharmacol. Sci.* 2017;38:226–56.
294. Gerges NZ. Independent Functions of hsp90 in Neurotransmitter Release and in the Continuous Synaptic Cycling of AMPA Receptors. *J. Neurosci.* 2004;24:4758–66.
295. Lauwers E, Wang YC, Gallardo R, Van der Kant R, Michiels E, Swerts J, et al. Hsp90 Mediates Membrane Deformation and Exosome Release. *Mol. Cell.* 2018;71:689–702.
296. Weidenauer L, Wang T, Joshi S, Chiosis G, Quadroni MR. Proteomic interrogation of HSP90 and insights for medical research. *Expert Rev. Proteomics.* 2017;14:1105–17.
297. Brehme M, Voisine C, Rolland T, Wachi S, Soper JH, Zhu Y, et al. A chaperome subnetwork safeguards proteostasis in aging and neurodegenerative disease. *Cell Rep.* 2014;9:1135–50.
298. McLean PJ, Lindberg I, Chiti F, Shorter J, Wiseman RL, Dickey C. Chaperones in Neurodegeneration. *J. Neurosci.* 2015;35:13853–9.
299. Luo W, Sun W, Taldone T, Rodina A, Chiosis G. Heat shock protein 90 in neurodegenerative diseases. *Mol. Neurodegener.* 2010;5:1–24.
300. McFarland NR, Dimant H, Kibuuka L, Ebrahimi-Fakhari D, Desjardins C, Danzer KM, et al. Chronic treatment with novel small molecule Hsp90 inhibitors rescues striatal dopamine levels but not  $\alpha$ -synuclein-induced neuronal cell loss. *PLoS One.* 2014;9:1–8.
301. Harding RJ, Tong Y. Proteostasis in Huntington’s disease: disease mechanisms and therapeutic opportunities. *Acta Pharmacol. Sin.* 2018;39:754–69.
302. Kandratavicius L, Hallak JE, Carlotti CG, Assirati J a., Leite JP. Hippocampal expression of heat shock proteins in mesial temporal lobe epilepsy with psychiatric comorbidities and their relation to seizure outcome. *Epilepsia.* 2014;55:1834–43.
303. Terracciano S, Russo A, Chini MG, Vaccaro MC, Potenza M, Vassallo A, et al. Discovery of new molecular entities able to strongly interfere with Hsp90 C-terminal domain. *Sci. Rep.* 2018;8:1–11.
304. Putcha P, Danzer KM, Kranich LR, Scott a., Silinski M, Mabbett S, et al. Brain-Permeable Small-Molecule Inhibitors of Hsp90 Prevent  $\alpha$ -Synuclein Oligomer Formation and Rescue  $\alpha$ -Synuclein-Induced Toxicity. *J. Pharmacol. Exp. Ther.* 2010;332:849–57.
305. Canella A, Welker AM, Yoo JY, Xu J, Abbas FS, Kesanakurti D, et al. Efficacy of Onalespib a long-acting second generation HSP90 Inhibitor as a single agent and in combination with Temozolomide against malignant gliomas. *Clin. Cancer Res.* 2017;23:6215–26.
306. Vermeulen K, Naus E, Ahamed M, Attili B, Siemons M, Luyten K, et al. Evaluation of [ $^{11}$ C]NMS-E973 as a PET tracer for *in vivo* visualisation of HSP90. *Theranostics.* 2019;9:554–72.
307. Antonios-McCrea W, Auberson Y, Bergstroem M, Briard E, Brinner K, Levine B, et al. Amino-quinazalone derivatives for use as radiotracers and imaging agents. 2008. p. 1–27.
308. Neubert T, Numa M, Ernst J, Clemens J, Krenitsky P, Liu M, et al. Discovery of novel oxazepine and diazepine carboxamides as two new classes of heat shock protein 90 inhibitors. *Bioorganic Med. Chem. Lett.* 2015;25:1338–42.
309. Shelton LB, Koren J, Blair LJ. Imbalances in the Hsp90 chaperone machinery: Implications for tauopathies. *Front. Neurosci.* 2017;11:1–12.
310. Sköld K, Alm H, Scholz B. The impact of biosampling procedures on molecular data interpretation. *Mol. Cell. Proteomics.* 2013;12:1489–501.
311. Mataka JJ, Silverman RB, Jansen Labby K, Hawker DD, Trippier PC. Target- and Mechanism-Based Therapeutics for Neurodegenerative Diseases: Strength in Numbers. *J. Med. Chem.* 2013;56:3121–47.
312. Stellas D, Karameris A, Patsavoudi E. Monoclonal antibody 4C5 immunostains human melanomas and inhibits melanoma cell invasion and metastasis. *Clin. Cancer Res.* 2007;13:1831–8.
313. McClung JP, Hasday JD, He J, Montain SJ, Cheuvront SN, Sawka MN, et al. Exercise-heat acclimation in humans alters baseline levels and ex vivo heat inducibility of HSP72 and HSP90 in peripheral blood mononuclear cells. *Am. J. Physiol. Integr. Comp. Physiol.* 2007;294:185–91.

314. Erkeller-Yüksel FM, Isenberg D a., Dhillon VB, Latchman DS, Lydyard PM. Surface expression of heat shock protein 90 by blood mononuclear cells from patients with systemic lupus erythematosus. *J. Autoimmun.* 1992;5:803–14.
315. Yong K, Cavet J, Johnson P, Morgan G, Williams C, Nakashima D, et al. Phase I study of KW-2478, a novel Hsp90 inhibitor, in patients with B-cell malignancies. *Br. J. Cancer* 2016;114:7–13.
316. Van De Bittner GC, Ricq EL, Hooker JM. A philosophy for CNS radiotracer design. *Acc. Chem. Res.* 2014;47:3127–34.
317. Zhang L, Villalobos A, Beck EM, Bocan T, Chappie T, Chen L, et al. Design and selection parameters to accelerate the discovery of novel central nervous system positron emission tomography (PET) ligands and their application in the development of a novel phosphodiesterase 2A PET ligand. *J. Med. Chem.* 2013;56:4568–79.
318. Zhang L, Villalobos A. Strategies to facilitate the discovery of novel CNS PET ligands. *EJNMMI Radiopharm. Chem.* 2016;1:1–12.
319. Gromek SM, Demayo J, Maxwell AT, West AM, Pavlik CM, Zhao Z, et al. Synthesis and biological evaluation of santacruzamate A analogues for anti-proliferative and immunomodulatory activity. *Bioorganic Med. Chem.* 2016;24:5183–96.
320. Randino R, Gazzerro P, Mazitschek R, Rodriguez M. Synthesis and biological evaluation of Santacruzamate-A based analogues. *Bioorganic Med. Chem.* 2017;25:6486–91.
321. Bantscheff M, Hopf C, Savitski MM, Dittmann A, Grandi P, Michon A-M, et al. Chemoproteomics profiling of HDAC inhibitors reveals selective targeting of HDAC complexes. *Nat. Biotechnol.* 2011;29:255–65.
322. Wanka L, Iqbal K, Schreiner PR. The lipophilic bullet hits the targets: Medicinal chemistry of adamantane derivatives. *Chem. Rev.* 2013;113:3516–604.
323. Herraiz T. Tetrahydro- $\beta$ -carboline, potential neuroactive alkaloids, in chocolate and cocoa. *J. Agric. Food Chem.* 2000;48:4900–4.
324. Renou J, Loidice M, Arboléas M, Baati R, Jean L, Nachon F, et al. Tryptoline-3-hydroxypyridinaldoxime conjugates as efficient reactivators of phosphylated human acetyl and butyrylcholinesterases. *Chem. Commun.* 2014;50:3947–50.
325. D. Westerheide S, Raynes R, Powell C, Xue B, N. Uversky V. HSF Transcription factor family, heat shock response, and protein intrinsic disorder. *Curr. Protein Pept. Sci.* 2012;13:86–103.
326. Wiley JL. Resorcinol derivatives: A novel template for the development of cannabinoid CB1/CB2 and CB2-selective agonists. *J. Pharmacol. Exp. Ther.* 2003;301:679–89.
327. Zong H, Gozman A, Caldas-Lopes E, Taldone T, Sturgill E, Brennan S, et al. A hyperactive signalosome in acute myeloid leukemia drives addiction to a tumor-specific Hsp90 species. *Cell Rep.* 2015;13:2159–73.
328. Bhatia A, O'Brien K, Guo J, Lincoln V, Kajiwara C, Chen M, et al. Extracellular and non-chaperone function of heat shock protein-90 $\alpha$  is required for skin wound healing. *J. Invest. Dermatol.* 2018;138:423–33.
329. Tarone G, Brancaccio M. Keep your heart in shape: Molecular chaperone networks for treating heart disease. *Cardiovasc. Res.* 2014;102:346–61.
330. Yu S, Cai X, Wu C, Liu Y, Zhang J, Gong X, et al. Targeting HSP90-HDAC6 regulating network implicates precision treatment of breast cancer. *Int. J. Biol. Sci.* 2017;13:505–17.
331. Ahamed M, Attili B, van Veghel D, Ooms M, Berben P, Celen S, et al. Synthesis and preclinical evaluation of [ $^{11}\text{C}$ ]MA-PB-1 for *in vivo* imaging of brain monoacylglycerol lipase (MAGL). *Eur. J. Med. Chem.* 2017;136:104–13.

# SCIENTIFIC ACKNOWLEDGEMENTS AND CONFLICT OF INTEREST

**Chapter II:** Muneer Ahamed and **Koen Vermeulen** are joint first authors.

Muneer Ahamed performed organic synthesis and subsequent characterization of compounds 2-4, 5-7 and molecular docking studies. **Koen Vermeulen** performed organic synthesis (compounds 2-4, 5-7). Michael Schneckenburger and Lise Román Moltzau performed biological experiments. Finn Olav Levy, János Marton, Dag Erlend Olberg performed organic synthesis/radiosynthesis and characterization of compounds 9 and 10. Mathy Froeyen performed molecular docking studies. Muneer Ahamed, **Koen Vermeulen**, Michael Schneckenburger, Marc Dietrich, Dag Erlend Olberg and Guy Bormans designed the research, made data interpretation and prepared the manuscript. All authors reviewed the results and approved the final version of the manuscript.

Michael Schneckenburger is supported by a “Waxweiler grant for cancer prevention research” from the Action Lions “Vaincre le Cancer”. This work was supported by the “Recherche Cancer et Sang” foundation, the “Recherches Scientifiques Luxembourg” association, by the “Een Häerz fir kriibskrank Kanner” association, by the Action LIONS “Vaincre le Cancer” association and by Télévie Luxembourg. Marc Dietrich is supported by the NRF by the MEST of Korea for Tumor Microenvironment GCRC 2012-0001184 grant and by Brain Korea (BK21) PLUS program. Lise Román Moltzau and Finn Olav Levy are supported by The Norwegian Council on Cardiovascular Diseases, The Research Council of Norway, The Kristian Gerhard Jebsen foundation, Anders Jahre’s Foundation for the Promotion of Science, The Family Blix foundation, The Simon Fougner Hartmann family foundation and grants from the University of Oslo. Muneer Ahamed and **Koen Vermeulen** are supported by IMIR (*In Vivo* Molecular Imaging Research group) at KU Leuven, Belgium.

Conflict of interest: The authors have declared that no competing interest exists.

## Chapter III

**Koen Vermeulen** developed and performed radiosynthesis, organic synthesis and experiments with radioactive compounds. Muneer Ahamed performed organic synthesis, analysis and characterization of synthesized compounds. Kaat Luyten provided tumour-inoculated mice. **Koen Vermeulen**, Muneer Ahamed and Guy Bormans designed the study, performed statistical analysis or writing and revision of the manuscript.

The authors would like to thank Julie Cornelis, Ivan Sannen, Pieter Haspeslagh, Jeroen Peetroons and Jana Hemelaers (Laboratory for Radiopharmaceutical Research), Ann Van Santvoort, Tine Buelens and Jens Wouters (Department of Nuclear Medicine). The Laboratory for Radiopharmaceutical Research was supported by grants from the Flanders Agency for innovation by Science and Technology and the Programme funding IMIR (KU Leuven).

Conflict of interest: The authors have declared that no competing interest exists.

**Chapter IV:** **Koen Vermeulen** and Evelyne Naus are joint first authors.

**Koen Vermeulen** developed and performed radiosynthesis, organic synthesis and experiments with radioactive compounds. Evelyne Naus performed cellular and biochemical analyses. Muneer Ahamed performed organic synthesis, analysis and characterization of synthesized compounds. Bala Atilli and Sofie Celen aided in performing experiments with radioactivity. Maxime Siemons and Kaat Luyten provided tumour-inoculated mice. **Koen Vermeulen**, Evelyne Naus, Muneer Ahamed, Joost Schymkowitz, Frederic Rousseau and Guy Bormans designed the study, performed statistical analysis or writing and revision of the manuscript.

The authors would like to thank Julie Cornelis, Ivan Sannen, Pieter Haspeslagh, Jeroen Peetroons and Jana Hemelaers (Laboratory for Radiopharmaceutical Research), Ann Van Santvoort and Tine Buelens (Department of Nuclear Medicine). The Switch Laboratory was supported by grants from the European Research Council under the European Union's Horizon 2020 Framework Programme ERC Grant agreement 647458 (MANGO) to JS, the Flanders institute for biotechnology (VIB), the University of Leuven ("Industrieel Onderzoeksfonds"), the Flanders Research Foundation (FWO), the Flanders Agency for innovation by Science and Technology (IWT, SBO grant 60839) and the Federal Office for Scientific Affairs of Belgium (Belspo), IUAP, grant number P7/16. Evelyne Naus was supported by a PhD fellowship from the IWT. The Laboratory for Radiopharmaceutical Research was supported by grants from the Flanders Agency for innovation by Science and Technology (IWT, SBO grant 130065) and the Programme funding IMIR (KU Leuven).

Conflict of interest: The authors have declared that no competing interest exists.

### **Chapter V**

**Koen Vermeulen** developed and performed radiosynthesis, organic synthesis and experiments with radioactive compounds. Emmanuelle Briard, Yves Auberson and Joseph Schöfer provided reference compound YC-72-AB85. Christopher Cawthorne aided in  $\mu$ PET data analysis and reconstruction. **Koen Vermeulen**, Emmanuelle Briard, Yves Auberson, Joseph Schöfer and Guy Bormans designed the study, performed statistical analysis or writing and revision of the manuscript.

The authors would like to thank Julie Cornelis, Ivan Sannen, Pieter Haspeslagh, and Jeroen Peetroons (Laboratory for Radiopharmaceutical Research), Jens Wouters (Department of Nuclear Medicine).

Conflict of interest: Emmanuelle Briard, Yves Auberson and Joseph Schöfer are employees of Novartis, Basel.

# CURRICULUM VITAE

## ***Personal information***

Name: Koen Vermeulen  
E-mail: k-vermeulen4@hotmail.com - koenvermeulen8@gmail.com  
Date of birth: 21-04-1991  
Place of birth: Geel, Belgium

## ***Education***

2014-2019                      PhD in Pharmaceutical Sciences.  
  
*Research topic:* Development and evaluation of HDAC and Hsp90 PET ligands.  
  
Laboratory for Radiopharmaceutical Research, Faculty of Pharmaceutical Sciences, KU Leuven, Leuven, Belgium.

2012-2014                      Master in Pharmaceutical Sciences - Drug Development.  
  
*Master thesis:* Visualisation of PDE10A with the PET tracer [<sup>18</sup>F]JNJ152, *in vivo* and *in vitro* protocol optimization and implementation.  
  
Laboratory for Radiopharmacy, Faculty of Pharmaceutical Sciences, KU Leuven, Leuven, Belgium.

2009-2012                      Bachelor in Pharmaceutical Sciences.  
  
Faculty of Pharmaceutical Sciences, KU Leuven, Leuven, Belgium.

2003-2009                      ASO: Modern Languages - Sciences.  
  
St.-Dimpna College, Geel, Belgium.

## ***Additional courses and training***

2014                              Laboratory animal science module I.

2018-2019                      Courses followed to attain official recognition as radiopharmacist by FANC

- Introduction to nuclear physics
- Radiobiology
- Radioprotection
- Radiopharmaceutical analysis
- Radiopharmaceuticals and contrast enhancing products

## LIST OF PUBLICATIONS

### ***Publications in international peer reviewed journals***

Ahamed M, **Vermeulen K\***, Schnekenburger M, Moltzau LR, Levy FO, Marton J, Froeyen M, Olberg DE, Diederich M and Bormans G. Synthesis, enzyme assays and molecular docking studies of fluorinated bioisosteres of Santacruzamate A as potential HDAC tracers. *Lett. Drug Des. Discov.* 2017; 14:787–97. (\*Joint first authorship)

**Vermeulen K\***, Naus E\*, Ahamed M, Attili B, Siemons M, Luyten K, Celen S, Schymkowitz J, Rousseau F, Bormans G. Evaluation of [<sup>11</sup>C]NMS-E973 as a PET tracer for *in vivo* visualisation of HSP90. *Theranostics.* 2019; 9:554-572 (\* Joint first authorship)

**Vermeulen K**, Ahamed M, Luyten K, Bormans G. Evaluation of [<sup>11</sup>C]KB631 as a PET tracer for *in vivo* visualisation of HDAC6 in B16.F10 melanoma. *Nucl. Med. Biol.* Accepted for publication (2019).

### ***Participation at international meetings and published abstracts***

Synthesis of [<sup>18</sup>F]-FE-Martinostat for *in vivo* visualisation of histone deacetylase 2. Belnuc, Maastricht, The Netherlands, 08-09/05/2015, poster presentation.

Radiosynthesis of a selective HDAC6 inhibitor [<sup>11</sup>C]KB631 and *in vitro* and *ex vivo* evaluation, ESRR, Salzburg, Austria, 07-10/04/2016, oral presentation.

Development and evaluation of [<sup>11</sup>C]NMS-E973, a specific Hsp90 PET ligand for the use as a tumour imaging agent. MedChem, Mont-Saint-Guibert, Belgium, 18/11/2016, poster presentation.

*In vitro* and *ex vivo* evaluation of [<sup>11</sup>C]KB631, an HDAC6 selective PET tracer. Belnuc, Ghent, Belgium, 05-07/05/2017, oral presentation.

Development and evaluation of [<sup>11</sup>C]NMS-E973, a specific Hsp90 PET ligand for the use as a tumour imaging agent. ISRS, Dresden, Germany, 14-19/05/2017, poster presentation.

*In vitro* and *ex vivo* evaluation of [<sup>11</sup>C]KB631, an HDAC6 selective PET tracer. ULLA Summer School, Leuven, Belgium, 10-14/07/2017, poster presentation.

Development and evaluation of [<sup>11</sup>C]NMS-E973, a PET radiotracer for *in vivo* visualisation of Hsp90. EMIM, San Sebastian, Spain, 20-23/03/2018, poster presentation.

PET imaging with [<sup>11</sup>C]NMS-E973 reveals difference between healthy and malignant expressed Hsp90. ISRS, Beijing, People's Republic of China, 26-31/05/2019, poster presentation.

